

**Development of RAC devices fabricated using e-beam
lithography for Chirp Transform Spectrometers**

Dissertation

zur Erlangung des Doktorgrades
der Technischen Fakultät
der Albert-Ludwigs-Universität Freiburg im Breisgau
von

Xianyi Li
aus Xin Jiang, China

Freiburg im Breisgau
2010

Bibliografische Information der Deutschen Nationalbibliothek

Die Deutsche Nationalbibliothek verzeichnet diese Publikation in der Deutschen Nationalbibliografie; detaillierte bibliografische Daten sind im Internet über <http://dnb.d-nb.de> abrufbar.

Dekan : Prof. Dr. Hans Zappe, Univ. Freiburg.
Referent : Prof. Dr. Oliver Paul (Chair), Univ. Freiburg.
: Prof. Dr. Holger Reinecke (Co-Chair), Univ. Freiburg.
: Prof. Dr. Leonhard Reindl (Supervising Tutor), Univ. Freiburg.
: Prof. Dr. Robert Weigel (Examiner), Univ. Erlangen.
Datum der Promotion : 26.07.2010

ISBN 978-3-942171-38-0

uni-edition GmbH 2010

<http://www.uni-edition.de>

© Xianyi Li



This work is distributed under a
Creative Commons Attribution 3.0 License

Printed in Germany

**DEDICATED TO
MY PARENTS!**

Contents

Zusammenfassung	xv
Abstract	xvii
List of Abbreviations	xix
1 Introduction	1
1.1 Applications for CTS in radio astronomy	1
1.2 Chirp Transform Spectrometer (CTS)	3
1.2.1 Basic principle of CTS	4
1.2.2 Advantages and limitations of the CTS	7
1.3 Motivations for developing large time bandwidth product RACs	8
1.4 RAC devices - literature review	9
1.5 A brief summary of the PhD work	12
2 Design and modeling of groove reflective array	13
2.1 Design of the groove reflective array	13
2.1.1 Groove pitch and groove oblique angle	13
2.1.2 Groove position	14
2.2 First order impulse response model for reflective array	16
2.3 The reflection loss for reflective array	19
2.4 Other loss items of a RAC	21
2.4.1 Propagation loss	22
2.4.2 Transmission loss	23
2.5 Experimental results compared to the first order simulations	24
3 Building blocks of RAC devices	29
3.1 RAC layout	29
3.2 Optimized interdigital transducer (IDT)	30
3.2.1 FEM/BEM simulation of the IDT performance	33
3.2.2 Simple delay line measurement and IDT loss characterization	37
3.3 Single groove reflectivity for oblique SAW incidence	44
3.4 Single electrode parameter extraction on 128° YX LiNbO ₃	46
3.4.1 S_{11} parameter analysis	47
3.4.2 Theory for parameter extraction	48
3.4.3 Measurement results	50
3.5 Extra grooves at array ends	52

3.6	RAC encapsulation and matching	55
3.6.1	Equivalent circuit of RACs' input and output ports	55
3.6.2	Matching network numerical filtering	57
4	Weighting techniques in RAC design using e-beam lithography	61
4.1	Motivations	61
4.1.1	Correction of the passband shape nonuniformity	61
4.1.2	Reduction of the multiple reflections at high frequencies	62
4.2	Compressed pulse calculation for the fabricated RAC filters	66
4.3	Amplitude weighting techniques	66
4.3.1	Conventional groove depth profile weighting	68
4.3.2	Aperture weighting	68
4.3.3	Groove duty cycle weighting	73
4.3.4	Pair grooves position weighting	78
5	Phase deviation compensation for RAC devices	81
5.1	Determination of phase deviation from measurement	81
5.2	Phase compensations by 50 nm Al stripe	83
5.3	Experiments for phase compensation	85
5.3.1	Extraction of compensation constant using measured magnitude	85
5.3.2	Extraction of the compensation constant using measured phase	89
6	Developed RAC filters	93
6.1	Development of RAC filter I	93
6.1.1	Design parameters of RAC filter I	93
6.1.2	Magnitude optimization for RAC filter I	93
6.1.3	Dose variation for groove array exposure	97
6.1.4	Measurement result and discussion	98
6.2	Development of RAC filter II	98
6.2.1	Design parameters for RAC filter II	98
6.2.2	Magnitude optimization	98
6.2.3	Dose variation for groove array exposure	100
6.2.4	Measurement result and discussions	101
7	Summary and conclusion	107
7.1	Estimation of available RAC parameters on YZ-LiNbO ₃	107
7.1.1	The maximum bandwidth on YZ-LiNbO ₃	107
7.1.2	The maximum dispersive delay on YZ-LiNbO ₃	108
7.1.3	The maximum time bandwidth product (<i>BT</i>) on YZ-LiNbO ₃	108
7.2	Future work	108
A	Magnitude optimization of RACs (simulations)	111
A.1	$B = 400$ MHz, $T = 30$ μ s, $f_c = 1$ GHz RAC	111
A.2	$B = 400$ MHz, $T = 40$ μ s, $f_c = 1$ GHz RAC	113
A.3	$B = 700$ MHz, $T = 10$ μ s, $f_c = 1.35$ GHz RAC	115

B	Electrode parameter extraction from TS1, 2 and 3	117
B.1	TS1, electrode: $a = 0.8 \mu\text{m}$, $a/p = 0.4$, $h = 100 \text{ nm}$	118
B.2	TS2, electrode: $a = 1.2 \mu\text{m}$, $a/p = 0.6$, $h = 200 \text{ nm}$	119
B.3	TS3, electrode: $a = 1.0 \mu\text{m}$, $a/p = 0.5$, $h = 100 \text{ nm}$	120
C	Electron beam lithography	121
C.1	Advantages and drawbacks of e-beam lithography	121
C.2	Building blocks of the EBPG5000+ electron beam lithography machine .	121
C.3	Electron scattering and proximity effect	123
D	Fabrication processes flow for RACs	127
E	Transformation between S, Y and Z parameters [81]	129
F	Holder case design for $T = 10 \mu\text{s}$ RAC	131
	Bibliography	133
	Publications	141
	Acknowledgements	143

List of Figures

1.1	Planetary atmosphere molecular absorptions	2
1.2	Block diagram of a heterodyne system	3
1.3	Pressure and thermal broadening effect of gas molecular rotational transition spectral line	4
1.4	230 GHz CO absorption line retrieval from the atmosphere of Venus	5
1.5	Principle of the Chirp Transformation	6
1.6	Different spectrometer types and techniques	7
2.1	SAW reflection by two adjacent grooves	13
2.2	Down chirp filter frequency delay relationship	15
2.3	Illustration for groove positions of RAC device	16
2.4	SAW reflection from one pair of grooves	17
2.5	Impulse response simulation of the groove array	17
2.6	SAW propagation path in RAC devices	18
2.7	Stationary reflection phase	20
2.8	Cornu-Spiral of impulse response model simulation at 1 GHz	21
2.9	Geometrical factor for reflection loss	22
2.10	Propagation loss for $f_c = 1$ GHz, $B = 400$ MHz and $T = 10 \mu s$ down chirp filter	23
2.11	Transmission loss for $f_c = 1$ GHz $B = 400$ MHz and $T = 10 \mu s$ down chirp filter	24
2.12	Comparison of experiment with impulse response model and SPA approximation simulations for $BT = 4000$ RAC	25
2.13	Rectangular shape groove array versus parallelogram shape groove array	26
2.14	Comparison of experiment with SPA approximation simulation for $BT = 8000$ RAC	27
3.1	Layout of the RAC filter with $T = 10 \mu s$	29
3.2	Uniform IDT geometry	30
3.3	One pair reverted IDT geometry	31
3.4	Impulse response comparison between uniform IDT and one pair reverted IDT	31
3.5	Magnitude comparison between uniform IDT and pair reverted IDT	32
3.6	SEM image for pair reverted IDT	33

3.7	FEM/BEM simulated S_{11} and S_{22} parameters in the Smith chart for uniform IDT with center frequency $f_c = 1$ GHz, five electrodes and aperture $W = 780 \mu\text{m}$. The influence of the package parasitics and the matching network are not taken into account.	34
3.8	Measured S_{11} and S_{22} parameters in the Smith chart of the uniform IDT with center frequency $f_c = 1$ GHz, five electrodes and aperture $W = 780 \mu\text{m}$. The package parasitics and the matching network are included in the measurement.	35
3.9	Delay line insertion loss comparison between FEM/BEM simulation and experimental result for aperture $W = 780 \mu\text{m}$, 1 GHz, 5 electrodes uniform IDT	35
3.10	Measured impulse response for the uniform IDT delay line.	36
3.11	FEM/BEM simulated impulse response for the uniform IDT delay line.	37
3.12	Propagation path for pulses in Figure 3.10 and Figure 3.11	38
3.13	Delay line phase and delay comparison between FEM/BEM simulation and measurement for aperture $W = 780 \mu\text{m}$, 1GHz, 5 electrodes uniform IDT	39
3.14	Delay line layout for aperture $W = 780 \mu\text{m}$, eight electrodes pair reverted transducer centered at 1 GHz	39
3.15	Measured S_{11} and S_{22} parameters in the Smith chart of the pair reverted transducer with center frequency $f_c = 1$ GHz, eight electrodes and aperture $W = 780 \mu\text{m}$	40
3.16	Measured phase of the PRT delay line with eight electrodes and aperture $W = 780 \mu\text{m}$	40
3.17	Measured delay of the PRT delay line with eight electrodes and aperture $W = 780 \mu\text{m}$	41
3.18	Measured insertion attenuation of the PRT delay line with eight electrodes and aperture $W = 780 \mu\text{m}$	41
3.19	Impulse response of eight electrodes aperture $W = 780 \mu\text{m}$ PRT	42
3.20	Propagation path of pulses P0, P1, P2, P3 and P4	42
3.21	Time gating for IDT loss characterization	43
3.22	Magnitude curve of PRT after time gating	43
3.23	TEM image for 40 nm single groove	44
3.24	Illustration for 90° SAW reflection by a single groove	45
3.25	Layout for parameter extraction test structures	47
3.26	Propagation path of reflected signal S_1, S_2, S_3 and S_4	48
3.27	Measured S_{11} parameter of the test structure	50
3.28	Four required pulses for parameter extraction in the time domain from TS2 measurement	51
3.29	Extracted propagation coefficients k and γ from TS2 measurement.	52
3.30	Rectangular shape groove array versus parallelogram shape groove array	53
3.31	RAC measured magnitude comparison between the parallelogram shape groove array layout and rectangular shape groove array layout.	54
3.32	Encapsulation of RAC filter top view	55
3.33	Encapsulation of RAC filter bottom view	56
3.34	Equivalent circuits of the input and output ports for encapsulated RAC	56

3.35	Measured magnitude of S_{21} and S_{11} parameters for unweighted $BT = 4000$ RAC before the matching network is optimized, the nonuniformity of the S_{21} magnitude in the passband is about 14 dB.	57
3.36	S_{11} parameter in Smith chart before and after matching is optimized.	58
3.37	Numerical filtering for required matching network	58
3.38	Measured S_{21} and S_{11} parameters magnitude after the optimized matching, the S_{21} magnitude nonuniformity in the passband is reduced to only 7 dB.	59
4.1	Insertion Loss curve without amplitude weighting	62
4.2	Compressed pulse for the unweighted RAC filter	63
4.3	Reflection loss simulation of 40 nm groove depth reflective array using stationary phase approximation	63
4.4	Phase deviation caused by multiple reflections	64
4.5	Magnitude ripples caused by multiple reflections	64
4.6	Reflection loss simulation of 25 nm groove depth reflective array	65
4.7	Phase deviation with small multiple reflections	65
4.8	Illustration of the magnitude correction factor calculation	67
4.9	Machine for depth profile etching	69
4.10	Aperture weighting without extra dummy grooves	70
4.11	SAW propagation in the aperture weighted groove array	70
4.12	Measured filter magnitude using aperture weighting without extra dummy grooves	71
4.13	Aperture weighting with extra dummy grooves on both sides	71
4.14	Measured filter magnitude using aperture weighting with extra dummy grooves on both sides	72
4.15	Aperture weighting with extra grooves on one side	72
4.16	Measured filter magnitude using aperture weighting with extra dummy grooves on one side	73
4.17	Principle of the groove duty cycle weighting	74
4.18	Duty cycle profile for $BT = 4000$, $f_c = 1$ GHz RAC filter	74
4.19	The Atom Force Microscope (AFM) images for the 18% duty cycle high frequency grooves and 50% duty cycle low frequency grooves, they are all with 40 nm constant depth.	75
4.20	Measured filter magnitude using the duty cycle weighting for $BT = 4000$, $f_c = 1$ GHz filter	75
4.21	Compressed pulse from the duty cycle weighted RAC filter	76
4.22	Phase deviation of the duty cycle weighted RAC filter	77
4.23	Principle of the position weighting	78
5.1	Measured quadratic phase curve for a $BT = 4000$ RAC filter	82
5.2	Measured phase deviation for a $BT = 4000$ RAC filter	83
5.3	SAW velocity change caused by Al film on $YX\text{-LiNbO}_3$	84
5.4	Calculated phase stripe width for phase deviation compensation	84
5.5	Designed Al stripes for the phase compensation experiment	85
5.6	Measured filter magnitude before the Al stripes are added	86

5.7	Measured filter magnitude after the phase compensation	86
5.8	Explanation for the magnitude attenuation peaks	87
5.9	Groove reflection vector summing	87
5.10	Left and right SAW beam vector summing	88
5.11	Extracted phase compensation coefficient according to ΔIL_i	89
5.12	Phase jumps generated by the added Al stripes	90
5.13	Extracted phase compensation coefficient according to the measured phase jumps	91
6.1	Upper one is the measured S_{21} magnitude for the aperture $W = 550 \mu\text{m}$ and eight electrodes transducer with one pair reverted IDT (the structure is shown in Figure 3.3). The lower one is its performance after the time gating shown in Chapter 3.	94
6.2	Groove array reflection loss simulation for RAC filter I before weighting is applied	94
6.3	The simulated SAW propagation loss in RAC filter I	95
6.4	Insertion loss simulation for RAC filter I before weighting is applied	95
6.5	Optimized duty cycle profile for RAC filter I	96
6.6	Filter I groove array reflection loss simulation after the duty cycle weighting	96
6.7	Insertion loss comparison between simulation and experimental result for RAC filter I.	97
6.8	Layout of RAC filter I	97
6.9	Measured phase and the phase deviation of RAC filter I.	99
6.10	Measured group delay and compressed pulse of RAC filter I.	100
6.11	Upper one is the measured S_{21} magnitude for aperture $W = 780 \mu\text{m}$ and eight electrodes transducer with one pair reverted transducer as shown in Figure 3.3. The lower one is its performance after the time gating as shown in Chapter 3.	101
6.12	The simulated reflection loss and transmission loss of the groove array in RAC filter II before the weighting is applied.	101
6.13	The simulated SAW propagation loss in RAC filter II	102
6.14	Synthesized insertion loss for RAC filter II before weighting is applied	102
6.15	Optimized duty cycle profile for RAC filter II	103
6.16	The simulated reflection loss and transmission loss of the groove array after the duty cycle profile of the groove array is optimized.	103
6.17	Comparison of the insertion loss between the simulation and experimental result for RAC filter II.	104
6.18	Layout of RAC filter II	104
6.19	Measured phase and phase deviation of RAC filter II.	105
6.20	Measured group delay and compressed pulse of RAC filter II.	106
7.1	Maximum fractional bandwidth for ST quartz and YZ lithium niobate	107
A.1	Magnitude optimization for $B = 400 \text{ MHz}$, $T = 30 \mu\text{s}$, $f_c = 1 \text{ GHz}$ RAC filter (part 1).	111
A.2	Magnitude optimization for $B = 400 \text{ MHz}$, $T = 30 \mu\text{s}$, $f_c = 1 \text{ GHz}$ RAC filter (part 2).	112

A.3	Magnitude optimization for $B = 400$ MHz, $T = 40$ μ s, $f_c = 1$ GHz RAC filter (part 1).	113
A.4	Magnitude optimization for $B = 400$ MHz, $T = 40$ μ s, $f_c = 1$ GHz RAC filter (part 2).	114
A.5	Magnitude optimization for $B = 700$ MHz, $T = 10$ μ s, $f_c = 1.35$ GHz RAC filter (part 1).	115
A.6	Magnitude optimization for $B = 700$ MHz, $T = 10$ μ s, $f_c = 1.35$ GHz RAC filter (part 2).	116
B.1	Parameter extractions from TS1 for floating electrode: $a = 0.8$ μ m, $a/p = 0.4$, $h = 100$ nm.	118
B.2	Parameter extractions from TS2 for floating electrode: $a = 1.2$ μ m, $a/p = 0.6$, $h = 200$ nm.	119
B.3	Parameter extractions from TS3 for floating electrode: $a = 1.0$ μ m, $a/p = 0.5$, $h = 100$ nm.	120
C.1	Photo of the EBPG5000+ e-beam lithography system in the clean room	122
C.2	Building blocks of EBPG5000+ e-beam lithography system	122
C.3	Monte Carlo simulation of trajectories for 200 electrons in Cr (20 nm)/PMMA (220 nm)/YZ-LiNbO ₃ for 500 nm depth.	124
C.4	Monte Carlo simulation of trajectories for 200 electrons in Cr (20 nm)/PMMA (220 nm)/YZ-LiNbO ₃ for 18 000 nm depth.	125
F.1	Holder case top view	131
F.2	Holder case front view	131
F.3	Holder case bottom view	132

List of Tables

1.1	The history of CTS developments in the MPS until 2005 [29].	9
1.2	Two types of down chirp RAC developed during the PhD.	12
3.1	Distances of D1 D2 and D3 in the IDT layout	38
3.2	Delay time of the pulses P0, P1, P2, P3 and P4	42
3.3	Fitted constants C and C' from measurements	46
3.4	Electrode types in TS1, 2 and 3	47
3.5	Delay time of signal S_1, S_2, S_3 and S_4	48
3.6	Extracted parameter from TS1, 2 and 3 compared with Sanna Harma, Saku Lethonen and Weibiao Wang's work	53
5.1	Experimental phase compensation constant extraction from the measured magnitude attenuation peaks	89
5.2	Experimental phase compensation constant extraction from the measured phase jumps	90
D.1	Fabrication processes flow for RACs	128

Zusammenfassung

Der *Reflective Array Compressor* (RAC) ist ein Hochleistungsgerät, das weite Verbreitung in Radargeräten findet und auf akustische Oberflächenwellen (AOW) basiert. Diese Doktorarbeit befasst sich mit einem weiteren wichtigen Anwendungsgebiet von RACs: dem *Chirp Transform Spectrometer* (CTS). Dieses Messinstrument ist aufgrund seines geringen Gewichts und der niedrigen Leistungsaufnahme gut geeignet für integrierte (*on Board*) Anwendungen in der Weltraumforschung; hier vor allem bei der Erfassung von planetaren Atmosphären.

Die Leistungsdaten des CTS, wie zum Beispiel Bandbreite und Frequenzauflösung werden hauptsächlich durch den verwendeten RAC-Filter bestimmt. Daher ist die Entwicklung eines RAC-Filters mit einem grossen Zeit-Bandbreite-Produkt in der CTS-Technologie für die Radioastronomie entscheidend bei der Bestimmung planetarer Atmosphären mittels Mikrowelle.

Diese Dissertation konzentriert sich auf den Aufbau, die Modellierung und Entwicklung von auf AOW basierenden Chirp-Filtern, welche mittels Elektronenstrahlolithographie (ESL) hergestellt werden.

Wichtige Bausteine eines RACs sind verlustarme Wandler mit hoher Bandbreite und das *Weighted Reflector Array*. Die simultane Optimierung beider Einheiten ist notwendig, um eine gleichmässige Amplitude der Transferfunktion mit minimalen Phasenfehlern zu erreichen. Wir verwenden von uns entwickelte, experimentell untersuchte und optimierte *Pair Reverted Interdigital Transducers* (PRT). Die *Depth Profile Weighting*-Methode, welche üblicherweise in früheren Entwicklungen verwendet wurde, konnte aufgrund des Fehlens einer entsprechenden speziellen *Scanning Ion Beam Etching*-Anlage in der Physikalisch Technischen Bundesanstalt Braunschweig (PTB) nicht verwendet werden. Deshalb wurden andere Methoden der Amplitudengewichtung für die Filter-Amplitudenmanipulation bei konstanter Spurtiefe erforscht, inklusive Gewichtung der Blendenöffnung und des Spur-Tastverhältnisses. Wir zeigen, dass die Gewichtung des Spur-Tastverhältnisses gut geeignet ist bei der Herstellung von RAC-Filtern mittels Elektronenstrahlolithographie, da mittels ESL Spurbreiten im Submikronbereich erreicht werden können. Dadurch wird eine Kontrolle der Reflektivität in einem weiten Bereich möglich. Mit dieser Methode kann eine optimierte Rechteckantwort des Filters mit ausreichend niedriger Phasenabweichung erzielt werden.

Mit Hilfe dieser Gewichtungsmethode wurden zwei Typen von RAC mit einem grossen Zeit-Bandbreite-Produkt (BT) und guten Leistungsdaten entwickelt (Einer mit $BT = 4000$ und der Andere mit $BT = 8000$). Drei weitere Typen von RAC-Filtern mit gleichen oder grösseren Werten für BT ($BT = 7000, 12000$ und 16000) wurden, basierend auf experimentell charakterisierten PRTs, mit Hilfe der *Stationary Phase Approximation Reflective Array Simulation* simuliert. Abschliessend wurde das maximale erreichbare BT von

RAC-Filtern mit $BT = 16000$ für $YZ\text{-LiNbO}_3$ bestimmt.

Als ein Nebenprodukt wurden drei Elektrodentypen, mittels der experimentellen Methode zur Bestimmung ihrer frequenzabhängigen Reflektion und der Parameter der Transmission und Volumenwellendiffusion, auf 128° $YZ\text{-LiNbO}_3$ charakterisiert. Diese Parameter können zur Entwicklung von auf akustische Oberflächenwellen basierenden Anwendungen wie *SAW-Tags* (RFID), SAW-Sensoren oder *Inline Refelected Array Chirp Filter* verwendet werden. Zusätzlich wurden Versuche mit 50 nm dicken Aluminiumstreifen zwischen den beiden Reflektoreinheiten durchgeführt. Die effektive Phasenkompensation wurde aus den Messergebnissen abgeleitet.

Abstract

Based on surface acoustic waves (SAW), the reflective array compressor (RAC) is a high performance device widely used in modern radars. This thesis deals with another important application of RACs – the Chirp Transform Spectrometer (CTS). This instrument due to its low weight and power consumption, can be used for on-board applications in space research, in particular for the remote sensing of planetary atmosphere.

The performances of the CTS, such as input bandwidth and frequency resolution, are mainly determined by the performance of the RAC filter used in it. Thus, the development of a large time bandwidth product RAC filter is essential for CTS technology in microwave atmospheric remote sensing for radio astronomy.

This dissertation focuses on the design, modeling and development of the surface acoustic wave RAC type chirp filters using standard electron beam lithography (EBL) technology.

Important building blocks of the RAC are the low loss wide bandwidth transducer and the weighted reflector array. The simultaneous optimization of both is necessary to achieve an uniform response with minimal phase errors. We used optimized pair reverted interdigital transducers (PRT) which we designed and studied experimentally. As the depth profile weighting method used in early developments is not available for us at the Physikalisch-Technische Bundesanstalt (PTB) due to the lack of related special scanning ion beam etching equipment, other kinds of amplitude weighting methods were researched for the filter magnitude modulation with constant groove depth, including aperture weighting and duty cycle weighting. We showed that the duty cycle weighting method is an effective method in the fabrication of RAC type filters using e-beam lithography, as with EBL we can make grooves of submicron width, which allows us to control the reflectivity in a wide range. Using this method, an optimized rectangular passband shape with reasonably small phase deviation can be achieved.

Utilizing this kind of weighting technique, two types of large time bandwidth product RAC filters with good performances were developed (one with $BT = 4000$ and the other with $BT = 8000$). Three other types of RAC filters with equal or higher time bandwidth products ($BT = 7000$, $12\,000$ and $16\,000$) were simulated based on the experimental characterized PRT and stationary phase approximation reflective array simulation. Finally, the maximum achievable time bandwidth product of RAC type filters was estimated to be about $16\,000$ for YZ-LiNbO₃.

As a “side product” three types of single electrodes were characterized using the experimental method for their frequency dependent reflection, transmission and bulk wave scattering parameters on 128° YX LiNbO₃. These parameters can be used in the design of SAW radio frequency identifications (RFIDs), SAW sensors or inline reflective array chirp filters.

Also experiments were performed for phase deviation compensations using 50 nm Al stripes between the two arrays of reflectors. The practical phase compensation coefficient was derived using the measurement results.

List of Abbreviations

ACF	Autocorrelation Function
ADC	Analog to Digital Converter
AFM	Atom Force Microscope
AOS	Acousto-Optical Spectrometer
BAW	Bulk Acoustic Wave
BPF	Bandpass Filter
CCD	Charge-Couple Device
CD	Critical Dimension
CTS	Chirp Transform Spectrometer
CVD	Chemical Vapor Deposition
DAC	Digital to Analog Converter
DAS	Digital Autocorrelation Spectrometers
DCW	Duty Cycle Weighting
DDL	Dispersive Delay Line
EBL	Electron Beam Lithography
FEM/BEM	Finite Element Method/Boundary Element Method
FFT	Fast Fourier Transform
FFTS	Fast Fourier Transform Spectrometer
FPGA	Field Programmable Gate Arrays
GREAT	German REceiver for Astronomy at Terahertz frequencies
IDT	Interdigital Transducer
IF	Intermediate Frequency
LFM	Linear Frequency Modulation
MPS	Max Planck Institut for Solar System Research
MIRO	Microwave Instrument for Rosetta Orbitor
PRT	Pair Reverted Transducer
PTB	Physikalisch-Technische Bundesanstalt
RFID	Radio-Frequency Identification
RAC	Reflective Array Compressor
RDA	Reflective Dot Array
SAW	Surface Acoustic Wave
SEM	Scanning Electron Microscope
SOFIA	Stratospheric Observatory For Infrared Astronomy
SPA	Stationary Phase Approximation
SPUDT	Single Phase UniDirection Transducer
TEM	Transmission Electron Microscope
VNA	Vector Network Analyzer

1 Introduction

1.1 Applications for real time Chirp Transform Spectrometers in radio astronomy

If people use a radio telescope to observe the emissions and absorptions from earth's or another planet's atmosphere, the received electromagnetic signals are normally generated by the rotational quantum transitions of the nonsymmetrical gas molecules in the atmosphere, e.g. CO , O_3 , water vapor, HCN etc. As normally these molecules' rotational statuses are at discrete quantum energy levels, when they receive or lose rotational momentum, the emitted or absorbed radiowave signals are at a certain fixed center frequency due to Planck's law. For example, the center frequencies of radiowave absorptions for responsible gases in the atmospheres of earth and other planets are shown in Figure 1.1. As we can see that these signals are mostly centered at a several hundred GHz frequency (microwave range), it is necessary to use heterodyne technology to down convert the emissions or absorptions to the center frequency of several GHz (see Figure 1.2). Then it is possible to use a spectrometer to analyze the down converted signals in the spectrum domain.

There are many available technologies for performing the spectrum domain analysis (real time Fourier Transformation). These different technologies will be discussed and compared in detail in the next section. Among these technologies, the Chirp Transform Spectrometer (CTS) is one of the most important methods. Such features of the CTS as low power, small mass and volume and high spectral resolution, are very suitable for space-based observatory in radio astronomy.

The history of the development of this technology started in the 1970s, and the Max Planck Institute for Solar System Research (MPS) started CTS development in the 1980s (see Table 1.1). The past development effort of CTS in the MPS was quite successful, and the hardware was successfully applied in different projects (for spacecraft, aerospace and also ground-based observatories). Three examples are provided in the following.

1. CTS for the MIRO (Microwave Instrument for Rosetta Orbiter) project [3]: This is the first CTS application in the spacecraft-based observatory. It is installed on the European Space Agency Rosetta Spacecraft which was launched on March 2, 2004 toward comet 67P/Churyumov-Gerasimenko. The CTS was developed (starting in 1997) with a 180 MHz bandwidth, and a total of 4096 frequency channels in band, centered at 1.35 GHz center frequency. This spectrometer is designed for collecting six kinds of different molecules' (three volatile species: CO , CH_3OH , NH_3 and three, oxygen-related isotopologues of water, $H_2^{16}O$, $H_2^{17}O$ and

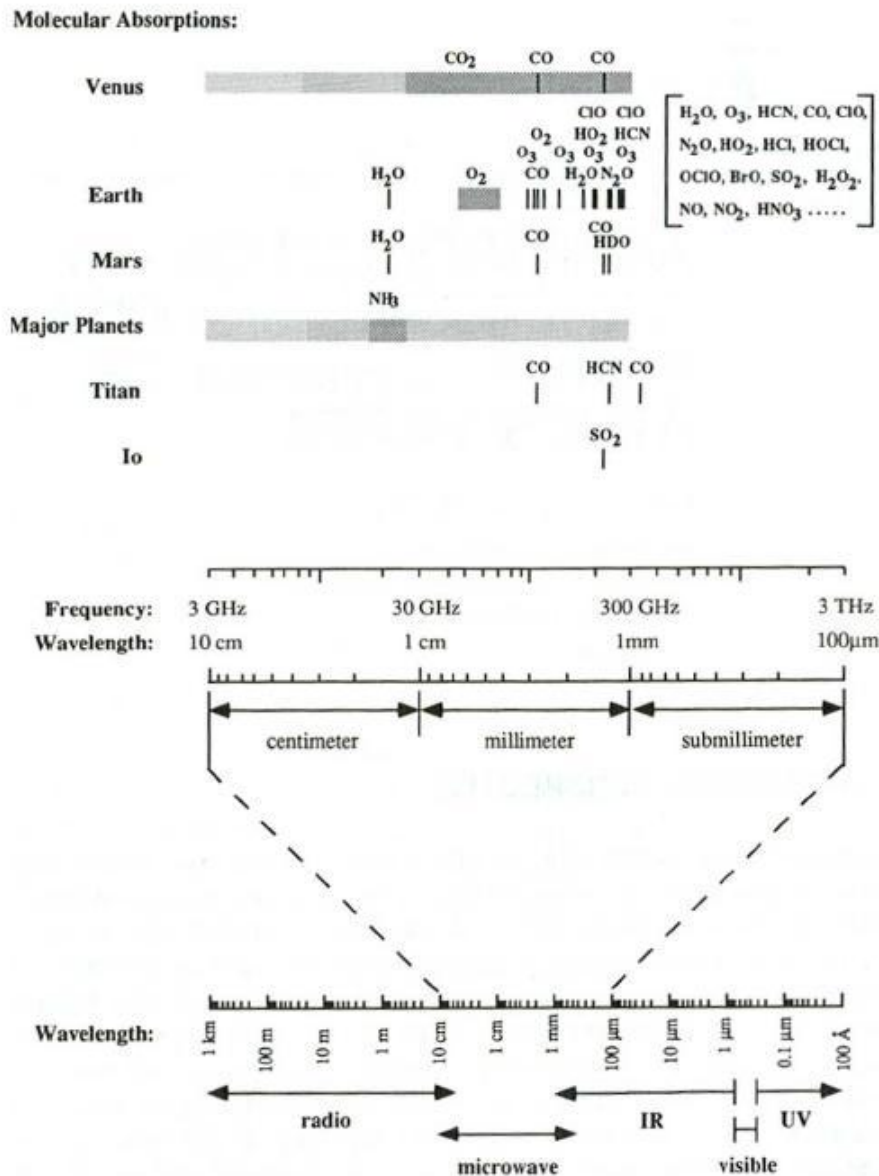


Figure 1.1: Gases responsible for absorption of radiowaves in the atmospheres of the earth and other planets, from Janssen [1] 1993.

$H_2^{18}O$) rotational transitions from comet 67P/Churyumov-Gerasimenko. Each kind of molecule needs 30 MHz bandwidth, in total 180 MHz bandwidth. For this spectrometer, the total power consumption is less than 15 W and the mass is only about 2.3 kg (see Table 1.1 for year 1997).

2. CTS for the SOFIA (Stratospheric Observatory For Infrared Astronomy) project [31]: A CTS was developed with a 220 MHz bandwidth and 7500 channels centered at 2.1 GHz as part of the “German REceiver for Astronomy at Terahertz frequencies” (GREAT) on the SOFIA (starting in 1998). “This receiver is with a low-frequency band at 1.6 - 1.9 THz; a mid-frequency band centered on the cosmologically relevant 1-0 transition of deuterated molecular hydrogen at 2.6 THz;

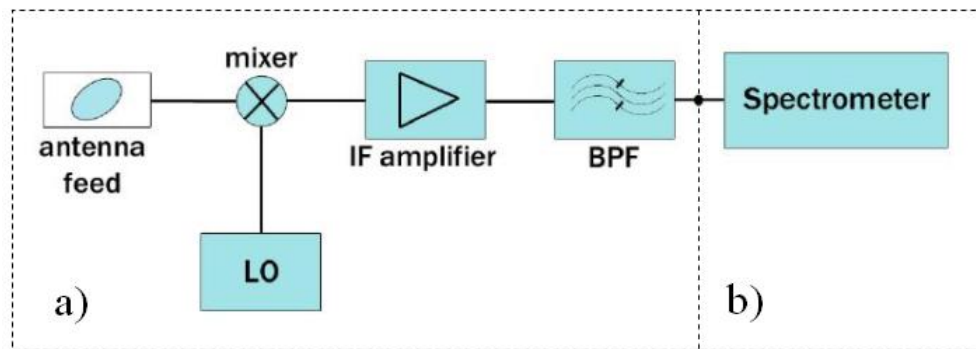


Figure 1.2: Block diagram of a heterodyne receiver system composed of a) front end: the antenna, mixer, local oscillator (LO), bandpass filter (BPF) and intermediate frequency amplifier; b) back end: spectrometer. [33]

and a high-frequency band located in the far-IR region targeting the 4.7 THz fine-structure transition of atomic oxygen. The coverage of such broad frequency bands, combined with the remarkable improvement in sensitivity if compared to ground-based observatories by flying at 15 km altitude with SOFIA, offers the possibility to detect a large number of molecules.”[32] The CTS is used as a unique tool to remotely sense planetary atmospheres, obtaining circulation information (winds, temperatures) and vertical profiles of minor species as retrieved from the highly resolved spectral lines.

3. The same kind of CTS as in the SOFIA project is also being developed and integrated into the ground-based observatory - the Heinrich Hertz Submillimeter Telescope at Mt. Graham in Arizona. “It was used for a wide range of topics concerning modern astrophysics, from questions about comets, planetary atmospheres and the interstellar medium in the galaxy, to investigations related to the early Universe.” [32]

In Figure 1.4, one observation for the CO absorption spectral line centered at 345 GHz from the atmosphere of Venus is shown. Due to the pressure and thermal broadening effect for the spectral line shape (see Figure 1.3) with altitude decreases, the temperature and volume mixing ratio distributions versus altitude for the CO molecules could be retrieved from the measured spectral line using CTS. These measured values are shown in the right half of Figure 1.4. This information is of the most interest to astronomers [2].

1.2 Chirp Transform Spectrometer (CTS)

From the discussions presented above, one can see that the Chirp Transform Spectrometer (CTS) is a very powerful tool for planetary microwave atmospheric remote sensing. In the following sections the principles of the CTS are reviewed in more detail.

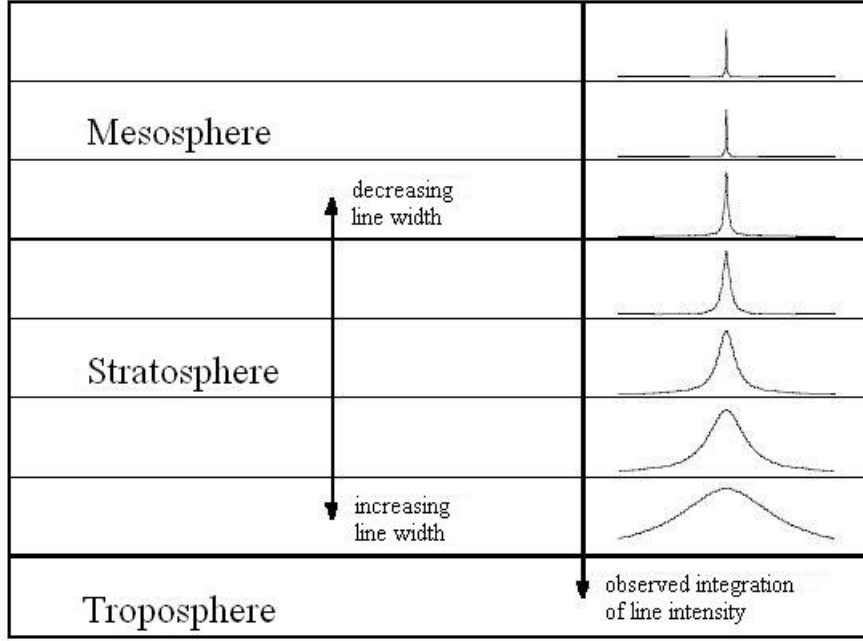


Figure 1.3: The rotational transition spectral line shape from different layers of the atmosphere at different altitudes.

1.2.1 Basic principle of CTS

The principle of the Chirp Transformation is derived from the Fourier Transformation in Equation 1.1 [4].

$$F(\omega) = \int_{-\infty}^{+\infty} f(t) \cdot e^{-j\omega t} dt \quad (1.1)$$

Let us consider a linear chirp signal which is also called a linear frequency modulated signal. It is defined in Figure 1.2 for an up chirp and in Equation 1.3 for a down chirp, both with quadratic phase modulation. Up chirp stands for a signal starting with a low and ending a high frequency while a down chirp starts with a high frequency and ends with a low frequency.

$$Ch_+(t) = e^{j\frac{1}{2}2\pi\mu t^2} \quad (1.2)$$

$$Ch_-(t) = e^{-j\frac{1}{2}2\pi\mu t^2} \quad (1.3)$$

If we take Equation 1.1 and replace the exponent of the Fourier Transform by a linear chirp component $\omega = 2\pi\mu \cdot t$, the Fourier Transform becomes:

$$F(\mu t) = \int_{-\infty}^{+\infty} f(\tau) \cdot e^{-j2\pi\mu t\tau} d\tau \quad (1.4)$$

For any t and τ values, the following relationship is valid:

$$t\tau = -\frac{1}{2}(t - \tau)^2 + \frac{1}{2}t^2 + \frac{1}{2}\tau^2 \quad (1.5)$$

When Figure 1.5 is substituted into Figure 1.4, the Chirp Transform can be derived.

$$F(\omega) = F(\mu t) = e^{j\frac{1}{2}2\pi\mu t^2} \cdot \int_{-\infty}^{+\infty} [f(\tau) \cdot e^{j\frac{1}{2}2\pi\mu\tau^2}] \cdot e^{-j\frac{1}{2}2\pi\mu(t-\tau)^2} d\tau \quad (1.6)$$

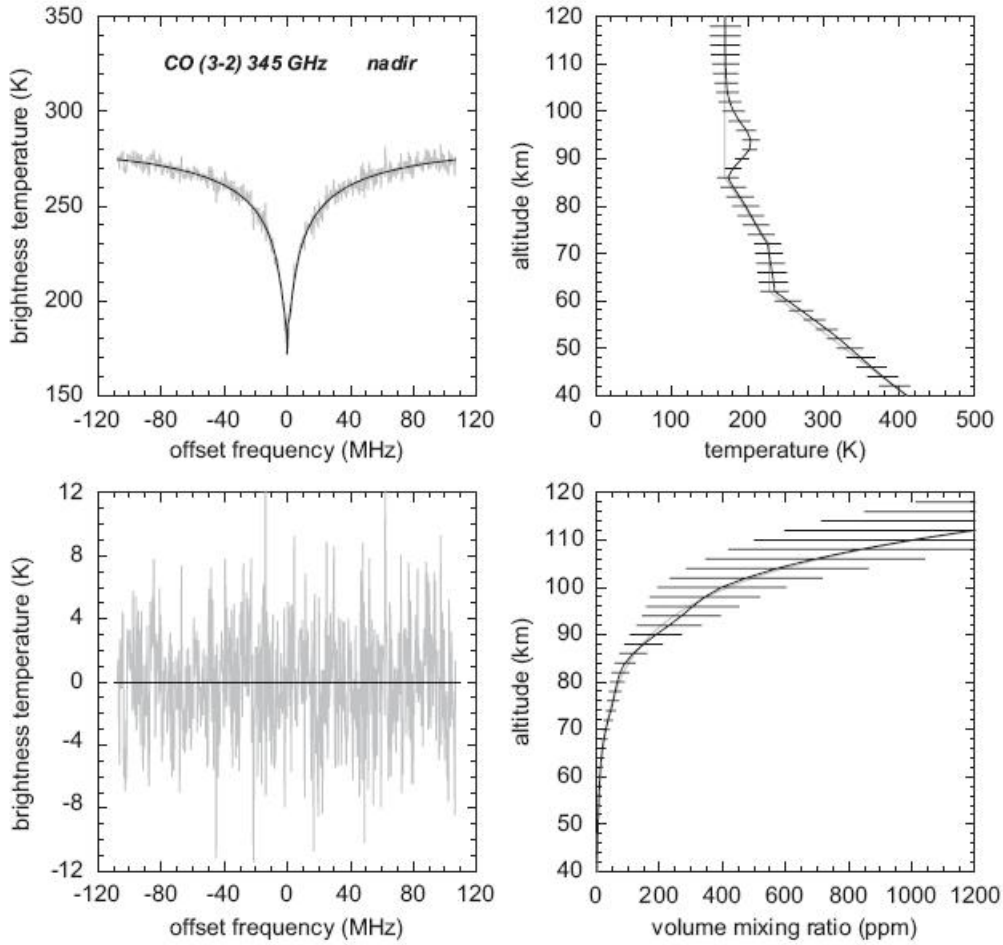


Figure 1.4: The 230 GHz CO absorption line retrieval from the atmosphere of Venus. The upper left panel shows the synthetic spectra solution for the observed spectra; the lower left panel, the difference between the observed and fitted spectra. The upper and lower right panels indicate the retrieved temperature and CO abundance profiles derived from the spectrum. The gray lines show the initial profiles, and the horizontal lines are the error bars. [2]

By substituting Equation 1.2 and Equation 1.3 into Equation 1.6, the final form of the Chirp Transformation becomes:

$$F(\mu t) = Ch_-(t) \cdot [(f(t) \cdot Ch_+(t)) \otimes Ch_-(t)] \quad (1.7)$$

As shown above, the chirp transform consists of a multiplication of the signal to be analyzed with the down chirp signal, then a convolution with a matched up chirp signal and another multiplication with the down chirp signal as in the first one. Hence, this kind of system is called an M-C-M system. The purpose of the last multiplication is to correct the phase of the output of the chirp transformer. If we do not need the spectral phase of the signal, the last mixing can be omitted. Then only the power spectrum of the signal is calculated. The chirp transform with the last multiplication omitted is called an M-C system. A typical M-C transformation system which can perform the power spectrum calculation

is shown in Figure 1.5. The up chirp signal for the first multiplication is supplied by the

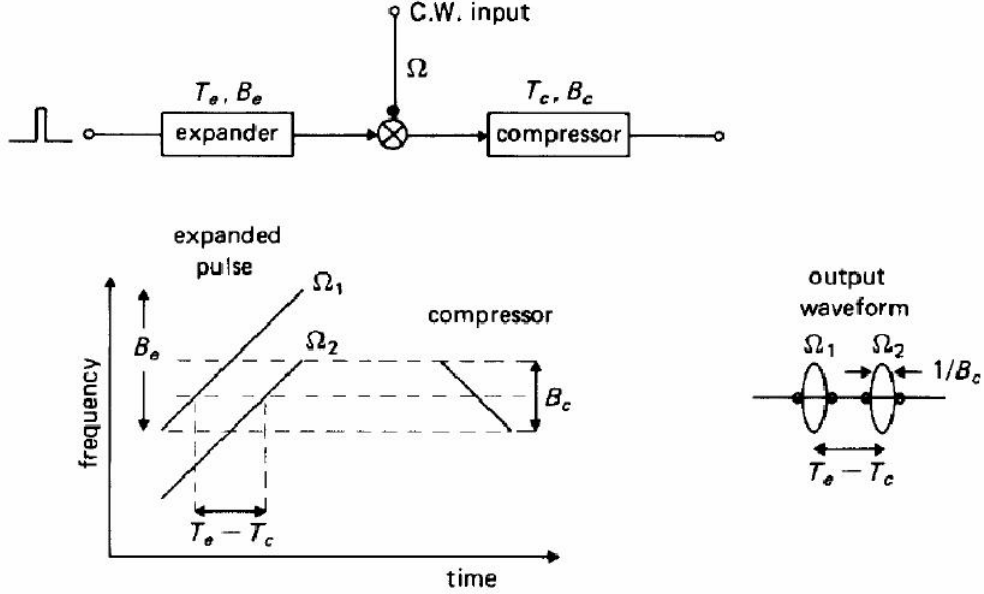


Figure 1.5: The basic structure for M-C chirp transform spectrometer [13].

impulse response of the so-called expander chirp filter. After the input signal is mixed with the impulsed up chirp signal, the expanded input signal is then fed into a matched down chirp filter, where it is compressed to a short pulse. This down chirp filter is, thus, called a compressor. It performs the convolution in Equation 1.7. In the time domain for a chirp signal, its convolution with a chirp signal of the opposite chirp slope is equivalent to the autocorrelation function for this chirp signal. The bandwidth and dispersive delay of the expander and compressor can be denoted with B_e, T_e and B_c, T_c , respectively. For an optimized CTS setup, the following relation applies: $B_e = 2B_c$ and $T_e = 2T_c$. Under these conditions, the spectrometer can achieve a certain resolution and input bandwidth with the minimum $(B_e \cdot T_e)$ value.

From Figure 1.5, we can see that the performance of the optimized Chirp Transform Spectrometer is mainly determined by the performance of the expander and the compressor filter.

1. The input bandwidth of the CTS is determined by the bandwidth of the compressor filter $B_{cts} = B_e - B_c = B_c (B_e = 2B_c)$.
2. The frequency resolution of the CTS is determined by the width of the compressed pulse, which is $\Delta f_{cts} = \frac{\mu}{B_c} = \frac{1}{T_c}$. This is determined by the dispersive delay of the compressor filter.
3. The number of spectral channels of the CTS is determined by the time-bandwidth product of the compressor filter, which is $N_{cts} = \frac{B_{cts}}{\Delta f_{cts}} = T_c \cdot B_c$.

1.2.2 Advantages and limitations of the CTS

Due to the fact that commercially available spectrum analyzers have duty-cycles far below 100%, they are not sensitive enough for radio astronomical applications. Therefore, dedicated instruments have been developed for spectral analysis. One can identify five basic types of spectrometers: analog filter banks, Acousto-Optical Spectrometers (AOS), Chirp Transform Spectrometers (CTS), autocorrelators and Fast Fourier Transform Spectrometers (FFTS) [24]. In Figure 1.6 these different types of spectrometers are listed and compared for radio astronomy purposes.

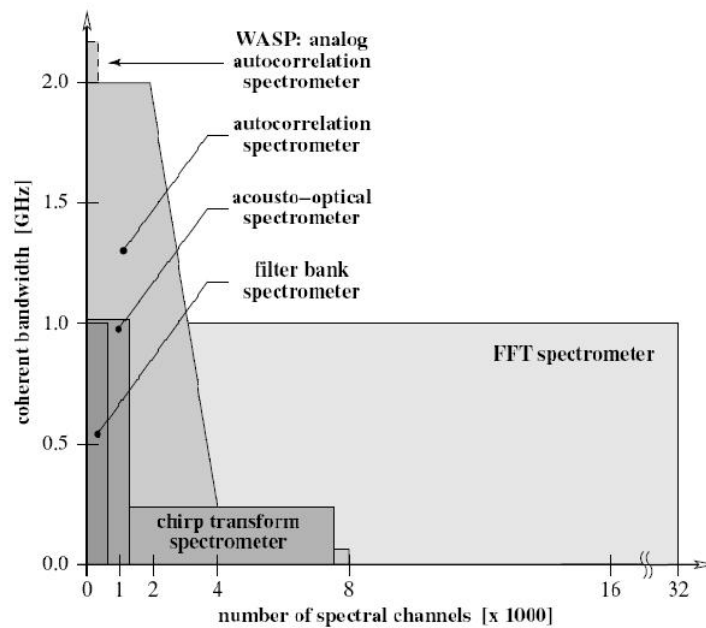


Figure 1.6: Comparison of different spectrometer types in terms of coherent bandwidth and spectral channel number applied in radio astronomy [24].

Early on, spectrometers were built using analog bandpass filters and detectors, which were then assembled into filter banks. The bandwidth and spectral resolution of this kind of spectrometer are limited by the number of used filters. There are also other practical limitations for filter banks in terms of channel numbers, since in general there is only limited space available. Also each frequency channel needs its individual square law detector, and differences in the linearity of the individual detectors may lead to systematic errors on the measured spectrum.

Acousto-Optical Spectrometers were developed later to allow for a wider bandwidth and a larger number of spectral channels. AOSs can currently cover bandwidths up to about 4 GHz with approximately 2000 spectral channels [23]. Also their power consumption is relatively low, since data reduction is done by the fact that the Charged Coupled Devices (CCDs) used average a couple of hundreds or even thousands of spectra before readout. However, due to their design, they need a stable and thermally controlled environment, which puts very tight constraints on their operability.

Another widely used type of spectrometer in radioastronomy is the Digital Autocorrelation Spectrometer (DAC). As the name says, it calculates the autocorrelation function

(ACF) of the input signal. The autocorrelation process at the same time reduces the input data rate. After the data rates are reduced by several orders of magnitude, the spectrum is calculated by Fourier Transformation of the autocorrelation function (Wiener-Khinchin theorem). The number of operations of a Fast Fourier Transform (FFT) is then much smaller compared with calculating the ACF.

Recently, the rapid increase of the sampling rate (≥ 2 GS/s) of commercially available analog-to-digital converters (ADCs) and the calculation power of field programmable gate arrays (FPGAs) has led to the possibility to directly digitize the down-converted intermediate frequency (IF) signals of coherent radio-receivers, and then transform the digital signal into a spectrum in real-time. For this kind of complete digital spectrometer Fast Fourier Transform Spectrometer (FFTS), the main advantage is that it can provide both wide bandwidths (up to 1.5 GHz) and an impressive number of spectral channels (up to 32 768) - thus, quite a high frequency resolution. Unfortunately, at present this kind of spectrometer still has a very high power consumption. For the FFTS developed in 2006 [24], its power consumption was larger than 100 W, and the power dissipation to heat is also quite high.

Before the novel FFT spectrometers were introduced, high resolution spectroscopic observations with several thousands of spectral channels were only possible with Chirp Transform Spectrometers. They can provide up to 10 000 spectral channels at a bandwidth of 700 MHz. For this kind of analog computation technique, several advantages still make it popular for certain applications.

1. As the CTS is mainly based on passive SAW chirp filters, its power consumption can be very low (typically less than 15 W).
2. The analog device-based system for CTS is very reliable for space applications compared to full digital ones [3], because the analogous devices such as SAW chirp filters are not as sensitive as semiconductor ICs to cosmic radiations.
3. The power dissipation to heat is much lower for CTS compared to digital spectrometers. This leads to significantly less cooling problems for space applications.

The only disadvantages of the CTS are the limited bandwidths of up to 700 MHz and the number of frequency channels which can hardly be more than 10 000. This is determined by the limitation of the bandwidth and time bandwidth product of the chirp filter used in it. We will discuss these limitations for RAC type chirp filters in the last chapter.

The Max Planck Institute for Solar System Research has a very long history of developing Chirp Transform Spectrometers. The CTSs developed till 2005 are shown in Table 1.1. From the parameters for the power consumption and the mass of CTSs in the years 2003 and 2005, we can see that it is still quite competitive for space applications compared to the digital FFTS, even with a limited bandwidth and channel number.

1.3 Motivations for developing large time bandwidth product RACs

From the basic principle of the Chirp Transform Spectrometers discussed in section 1.2.1, we can see that the performance of the chirp filter is essential for the performance of a

	1983	1984	1985	1987	1991	1992	1997	2003	2005	Unit
Input Center Frequency	180	300	1350	300	300	1350	1350	3000	2100	MHz
Input Bandwidth	25	22	40	40	40	40	178	400	400	MHz
Spectral Resolution	500	150	50	50	22	50	43	100	100	kHz
Passband Ripple	3	6	1	1	1	1	2	2	1	dB
Dynamic Range	18	27	26	15	30	30	29	25	40	dB
Frequency Linearity	20	8	1	1	1	1	2	2	0.5	kHz
Absolute Allan Variance	100	1100	90	100	1000	900	300	300	600	S
Frequency Scale Stability	50	1	5	2	2	2	5	10	5	kHz
Power Consumption	420	520	530	430	50	30	≤ 15	5	≥ 10	W
Mass	22	20	20	25	10	10	2.3	1	≤ 10	kg

Table 1.1: The history of CTS developments in the MPS until 2005 [29].

CTS. If we had the compressor chirp filter used in the CTS with a larger bandwidth, then the CTS could have a larger input bandwidth, $B_{cts} = B_c$; and if we had a longer compressor chirp filter dispersive delay, then the CTS could have a higher frequency resolution, as $\Delta f_{cts} = \frac{1}{T_c}$; a larger bandwidth and dispersive delay gives a larger time bandwidth product of a chirp filter, which will make more frequency channels in the input bandwidth for CTS. By making the improvements mentioned above, the weakness of CTS compared to the FFTS for limitations on bandwidth and frequency channel number will be greatly improved. Together with the several intrinsic advantages discussed in the last section, the CTS remains a promising passive device-based instrument for microwave spectroscopy in atmospheric remote sensing when competing with digital technologies like FFTS. Hence, the development of large time bandwidth product RAC with an optimized insertion loss level is very important for CTS technology in microwave spectroscopy for astronomy.

1.4 RAC devices - literature review

At the beginning of the 1970s, due to the rise of the requirements for pulse compression in military radar applications, efforts were focused on developing large time bandwidth product dispersive delay lines.

The first large time bandwidth product dispersive delay line (DDL) using a herring bone pattern double reflection reflector array was introduced by Tom A. Martin [17] in 1973. This kind of bulk wave DDL was called IMCON. It uses bulk wave transducers on the steel stripes; the dispersive function was realized by the etched reflective chirp gratings on the steel stripes. In Martin's paper, the first order impulse response model was established for such a herring bone structure, whereas the analytic closed form of its transfer function was deduced from this model using stationary phase approximation. Due to the limitation of its bulk wave transducers, the bandwidth of IMCON can only reach up to 15 MHz. On the other hand, the dispersive delay reached about 300 μs , and the time bandwidth product reached about several thousand.

Then R. C. Williamson [5] adopted the same kind of structure as IMCON, but used surface acoustic wave reflections. Hence, a new kind of SAW DDL was developed on the YZ-LiNbO₃ substrate, which is called the reflective array compressor (RAC). In Williamson's paper, the basic building blocks of the RAC were studied, especially the normal incident SAW reflectivity for single grooves; and the design parameters were discussed such as the groove oblique angle and groove positions; also the proper fabrication techniques for RACs were introduced (e.g. the depth profile etching method for amplitude weighting).

In 1974, the first world record time bandwidth product 10 000 RAC filter was developed by H. M. Gerard and O. W. Otto [11]. In their work, the closed form reflection loss for the groove array was derived and the depth profile calculation for flat amplitude weighting of insertion loss was discussed in detail. The pair reverted IDTs (PRTs) were introduced for the first time for making larger bandwidths than the uniform IDTs.

A year later, single groove reflectivity for the SAW oblique incident on YZ-LiNbO₃ was modeled and measured precisely by R. C. M. Li [21] and J. Melngailis [20]. The empirical reflectivity calculation equation was derived using the experimental fitted parameters and the energy storage effect was discovered for SAW passing through single grooves.

Later that year, new material was tried for RAC filters by V. S. Dolat and R. C. Williamson [40] where Bismuth Germanium Oxide (BGO) was used. As the SAW phase velocity on BGO ($v_p \approx 1681$ m/s) is only about one half of the velocity on YZ-LiNbO₃, BGO is very suitable for making very long delay chirp filters. This is because the filter chip size can be about only half of the chip based on YZ-LiNbO₃ with the same delay time. However, the electro-mechanical coupling coefficient for BGO is rather small ($K_e^2 = 1.4\%$), so the filter bandwidth can also only be very small. In their work [40], the designed RAC filter bandwidth is only 2.5 MHz, and yet the dispersion reached up to 125 μs .

The multiple reflection effect of SAW inside the uniform reflective array was originally researched by Oberdan W. Otto [26] using numerical methods. The uniform groove array was modeled using small four-port cells where in each cell there is only one groove, and was modeled by a 2×2 S matrix. By cascading all the cells in the whole groove array, the solution for the whole groove array could be found numerically. By using this method, several kinds of SAW propagation path were investigated, such as L-path, U-path and Z-path. It was found that for different groove array arrangements, using U-path propagation for SAW, the SAW beam profile was influenced the least by the multiple reflections. In 1978, this method was extended to the analysis of chirped groove array by

P. D. Bloch [27]. A special cascading method was introduced to have all the cells reliably cascaded in the chirped groove array. Full simulation of the reflective array could be derived using this numerical method even when the role of multiple reflections become non-negligible, resulting in deviations of phase from quadratic dependence on frequency. The phase deviation could be evaluated using this model for different designed groove depth.

The nonsynchronous scattering from SAW to BAW was discovered in up chirp RAC filters by Oberdan W. Otto [10]. This loss item was then measured in his work for their special filter configurations. The optimized groove depth was derived for including this new kind of loss item, and the loss mechanism of RAC was finally separated into several independent items.

For different amplitude weighting techniques:

1. The RAC filter design using constant groove depth was introduced by H. M. Gerard [28]. Instead of using the conventional depth profile weighting, a new kind of weighting method – aperture weighting was used. The aperture weighting method avoided the depth profile etching of groove array that is time consuming and expensive. In his paper, the analytic relationship between the reflection loss and groove aperture was given, acting as the kernel function for this new technique.
2. Then in 1990, the couple grooves position weighting method was proposed by S. Gopani [50]. It uses the variation of the relative position of each couple of grooves in the array to modulate the total reflection loss of the reflective array. This method shares the same advantage with aperture weighting for using the constant groove depth.

Several other kinds of RAC structure studies soon followed e.g.: the weighted in line reflective array filter by R. E. Chapman [44]; the slanted reflective array filter using slanted chirp transducers by B. R. Potter and C. Waterkeyn [41; 42]; and also the metalized RAC design using open or shorted chirp electrodes for reflectors by Kitano and Godfrey [45; 46]. The development of metalized RAC mainly focused on the simplification of the fabrication processes of the conventional RACs. The conventional RACs have two main processes, one is for IDT evaporation, and the other is for groove ion beam etching. The two processes need two separate exposures, and they need to be aligned precisely. For metallized RACs, the processes are reduced to only one evaporation; the extra exposure and alignment is avoided, which is suitable for mass productions. The downside is that the electrodes normally have much higher reflectivity for SAW than grooves, so it is difficult to make very long delay RACs.

Reflective dot array (RDA) was studied by H. Van de Vaart and Frederick Huang [43; 51], they used metalized dots instead of continuous grooves or electrodes. The reflectivity can be controlled by the density and size of the dots.

A recent paper by Junjie Gong and Paul Hartogh [7] published in 2006 introduced the magnitude response improvements using extra grooves at groove array ends for suppressing high frequency end magnitude peaks. They also introduced a new phase compensation method by shifting each single groove in the reflective array by small distances.

1.5 A brief summary of the PhD work

A designing program for the reflective array in RAC is developed according to the algorithm which will be described in Chapter 2, it calculates the chirped groove array geometries (i.e. polygon vertex coordinates for all grooves in the layout). The same kind of program is also developed to generate the uniform or pair reverted interdigital transducer layout according to the required center frequency and bandwidth.

A loss mechanism model for the RAC type filter has been developed for the simulation and optimization of RAC performance, based on the existing literature, and a transmission loss item is included phenomenologically according to our measurement experiences. This will also be discussed in detail in Chapter 2.

The basic building blocks of the RAC type filter (eg: the optimized uniform IDT or pair reverted IDT, the single groove and single electrode), are characterized using the experimental method or published results. Details are presented in Chapter 3.

To avoid using non-standard equipment for the depth profile etching of groove arrays, another kind of duty cycle weighting method using e-beam lithography was developed for RACs (see Chapter 4).

The methods for the correction of the phase deviations of RAC response from the ideal quadratic law were studied experimentally. The dependence between the correcting Al stripe width and additional phase shift were determined. Although in designed RAC devices these methods were not used - the phase deviations were acceptable without correction - in future work, for low loss RAC devices with deep grooves, such a correction may be necessary. This will be discussed in detail in Chapter 5.

Chirp Filter	Center Frequency	Bandwidth	Chirp Delay	Insertion Loss	Magnitude Ripple	Phase Error
I	1 GHz	400 MHz	10 μ s	43 dB	± 1 dB	19 $^\circ$ ($\Delta\varphi_{rms}$)
II	1 GHz	400 MHz	20 μ s	55 dB	± 2 dB	16 $^\circ$ ($\Delta\varphi_{rms}$)

Table 1.2: Two types of down chirp RAC developed during the PhD.

Finally two types of down chirp RAC filters ($BT = 4000$ and 8000) with good performance were developed and delivered to the MPS. The above table listed the measurement specifications for these two types of filters. Their measurement results are shown and discussed in detail in Chapter 6.

2 Design and modeling of groove reflective array

2.1 Design of the groove reflective array

To design the reflective array in the RAC means to calculate its geometry, this includes the position of each groove, the width of each groove and also the aperture of the whole groove array. In the following we shall discuss the calculation of all those design parameters.

2.1.1 Groove pitch and groove oblique angle

Suppose we have two adjacent arbitrary grooves, indexed by n and $n+1$. The Figure 2.1 shows how the Rayleigh wave is reflected by these two grooves. In Figure 2.1, the X-axis coincides with the crystalline Z-axis of LiNbO_3 , and the Y-axis coincides with the crystalline X-axis of LiNbO_3 . (In this chapter, the XY coordinate system for layout always has the above coinciding.) Here the dashed line is the center of the groove n

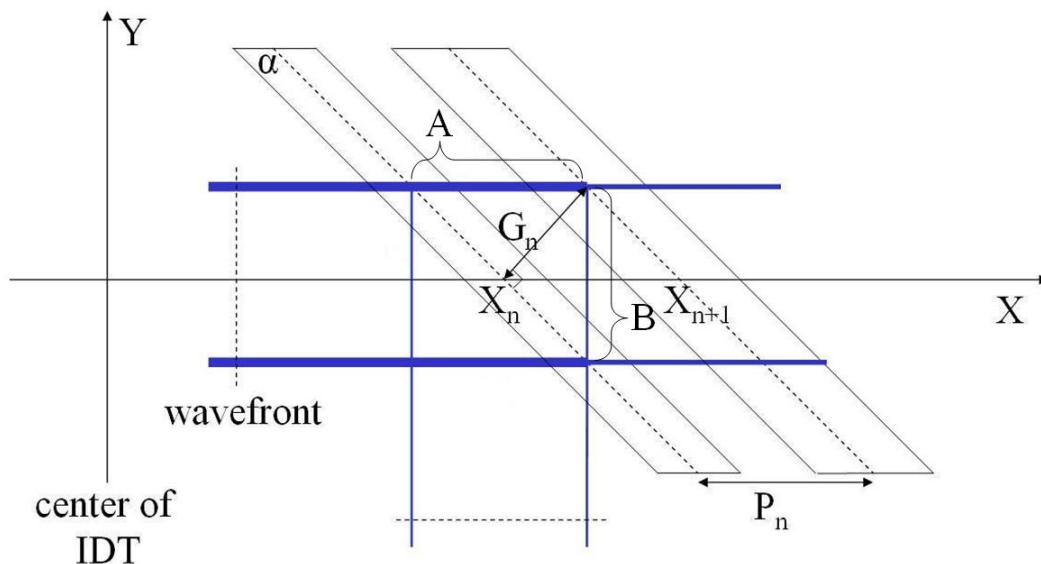


Figure 2.1: SAW reflection by groove n and $n+1$, X_n and X_{n+1} are their center positions respectively.

and $n+1$, which is also the reflection center of each groove for SAW. The blue line is a

beam of SAW and the wave front of the SAW is the normal dashed line. As we want the SAW to be reflected by the grooves by 90 degrees and the adjacent two grooves should reflect synchronously, two conditions must be satisfied for the groove geometry as shown in Equation 2.1:

1. The phase shift at distance A ($\Delta\varphi_A$) and distance B ($\Delta\varphi_B$) should be the same.
2. The phase shift at distance A ($\Delta\varphi_A$) and distance B ($\Delta\varphi_B$) should be 2π .

$$\Delta\varphi_A = \Delta\varphi_B = 2\pi \quad (2.1)$$

The above conditions in Equation 2.1 can be expressed further by Equation 2.2:

$$k_x \cdot \frac{G_n}{\sin \alpha} = k_y \cdot \frac{G_n}{\cos \alpha} = 2\pi \quad (2.2)$$

where $k_x = \frac{2\pi f}{v_{px}}$ and $k_y = \frac{2\pi f}{v_{py}}$ are the SAW wave number on the X and Y direction, respectively; and $v_{px} = 3488$ m/s, $v_{py} = 3717$ m/s are the SAW phase velocity on the X and Y direction respectively; G_n is the normal distance between groove n and n+1; α is the oblique angle of groove referenced to the X direction in Figure 2.1. From Equation 2.2, the value of α for YZ-LiNbO₃ should be:

$$\alpha = \arctan\left(\frac{v_{py}}{v_{px}}\right) = \arctan\left(\frac{3717}{3488}\right) \approx 46.82^\circ \quad (2.3)$$

Then the groove center distance in the X direction between groove n and n+1 can be derived:

$$P_n = X_{n+1} - X_n = \frac{G_n}{\sin \alpha} = \frac{v_{px}}{f_n} = \lambda_x(f_n) \quad (2.4)$$

From Equation 2.4 we can see that the groove pitch is equal to the local SAW wavelength.

2.1.2 Groove position

The RAC groove position calculation equation was first given in [5]. In the following text, a brief description is given according to [5] showing how the position calculation is derived.

Let us consider a down chirp filter, the linear delay-frequency relationship (see Figure 2.2) can be expressed with Equation 2.5 (μ is the constant chirp slope). f_1 and t_1 denote the high frequency band edge and its related delay. f_n is an arbitrary frequency in the filter bandwidth, and t_n represents its related delay time.

$$f_n = f_1 - \mu \cdot (t_n - t_1) \quad (2.5)$$

As the phase of the filter is the integration of the angular frequency over the filter delay, the phase formula can be derived from Equation 2.5 quadratically into:

$$\Delta\varphi(t_n - t_1) = 2\pi \int_{t_1}^{t_n} f \cdot dt = 2\pi \left[f_1(t_n - t_1) - \frac{1}{2}\mu(t_n - t_1)^2 \right] \quad (2.6)$$

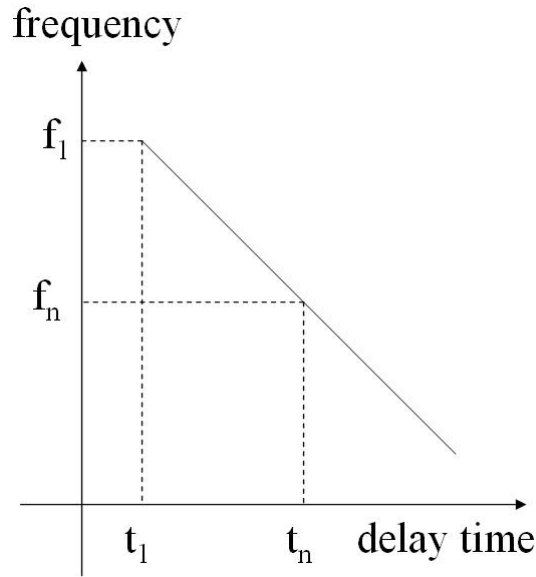


Figure 2.2: The linear delay-frequency relation for down chirp filter.

From Equation 2.4 it is possible to see that for one time reflection, the phase shift between two adjacent grooves is 2π . So for two reflections in the ‘U’ path, the total phase shift between the symmetrical adjacent two groove pairs will be 4π :

$$\Delta\varphi(t_n - t_{n-1}) = 4\pi \quad (2.7)$$

Thus, the total phase shift from an arbitrary groove pair n to the first groove pair indexed by 1, can be derived from Equation 2.7 by recursion:

$$\Delta\varphi(t_n - t_1) = 4(n - 1)\pi \quad (2.8)$$

If we substitute Equation 2.8 into Equation 2.6, we could obtain a quadratic equation with $(t_n - t_1)$ as unknown:

$$2\pi[f_1(t_n - t_1) - \frac{1}{2}\mu(t_n - t_1)^2] = 4(n - 1)\pi \quad (2.9)$$

Because LiNbO_3 is a nondispersive material, the groove position difference $(X_n - X_1)$ (the groove positions X_n is as shown in Figure 2.3) and the delay time difference $(t_n - t_1)$ have the following linear dependency as shown in Equation 2.10; v_{px} is the SAW phase velocity in the X direction:

$$t_n - t_1 = \frac{2(X_n - X_1)}{v_{px}} \quad (2.10)$$

By combining Equation 2.9 and Equation 2.10, we could solve for two positive roots for the groove positions:

$$X_n - X_1 = v_{px} \cdot \left[\frac{f_1 \mp \sqrt{f_1^2 - 4\mu(n - 1)}}{2\mu} \right] \quad (2.11)$$

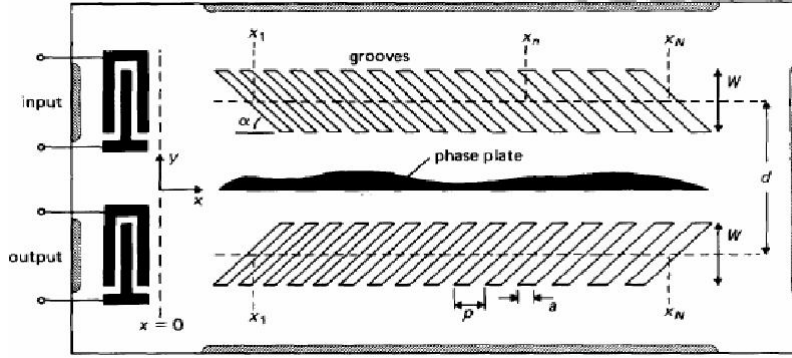


Figure 2.3: Groove positions in the RAC layout [13].

For the device design, the smaller root which is with a physical meaning is chosen for the position calculation as Equation 2.12 (the other root is not physical, for $n=1$ the result is senseless):

$$X_n = v_{px} \cdot \left[\frac{f_1 - \sqrt{f_1^2 - 4\mu(n-1)}}{2\mu} \right] + X_1 \quad (2.12)$$

$f_1 = f_c + \frac{B}{2}$ is the high frequency band edge for the down chirp filter, $\mu = \frac{B}{T}$ is the chirp slope constant and X_1 is the first groove position (it is dependent on where we would put the groove array in our layout system). If we substitute the filter specification and material constants [B, T, f_c, v_{px}] into Equation 2.12, each groove center position X_n can be calculated. The total number of grooves in one symmetrical array can be determined by Equation 2.13:

$$N_g = f_c \cdot \frac{T}{2} + 1 \quad (2.13)$$

We can see from Equation 2.2 that for each period of the impulse response of the chirp filter, one groove is needed for reflection, so the total number of grooves in the whole array is equal to the number of periods in the impulse response. For a linear chirp signal as shown in Figure 2.2, the total number of periods can be found $2 \cdot N_g$ using Equation 2.13.

2.2 First order impulse response model for reflective array

If the single groove reflectivity Γ_g is small enough ($W/\lambda \cdot \Gamma_g \ll 1$, here W/λ is the groove array aperture divided by the SAW wavelength), we can ignore multiple reflections inside the array. The transfer function of the designed groove array can then be simulated using a first order impulse response model [17]. The principle of the impulse response model for the reflective array is shown in Figure 2.4. One reflection from one arbitrary pair of grooves (groove m and groove n) can be simulated using a single delta pulse using $A_{nm} \cdot \delta(t - t_{nm})$ in the time domain. Then for the whole array, the total impulse response in time domain (Equation 2.14) can be as shown in Figure 2.5.

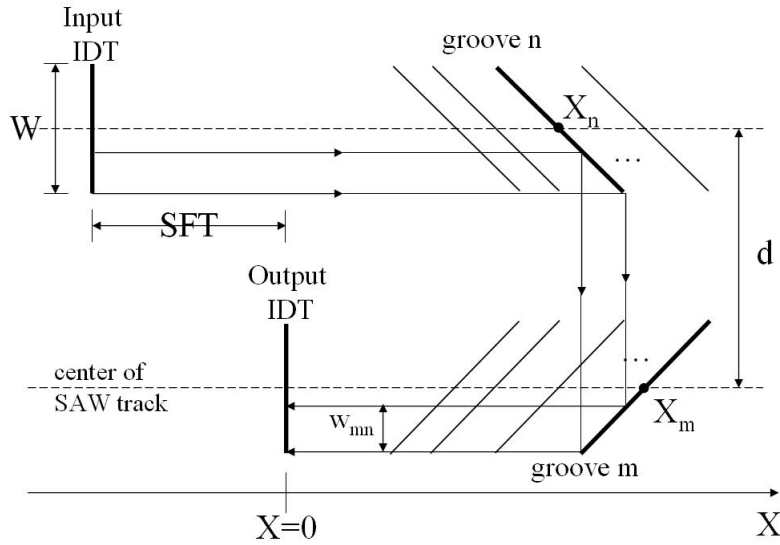


Figure 2.4: Reflection from one pair of arbitrary grooves (groove m and n) [13]. Here SFT is the two IDTs shifted distance in X direction, X_n and X_m are the two grooves' center position; d is the distance between the centers of the symmetrical two groove array in Y direction and w_{nm} is the geometrical overlap of groove m and groove n.

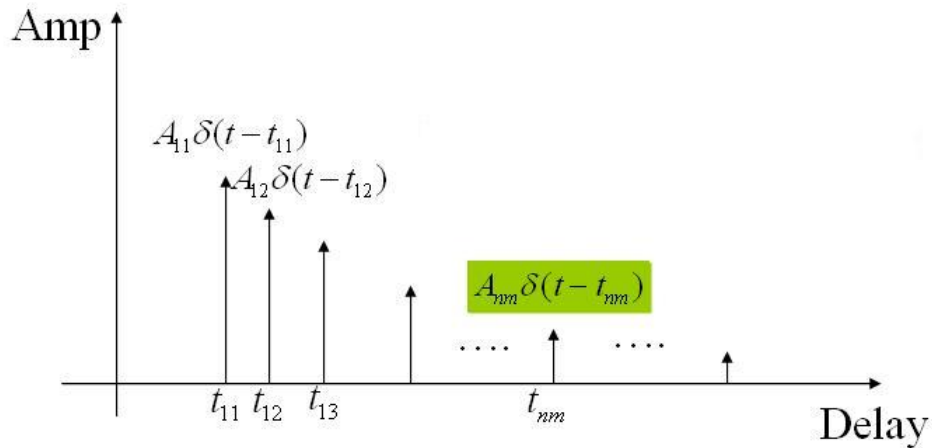


Figure 2.5: Impulse response simulation of the groove array, A_{nm} is the amplitude of the single pulse (every two reflections), and t_{nm} is the corresponding delay time of it.

$$h(t) = \sum_{n=1}^{N_g} \sum_{m=1}^{N_g} A_{nm} \cdot \delta(t - t_{nm}) \quad (2.14)$$

For this linear system the transfer function of the groove array can be derived using a Fourier transformation of its impulse response.

$$H(f) = \mathcal{F}[h(t)] = \sum_{n=1}^{N_g} \sum_{m=1}^{N_g} A_{nm} \cdot e^{-j\omega t_{nm}} \quad (2.15)$$

Here A_{nm} is the amplitude of every reflection pulse, and t_{nm} is the corresponding delay of the reflection.

A_{nm} can be simulated using Equation 2.16 as shown in Figure 2.4:

$$A_{nm} = \Gamma_{gn} \cdot \Gamma_{gm} \cdot w_{mn} \cdot PL(t_{nm}) \cdot \prod_{i=1}^{n+m-2} \eta_i \quad (2.16)$$

Γ_{gm} and Γ_{gn} are the reflectivities of groove m and n in the upper and lower array, respectively; $w_{mn} = 1 - \left| \frac{X_n - X_m}{W_{proj}} \right|$ is the geometrical overlap of groove m and groove n, where $W_{proj} = \frac{W}{\sin \alpha}$ is the projection of aperture W in the SAW propagation direction, $\alpha \approx 46.82^\circ$ is the oblique angle of the groove reference to the SAW propagation direction; $PL(t_{nm})$ is the pulse free surface propagation loss; and $\eta_i = \sqrt{1 - \Gamma_{gi}^2}$ is the single groove transmission coefficient. As for the down chirp filter, we assume there is no bulk wave scattering for the shallow grooves. However, for the up chirp filter, there will be nonsynchronous bulk wave scattering that should be taken into account in the transmission coefficient [9].

The delay of each single pulse can be simulated using Equation 2.17 as shown in Figure 2.6:

$$t_{nm} = \frac{X_n + X_m + SFT}{v_{px}} + \frac{d}{v_{py}} \quad (2.17)$$

X_n and X_m in Equation 2.17 are the groove m and n center positions; SFT is the shift dis-

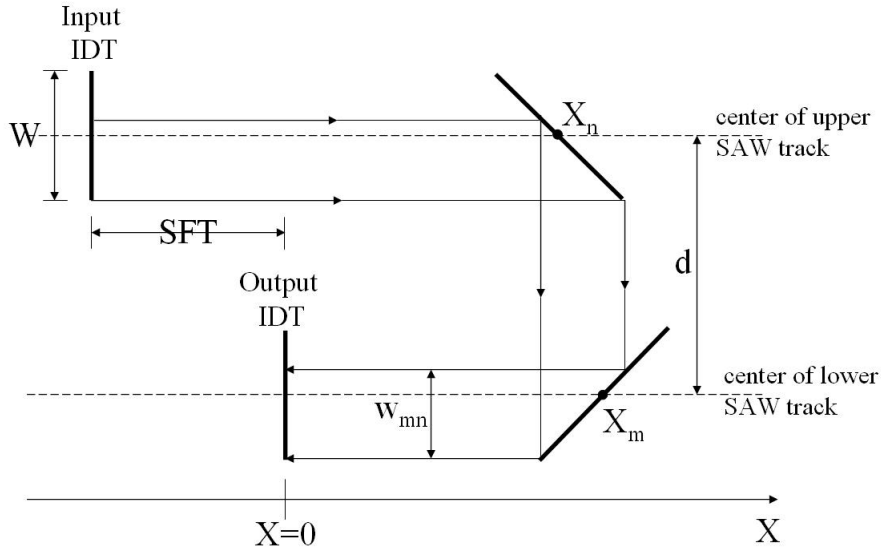


Figure 2.6: Propagation path of a pulse generated by two arbitrary groove reflections. Here SFT is the two IDTs shifted distance in X direction, X_n and X_m are the two grooves' center position; d is the distance between the centers of the symmetrical two groove array in Y direction and w_{mn} is the geometrical overlap of groove m and groove n.

tance between two IDTs in the SAW propagation direction for electromagnetic feedthrough suppression; $v_{px} = 3488$ m/s and $v_{py} = 3717$ m/s are the SAW phase velocities in the Z and X direction, respectively, on YZ-LiNbO₃; and d is the distance between the upper and lower groove array centers as shown in Figure 2.4.

For this double summing impulse response model, the main disadvantage is that the required calculation time is much too long, as N_g^2 complex adding is needed to evaluate

each frequency point, and here $N_g = f_c \cdot T/2$. Therefore, though it can be used to precisely calculate the response of the reflective array when single groove reflectivity is small, it can hardly be used for optimizations as the calculation time is too long and not acceptable. A simpler closed form approximation for this double summing calculation is needed to evaluate the reflective array loss in a faster way [11], which will be discussed in the next section.

In addition, this is just a first order model, it simply sums up all the one groove pair reflection pulses. When the single groove reflectivity is high, the total reflection coefficient of the whole array can saturate, then the multiple reflection inside the groove array will play an important role. Hence, the reflective array can not be accurately simulated using this first order impulse response model. For taking multiple reflections into account in the simulation, other numerical models are available as proposed by Otto et al [26].

2.3 The reflection loss for reflective array

The most commonly used approximation for the double summing impulse response model is the stationary phase approximation [16] [17].

The reflection phase of the inner summing part in the impulse response model as a function of the groove number n (see Equation 2.18) at 1 GHz center frequency is calculated and shown in Figure 2.7 the black curve; we can see that it has a stationary section (slowly varying).

$$\Delta\phi(n) = \angle \left(\sum_{m=1}^{N_g} A_{nm} \cdot e^{-j\omega t_{nm}} \right) \quad n = 1 .. N_g \quad (2.18)$$

$$\Gamma(i) = \left| \sum_{n=1}^i \sum_{m=1}^{N_g} A_{nm} \cdot e^{-j\omega t_{nm}} \right| \quad i = 1 .. N_g \quad (2.19)$$

For the total reflectivity of the whole groove array at a certain frequency, it is mainly contributed to by the grooves which have the stationary reflection phase at this frequency; for the grooves which have the fast varying reflection phase, the outer summing will let them cancel each other. From the red curve in Figure 2.7 which shows the transfer function magnitude increment as a function of the index n of the outer summing Equation 2.19, we can see that, at the phase fast varying area the groove array's reflectivity do not change very much; the main increment area of the reflectivity coincides with the stationary phase section.

If we plot the transfer function of the groove array in a Cornu-Spiral as shown in Figure 2.8, we can see that the fast varying phase section mainly cause the vector summing of the transfer function to circle at the beginning and the end of the curve; the stationary phase section actually carry the transfer function from its original value (0,0) to its final value.

Thus using the stationary phase approximation, the number of the grooves that are reflecting SAW in phase can be approximated as follows using $N_{eff}(f)$ [12]:

$$N_{eff}(f) = \frac{f \cdot T}{2\sqrt{B \cdot T}} \quad (2.20)$$

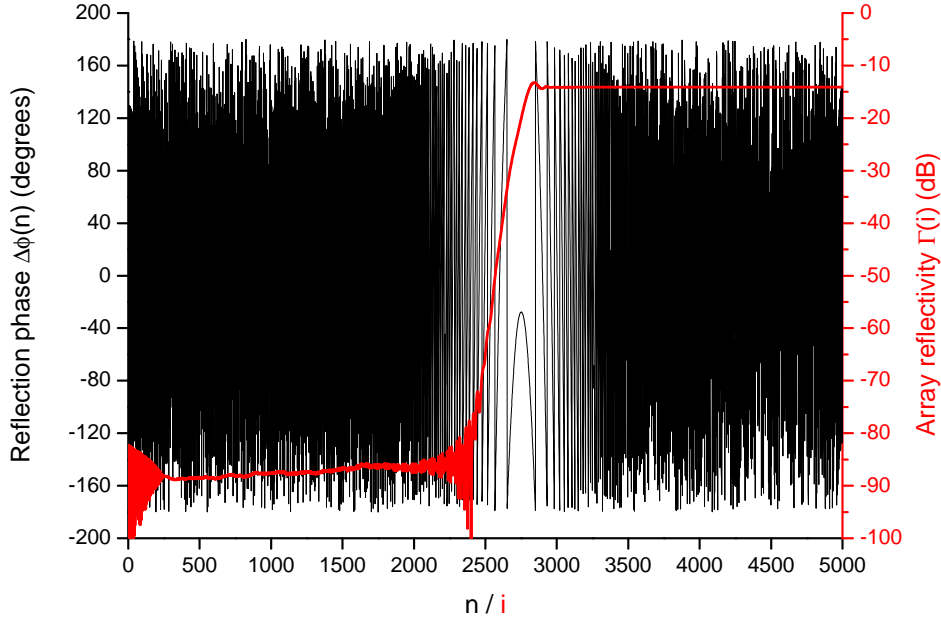


Figure 2.7: The black curve shows the reflection phase of the inner summing part as a function of the outer summing index n for $f_c = 1\text{GHz}$, $BT = 4000$ reflective array (see Equation 2.18). The red curve shows the groove array transfer function magnitude increment as a function of the outer summing index n , for $f_c = 1\text{GHz}$, $BT = 4000$ reflective array (see Equation 2.19).

The reflection loss of the whole groove array can then be calculated according to the stationary phase approximation (SPA) [17], which says that the total reflectivity $R(f)$ of the groove array is mainly contributed to by the group of grooves which are reflecting the Rayleigh wave synchronously:

$$R(f) = (\Gamma_g(f) \cdot N_{eff}(f))^2 \cdot \text{Geom}\left(\frac{W}{L_a \cdot \tan \alpha}\right) \quad (2.21)$$

where $\text{Geom}\left(\frac{W}{L_a \cdot \tan \alpha}\right)$ is the geometrical factor which is only related to the groove array aperture W , and is frequency independent. This factor describes the dependency of the groove array's total reflectivity on its geometry - the aperture W . This factor $\text{Geom}()$ can be calculated numerically from the complete double summing impulse response model, it is shown in Figure 2.9. In the work by Gerard et al [28], this curve is fitted to a closed form expression as Equation 2.22. The numerical calculated geometrical factor and the closed form approximation are compared in Figure 2.9.

$$\text{Geom}\left(\frac{W}{L_a \cdot \tan \alpha}\right) \approx \frac{\frac{W}{L_a \cdot \tan \alpha}}{\left[1 + \left(\frac{W}{L_a \cdot \tan \alpha \cdot 1.85}\right)^5\right]^{0.2}} \quad (2.22)$$

In Equation 2.21 and Figure 2.9, L_a is the active reflecting length of the groove array at a certain frequency, which is the length of the group of grooves that are reflecting the SAW

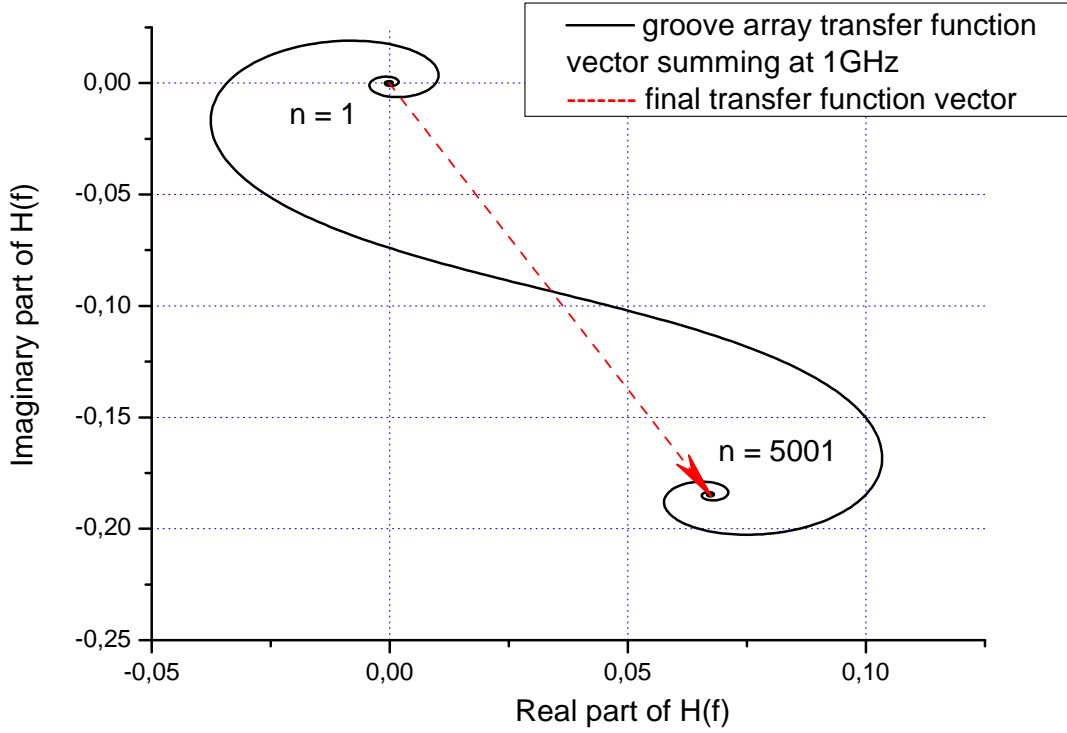


Figure 2.8: Cornu-Spiral of the impulse response model simulated groove array transfer function VS the outer summing groove index n in Equation 2.15, the red dashed curve shows the final vector for the transfer function. The groove array is of $f_c = 1\text{GHz}$ and $BT = 4000$.

in phase [11].

$$L_a = N_{eff}(f) \cdot \lambda = \frac{v_{px} \cdot T}{2 \cdot \sqrt{B \cdot T}} = \frac{L}{\sqrt{B \cdot T}} \quad (2.23)$$

In Equation 2.23 L is the total length of the groove array. We can see that the L_a of groove array is independent of frequency. It is a constant when the value of B, T for a specific filter is fixed.

From the curve in Figure 2.9, we can see that for $W < 2 \cdot L_a$, $Geom()$ increases almost linearly with the aperture W , but when $W > 2 \cdot L_a$, $Geom()$ is going to saturate gradually. So for maximum efficiency (maximum reflectivity of the groove array), we choose $W = 2 \cdot L_a$, where $Geom(2) \approx 1.75$ is about to saturate.

2.4 Other loss items of a RAC

With the reflection loss of the RAC derived, the total insertion loss of the RAC can then be considered to be composed of several separate parts according to [9] as follows (all the loss items are frequency dependent and given in dB):

$$IL(f) = R(f) + IDT(f) + Prop(f) + Tran(f) \quad (2.24)$$

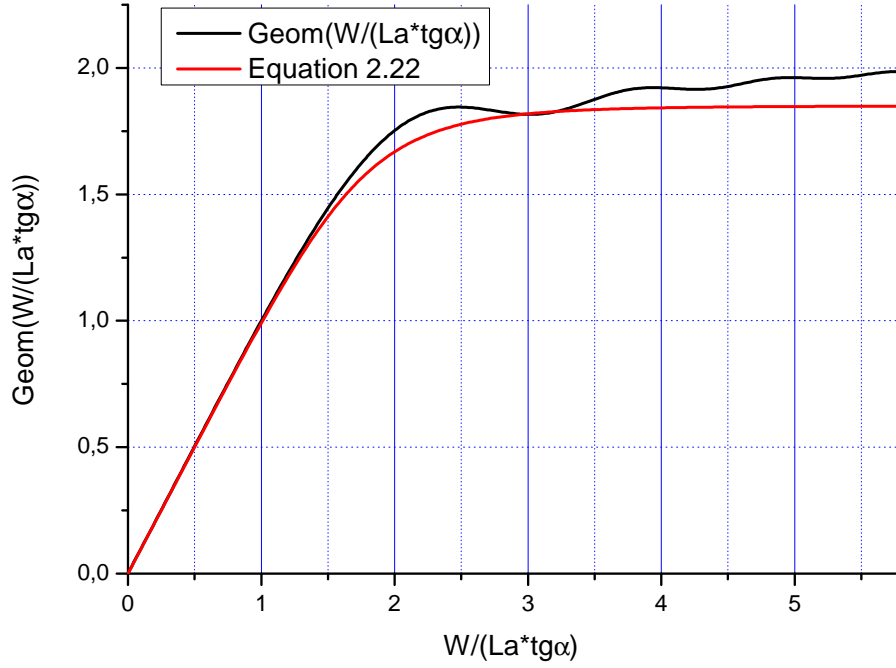


Figure 2.9: Geometrical factor of groove array: black curve is numerically calculated from the impulse response model, the red curve is the closed form approximation of the black curve.

$R(f)$ represents the groove array reflection loss as described in the last section, $IDT(f)$ is the transducer transduction loss, $Prop(f)$ is the SAW propagation loss on the YZ-LiNbO₃ free surface (with air loading), and $Tran(f)$ is the loss due to the transmissions through grooves from the beginning of the array to the in phase reflecting section for a certain frequency.

2.4.1 Propagation loss

According to A. J. Slobidnik [15], the propagation loss (dB/ μ s) of Rayleigh wave on YZ-LiNbO₃ free surface is proportional to $f^{1.9}$ plus a linear term which describes the air loading effect (f is in the unit of GHz):

$$Att(f) = 0.19f + 0.88f^{1.9} \quad (2.25)$$

For the down chirp filter, the propagation delay of the SAW at a certain frequency can be found according to Equation 2.5. Thus, by combining Equation 2.25 and Equation 2.5, the RAC total propagation loss (in dB) can be calculated as follows:

$$Prop(f) = -Att(f) \cdot [t_1 + (f_1 - f) \cdot T/B] \quad (2.26)$$

t_1 stands for the initial delay time of the device, and $f_1 = f_c + B/2$ is the high end frequency of the bandwidth. For the designed $f_c = 1$ GHz, $B = 400$ MHz, $T = 10 \mu$ s down chirp filter, the propagation loss simulation is shown in Figure 2.10.

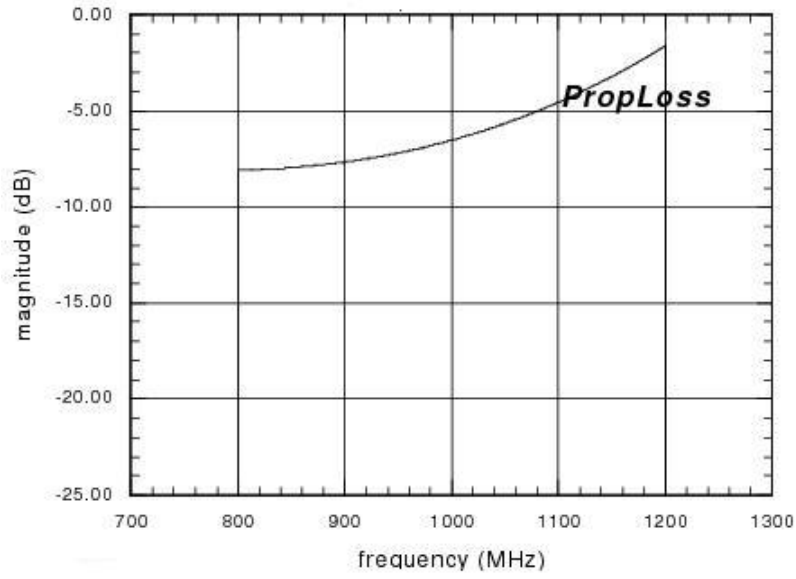


Figure 2.10: Propagation loss simulation for $f_c = 1$ GHz, $B = 400$ MHz and $T = 10 \mu\text{s}$ down chirp RAC filter.

From Equation 2.26, we can see that this loss item is only dependent on the signal frequency f and its corresponding delay time t which is related to the groove positions. To reduce this material dependent intrinsic loss item, one method can be applying vacuum above the substrate surface to remove the air loading loss part, another method can be reducing the temperature of the substrate to have weaker SAW phonon thermal scattering by the crystal lattice.

2.4.2 Transmission loss

As the SAW is propagating through the whole grating until it arrives at the synchronously reflecting zone for a given frequency, the transmission for the SAW going through grooves in the path will also give contributions to the loss. We could estimate this proportion of loss (in dB) phenomenon logically using the following formula (simply multiply the grooves' transmission coefficients):

$$Tran(f) \approx \sum_{n=1}^{n_f - N_{eff}(f)/2} [20 \cdot \lg(1 - \Gamma_{gn}^2(f))] \quad (2.27)$$

Here n_f is the local groove index at frequency f , and $N_{eff}(f)$ is the effective number of in phase reflecting grooves at frequency f as in Equation 2.20, $\Gamma_{gn}(f)$ is the frequency dependent amplitude reflectivity of a single groove indexed by n for SAW oblique incidence. Due to the energy conservation law, the single groove's transmission coefficient $\eta_n(f)$ as Equation 2.28 is used.

$$\eta_{gn}(f) = \sqrt{1 - \Gamma_{gn}^2(f)} \quad (2.28)$$

The simulation of this loss item for the designed $f_c = 1$ GHz, $B = 400$ MHz, $T = 10 \mu\text{s}$

down chirp filter is shown in Figure 2.11. For this filter, the groove array has a constant groove depth $h = 50$ nm, and no weighting technique is used.

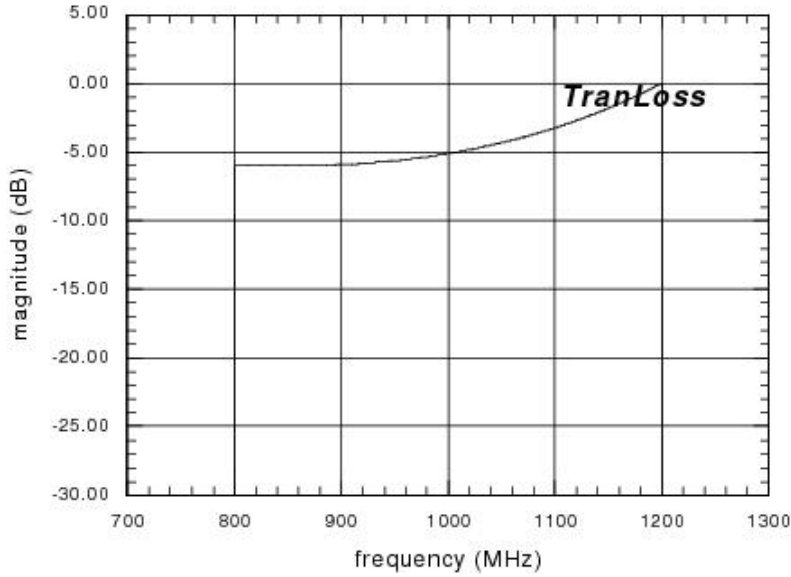


Figure 2.11: Transmission loss simulation for $f_c = 1$ GHz, $B = 400$ MHz and $T = 10 \mu\text{s}$ down chirp RAC filter.

For down chirp filters, the grooves in the ‘U’ path which are with a period less than the SAW wavelength propagating through, do not scatter bulk waves from the SAW. Thus, the bulk wave scattering coefficients are not taken into account here in the transmission coefficient. However, from the experiments for up chirp filters, Otto et al [9; 10] have found that nonsynchronous scattering from the SAW to the BAW happens when the SAW propagates through grooves with a period larger than the wavelength of the SAW. So for up chirp filters, the transmission coefficient of a single groove should be described as follows:

$$\eta(f) = \sqrt{1 - \Gamma_g^2(f) - sc_g^2(f)} \quad (2.29)$$

where $sc_g(f)$ is the frequency dependent bulk wave scattering coefficient for the SAW travelling through a single groove, it was determined using experimental method [9; 10].

2.5 Experimental results compared to the first order simulations

Using the first order impulse response model and stationary phase approximation as described above, it is possible to simulate the reflective array loss of the RAC. The IDT transduction loss however must be measured experimentally. In order to evaluate the feasibility of the modeling of the reflective array discussed before, we made some comparisons of the model simulations with the experiments for two types of early developed nonweighted RAC filters.

Figure 2.12 shows the comparison of the simulated and measured $BT = 4000$ RAC insertion loss curves: the black curve shows the measured IDT loss plus the stationary phase

approximation (SPA) for the reflective array loss (using Equation 2.24); the red curve is the measured IDT loss plus the impulse response model (IMP) (using Equation 2.15) simulated reflective array loss; finally the blue curve shows the experimental-measured RAC insertion loss. Here, the RAC is of $B = 400$ MHz, $T = 10 \mu\text{s}$ and $f_c = 1$ GHz. It is designed with an uniform groove depth of $h = 23$ nm, a $W = 780 \mu\text{m}$ uniform aperture, and 50% uniform groove duty cycles. Here the duty cycle of the groove is defined as $\frac{w}{p}$, w is the groove width and p is the groove period (in the following chapters the terms duty cycle of groove are all defined like this). As we can see in Figure 2.12, the measured

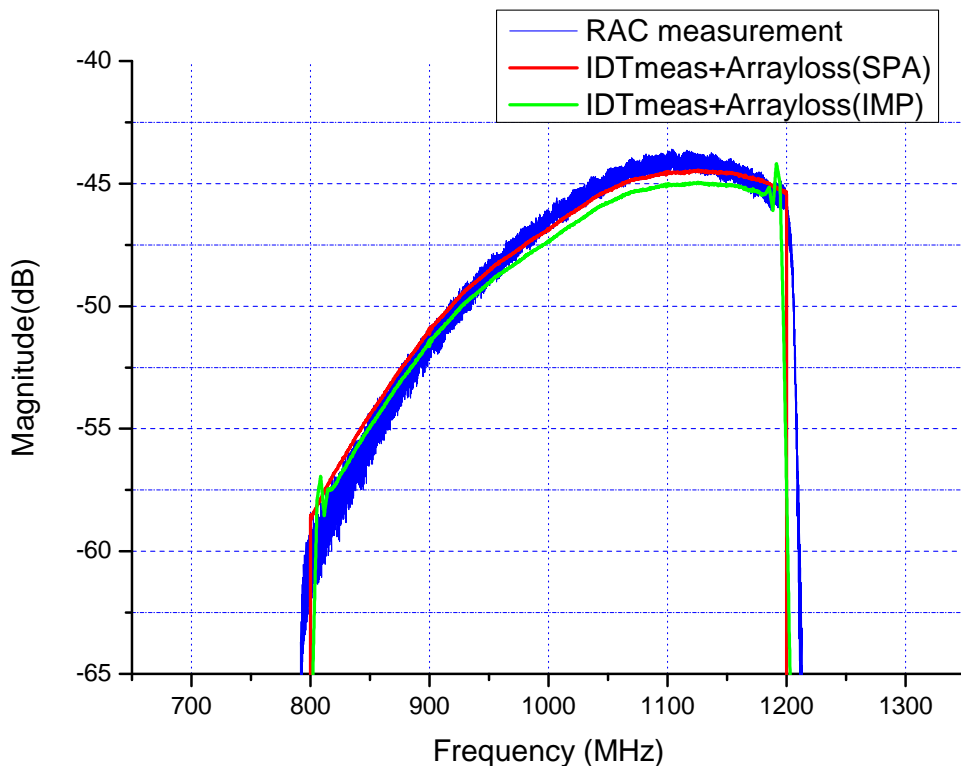


Figure 2.12: Comparison between the impulse response model (Equation 2.15), the stationary phase approximation (Equation 2.24) and the experiment for insertion loss curve of $B = 400$ MHz, $T = 10 \mu\text{s}$ and $f_c = 1$ GHz down chirp RAC ($h = 23$ nm, $W = 780 \mu\text{m}$). IDTmeas: measured idt transduction loss. SPA: stationary phase approximation of reflective array loss. IMP: impulse response model-simulated reflective array loss.

blue curve has slightly larger bandwidth than the simulation results. This is because in the fabricated RAC, the groove array is in the rectangular shape (the yellow area plus the blue area as shown in Figure 2.13), so compared with the parallelogram shape groove array (the yellow area as shown in Figure 2.13) used in the SPA and IMP simulations, there are two triangle areas with extra grooves at the beginning and end of the parallelogram shape groove array (the blue area as shown in Figure 2.13). These extra grooves contribute the slight larger bandwidth than 400 MHz. They also eliminate the magnitude peaks at the beginning and end of the bandwidth. As we can see, the green line in Figure

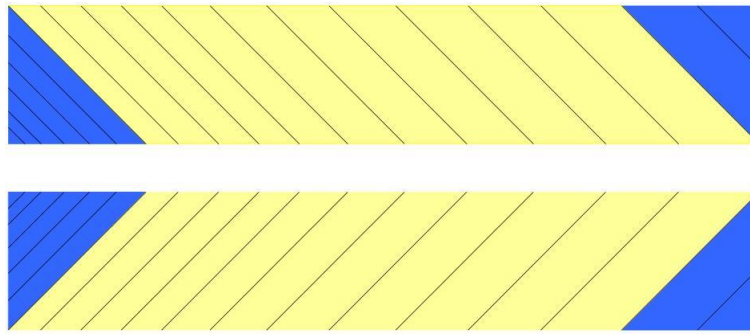


Figure 2.13: Comparison between the geometry of the rectangular shape groove array and the parallelogram shape groove array.

2.12 has peaks at the beginning and also the end of the bandwidth. This is because the impulse response model (IMP) used here only simulates the parallelogram shape groove array. The extra grooves at both ends of the array have not been taken into account, but in the experiment we have them. The functionality of the extra grooves at both ends of the groove array for eliminating the peaks at the beginning and end of the bandwidth of filter will be explained in detail in the next chapter.

Another comparison for the nonweighted $BT = 8000$ RAC's ($B = 400$ MHz, $T = 20 \mu\text{s}$, $f_c = 1$ GHz) simulated and measured insertion loss curve is shown in Figure 2.14. The red curve represents the measured IDT loss plus the stationary phase approximation for the groove array (using Equation 2.24); the blue curve is the measured RAC loss curve and the green curve is the feedthrough time gated result from the blue one. From the comparison between the blue and green curve, we could see that, after the feedthrough time gating the high magnitude ripples in the whole passband is reduced, especially in the low frequency area. The high amplitude ripples at the low frequencies of the measurement result are mainly due to the fact that the magnitude there is quite low and very close to the out of bandwidth feedthrough level, the feedthrough noise contributes very much to the ripples. So the magnitude for the filter at the low frequencies need to be increased. Otherwise the feedthrough will introduce high level of magnitude ripples to the high loss low frequencies.

From these simulations and experiments shown in Figure 2.12 and Figure 2.14, we can also see that for the uniform depth and duty cycle groove array design, there are big magnitude nonuniformity in the 400 MHz wide bandwidth (about 15 dB in Figure 2.12 and 20 dB in Figure 2.14). Because the passband flatness is important to the frequency resolution of the CTS (the reason will be explained in the first section of Chapter 4), certain amplitude weighting technique will be needed for correcting this nonuniformity, this kind of technique will be discussed in detail in Chapter 4.

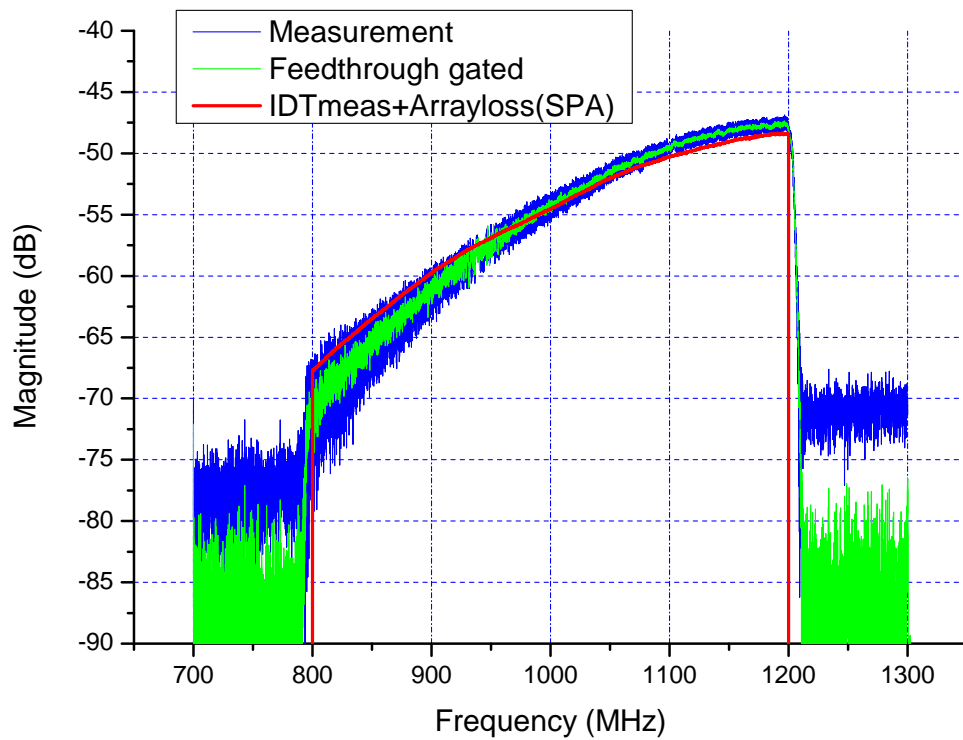


Figure 2.14: Comparison between the stationary phase approximation and the experiment for the insertion loss of $B = 400$ MHz, $T = 20 \mu\text{s}$, $f_c = 1$ GHz down chirp RAC ($h = 15$ nm, $W = 1100 \mu\text{m}$). IDTmeas: measured idt transduction loss. SPA: stationary phase approximation of the reflection loss of the reflective array.

3 Building blocks of RAC devices

3.1 RAC layout

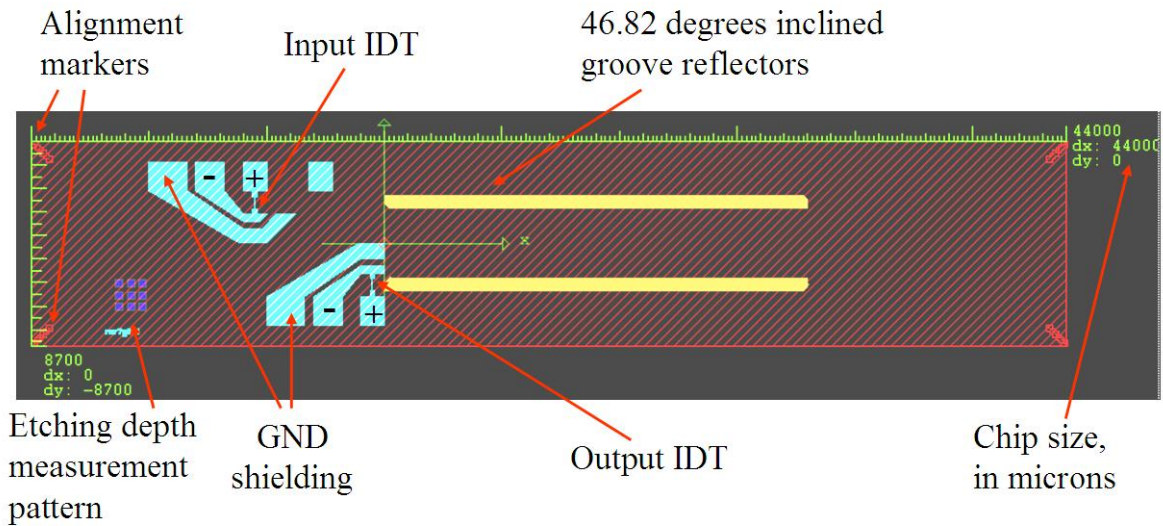


Figure 3.1: Layout of the RAC with $B = 400$ MHz, $T = 10 \mu\text{s}$ and $f_c = 1$ GHz, the X-axis coincides with crystalline Z-axis of LiNbO_3 , and Y-axis coincides with crystalline X-axis of LiNbO_3 (In this chapter, the XY coordinate system for layout always have the aboving coinciding).

Figure 3.1 shows the RAC layout designed with $B = 400$ MHz, $T = 10 \mu\text{s}$ and $f_c = 1$ GHz. The connected square areas at the four corners of the chip are made of 60 nm AuPd film and are used as markers for the e-beam lithography. Because during the fabrication of the RAC filters, two processing steps are needed: one is the evaporation of the Al interdigital transducers; the other is the ion-beam etching of the reflective groove array (colourful area). These two processes need two separate exposures, and they need to be aligned precisely. Otherwise the SAW generated by the interdigital transducer can not be reflected correctly by the groove array. Those markers were used by the e-beam machine as a coordinate system for both exposures of the IDT and the groove array.

In order to suppress the feedthrough between the two IDTs, which will generate magnitude ripples in the filter passband, the input IDT was shifted 6 mm in X direction away from the output IDT. With this geometry on the self-focusing cut YZ- LiNbO_3 , the diffraction of SAW is very small. Additional shielding pads are added to isolate the input and

output IDTs to further enhance the feedthrough suppression. These shielding pads are connected to the holder case. The distance between the symmetrical upper and lower groove arrays in Y direction is increased to 3 mm. This will lead to about 1 dB more propagation loss for the SAW, but more feedthrough suppression is obtained.

The chip serie number and etching depth measurement pattern are on the lower left corner of the chip. This depth measurement pattern is a 3×3 squares array, each square is with the dimension of $100 \mu\text{m} \times 100 \mu\text{m}$. Because the profiler for measuring the profile of the substrate surface has a needle tip size of $12.5 \mu\text{m}$ in diameter, which is not possible to measure the groove depth directly, as the grooves are only several microns wide. Because the Ar ion beam etching is a physical bombardment etching, the etching rate will not depend on the pattern (this is varified with the atom force microscope (ATM) by comparing the depth of the small grooves and the big patterns). The big measurement pattern was exposed together with the grooves, and it is etched together with the grooves for the same depth, and then these big squares can be easily measured using the profiler.

The chip size is $44 \text{ mm} \times 8.7 \text{ mm}$ for the $10 \mu\text{s}$ dispersive delay RAC.

3.2 Optimized interdigital transducer (IDT)

The interdigital transducer used at the beginning of this work is uniform IDT, the geometry is shown in Figure 3.2. For achieving -3 dB fractional bandwidth of 40%, the number of IDT's fingers must be very small, $N_f = \frac{2}{40\%_{-3 \text{ dB}}} = 5$ [13].

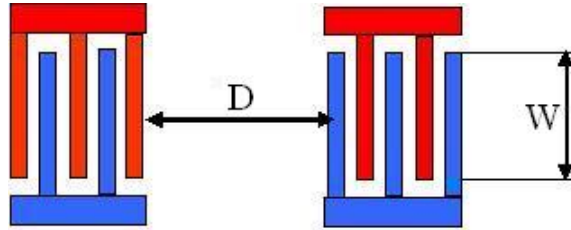


Figure 3.2: The geometry of the uniform IDT, red is hot and blue is ground.

The electrical period p_e of the IDT is chosen to be equal to the SAW wavelength at the center frequency: $p_e = \frac{v_{ps}}{f_c}$. So at center frequency f_c the SAW exited by each finger pairs in the IDT will be all in phase. The mark to pitch value $2a/p_e$ in each electrical period is uniformly 50%, here a is the finger width.

The aperture of the IDT used here is $W = 2 \cdot L_a$, the geometrical factor for the reflective array is $Geom(2) \approx 1.75$. For the geometrical factor this aperture is the turning point for the curve to go saturate as shown in Figure 2.9. It can guarantee that the reflective array have a good efficiency ($Geom()$ is large enough), and meanwhile it is not too large and will not distort the groove array's transfer function and bring extra phase errors [11]. Here L_a is the active length of the groove array for SAW reflection in Equation 2.23.

Then, in order to make the bandwidth wider, we changed to one pair reverted IDT with eight electrodes [11], the geometry is shown in Figure 3.3. The extra pair with reverted polarization serves to add a negative side lobe in the impulse response of IDT in the time domain as shown in Figure 3.4. By doing this, the -3 dB fractional bandwidth of the IDT can reach up to about 50% as shown in Figure 3.5.

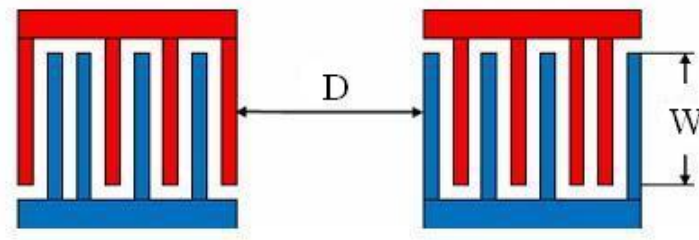


Figure 3.3: Geometry of the pair reverted IDT, red is hot and blue is ground.

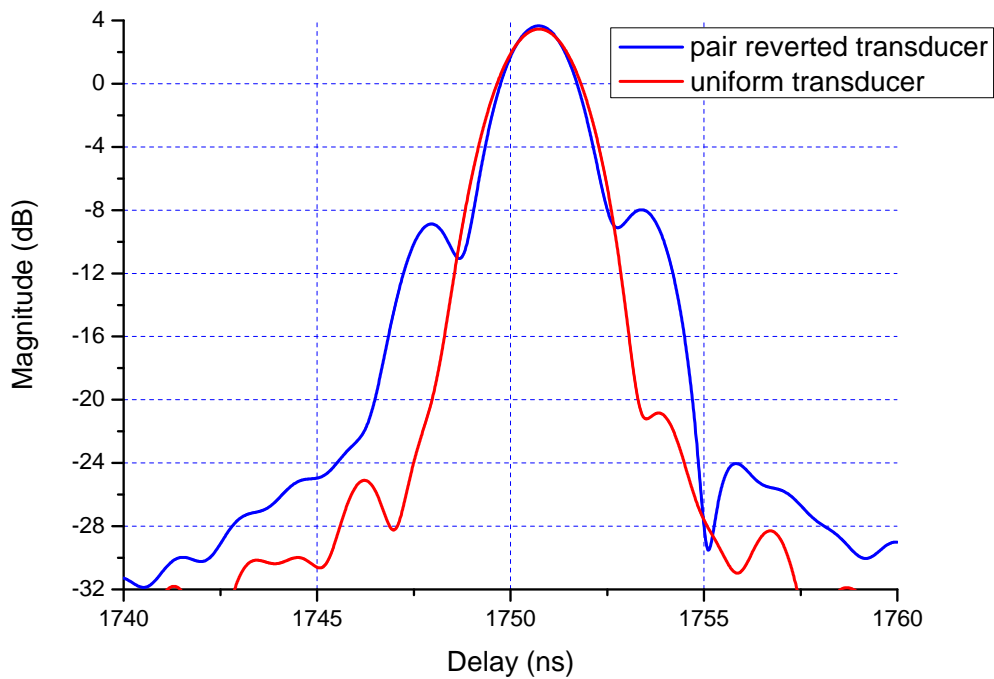


Figure 3.4: The measured impulse response comparison between the uniform IDT and the pair reverted IDT in time domain: red curve is the single transit main pulse for the uniform IDT with aperture $W = 780 \mu\text{m}$ (the geometry is shown in Figure 3.2, $D = 6100 \mu\text{m}$); blue curve is the single transit main pulse for pair reverted IDT with aperture $W = 780 \mu\text{m}$ (IDT geometry is shown in Figure 3.3, $D = 6100 \mu\text{m}$).

The ohmic loss of the IDT is mainly determined by its metal thickness. The Al finger resistance can be approximated as follows. For a single square area on the finger, the resistance is measured to be: $R_{square} = \frac{0.04}{h(\mu\text{m})}$ (Ω) [64] (here h is the Al film thickness in microns); for one finger, the total resistance is one third of the series of R_{square} , $R_{finger} = \frac{1}{3}R_{square}N_{square}$ (Ω) (here N_{square} is the number of square areas in a finger); then the whole IDT resistance is the parallel of all the finger pairs ($2 \cdot R_{finger}$), $R_{ohmic} = \frac{2}{N_{pairs}}R_{finger}$ (Ω). Using the above approximation, the static finger resistance can be derived according to

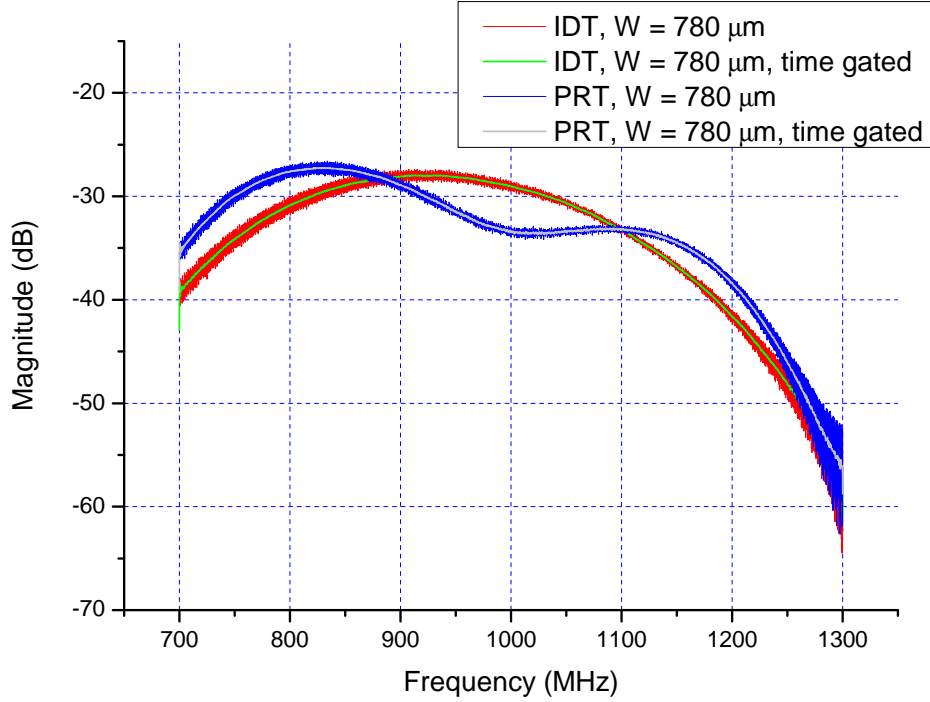


Figure 3.5: The bandwidth comparison between the uniform IDT and pair reverted IDT in frequency domain: red curve is the measured magnitude of uniform IDT with aperture $W = 780 \mu\text{m}$ (geometry is shown in Figure 3.2); green curve is the performance for only the single transit main pulse (the other pulses are time gated); blue curve is the measured magnitude of pair reverted IDT with aperture $W = 780 \mu\text{m}$ (geometry is shown in Figure 3.3); also grey curve is the performance for the single transit main pulse.

the metal thickness h as shown in Equation 3.1 (in Ω).

$$R_{ohmic} = \frac{2}{3} R_{square} \cdot \left(\frac{W}{\lambda}\right) \frac{4}{N_{pairs}} \quad (3.1)$$

For the IDT series acoustic resistance, it can be approximated using Equation 3.2 (in Ω), which is independent of the IDT finger pairs N_{pairs} [79]:

$$R_s = \frac{\Delta v}{v} \cdot \frac{\tilde{G}}{2\pi v \cdot \frac{W}{\lambda} (\epsilon_0 + \epsilon_p)} \quad (3.2)$$

In Equation 3.2, $\Delta v = v - v_m$, v is SAW phase velocity on free surface and v_m is SAW phase velocity on shorted surface, for YZ-LiNbO₃, we have $\frac{\Delta v}{v} = 2.4\%$. $\frac{W}{\lambda}$ is IDT aperture divided by SAW wave length. $\tilde{G} = 2.871$ is for two fingers per period uniform IDTs. For YZ-LiNbO₃, $(\epsilon_0 + \epsilon_p) \approx 47 \cdot \epsilon_0 \approx 4.16 \cdot 10^{-10}$ F/m [13].

The overall IDT resistance is a series of R_s and R_{ohmic} . The input power dissipated on R_s will generate SAW, and power dissipated on R_{ohmic} will turn to heat. To choose the optimized thickness of the deposited Al, we can make $R_{ohmic} < R_s$, or the ohmic loss of the IDT will be high and, hence, increase the IDT pair transduction loss.

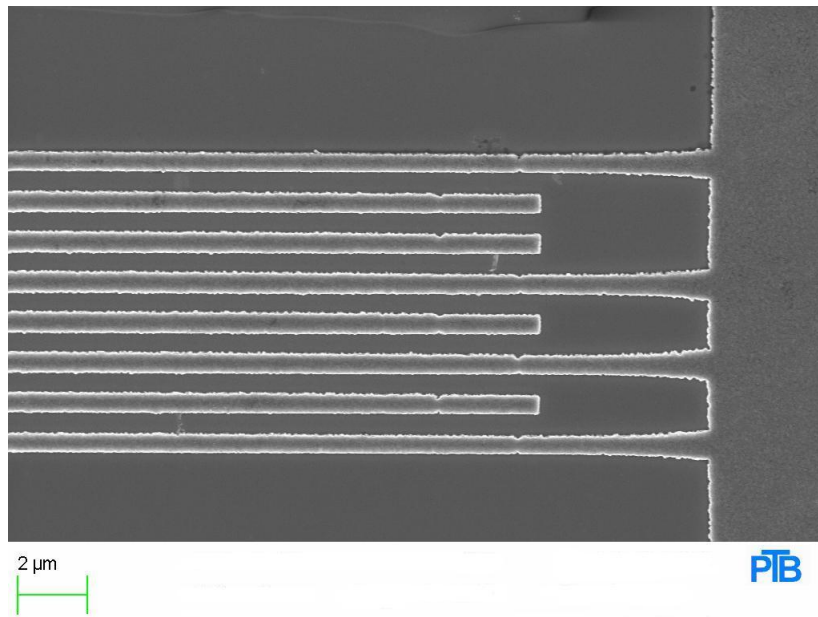


Figure 3.6: Scanning Electron Microscope (SEM) image for one pair reverted transducer (PRT) with 200 nm thick Al film of 1 GHz center frequency on YZ-LiNbO₃.

For our applications, we use 200 nm Al film for the IDTs. Hence, when the aperture of the IDT $W = 550 \mu\text{m}$, $R_s \approx 47.8 \Omega$, and the ohmic resistance is $R_{ohmic} \approx 33.6 \Omega$. We can see that using this thickness the ohmic resistance of the IDT R_{ohmic} is reasonably small compared to its acoustic resistance R_s . If we use only 100 nm Al film for the IDTs, then the R_{ohmic} is about 67.2 Ω , and the R_s is still about 47.8 Ω , then we will have $R_{ohmic} > R_s$. In this case, the transduction loss of the IDT will be increased a lot.

3.2.1 FEM/BEM simulation of the IDT performance

We discussed the simulation of the reflective array's transfer function in last chapter, however, we still need to evaluate the performance of the transducer to have a complete simulation of the whole RAC device. For the characterization of the transducer, firstly a FEM/BEM software is used to simulate the IDT performance. Using the FEM/BEM tool it is possible to have a fast simulation of the transducer design before the real device is fabricated.

In the 1990s, SAW device analysis were based mainly on models only approximating the device physics (i.e. phenomenological models), e.g. the impulse response model, the equivalent circuit model and the coupling of modes model. Basically these models adopt similar concepts from other areas, e.g. circuit analysis for equivalent circuit models. These models can only provide a fast but approximated analysis, as they does not precisely describe the physics of the device. Also, these models needs external frequency dependent parameters extracted from experiments or another more rigorous analysis to make a precise simulation [18].

Generalized Green's function is the rigorous analysis method for wave propagation in homogeneous semi-infinite material, because it describes the physics precisely. Based on the generalized Green's function (using the Boundary Element Method (BEM)), it is

possible to simulate the acoustic wave excitations by the stress and charges on the surface of homogeneous semi-infinite piezoelectric material [52]. The Finite Element Method (FEM) can be used to solve the electrode's mass loading effect, which allows us to get the relationship between displacement and stress on the interface of the electrodes and the substrate [53; 55; 54].

Combining the FEM and BEM, the solution of the system's set of linear equations can be found. Using this method it is possible to rigorously simulate the performance of finite SAW devices, e.g. to precisely evaluate the insertion loss etc. It can take into account the short structure's end effect, and thus the loss due to bulk wave scattering [19].

So before the fabrication of the real device, we used the FEM/BEM software (simulation supplied by Dr. Victor Plessky from GVR Trade) to simulate the performance, electrical Y parameters of the device are obtained ($Y_{11}, Y_{12}, Y_{21}, Y_{22}$). We simulated the uniform IDT delay line, the layout is shown in Figure 3.2, the aperture of the IDT is $W = 780 \mu\text{m}$, the separation of the two IDTs is $D = 6100 \mu\text{m}$, and the IDT are designed with 1 GHz center frequency. In the following we shall compare the simulated result with the measurement result.

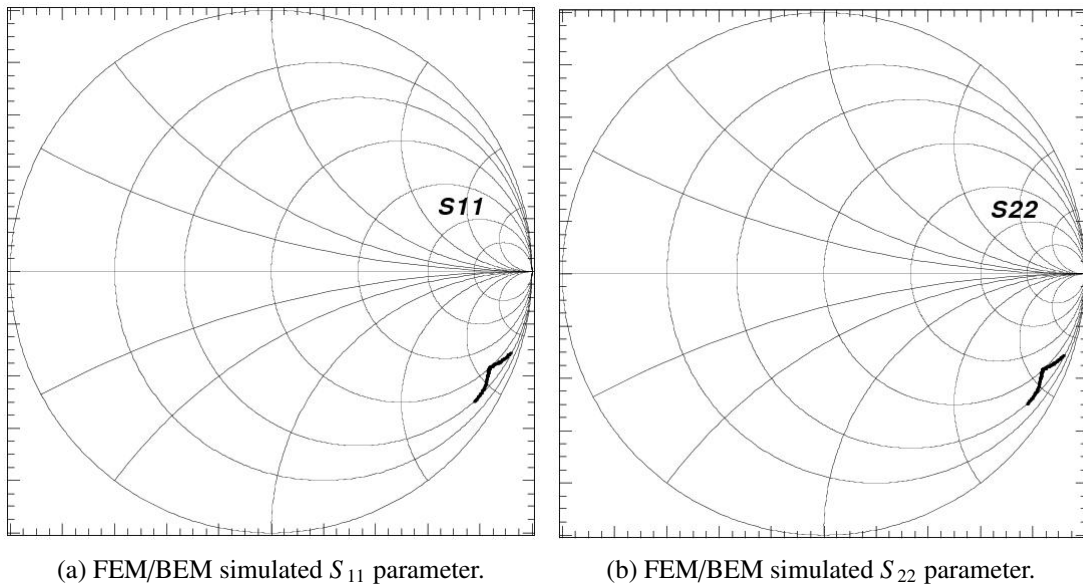


Figure 3.7: FEM/BEM simulated S_{11} and S_{22} parameters in the Smith chart for uniform IDT with center frequency $f_c = 1 \text{ GHz}$, five electrodes and aperture $W = 780 \mu\text{m}$. The influence of the package parasitics and the matching network are not taken into account.

Figure 3.7 shows the FEM/BEM simulated S_{11} and S_{22} parameters. Figure 3.8 shows the corresponding measurement results. Due to the influence of the package and contact pads' parasitics and the matching network in the measurement setup, the impedance is with big difference. The equivalent circuit of the package parasitics and also the matching network will be discussed in detail in Section 3.5.

From the comparison of the delay line's insertion loss in Figure 3.9, we can see that the FEM/BEM has very high precision in predicting insertion loss, the differences between the simulation and the experimental results should be due to the fabrication imperfections such as the electrode shape being not perfectly rectangular, and also the real life pack-

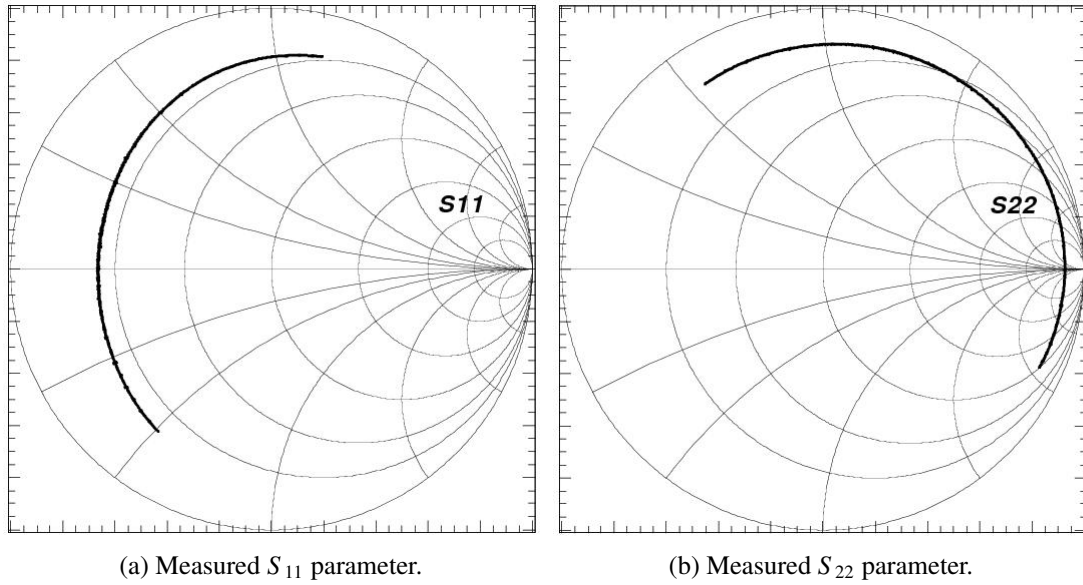


Figure 3.8: Measured S_{11} and S_{22} parameters in the Smith chart of the uniform IDT with center frequency $f_c = 1$ GHz, five electrodes and aperture $W = 780 \mu\text{m}$. The package parasitics and the matching network are included in the measurement.

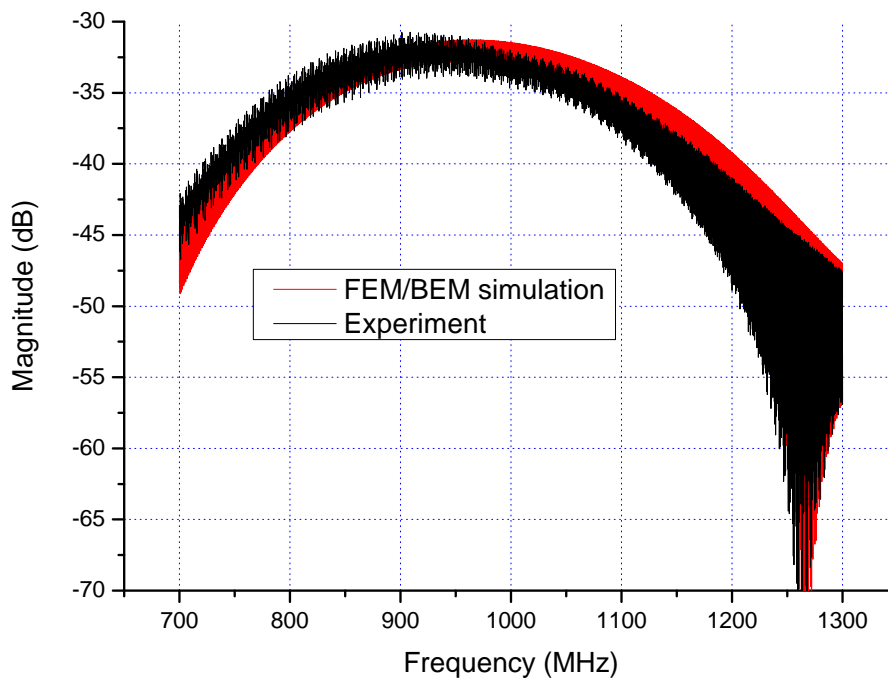


Figure 3.9: Comparison of the delay line's insertion loss between FEM/BEM simulation and experimental result for aperture $W = 780 \mu\text{m}$ five electrodes 1 GHz center frequency uniform IDT on YZ-LiNbO₃, the IDT geometry is as shown in Figure 3.2, $D = 6100 \mu\text{m}$.

age parasitics and the matching networks which were not taken into account (due to the impedance difference as shown in Figure 3.7 and Figure 3.8).

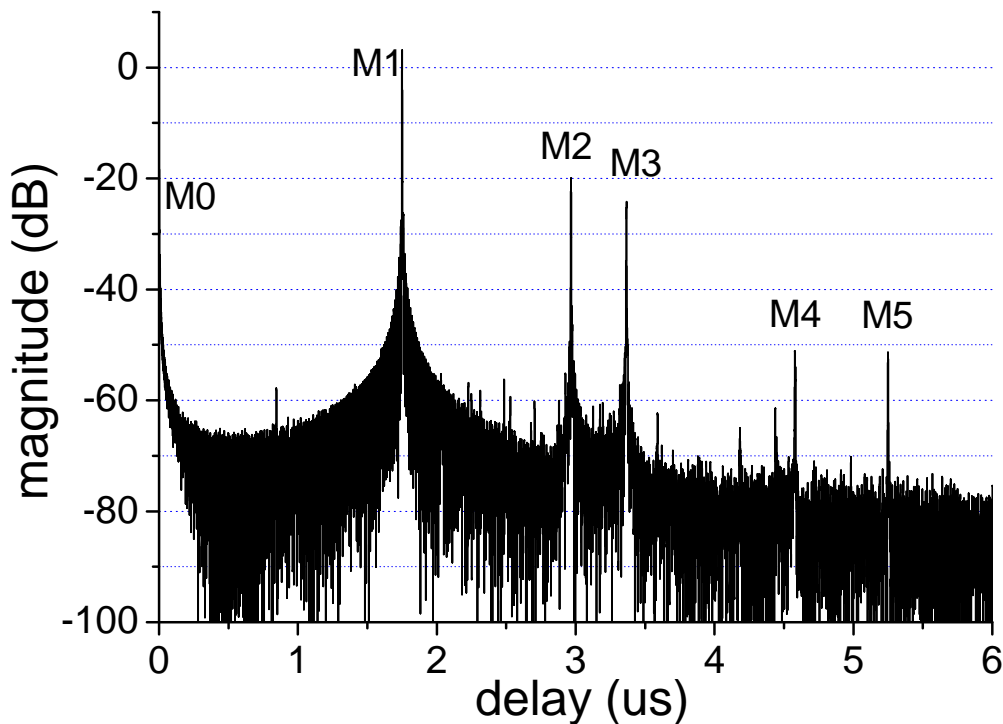


Figure 3.10: The measured impulse response of aperture $W = 780 \mu\text{m}$, five electrodes, 1 GHz center frequency uniform IDT delay line on YZ-LiNbO₃. The IDT's geometry is as shown in Figure 3.2, the distance between the two IDTs is: $D = 6100 \mu\text{m}$.

From the comparison of Figure 3.10 and Figure 3.11, we can see the difference of the impulse response of the delay line in the time domain between the measurement result and the FEM/BEM simulation. In Figure 3.10, there is a pulse M0 at $0 \mu\text{s}$ which is the electromagnetic feedthrough and the magnitude is -16.7 dB ; correspondingly there is a pulse F0 in Figure 3.11 which is with -18 dB magnitude. For the single transit main pulse M1 and F1 in both figures, we can see that they fit very well with each other on delay time and also magnitude. Pulse M2 and M3 in the measurement are reflections from the left and right chip edges; in the FEM/BEM simulation, as the substrate surface is assumed to be infinitely large, so these two pulses do not exist. Pulse M5 in the measurement is the triple transit echo, it is very well simulated in the FEM/BEM calculation by pulse F3. Pulse F2 in Figure 3.11 is caused by the double transit SAW which is excited by the feedthrough between the input port and output port. In the measurement, this F2 disappeared, as shielding was used between the input and output IDTs, the pulse magnitude is, therefore, suppressed to a very small level. Pulse M4 in Figure 3.10 is caused by double reflections from both the left and right chip edges; and for the same reason like pulse M2 and M3, it is not simulated in Figure 3.11. The propagation path of all these pulses are illustrated in Figure 3.12.

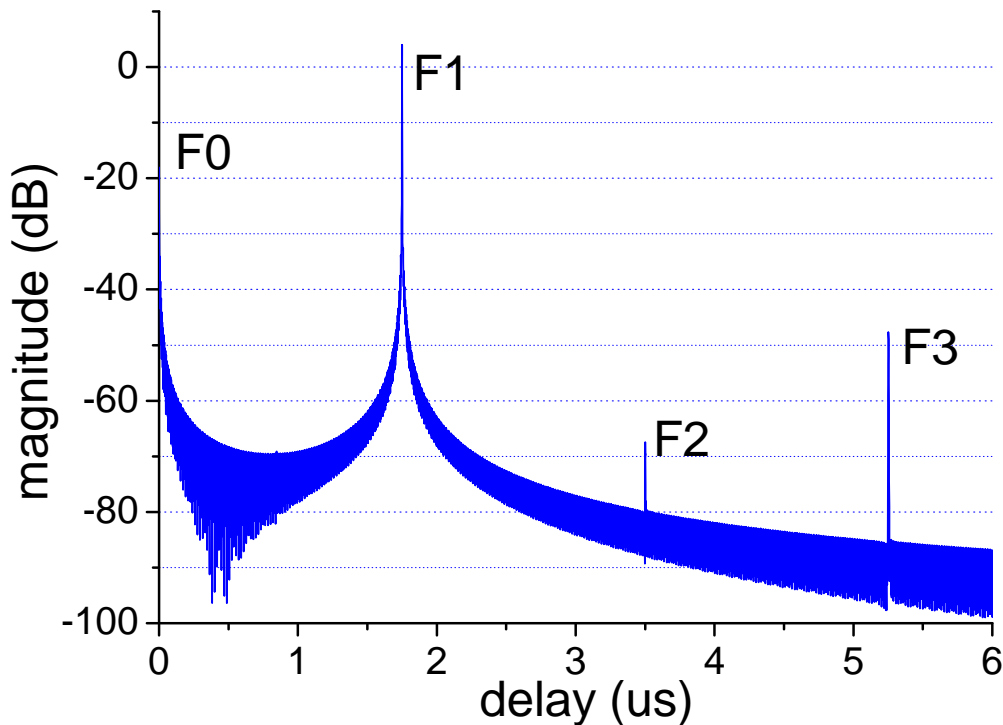


Figure 3.11: The FEM/BEM simulated impulse response of aperture $W = 780 \mu\text{m}$, five electrodes, 1 GHz center frequency uniform IDT delay line on YZ-LiNbO₃, the IDT's geometry is as shown in Figure 3.2, the distance between the two IDTs is $D = 6100 \mu\text{m}$.

The comparison of the delay line's frequency dependent phase and delay between the FEM/BEM and the measurement is shown in Figure 3.13. We can see that the simulation fits the experiment very well.

From the above comparison we can see that, as the FEM/BEM simulation describes the physics in the SAW devices precisely, it has very high accuracy in predicting the performance of the device.

3.2.2 Simple delay line measurement and IDT loss characterization

In order to evaluate the IDT transduction more precisely including the influence of fabrication imperfections, package parasitics and matching networks, simple delay lines were fabricated and measured using a vector network analyzer (VNA). The layout of the IDT is shown in Figure 3.14. The distance D_1 (from the center of the input IDT to the left chip edge), D_2 (from the center of the input IDT to the center of the output IDT) and D_3 (from the center of the output IDT to the right chip edge) in the layout and their corresponding delay time τ_1 , τ_2 and τ_3 are listed in Table 3.1 (they are calculated according to the free surface SAW phase velocity $v_p = 3488 \text{ m/s}$ [13]).

This layout is created to fit the holder which is designed as shown in Appendix F from Figure F.1 to Figure F.3, especially for $T = 10 \mu\text{s}$ RACs. So when the measurement is

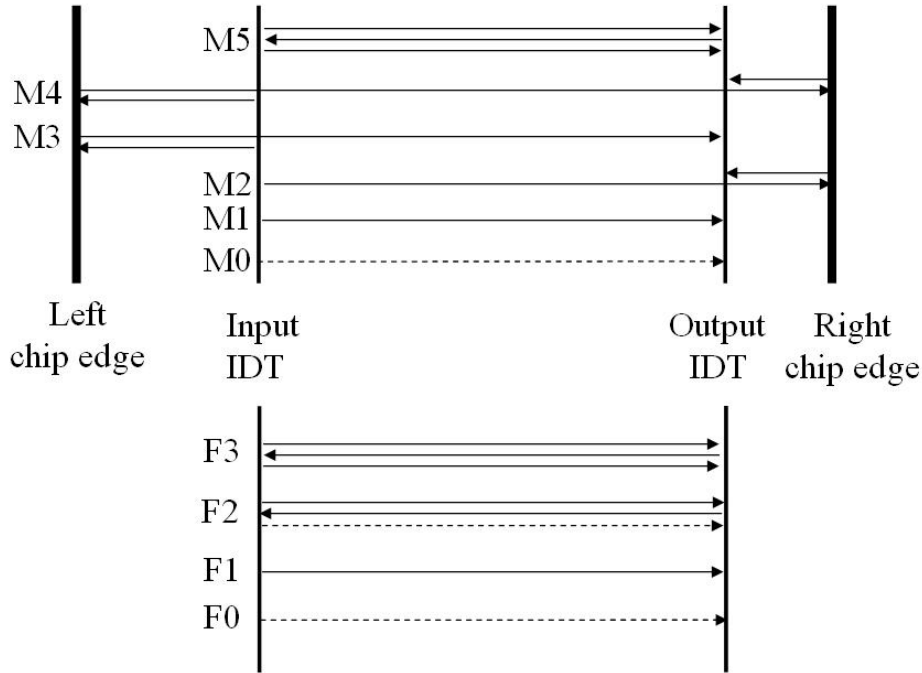


Figure 3.12: Propagation path of pulses in Figure 3.10 and Figure 3.11. Dashed line represent electromagnetic feedthrough, solid line represent SAW propagation.

performed, the influence of the matching network and also package parasitics are all taken into account. The measured pair reverted transducer performance using this layout will be, therefore, almost the same as the transducer in the RAC.

	length	delay
D1	2800 μm	$\tau_1=803$ ns
D2	6100 μm	$\tau_2=1749$ ns
D3	2100 μm	$\tau_3=602$ ns

Table 3.1: Distance of D1, D2, D3 in Figure 3.14 and corresponding delay

The measured S_{11} and S_{22} parameters of the delay line are shown in Figure 3.15a and Figure 3.15b in the Smith chart. The influence of the package parasitics and also the matching network are included in the measurement.

The frequency dependent phase and delay time of the PRT delay line which is calculated from the measured S_{21} parameter are shown in Figure 3.16 and Figure 3.17, respectively. As shown in Figure 3.3 we put the two pair reverted IDTs in the delay line symmetrically, then the dispersion generated by the reverted finger pair in the input IDT will compensate the dispersion generated by the pair in the output IDT. Thus, a linear phase as shown in Figure 3.16 like for the uniform IDT delay line is obtained. Without dispersion, the delay time is about a constant, the averaged value is approximately $\frac{6.1 \text{ mm}}{3.488 \text{ mm}/\mu\text{s}} \approx 1.75 \mu\text{s}$ as shown in Figure 3.17. Using this symmetrical arrangement of the PRT in the RAC, the quadratic phase required for the RAC will not be influenced by the phase of the transducer. It is, therefore, only determined by the design of the reflective

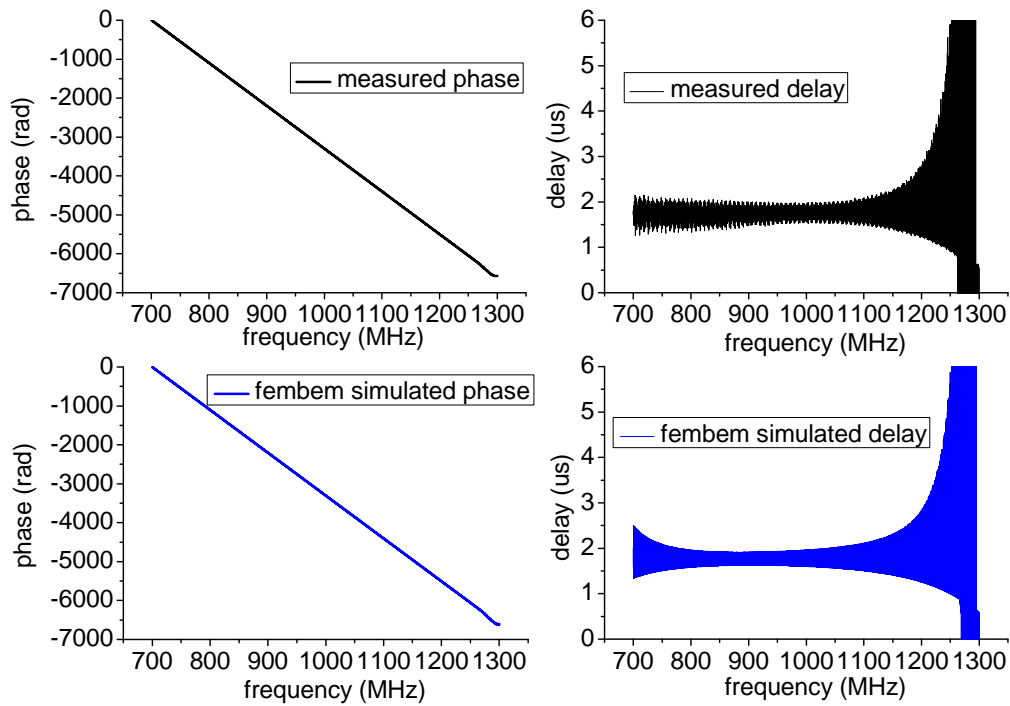


Figure 3.13: Comparison of the delay line's phase and delay between FEM/BEM simulation and measurement for aperture $W = 780 \mu\text{m}$, five electrodes, 1GHz center frequency uniform IDT on YZ-LiNbO₃, the IDT geometry is as shown in Figure 3.2, the distance D between two IDTs is $6100 \mu\text{m}$.

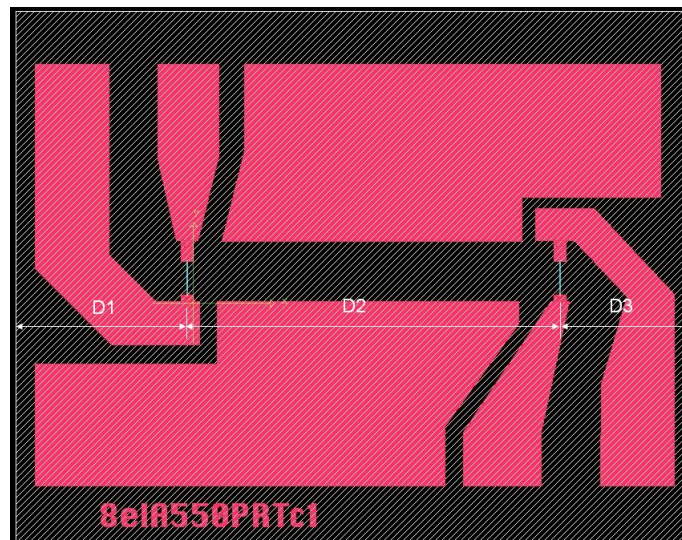


Figure 3.14: Delay line layout for the aperture $W = 780 \mu\text{m}$, eight electrodes pair reverted transducer (PRT) of 1 GHz center frequency.

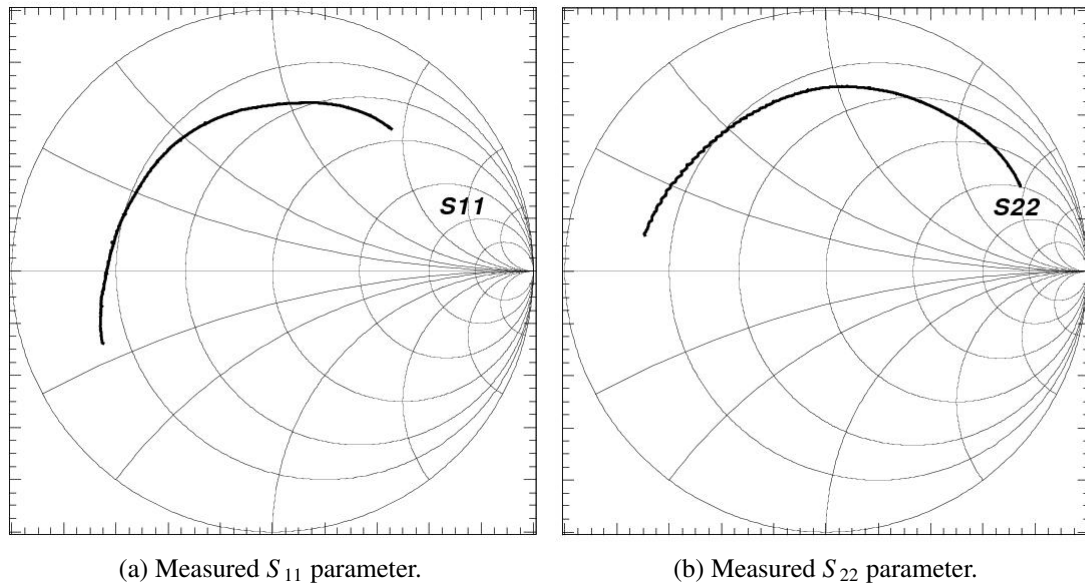


Figure 3.15: Measured S_{11} and S_{22} parameters in the Smith chart of the pair reverted transducer with center frequency $f_c = 1$ GHz, eight electrodes and aperture $W = 780 \mu\text{m}$.

array.

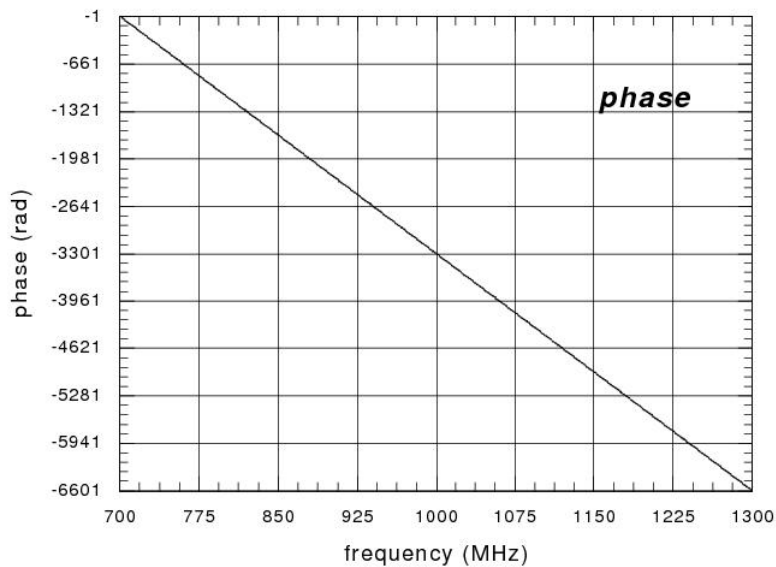


Figure 3.16: Measured phase of the PRT delay line with center frequency $f_c = 1$ GHz, eight electrodes and aperture $W = 780 \mu\text{m}$, the geometry is as shown in Figure 3.3 with $D = 6100 \mu\text{m}$.

The measured S_{21} parameter magnitude in frequency domain and its inverse Fourier transform in time domain are shown in Figure 3.18 and Figure 3.19, respectively. From Figure 3.19 we can see that there are five major pulses P0, P1, P2, P3 and P4 in the impulse response of the delay line in the time domain. Their respective delay time can be read from Figure 3.19 as listed in Table 3.2. From the relationship between P0 to P4's

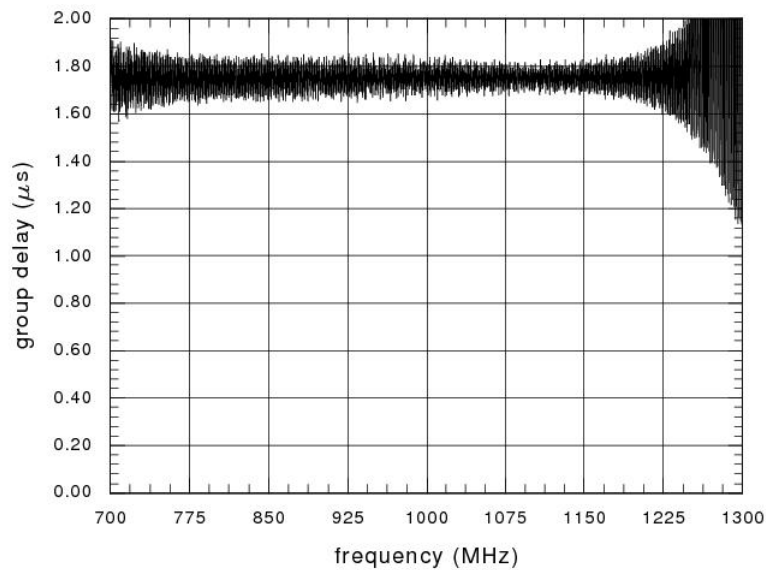


Figure 3.17: Measured delay of the PRT delay line with center frequency $f_c = 1$ GHz, eight electrodes and aperture $W = 780 \mu\text{m}$, the geometry is as shown in Figure 3.3 with $D = 6100 \mu\text{m}$.

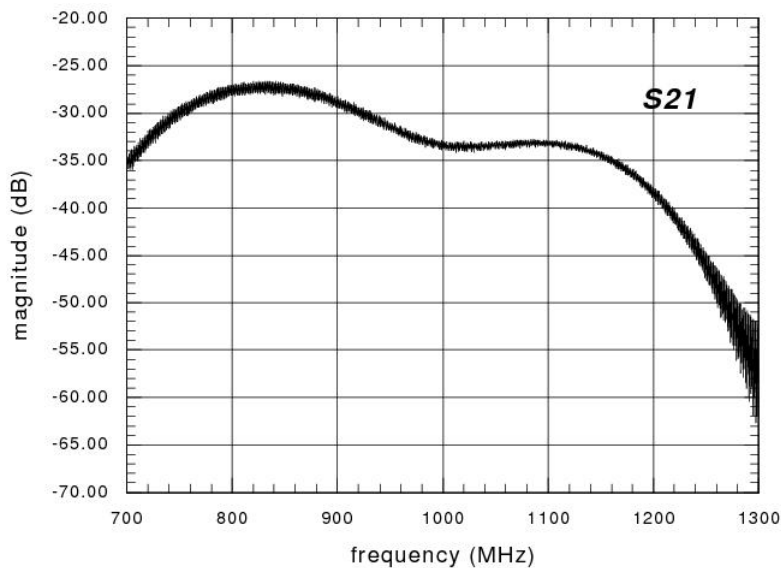


Figure 3.18: Measured insertion loss of the PRT delay line with center frequency $f_c = 1$ GHz, eight electrodes and aperture $W = 780 \mu\text{m}$, the geometry is as shown in Figure 3.3 with $D = 6100 \mu\text{m}$.

delay and $\tau_1 \tau_2 \tau_3$ (the SAW propagation time in D1 D2 and D3), we could deduce the SAW propagation path for each pulse as shown in Figure 3.20. From their propagation paths, we can see that pulse 0 is direct electromagnetic feedthrough, pulse 1 is the single transit main response, pulse 2 and 3 are the strong reflections from right and left chip edges separately, and pulse 4 is the triple transit echo. Because in our RAC, the two IDTs are shifted 6 mm from each other, so the feedthrough is suppressed to -75 dB; also silicon glue has been spread on four chip edges to suppress the reflections; and the triple transit

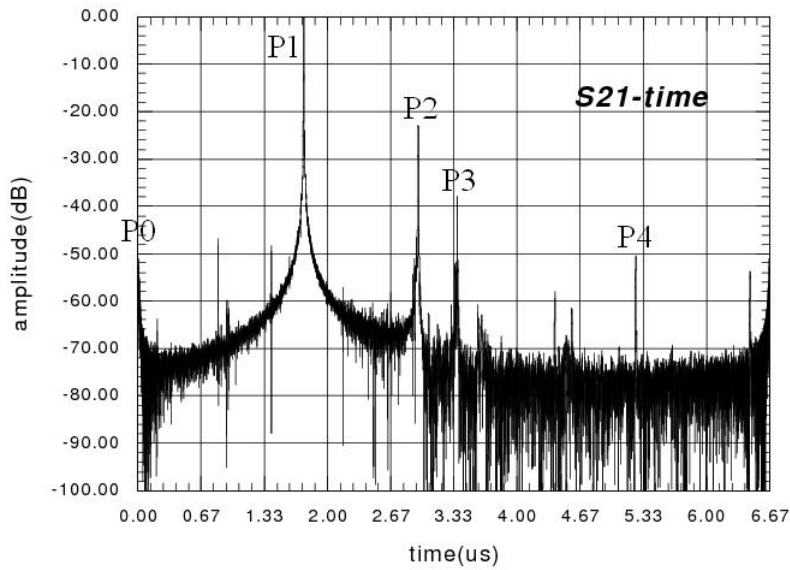


Figure 3.19: Measured impulse response of the PRT delay line with eight electrodes and aperture $W = 780 \mu\text{m}$ (the inverse Fourier transform of the measured S_{21} parameter).

pulse	delay	relation to $\tau_1\tau_2\tau_3$
P0	0 ns	0 ns
P1	1740 ns	τ_2
P2	2933 ns	$\tau_2 + 2\tau_3$
P3	3360 ns	$\tau_2 + 2\tau_1$
P4	5200 ns	$3 \cdot \tau_2$

Table 3.2: Delay time of the pulses P0, P1, P2, P3 and P4 in Figure 3.19 and their relationship with τ_1 , τ_2 and τ_3

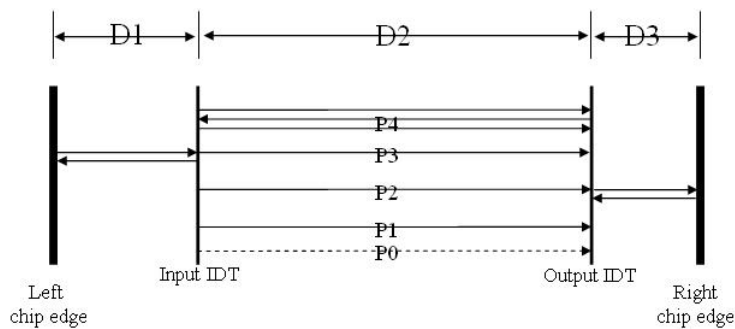


Figure 3.20: Propagation path of pulses P0, P1, P2, P3 and P4. Dashed line represent electromagnetic feedthrough, solid line represent SAW propagation.

echo does not exist due to the fact that the IDTs in the RACs are arranged at two ends of the ‘U’ shaped propagation path. So for characterizing the IDT loss transduction in the RAC correctly, pulses 0, 2, 3 and 4 are gated away to have only the single transit main response (pulse 1) left as shown in Figure 3.21. Then the gated signal was inverse Fourier

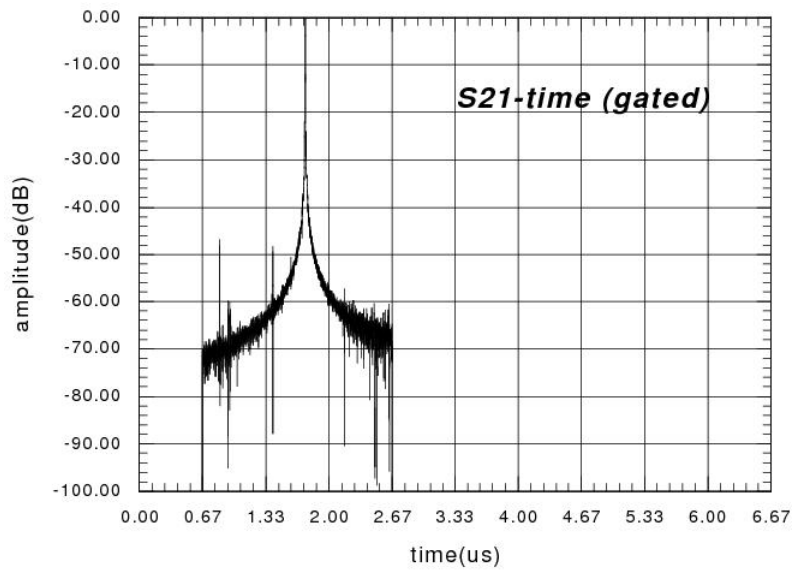


Figure 3.21: Time gating for IDT transduction loss characterization in the RAC.

transformed to the frequency domain; the result is shown in Figure 3.22. By comparing

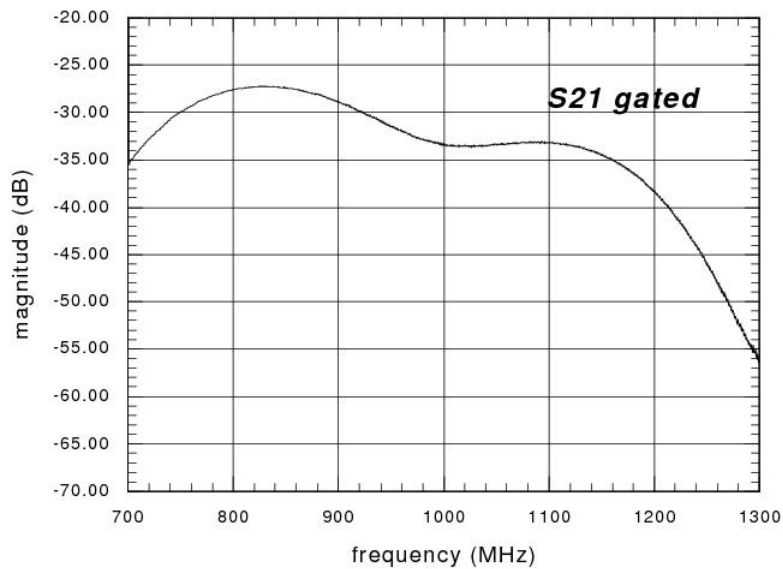


Figure 3.22: Magnitude curve of PRT in the frequency domain after time gating.

Figure 3.18 and Figure 3.22, we can see that after the time gating of the unwanted pulses, the magnitude ripple is removed. Then the very smooth magnitude curve in Figure 3.22 is the IDT transduction loss in RAC that we require, which now can be used for the RAC magnitude optimization. The optimization process will be discussed in detail in the next chapter.

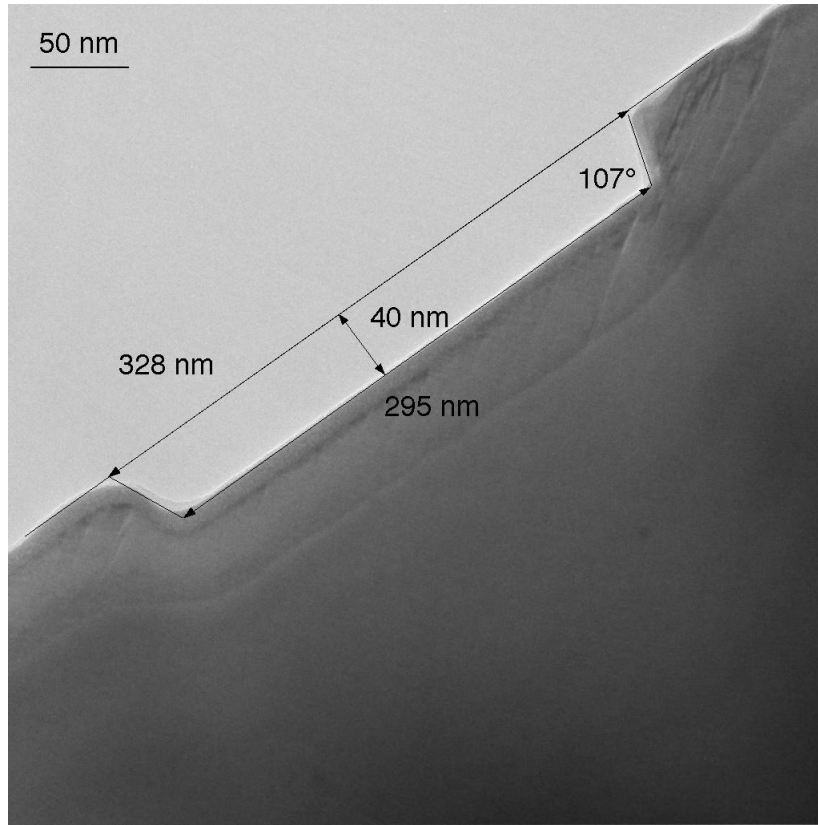


Figure 3.23: Transmission Electron Microscope (TEM) image for a 40 nm Argon ion-beam etched single groove with 10% duty cycle for 1.2 GHz SAW reflection.

3.3 Single groove reflectivity for oblique SAW incidence

Figure 3.23 is a transmission electron microscope image for the Argon ion-beam etched 40 nm single groove geometry on YZ-LiNbO₃. It is not a perfect rectangle, and the wall angle is about 110 degrees.

The Argon ion-beam etched single groove reflectivity for SAW normal incidence on YZ-LiNbO₃ was first measured by R. C. Williamson [5]. He found that the single groove reflectivity is linearly dependent on the groove depth h for 50% duty cycle grooves (Equation 3.3); and the slope that fitted from the measurement is $C_{normal} \approx \frac{1}{3}$.

$$\Gamma_g = C_{normal} \cdot \left(\frac{h}{\lambda}\right) \quad (3.3)$$

After that R. C. M. Li conducted a theoretical analysis of up and down steps on YZ-LiNbO₃ for the SAW normal incidence using the equivalent-network theory [21]. The amplitude reflectivity of the SAW from the up step Γ_u and the down step Γ_d , and the transmission coefficient τ (same for up or down step) on the substrate surface are derived as follows:

$$\Gamma_u = r - j\frac{\hat{B}}{2} \quad (3.4)$$

$$\Gamma_d = -r - j\frac{\hat{B}}{2} \quad (3.5)$$

$$\tau = 1 - \frac{r^2}{2} - \frac{\hat{B}}{2} \quad (3.6)$$

In the above equations, r is the impedance-mismatch contribution which is proportional to the step height h :

$$r = C \cdot \frac{h}{\lambda} \quad (3.7)$$

$\frac{\hat{B}}{2}$ is the energy-storage contribution which is proportional to h^2 :

$$\frac{\hat{B}}{2} = C' \cdot \left(\frac{h}{\lambda}\right)^2 \quad (3.8)$$

In Equation 3.7 and Equation 3.8, λ is the wavelength of the SAW, C and C' are the proportionality coefficients to be determined by experiments. Then the single groove reflectivity for the SAW oblique incidence and 90 degrees reflections on YZ-LiNbO₃ was measured by J. Melngailis [20]. He adopted the same expression for the SAW normal incidence on up and down steps as in Equation 3.4, Equation 3.5 and Equation 3.6 [21]. For a single groove with a down and then an up step, the illustration for the reflection of the SAW is as shown in Figure 3.24. The expression for the groove reflectivity Γ_g can be

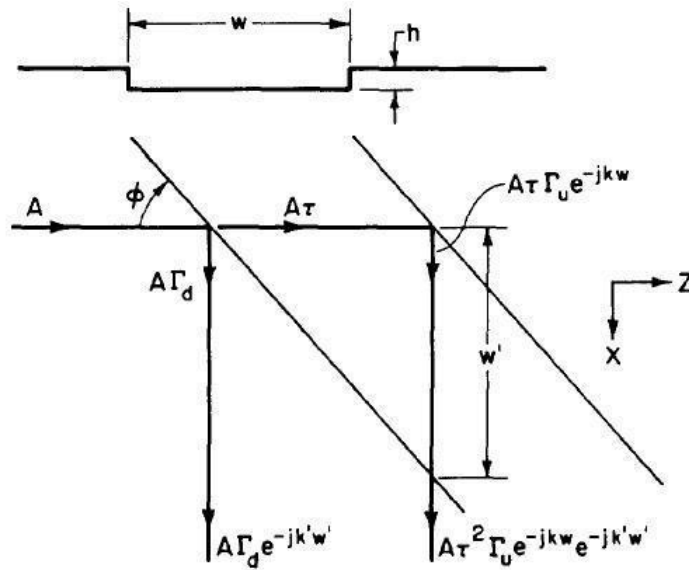


Figure 3.24: A surface wave of amplitude A is incident on the two groove edges inclined at an angle $\Phi = 46.82^\circ$ for a Z-to-X reflection on YZ-LiNbO₃. The amplitudes and phases of the parts of the beam reflected from the two edges are indicated. The total reflectivity of the groove can be deduced by adding the two parts of the beam reflected from the two edges [20].

derived using Equation 3.4, Equation 3.5 and Equation 3.6. If we follow the SAW beam as shown in Figure 3.24, ignore $e^{-jk'w'}$ which is the common propagation coefficient in X direction for the two beams reflected by the up and down steps, Equation 3.9 can be derived:

$$\Gamma_g = \Gamma_d + \tau^2 \Gamma_u e^{-jkw} \quad (3.9)$$

By ignoring the $\left(\frac{h}{\lambda}\right)^3$ and even higher orders, the above equation will become Equation 3.10.

$$\Gamma_g = -2je^{-j\theta}\left(r \cdot \sin \theta + \frac{\hat{B}}{2} \cos \theta\right) \quad (3.10)$$

Here, $k = \frac{2\pi}{\lambda}$ is the wave number of the SAW, and $\theta = \frac{kw}{2} + \frac{\hat{B}}{2}$. In [20], the two proportionality coefficients C and C' in Equation 3.7 and Equation 3.8 are fitted from the experiments, and they are listed in Table 3.3.

$r = C\left(\frac{h}{\lambda}\right)$	$\frac{\hat{B}}{2} = C'\left(\frac{h}{\lambda}\right)^2$
C	C'
0.51 ± 0.03	4.5 ± 0.4

Table 3.3: Constants of a single groove for a 90° SAW reflection on YZ-LiNbO₃ (from Z to X) in Equation 3.10 [21].

In order to avoid the multiple reflections inside the reflective array, the total reflectivity of the groove array need to be less than 1 ($R(f) \ll 1$). Therefor the grooves need to be very shallow ($\frac{h}{\lambda} \approx 1\%$). Then term $\frac{\hat{B}}{2}$ in Equation 3.10 which is for the energy storage effect can also be omitted. Because from Table 3.3, we can see that $r > 10 \cdot \frac{\hat{B}}{2}$ when $\frac{h}{\lambda} \approx 1\%$; and also $\theta = \frac{kw}{2} + \frac{\hat{B}}{2} \approx \frac{kw}{2} = \pi\frac{w}{\lambda} \approx \frac{\pi}{2}$ when the groove duty cycle ($\frac{w}{\lambda}$) is close to 50%, so the $\sin \theta$ item in Equation 3.10 approaches one and the $\cos \theta$ item approaches zero. So we only need to keep the first order term of $\frac{h}{\lambda}$ in Equation 3.10 when the groove duty cycle ($\frac{w}{\lambda}$) is close to 50% and the groove depth is shallow ($\frac{h}{\lambda} \approx 1\%$). Then we can get the approximation of the magnitude of single groove's reflectivity in the form of the following empirical formula [13]:

$$|\Gamma_g| \approx 2 \cdot 0.51 \left(\frac{h}{\lambda}\right) \sin\left(\pi\frac{w}{\lambda}\right) \quad (3.11)$$

Here, h is the groove depth, λ is the Rayleigh wave wavelength and w is the groove width. For very narrow grooves ($w \Rightarrow 0$) Equation 3.11 gives the reflectivity going to zero. That is evidently not exact, because even a very narrow gap will have finite reflectivity - the perturbation of the surface remains. This phenomenon was recently discussed by A. Darinskii [22].

3.4 Single electrode parameter extraction on 128° YX LiNbO₃

Single electrodes are very important building blocks for SAW Tags, SAW sensors and in line dispersive delay lines. In order to make a good design for these devices, the corresponding parameters for the single electrode are needed, e.g. reflection, transmission coefficient and bulk wave scattering coefficient for the SAW. The basic principle of these parameters' extraction is based on paper [25], in which they use the FEM/BEM simulation to get the test structure performance. In the following, we used a similar test structure, but the performance is obtained using measurements. The geometry of the test structure is shown in Figure 3.25; the IDT used is of a uniform type and has ten electrodes, which

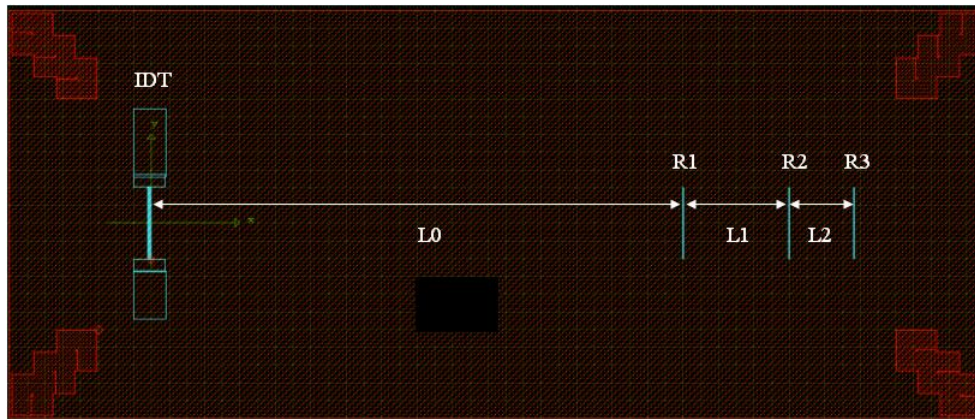


Figure 3.25: Geometry for test structures, where $L0 = 3000 \mu\text{m}$, $L1 = 600 \mu\text{m}$ and $L2 = 362.618 \mu\text{m}$, the reference plane is at the center of the IDT and center of each reflectors group.

are five pairs of alternating polarities. The aperture of the IDT is $400 \mu\text{m}$, the electrode pitch is $2 \mu\text{m}$, and the metalization ratio is 0.5. The substrate is 128° YX LiNbO₃, so the center frequency of the IDT is about 970 MHz.

The three identical reflector groups are placed in the acoustic path and each consists of three or nine floating electrodes. Using multiple electrodes in each reflector group is because for our measurements we have a certain level of noises, in order to make the reflected pulses visible (especially the four pulses needed for the parameter extraction need to be above the noise level in the time domain), and we need a certain reflectivity from each reflector group. We will discuss about how the number of the electrodes in each reflector group is determined in the next section.

The distances $L0 = 3000 \mu\text{m}$, $L1 = 600 \mu\text{m}$ and $L2 = 362.618 \mu\text{m}$ between the reflectors are chosen so that none of the first four reflections overlap each other, as these four reflections are essential for our extraction. The electrode types that we would like to characterize are listed in Table 3.4 (including the electrode thickness and width), and with each type of electrode we built a test structure denoted by TSi ($i=1,2,3$).

Test Structure	Metal Thickness h (nm)	$h/\lambda(\%)$	Reflector width $a(\mu\text{m})$	Metalization ratio (a/p)
TS1	100	2.5	0.8	0.4
TS2	200	5.0	1.2	0.6
TS3	100	2.5	1.0	0.5

Table 3.4: Thickness and metalization ratio for single electrodes in TS1, 2 and 3.

3.4.1 S_{11} parameter analysis

If we denote the i^{th} reflected signal of our interest (the i^{th} pulse) by S_i , then it can be written as the product of a frequency-dependent factor F_i and the input signal S_0 used for

exciting the device:

$$S_i = F_i \cdot S_0 \quad (i = 1..4) \quad (3.12)$$

where for those frequency-dependent factors F_i , the composition is shown from the equations Equation 3.13 to Equation 3.16 according to their propagation path for each pulse as illustrated in Figure 3.26.

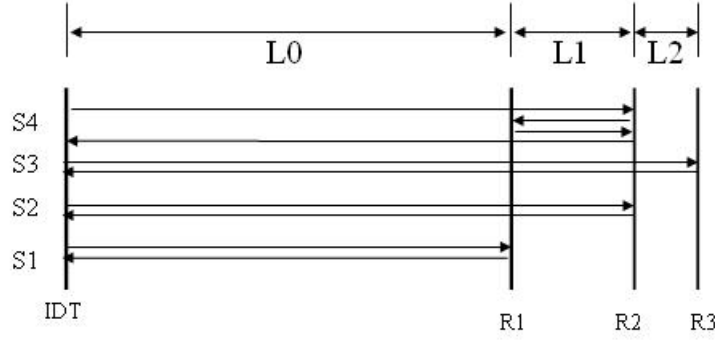


Figure 3.26: The propagation path of the signal S_1 , S_2 , S_3 and S_4 for the test structure.

$$F_1 = D \cdot P_0 \cdot R \cdot P_0 \cdot D = D^2 \cdot P_0^2 \cdot R \quad (3.13)$$

$$F_2 = D^2 \cdot P_0^2 \cdot T^2 \cdot P_1^2 \cdot R \quad (3.14)$$

$$F_3 = D^2 \cdot P_0^2 \cdot T^4 \cdot P_1^2 \cdot P_2^2 \cdot R \quad (3.15)$$

$$F_4 = D^2 \cdot P_0^2 \cdot T^2 \cdot P_1^4 \cdot R^3 \quad (3.16)$$

In the above equations, D is the IDT transduction coefficient. P_i ($i=0,1,2$) are the free surface propagation coefficients which have the form $P_i = e^{-\alpha L_i - jkL_i}$, here, α is the free surface attenuation coefficient, k is the wave number, and L_i the distances shown in Figure 3.25. The related delay times of each pulse for S_i ($i=1, 2, 3, 4$), are listed in Table 3.5 according to their propagation path. Here, we assume the SAW phase velocity on 128° YX LiNbO₃ is 3979 m/s [13].

Signal	Propagation path as shown in Figure 3.28	Delay (ns)
S_1	IDT-R1-IDT	1508
S_2	IDT-R2-IDT	1810
S_3	IDT-R3-IDT	1992
S_4	IDT-R2R1R2-IDT	2112

Table 3.5: Delay of S_1 , S_2 , S_3 and S_4 in Figure 3.28 assuming $v_p = 3979$ m/s [13].

3.4.2 Theory for parameter extraction

If the single electrode reflection and transmission coefficients are denoted R and T , respectively, then we assume they have the form $R = r \cdot e^{j\Phi_R}$ and $T = t \cdot e^{j\Phi_T}$. In these

two expressions, Φ_R and Φ_T are the phase shift due to reflection and transmission, respectively. Because D , α , k , r , t , Φ_R and Φ_T in the above expressions are all frequency dependent variables, they can be described by arrays of the measured S_{11} parameter which has the same number of frequency elements. The contents of Equation 3.13 to Equation 3.16 can be rewritten as:

$$\frac{S_2}{S_1} = T^2 \cdot P_1^2 \quad (3.17)$$

$$\frac{S_3}{S_1} = T^4 \cdot P_1^2 \cdot P_2^2 \quad (3.18)$$

$$\frac{S_4}{S_2} = R^2 \cdot P_1^2 \quad (3.19)$$

If we take Equation 3.17 squared then divide it by Equation 3.18, we can solve for α and k .

$$\frac{S_2^2}{S_1 \cdot S_3} = \left(\frac{P_1}{P_2}\right)^2 = e^{-2\alpha(L_1-L_2)-2jk(L_1-L_2)} \quad (3.20)$$

$$\alpha = \frac{1}{2(L_1 - L_2)} \cdot \ln \left| \frac{S_2^2}{S_1 S_3} \right| \quad (3.21)$$

$$k = \frac{1}{2(L_1 - L_2)} \cdot \angle \left(\frac{S_2^2}{S_1 S_3} \right) \quad (3.22)$$

Furthermore, using the P_1 obtained from the above α and k , it is possible to solve for R and T , which are composed of the absolute values and phase angles as follows:

$$r = \frac{1}{N_e} \cdot \sqrt{\left| \frac{S_4}{S_2 P_1^2} \right|} \quad (3.23)$$

$$t = \left(\sqrt{\left| \frac{S_2}{S_1 P_1^2} \right|} \right)^{\frac{1}{N_e}} \quad (3.24)$$

$$\Phi_R = \frac{1}{2} \angle \left(\frac{S_4}{S_2 P_1^2} \right) \quad (3.25)$$

$$\Phi_T = \frac{1}{N_e} \cdot \frac{1}{2} \angle \left(\frac{S_2}{S_1 P_1^2} \right) \quad (3.26)$$

In the above equations, N_e is the number of floating electrodes in each reflector group. The reason for using multiple electrodes in each reflector group is that the single electrode reflectivity is too small. From our measurement experiences, after using the FFT to transform the cosine square weighted measurement S_{11} parameter to time domain, the noise level is still quite high at about -90 dB. The single floating electrodes usually have only about several percent amplitude reflectivity for Rayleigh waves, e.g., 3%, then for a single electrode, the amplitude of the pulse S_4 will be $20 \cdot \lg(0.03^3) \approx -91$ dB, it will be buried under the -90 dB noise level, and is impossible to get using time gating. Thus, in order to make pulse S_4 stronger, at least above the -90 dB noise level in the time domain, the number of electrodes in each reflector group needs to be increased. E.g., if we use

$N_e = 10$, then for each reflector group, the total reflectivity will be increased by 10 times, and the magnitude of S_4 will be 60 dB higher. Then it is definitely above the -90 dB noise level, and possible to be separated from other pulses using time gating.

For our experimental extractions, we use $N_e = 3$ for TS2 and $N_e = 9$ for TS1 and TS3, as in TS1 and TS3 the electrode's reflectivity is very small.

3.4.3 Measurement results

The test structure was measured with a vector network analyzer using PicoProbe's microwave probes. The measurement frequency range is from 740 MHz to 1200 MHz, the incoming signal power is 0 dBm. The total number of frequency points is 1601, thus the measurement frequency step Δf is 287.5 kHz. The magnitude of the S_{11} parameter for TS2 measurement is shown in Figure 3.27. We used FFT to transform the measured sig-

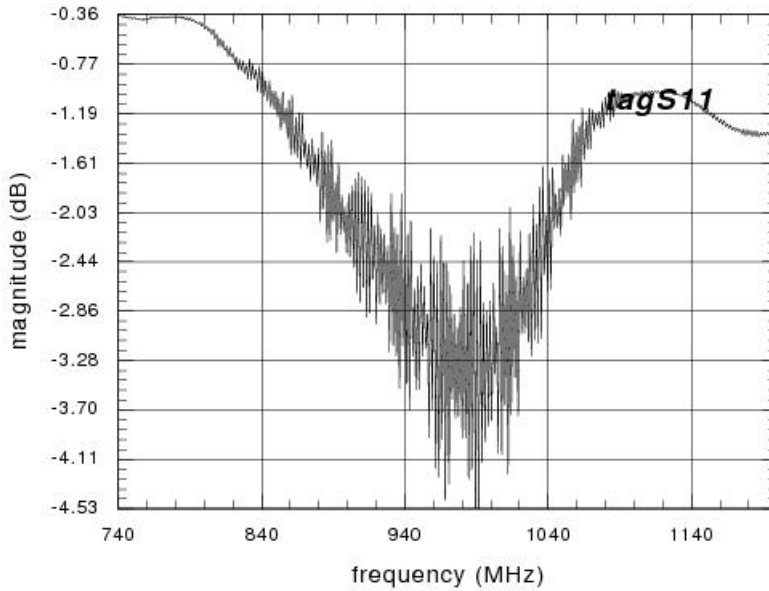


Figure 3.27: TS2 measured S_{11} parameter magnitude in the frequency domain.

nal from frequency domain to time domain. In time domain, the four pulses S_1 to S_4 of our interest can be identified by their delay time as shown in Table 3.5. Using a time gating technique, it is possible to select the pulse we need to have the signal S_i ($i=1,2,3,4$), respectively. With the time gated S_i ($i=1,2,3,4$), we can calculate the reflection, transmission and bulk wave scattering coefficients using the algorithm described in the previous section, and all these coefficients are frequency dependent.

Here, from the wave number extraction shown in Figure 3.29a, the phase velocity of the SAW on 128° YX LiNbO₃ can be obtained by fitting the wave number curve in Figure 3.29a into a linear polynomial ($a \cdot f + b$) in the IDT bandwidth from 950 MHz to 1050 MHz:

$$v_p = \frac{2\pi}{a} \approx 3970.34 \text{ m/s.}$$

It fits well with the result $v_p \approx 3978.97$ m/s in [30].

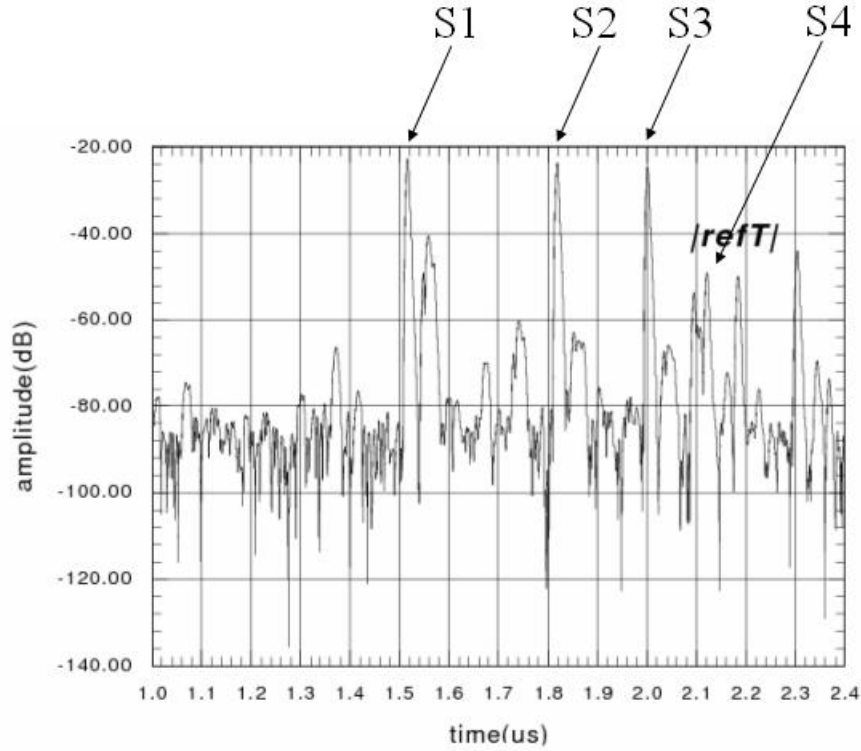


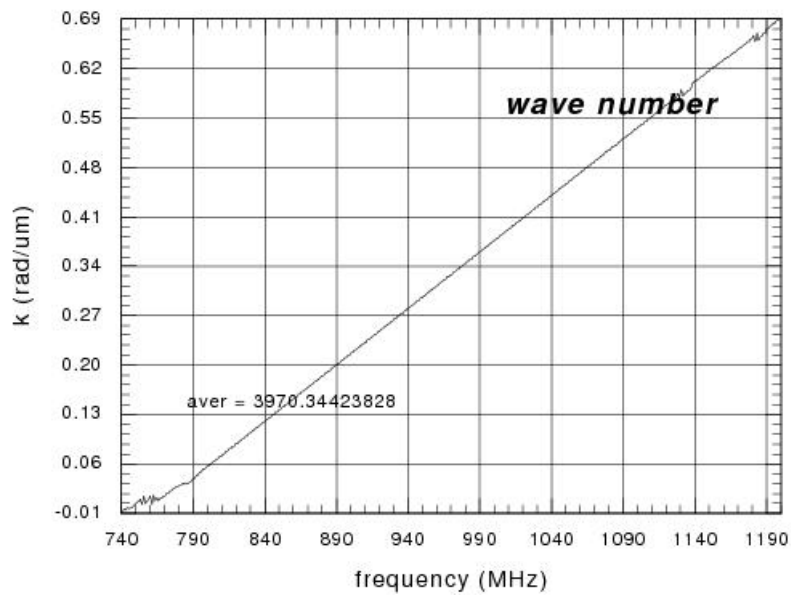
Figure 3.28: TS2 measured impulse response in time domain, S_1 , S_2 , S_3 and S_4 are the analyzed four pulses for our parameter extraction.

Also the propagation loss item α can be obtained, which is shown in Figure 3.29b. Here, the normalized propagation loss $\gamma_{dB/\lambda}$ in the unit of dB/ λ is:

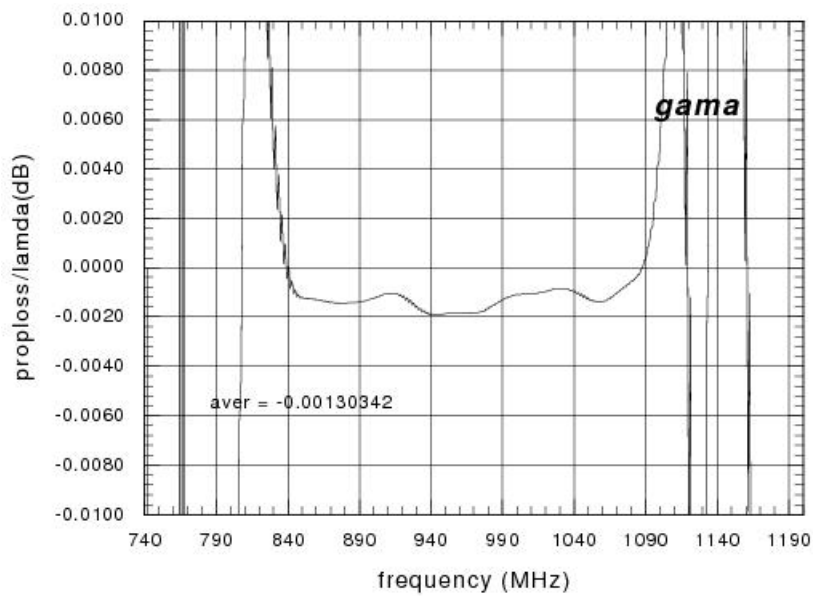
$$\gamma_{dB/\lambda} = -20 \lg(e)\alpha \approx -8.68\alpha.$$

The averaged value in the frequency range 950 MHz to 1050 MHz is -1.3034×10^{-3} dB/ λ , which is about five times of the value -2.76×10^{-4} dB/ λ for results obtained by Sanna Harma using a FEM/BEM simulation [30].

With the SAW propagation coefficients (see Figure 3.29), the single electrode's reflection transmission and bulk wave scattering coefficients can be extracted. The frequency dependent parameters are plotted from Figure B.2a to Figure B.2f. In order to compare our results with other researcher's work, we calculated an average value over the the frequency range from 950 MHz-1050 MHz for all the coefficients. This 100 MHz bandwidth is chosen for the averaging because it is the half-power bandwidth of the IDT, $BW_{-3\text{ dB}} = f_c \frac{1}{2Np}$. For each type of the test structure in Table 3.4, we made two samples, and both are measured. All the coefficients are averaged again using these two sample measurements. A comparison of the coefficients with Sanna Harma[30], Saku Lehtonen [34; 35; 36] and Weibiao Wang [37] is listed in Table 3.6 for three kinds of test structures. From this comparison, we can see that the magnitude for reflection and transmission coefficients are in good agreement with the FEM/BEM simulations, the difference is less than 1%; the phase of reflection coefficients has less than 10° difference; and for transmission coefficients it is even smaller.



(a) Extracted wave number k from TS2 measurement.



(b) Extracted propagation loss γ from TS2 measurement.

Figure 3.29: Extracted propagation coefficients k and γ from TS2 measurement.

The extracted frequency dependent parameter plottings from TS1 TS2 and TS3 for single electrodes listed in Table 3.4 are shown in Appendices C.1 C.2 and C.3.

3.5 Extra grooves at array ends

At the beginning of this work, the groove array in the RAC filter were designed with a parallelogram shape (the yellow area as shown in Figure 3.30). For such a kind of groove array, the measured passband shape always shows a high peak at the high frequency end

	TS1	S	L	TS2	S	L	TS3	W
$h/\lambda(\%)$	2.5	2.5	2.5	5.0	5.0	5.0	2.5	1.0
a/p	0.4	0.4	0.4	0.6	0.6	0.6	0.5	0.5
$ R $	0.0293	0.0348	0.034	0.0836	0.0978	0.092	0.0364	0.0282
$ T $	0.9954	0.9985	–	0.9835	0.9872	–	0.9921	0.9991
$\Phi_R(^{\circ})$	71.7	87.7	77.9	67.6	81.7	79.5	63.2	88.0
$\Phi_T(^{\circ})$	-2.02	-2.3	-2.0	-7.8	-6.8	-5.8	-2.99	-1.7
$E_{sc}(\%)$	0.84	0.17	–	2.56	2.57	–	1.44	0.21
$E_{sc}/ R ^2$	9.78	1.40	1.5	3.68	1.65	1.7	10.8	2.6

Table 3.6: Comparison of the extracted parameters for test structure TS1, TS2, TS3 with previous work from Sanna Harma(S), Saku Lethonen(L) and Weibiao Wang(W)

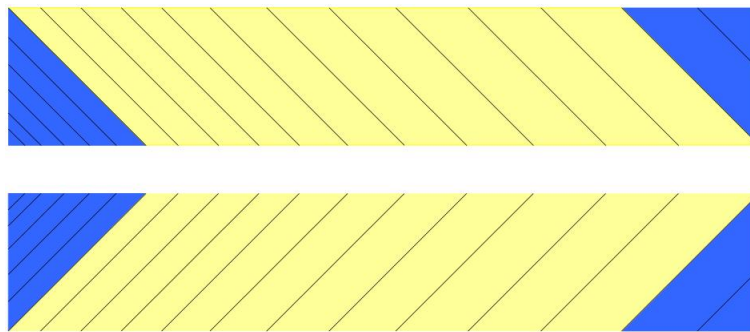


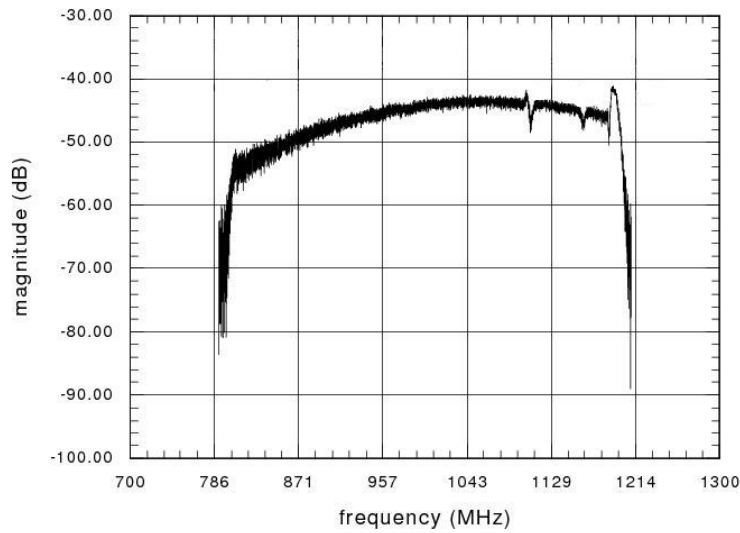
Figure 3.30: Comparison of the rectangular shape groove array and the parallelogram shape groove array.

as shown in Figure 3.31a.

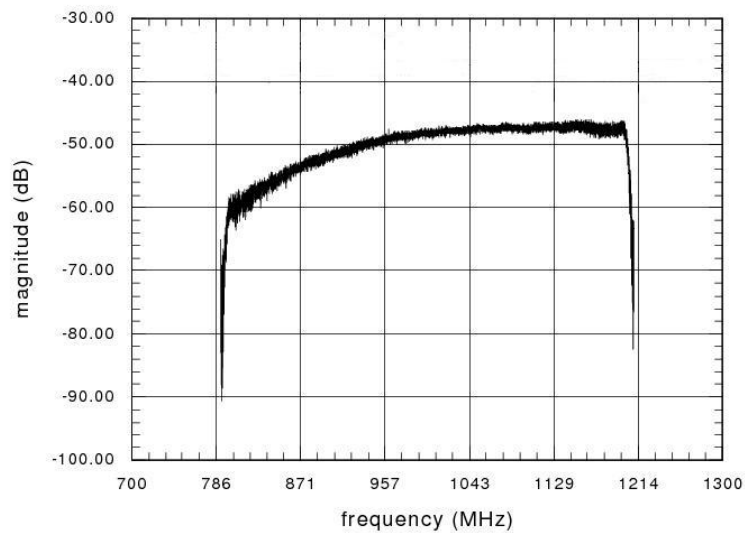
The reason for this phenomenon can be explained in two ways. Firstly, if we use the equivalent circuit model to explain it, and assume the free surface and the groove surface on the substrate have different acoustic impedance for the surface acoustic wave, then on the boundary between these two kinds of surfaces, there will be a large acoustic impedance mismatch, which leads to a strong reflection of the SAW, and this strong reflection will result in the high frequency peak. Secondly, if we use the impulse response model to explain this phenomenon for the parallelogram shaped groove array, the impulse response of the parallelogram shape groove array has an abrupt truncation at the beginning and end of the pulse series in the time domain, which will lead to an overshoot in the frequency domain, it is the so-called 'Gibbs Phenomenon'.

To get rid of such an unwanted peak at the high frequency end, extra grooves was added to fill up the triangular area on the left and right end of the parallelogram shaped groove array (the blue area as shown in Figure 3.30). The length of these grooves gradually increases on the left side along the array and decreases on the right side along the array.

For designing these extra grooves, we increase our required filter bandwidth B and dispersive delay T value both by 10%, then the chirp slope of the filter will not change. We use the expanded bandwidth and dispersive delay to calculate the groove array geometry as discussed in Chapter 2, we can get 10% more grooves. These 10% more grooves are used to fill the blue area as shown in Figure 3.30.



(a) RAC measured magnitude for parallelogram shape groove array layout (the yellow area as shown in Figure 3.30, there is a peak at the high frequency end in measurement).



(b) RAC measured magnitude for the rectangular shape groove array layout (the yellow area plus the blue area as shown in Figure 3.30, the peak at high frequency end is suppressed by the extra grooves (the blue area shown in Figure 3.30) at both ends of the array).

Figure 3.31: RAC measured magnitude comparison between the parallelogram shape groove array layout and rectangular shape groove array layout.

In the equivalent circuit model, these extra grooves can be modeled as the transient area between the free surface and groove surface. So on the boundary of the rectangular shaped groove array the acoustic impedance mismatch is much smaller compared to the parallelogram shape groove array; very high reflectivity for the SAW is then suppressed. In the impulse response model, those grooves in the triangular area get rid of the 'Gibbs Phenomenon'. Then in the frequency domain, the overshoot vanishes due to the smooth

varying impulse response in the time domain. In the measurement in Figure 3.31b for the RAC with a rectangular shaped groove array, we can see that the high peak at the high frequency end is very well suppressed.

3.6 RAC encapsulation and matching

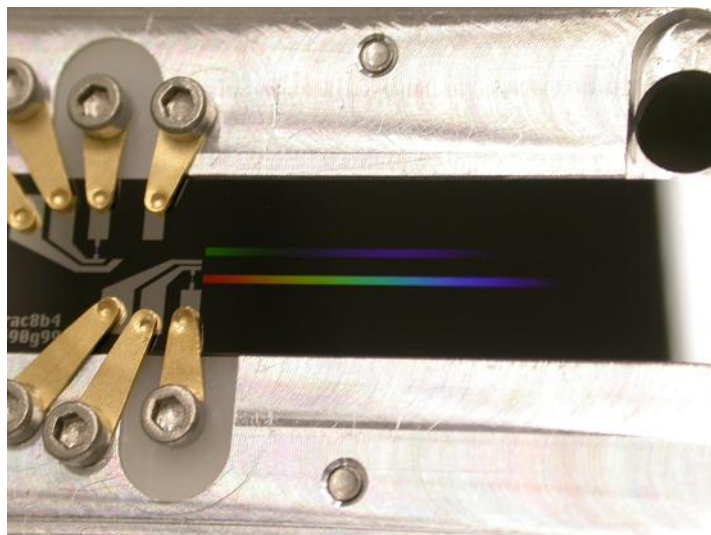


Figure 3.32: Photo of the RAC filter in the holder case (top view), the rainbow color is due to the scattering of visible light by the chirped gratings.

The filter chip needs to be encapsulated in a good holder case. The design of the holder is shown in Appendix F. Figure 3.32 is the photo of the encapsulation of the RAC filter. We use the copper tongue shaped contactors and screws to make the connections between the IDT on the chip and the SMA connectors in the holder. Because the gold film is very soft, and it is easier for the contactors with gold films to make a good contact with those Al pads on the filter chip, also they will not be scratched by the filmed contactors. 50 μm gold film was deposited on these copper contactors using the chemical deposition method. This makes the installation and dismounting of the chip easier, and the life time of the Al pads on the chip can be longer.

3.6.1 Equivalent circuit of RACs' input and output ports

As shown in Figure 3.33, we used copper wire to make the inductive matching network for our filter at both input and output ports. The diameter of our copper wires is 0.5 mm. The approximation formula for the inductance of the straight copper wire is as follows in Equation 3.27 [81]. Here, L is the wire inductance in nH unit, l is the wire length in mm, and d is the wire diameter which is also in mm.

$$L = 0.2 \cdot l \cdot \ln\left(\frac{4l}{d} - 1\right) \quad (3.27)$$

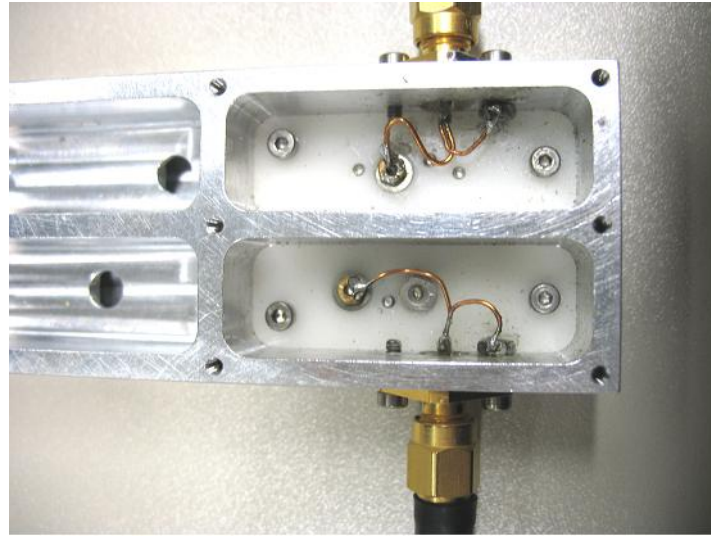


Figure 3.33: Photo of the copper wire matching network used for input and output ports for the RAC.

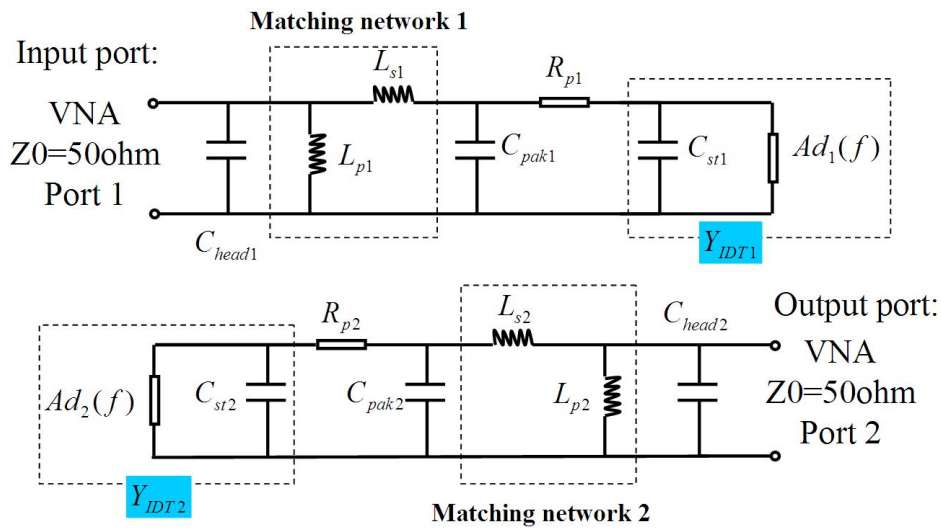


Figure 3.34: Equivalent circuits of the input and output ports of the RAC filter.

The equivalent circuit of the encapsulated RAC filter can be modeled as shown in Figure 3.34. In this circuit, C_{pak} is the package parasitic capacitance. It is measured from the empty holder case, which gives 1 pF. C_{head} is the SMA connectors' capacitance, the value is very small (to the level of 10^{-3} pF), so it can be ignored. The parasitic resistance R_p is composed of the IDT finger ohmic resistance which can be calculated using Equation 3.1, the Al contact pads resistance, the copper contactor resistance and the SMA connector resistance. L_s and L_p are the series and parallel copper wire inductances of the matching network. The length of these matching copper wires is calculated according to the required inductance using Equation 3.27. C_{st} is the IDT static capacitance:

$$C_{st} = W \cdot N_p \cdot C_0,$$

here W is the IDT aperture, N_p is the number of finger pairs in the IDT and $C_0 =$

0.5 pF/mm/pair for LiNbO₃ [79]. $Ad(f)$ is the frequency dependent acoustic admittance of IDT:

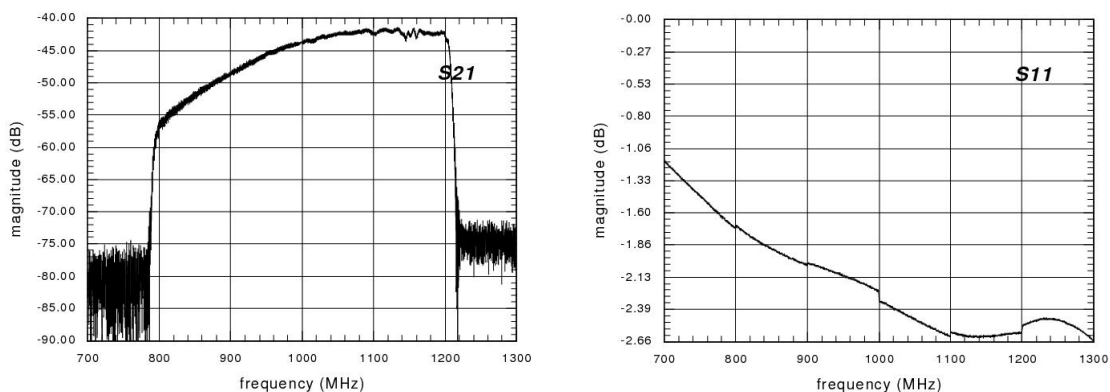
$$Ad(f) = G_a(f) + j \cdot B_a(f),$$

here $G_a(f)$ is the IDT acoustic conductance and $B_a(f)$ is the IDT acoustic susceptance [13]. Y_{IDT} is, therefore, the total admittance of IDT:

$$Y_{IDT} = Ad(f) + j\omega C_{st}.$$

3.6.2 Matching network numerical filtering

The RACs which were designed at the beginning of this work, were all without any weighting technologies. Their passband shape nonuniformity is as high as 14 dB for a filter of 10 μ s dispersive delay as shown in Figure 3.35 (the filter is measured with only a $L_{s-connect}$ series inductance for matching).



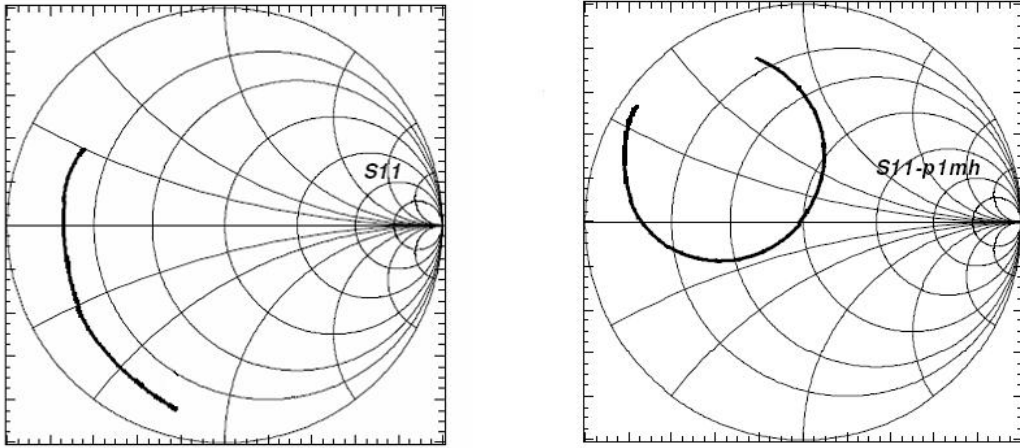
(a) Measured S_{21} magnitude before matching is optimized.

(b) Measured S_{11} magnitude before matching is optimized.

Figure 3.35: Measured magnitude of S_{21} and S_{11} parameters for unweighted $BT = 4000$ RAC before the matching network is optimized, the nonuniformity of the S_{21} magnitude in the passband is about 14 dB.

To compensate the very large 14 dB passband shape nonuniformity we have considered to use optimized matching network. The main idea is to compensate the acoustical roll off by a different matching between the low and high frequency ends in the passband.

From Figure 3.36a, we can see that if we only use an inductive series connection wire as matching network, almost all the frequency points in the passband are equally mismatched (every point in the impedance curve is almost the same distance from the 50 Ω center of the Smith chart). If we could perfectly match the filter at the 800 MHz low frequency end, and, at the same time, allow a large mismatch at the high frequency end, then this nonuniformity between the low and high frequency ends can be reduced. To calculate an appropriate matching network that can realize this matching, we have developed a numerical method for filtering the matching networks based on filter measurements as shown in Figure 3.37. First, we take a measurement using only the inductive series connection wire as the matching network; the measurement result is as shown in Figure 3.35



(a) The S_{11} parameter in Smith chart, here only a $L_{s-connect}$ series inductance is used for the matching. We can see that all the frequency points are more or less equally mismatched compared to Figure 3.36b.

(b) The S_{11} parameter in the Smith chart after the optimized matching. The 800 MHz point is perfectly matched to 50Ω .

Figure 3.36: S_{11} parameter in Smith chart before and after matching is optimized.

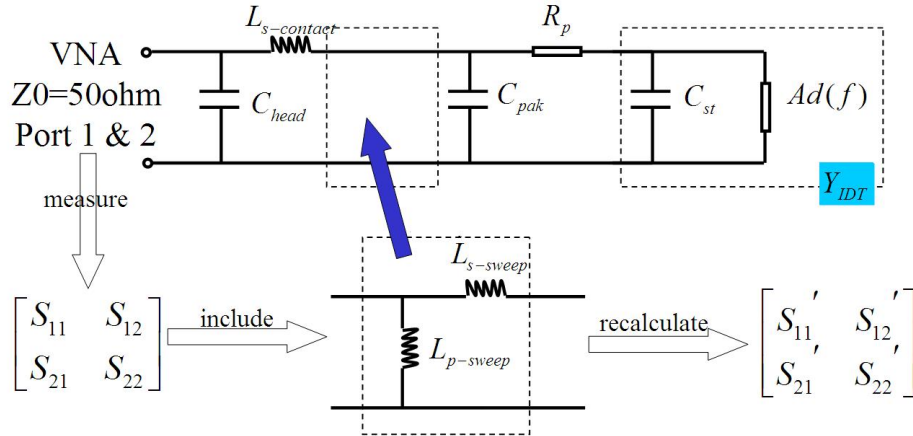


Figure 3.37: Matching network filtering using numerical method for the input and output ports of RAC.

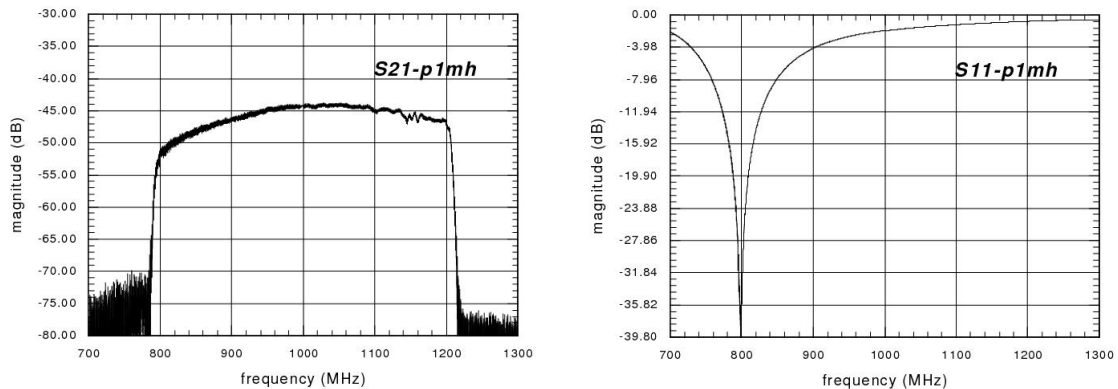
and Figure 3.36a. We obtain a set of S parameters ($S_{11}, S_{12}, S_{21}, S_{22}$). Then the virtual matching network (a series and a parallel inductance) is included into this set of S parameters numerically as shown in Figure 3.37. First, we transform this set of S parameters into Z parameters ($Z_{11}, Z_{12}, Z_{21}, Z_{22}$). After the series inductance is included, the Z_{11} parameter will become Equation 3.28.

$$Z'_{11} = Z_{11} + j\omega L_{s-sweep} \quad (3.28)$$

Next we transform the new set of Z parameters ($Z'_{11}, Z'_{12}, Z'_{21}, Z'_{22}$) into Y parameters ($Y'_{11}, Y'_{12}, Y'_{21}, Y'_{22}$). After that we include the parallel inductance into the Y parameters obtained as shown in Equation 3.29.

$$Y''_{11} = Y'_{11} + \frac{1}{j\omega L_{p-sweep}} \quad (3.29)$$

Here, $L_{s-sweep}$ is the virtual series trial inductance which will be swept from -10 nH to 10 nH with a 0.1 nH step; and $L_{p-sweep}$ is the virtual parallel trial inductance which will be swept from 0 nH to 20 nH also with a 0.1 nH step. Then the calculated Y parameters ($Y''_{11}, Y''_{12}, Y''_{21}, Y''_{22}$) are transformed back to S parameters ($S'_{11}, S'_{12}, S'_{21}, S'_{22}$) (the transformation between the S, Z and Y parameters can be found in Appendix E). The optimization condition was set to match the S'_{11} perfectly at 800 MHz.



(a) Measured S_{21} magnitude after optimized matching.

(b) Measured S_{11} magnitude after optimized matching.

Figure 3.38: Measured S_{21} and S_{11} parameters magnitude after the optimized matching, the S_{21} magnitude nonuniformity in the passband is reduced to only 7 dB.

After applying the optimized matching, the measured S_{21} and S_{11} magnitude become as shown in Figure 3.38. S_{11} is matched at 800 MHz. The nonuniformity in the magnitude of S_{21} is reduced to 7 dB, which is half of the value before the matching is optimized.

If we apply the same optimization routine at the output port (port 2), then the nonuniformity will almost disappear. However the filter passband shape can hardly be perfect rectangle by just optimizing the input and output ports matching, as we only have 4 degrees of freedom in designing the matching network. This implies that an additional amplitude weighting method is still necessary.

Later, the proper amplitude weighting method was found by changing the groove array structure, i.e. duty cycle weighting, which will be discussed in detail in the next chapter. The passband shape of the RAC after weighting can be good rectangle (nonuniformity in the passband less than 2 dB). Therefore, it is not necessary to match the filter perfectly at one frequency point any more, we can use only a $L_{s-connect}$ series inductance for matching network, and the filter passband shape correction can be done by amplitude weighting.

4 Weighting techniques in RAC design using e-beam lithography

4.1 Motivations

From the principle of the chirp transform spectrometer (CTS) introduced in Chapter 1, we know that the compressed pulse shape of the RAC filter is very important to the CTS performance. The compressed pulse main lobe width will determine the frequency resolution of the CTS; and its side lobe level will influence the dynamic range of the CTS. In order to have a rectangular passband shape for RAC filter which will lead to a minimum compressed pulse main lobe width, and to reduce the SAW multiple reflections inside the groove array which will lead to a smaller compressed pulse side lobe level, certain amplitude weighting technique is needed. Using the amplitude weighting method, we could make the compressed pulse of the RAC filter (the solid line as shown in Figure 4.2) converge with the standard sinc function shape (dashed line as shown in Figure 4.2).

4.1.1 Correction of the passband shape nonuniformity

For large bandwidth chirp filters of a constant groove depth and a 50% duty cycle for groove array, the single groove reflectivity (Equation 3.11), and the effective number (Equation 2.20) of reflecting grooves increase with the input frequency. In addition, the SAW propagation loss (Equation 2.26) and transmission loss (Equation 2.27) decrease with input frequency. A large nonuniformity of magnitude between the low and high frequency in the passband is generated. From the measurement results of the uniform groove array RAC filter, a total insertion loss nonuniformity in the 400 MHz bandwidth as large as 14 dB was found, as shown in Figure 4.1. This nonuniformity will distort the compressed pulse of RAC filter, because the filter's -3 dB bandwidth (B_{-3dB}) will become smaller due to this large nonuniformity, the compressed pulse width at -3 dB

$$\tau_{-3dB} \approx 0.885 \cdot \frac{1}{B_{-3dB}}$$

will then become wider. The calculated compressed pulse by feeding the synthesized up chirp signal into the measured down chirp filter is shown in Figure 4.2, where the main lobe -3 dB width is $\tau_{-3dB} \approx 2.632$ ns, which is wider than the theoretical sinc function -3 dB main lobe width

$$\tau_{ideal} \approx 0.885 \cdot \frac{1}{400 \text{ MHz}} = 2.213 \text{ ns}$$

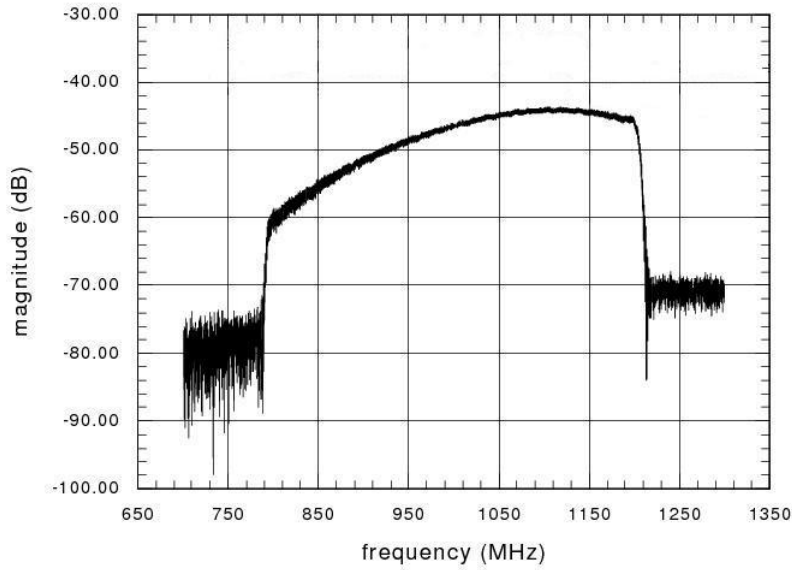


Figure 4.1: Measured insertion loss of RAC with 25 nm constant groove depth and 50% uniform duty cycle groove array. The nonuniformity is about 14 dB in the 400 MHz bandwidth.

for an ideal 400 MHz rectangular passband shape RAC filter.

For chirp transform spectrometers, as discussed in Chapter 1, the compressed pulse width for the compressor filter will determine the frequency resolution of the spectrometer (Equation 4.1).

$$\Delta f = \mu \cdot \tau_{-3dB} \quad (4.1)$$

The distortion caused by the nonuniformity will degrade the CTS's frequency resolution. This effect must, therefore, be corrected.

4.1.2 Reduction of the multiple reflections at high frequencies

To minimize insertion loss for the RAC filters, we need to increase the ion-beam etched groove depth (e.g. from 25 nm to 40 nm). When doing so, the reflectivity of the grooves will be too high at the high frequencies. The groove array reflection loss simulated using the 1st order model can be $R(f) > 0\text{dB}$ (for $f > 950\text{ MHz}$) as shown in Figure 4.3. This is physically not possible, which demonstrates that the groove array can not be described by the 1st order model any more. The 1st order model only take into account of the single reflections of the SAW by the grooves. Thus, there will be strong multiple reflections inside the groove array when $f > 950\text{ MHz}$, introducing large phase deviations from the ideal quadratic dependency (see Figure 4.4, $\Delta\varphi_{rms} \approx 28^\circ$). Also amplitude ripples will occur due to the multiple reflections as shown in Figure 4.5. In Figure 4.5 the magnitude nonuniformity was corrected using the optimized matching network (as described in Chapter 3).

For a RAC with shallow grooves (e.g. 25 nm), Figure 4.6 shows that the 1st order reflection loss simulation has $R(f) < 0\text{ dB}$ in the whole passband. The measured phase deviation is very small as shown in Figure 4.7 ($\Delta\varphi_{rms} = 9.61^\circ$) compared to Figure 4.4

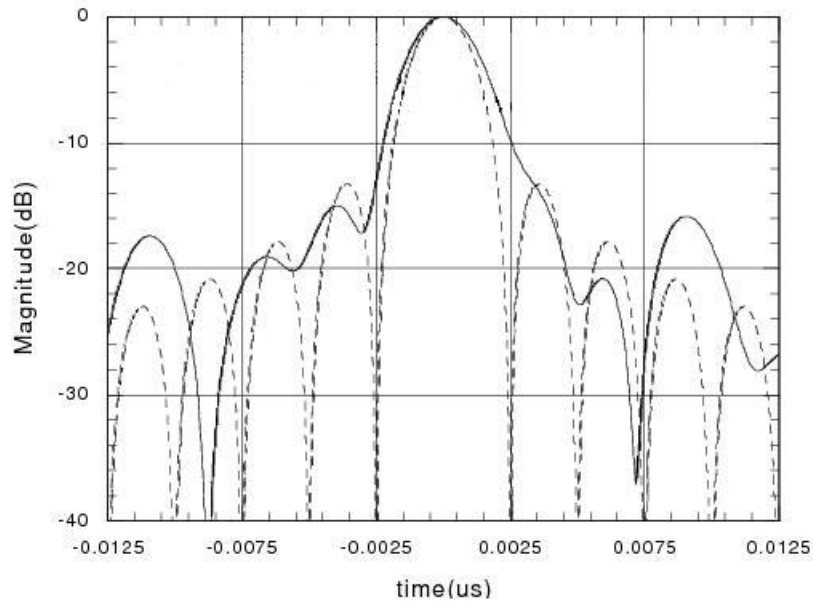


Figure 4.2: Compressed pulse for the unweighted RAC filter shown in Figure 4.1 (solid line), and compared with a ideal $\frac{\sin(\pi Bt)}{(\pi Bt)}$ curve (dashed line). The compressed pulse main lobe -3 dB width is 2.632 ns, and the ideal $\frac{\sin(\pi Bt)}{(\pi Bt)}$ curve main lobe -3 dB width is 2.213 ns.

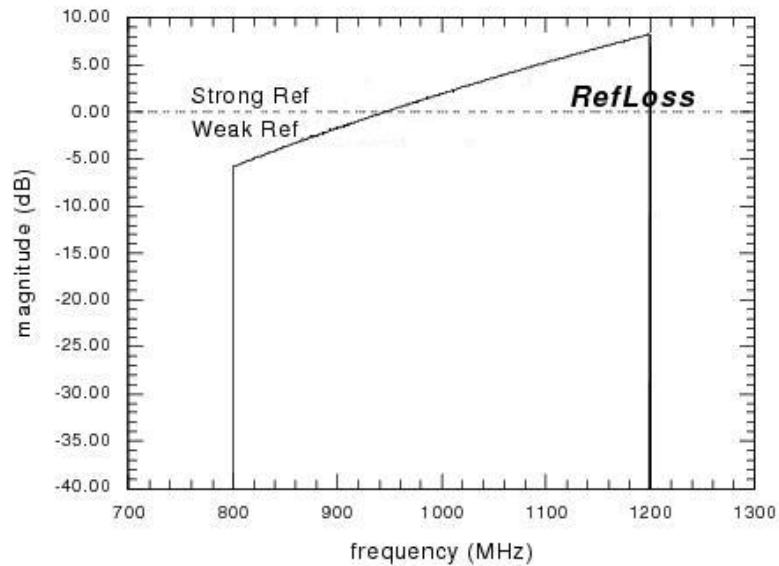


Figure 4.3: Reflection loss simulation of groove array with 40 nm uniform groove depth using stationary phase approximation (Equation 2.21).

($\Delta\varphi_{rms} = 28.18^\circ$). Also the amplitude ripple seen in Figure 4.1 disappear in Figure 4.5 when $f > 950$ MHz.

From the above considerations one can conclude that an amplitude weighting technique is needed. Firstly, it can correct the magnitude nonuniformity in the whole passband so as to reduce the compressed pulse main lobe width, which improves the CTS frequency

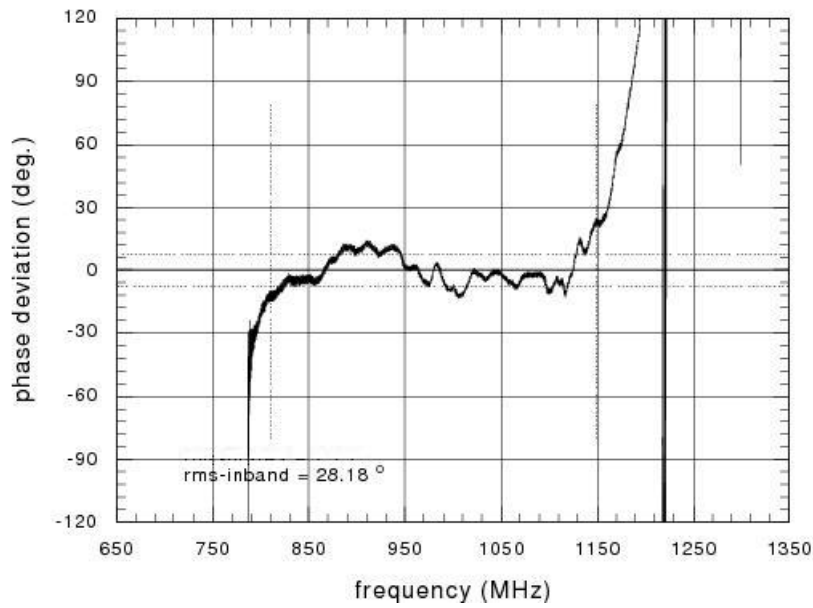


Figure 4.4: Large phase deviation caused by multiple reflections (here the groove depth is 40 nm). The root mean square value of the deviation in the 400 MHz bandwidth is $\Delta\varphi_{rms} = 28.18^\circ$.

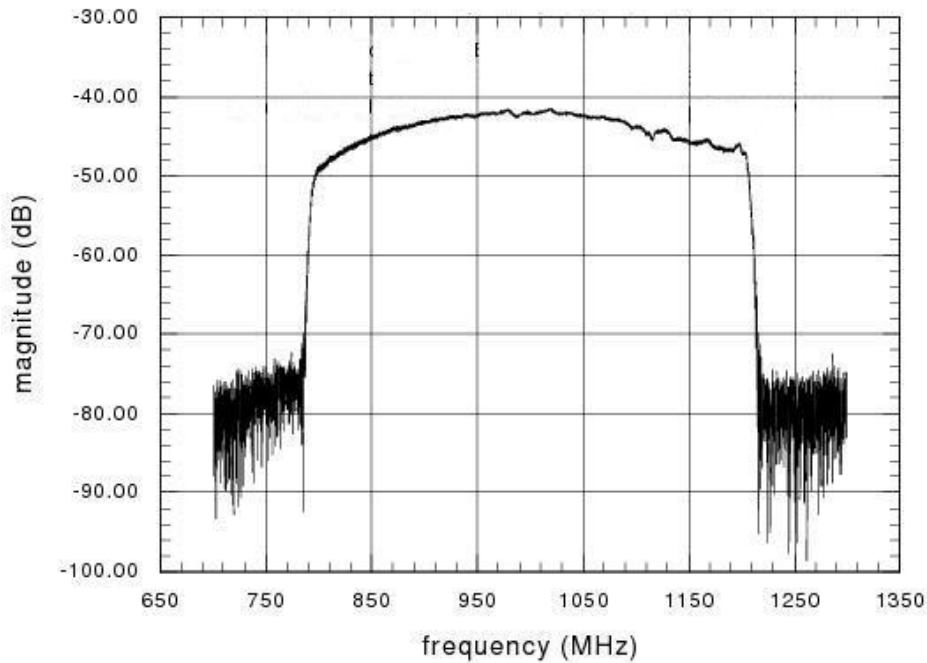


Figure 4.5: Measured insertion loss of RAC with unweighted groove array design. The groove depth is 40 nm. The magnitude nonuniformity is corrected using optimized matching network as described in Chapter 3. We can see the magnitude ripples caused by the multiple reflections when $f > 950$ MHz.

resolution; secondly, it can reduce the high frequency grooves' reflectivity, which guar-

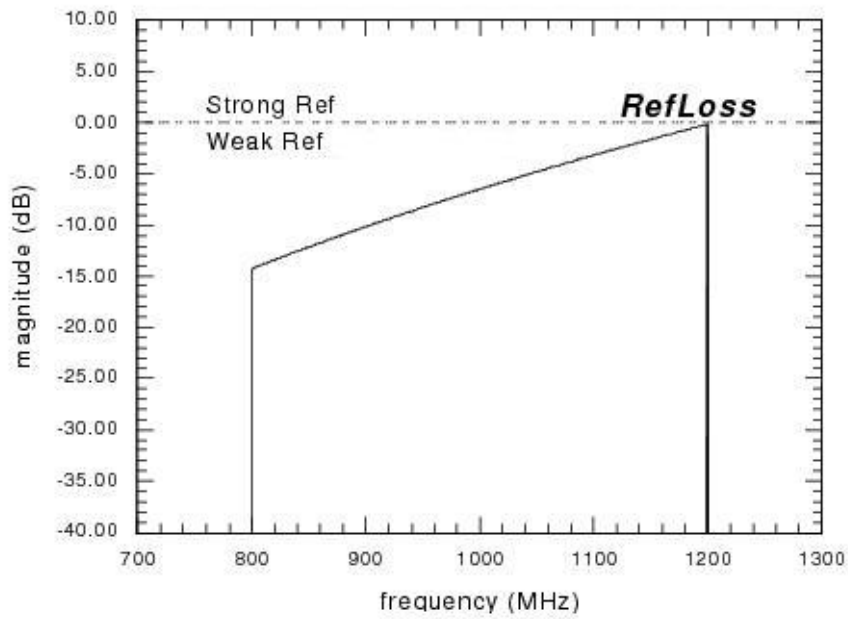


Figure 4.6: Simulated groove array reflection loss for 25 nm uniform groove depth.

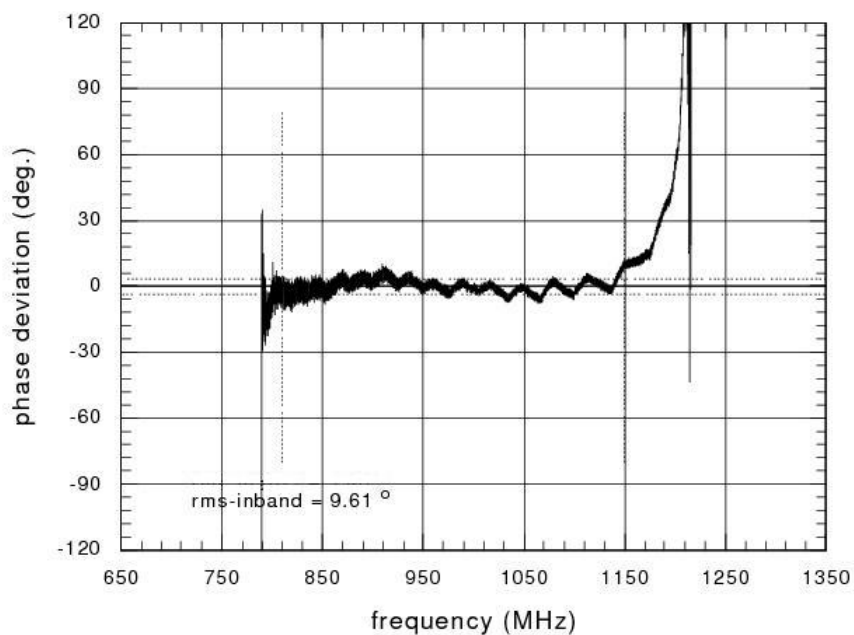


Figure 4.7: Phase deviation for RAC with small multiple reflections (the uniform groove depth is 25 nm).

antes the multiple reflections are reasonably low in the groove array and hance avoids amplitude ripples and the large deviation of phase from ideal quadratic dependency.

4.2 Compressed pulse calculation for the fabricated RAC filters

In Figure 4.2, the compressed pulse was calculated by feeding the measured filter with a synthesized matched up chirp signal followed by an inverse Fourier transform to the time domain. The matched up chirp signal is calculated as follows.

Since for the designed down chirp filter the linear time and delay relationship is as shown in Figure 2.2 and given by Equation 2.5, the matched up chirp signal can be as follows:

$$f_{up} = f_0 + \mu \cdot (t - t_0) \quad (4.2)$$

Here f_0 in Equation 4.2 is the band edge low frequency of the down chirp filter, and t_0 is its corresponding delay time. The up chirp signal phase can be derived from Equation 4.2 by integration of angular frequency over delay time:

$$\varphi_{up}(f) = 2\pi \left[\frac{f_0(f - f_0)}{\mu} - \frac{(f - f_0)^2}{2\mu} \right] \quad (4.3)$$

Then the formula for the matched up-chirp signal in the frequency domain can be derived:

$$Ch_+(f) = 1 \cdot (\cos \varphi_{up}(f) + j \cdot \sin \varphi_{up}(f)) \quad (4.4)$$

The compressed pulse in the time domain can be calculated using the inverse Fourier transform:

$$pulse(t) = \mathcal{F}^{-1} [Ch_+(f) \cdot S_{21}(f)_{measure}] \quad (4.5)$$

Here we should note that in order to match the synthesized up chirp signal to the response of the fabricated filter, the chirp slope should be taken from the fit of the RAC filter measurement (the fitting method will be discussed in detail in Chapter 5), since otherwise the compressed pulse will be distorted. From the calculated compressed pulse, one obtains the -3 dB main lobe width $\tau_{-3\text{ dB}}$, which determines the frequency resolution of the chirp transform spectrometer, Equation 4.1. One also obtains the side lobe suppression level from the magnitude difference of the main lobe and the first side lobe. For an ideal sinc function, the suppression is 13.6 dB as shown in Figure 4.2, dashed line, and the two first side lobes on the left and right should be symmetrical. Due to the RAC filter's phase deviation, the side lobes are not symmetrical, and the suppression level is less than 13.6 dB, as shown in Figure 4.2.

4.3 Amplitude weighting techniques

In order to apply the amplitude weighting technique for the design of RAC filters, the loss mechanism of RAC needs to be understood. As discussed in Chapter 2, the total insertion loss of the RAC can be evaluated considering several separate contributions as shown in Equation 2.24 (in dB).

$$IL(f) = R(f) + IDT(f) + Prop(f) + Tran(f)$$

Here the SAW propagation loss $Prop(f)$ is only related to substrate material and the SAW propagation length, and can not be influenced by weighting. For the IDT, as the finger

number is very small ($N_f = 5$), it is difficult to introduce amplitude weightings (e.g. apodization). Thus, only the reflection loss $R(f)$ and the transmission loss $Tran(f)$ can be manipulated by changing the groove structure. But $Tran(f)$ is very small, there are not much space for manipulation, so normally we change the reflection loss of the groove array according to Equation 2.21 and Equation 3.11 for realizing the amplitude weighting.

Using the stationary phase approximation described in Chapter 2, one can simulate the passband shape of a RAC which uses all uniform design parameters. Then it is possible to calculate the magnitude correction factor $Mag_{corr}(f)$ (in dB) from the difference between the unweighted filter magnitude $Mag_{uw}(f)$ and a desired magnitude $Mag_{desired}(f)$. In Figure 4.8, the calculation of this frequency dependent magnitude correction factor according to Equation 4.6 is shown. For the desired passband shape, it can be rectangular as the blue line shown in Figure 4.8. Hamming or other weighting windows are quite commonly used in the matched up chirp filter design for side lobe suppressions.

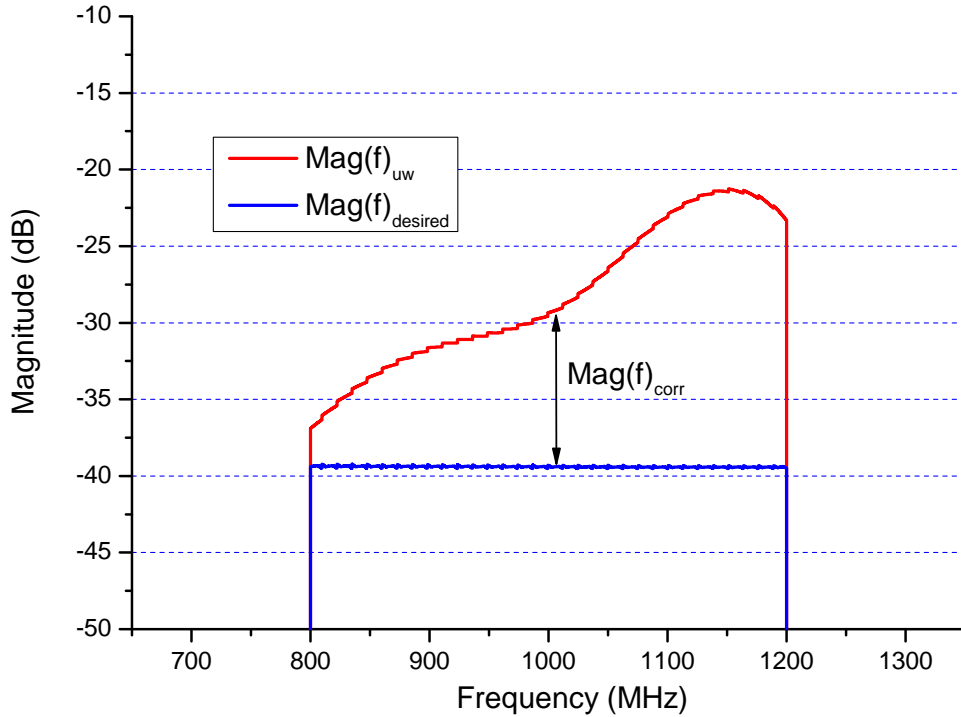


Figure 4.8: Illustration of the magnitude correction factor calculation for a $B = 400$ MHz, $T = 10 \mu s$ and $f_c = 1$ GHz RAC according to Equation 4.6.

$$Mag_{corr}(f) = Mag_{uw}(f) - Mag_{desired}(f) \quad (4.6)$$

This function $Mag_{corr}(f)$ can then be used to modify the unweighted reflective array structure to vary the reflection loss and transmission loss of the reflective array using different weighting methods.

4.3.1 Conventional groove depth profile weighting

The conventional method for amplitude weighting of RAC is to use a groove array with a depth profile. As discussed in the last chapter, the single groove reflectivity for the SAW in Equation 3.11 is proportional to $\frac{h}{\lambda}$. By changing the groove depth h along the groove array, the total reflectivity $R(f)$, therefore, can be modified at different frequencies. The depth profile $h(f)$ along the groove array for this weighting method can then be calculated according to Equation 2.21 using the required magnitude correction factor obtained from Equation 4.6.

$$\frac{h(f)}{h_0} = 10^{\frac{-Mag_{corr}(f)}{40}} \quad (4.7)$$

Here, h_0 is the constant groove depth used in the unweighted RAC. This method is calculationally straight forward, but in order to realize it, a special ion beam etching machine which can scan the ion beam along the substrate at a controllable velocity is needed [8]. Such an etching machine is shown in Figure 4.9. When the etching is performed, the exposed and developed substrate is put on a moving table, which is driven by a step motor. The speed of the table is controlled by a program. On top of the substrate, a chevron aperture mask is used to define the etching Ar ion beam, the width of the mask is $AperWidth$. Then, under the Ar ion beam, several grooves can be etched at the same time. As the etching dose of the Ar ion beam is uniform during the whole etching process, the groove depth is only determined by the dwell time of the structure under the ion beam as shown in Equation 4.8, where $h(x_n)$ is the position dependent groove depth profile along the groove array, $rate_{etch}$ is the constant etching rate of Ar ion beam for $LiNbO_3$, and $t_{dwell}(x_n)$ is the dwell time of position x_n under the Ar ion beam.

$$h(x_n) = t_{dwell}(x_n) \cdot rate_{etch} \quad (4.8)$$

The dwell time of each groove $t_{dwell}(x_n)$ under the etching ion beam can be determined by the velocity of the table $v_{table}(x_n)$:

$$t_{dwell}(x_n) = \frac{AperWidth}{v_{table}(x_n)} \quad (4.9)$$

Such a kind of etching machine is not commercially available. In the 1980s, when RACs were intensively studied, such machines were specially built for fabricating groove arrays with depth profile. The disadvantage is that the etching is very time consuming, as the $AperWidth$ in Equation 4.9 needs to be small, otherwise the depth resolution of the profile would be low and then the filter amplitude can not be precisely controlled. Hence, the filter can only be fabricated on a chip-by-chip basis using this technique. Other amplitude weighting techniques which are suitable for large volume production and also compatible with commercially available etching machines are needed.

4.3.2 Aperture weighting

According to Equation 2.21, the groove array reflectivity $R(f)$ is proportional to its geometrical factor $Geom(\frac{W}{L_a \cdot \tan \alpha})$; and from Figure 2.9, we see that the $Geom(\frac{W}{L_a \cdot \tan \alpha})$ is almost linearly dependent on the groove array aperture W when $0 < W < 1.75 \cdot L_a$. So groove array's reflectivity is, therefore, almost proportional to its aperture W when

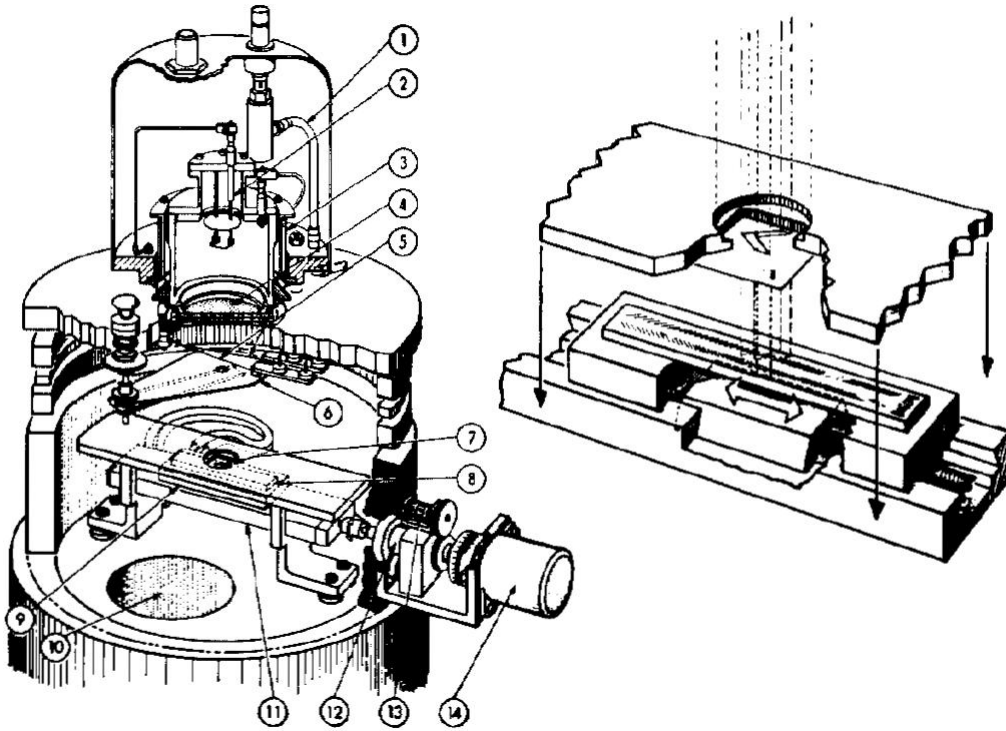


Figure 4.9: Special etching machine for fabricating depth profile [8]. (1) argon gas inlet, (2) arc filament, (3) magnet, (4) ion-beam extraction grids, (5) neutralising filament, (6) shutter, (7) chevron aperture, (8) RAC substrate, (9) water-cooled sample platform, (10) pumping port, (11) micrometer-slide assembly, (12) rotary-motion high vacuum feedthrough, (13) position indicator, (14) stepping motor.

$0 < W < 1.75 \cdot L_a$. Hence we can use this linear regime of $Geom(\frac{W}{L_a \cdot \tan \alpha})$ to do the reflectivity manipulation of the groove array by altering its aperture W [28]. The weighted aperture profile along the groove array, therefore, can be calculated according to the required filter magnitude correction factor $Mag_{corr}(f)$ using Equation 4.10.

$$\frac{W(f)}{W_0} = 10^{\frac{-Mag_{corr}(f)}{20}} \quad (4.10)$$

Here $W_0 = 1.75 \cdot L_a$ is the turning point of $Geom(\frac{W}{L_a \cdot \tan \alpha})$. When $W > W_0$, the geometrical factor will go saturate, and Equation 4.10 for weighting will not stand any more. So W_0 is chosen to be the maximum aperture of the groove array for using this weighting method.

Based on the aboving theory, several aperture weighting layouts were studied. Figure 4.10 shows the first aperture weighting layout without extra dummy grooves. The measured magnitude of a RAC device using this groove array layout is shown in Figure 4.12. It demonstrates that this layout failed to work properly. The reason could be illustrated as follows. We can consider a SAW beam reflected by an arbitrary groove in the aperture weighted groove array as shown in Figure 4.11. After the reflection, part of the beam propagates through the free surface (S1,S3), and part of it propagates through the weighted grooves (S2). We know that grooves can slow down SAW a little due to the energy storage effect (see Equation 3.8). So beam S1, S2 and S3 will have different phase

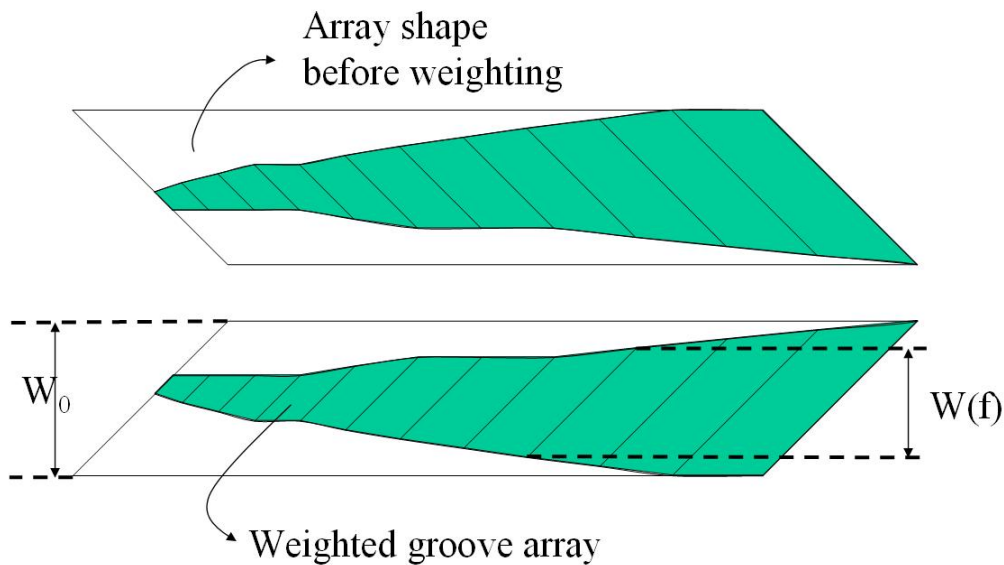


Figure 4.10: Aperture weighting of groove array without extra dummy grooves (the aperture weighted grooves are in the green area). W_0 is the maximum aperture of the groove array, and $W(f)$ is the aperture profile.

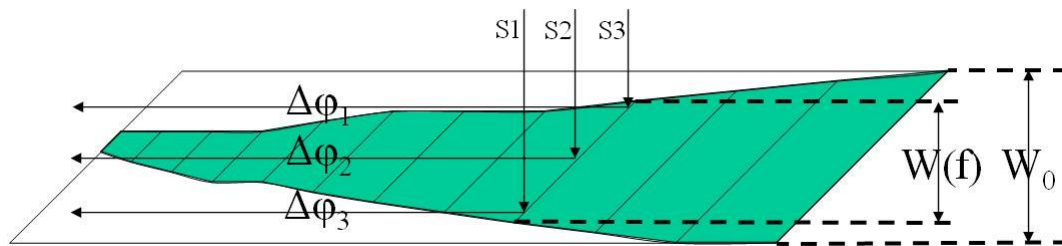


Figure 4.11: SAW beam reflection by an arbitrary groove in the weighted groove array (the weighted grooves are in the green area).

shift after they arrive at the IDT on the left side. As shown in Figure 4.11, we see the phase shift that S1, S2 and S3 got have the following relationship:

$$\Delta\phi_1 < \Delta\phi_3 < \Delta\phi_2$$

After the IDT does an average of these not in phase SAW beams, the magnitude becomes low.

As a solution for this problem we tried to add extra dummy grooves to fill up the free surface on both sides of the weighted grooves to keep the aperture uniform. Then all the SAW beams should have a more or less uniform propagation velocity. The dummy grooves are perpendicular to the weighted grooves, so they have the opposite reflection vector, and reflect the SAW in the opposite direction. This part of the reflected SAW should not reach the output IDT. The layout of such a kind of structure is shown in Figure 4.13. From the measurement for the RAC filter with the above groove array structure shown in Figure 4.14, we can see that it still failed to work properly. One reason could be that in order to increase the filter magnitude at the low frequency end for having a flat

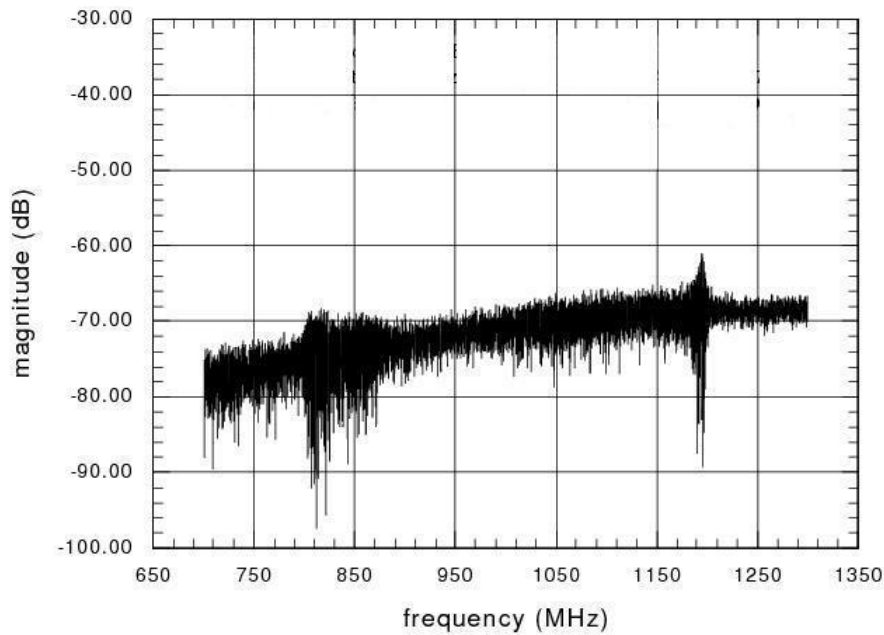


Figure 4.12: Measured filter magnitude using aperture weighting without extra dummy grooves.

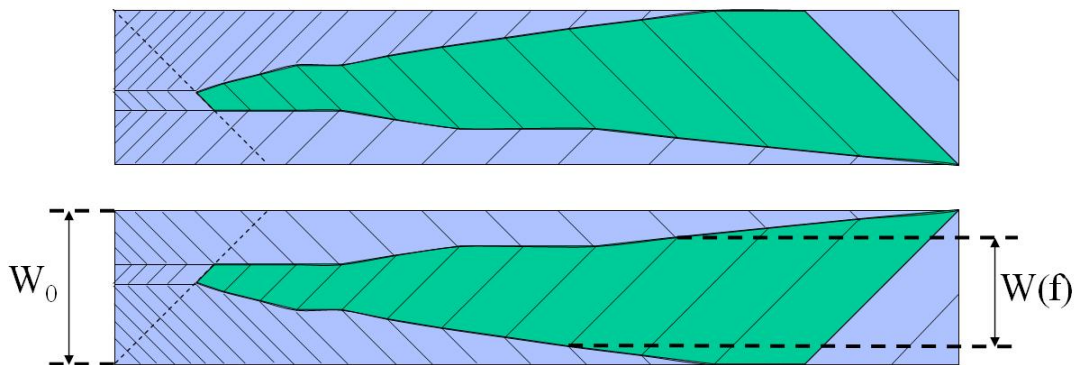


Figure 4.13: Aperture weighting with extra dummy grooves on both sides. The weighted grooves are in the green area; and the extra dummy grooves are in the blue area. The extra dummy grooves are connected to the weighted grooves. W_0 is the maximum aperture of the groove array, and $W(f)$ is the aperture profile.

magnitude after weighting, the grooves are etched deeply, i.e. $h = 40$ nm. Then for the high frequency grooves the reflectivity is too high, so there will be multiple reflections in both weighted grooves and dummy grooves. This could distort the required wave reflection by the weighted grooves. Also the dummy grooves are on both ends of the weighted grooves, and there are lots of dummy grooves in the SAW path between the symmetrical two arrays. These grooves will distort the waves propagating through them, especially for those at the high frequencies, as their reflectivity is too high. Another reason could be that those dummy grooves are designed to have the same width with the weighted grooves and they are connected to the weighted ones as shown in Figure 4.13. Due to the aperture variation of the weighted grooves, the position of those dummy groove

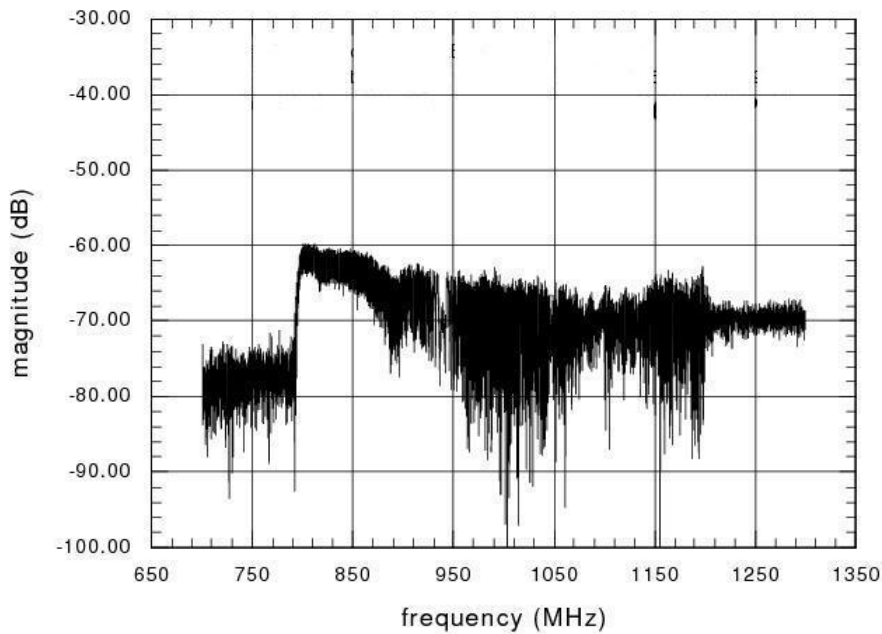


Figure 4.14: Measured filter magnitude using aperture weighting with extra dummy grooves on both sides.

are, therefore, unpredictable. These dummy grooves will have unpredictable influence to the SAW propagates through them. Better strategy of positioning these dummy grooves are needed.

From the aboving considerations we studied the third kind of aperture weighting structure as shown in Figure 4.15. All the dummy grooves are put at one side of the weighted grooves, so the SAW that propagates from the upper array to the lower array will not have interaction with the dummy grooves in between. For a structure of this kind with uniform

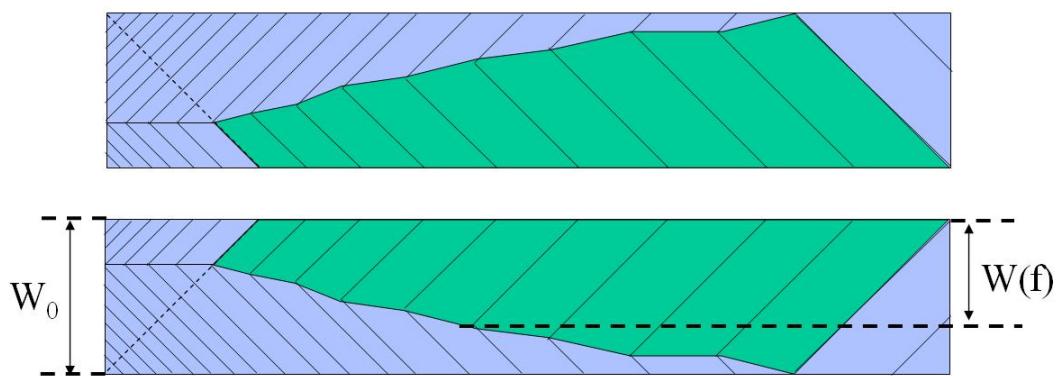


Figure 4.15: Aperture weighting with extra dummy grooves on one side of the array only (here the weighted grooves are in the green area; the extra dummy grooves are in the blue area). The dummy grooves are designed to be connected to the weighted groove. W_0 is the maximum aperture of the groove array, and $W(f)$ is the aperture profile.

groove depth (40 nm), the measured performance is shown in Figure 4.16. It works better than the structure with dummies on both sides, as the low frequency end has a much

higher magnitude. However, at the high frequency end the magnitude is still seriously distorted. The reason is still unclear.

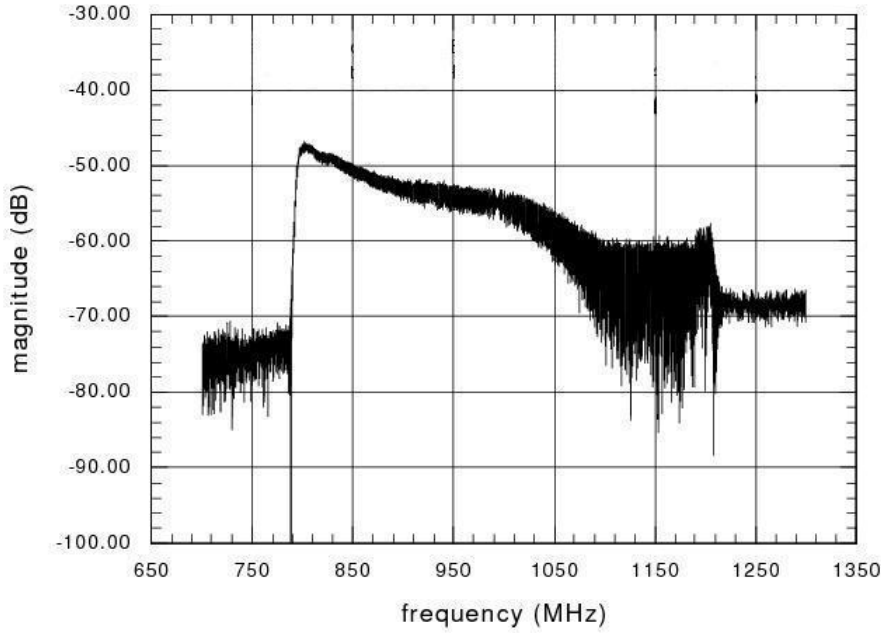


Figure 4.16: Measured filter magnitude using aperture weighting with extra dummy grooves on only one side.

From these examples, we see that the aperture weighting method is not very easy to handle. The main disadvantage is that this method can not modify the single groove reflectivity; it can only change a group of grooves' total reflectivity by modifying the beam width of the SAW reflected. Firstly for the deep grooves with high single groove reflectivity, this method can not eliminate the multiple reflections in the groove array at high frequencies. Secondly it is really complicated to design those dummy grooves in a proper way so that they will not influence the required filter response. It seems this kind of weighting method is only proper for RACs with quite shallow grooves [28], which implies that the insertion loss level will be high.

4.3.3 Groove duty cycle weighting

Besides changing the depth h of the single groove, there are other ways for modifying the single groove reflectivity according to Equation 3.11. As shown in Figure 4.17, by modifying the groove width w it is also possible to modulate the single groove reflectivity using the $\sin(\pi \cdot \frac{w}{\lambda})$ term in Equation 3.11, here we call $\frac{w}{\lambda}$ the duty cycle of groove. Therefore the groove array total reflectivity $R(f)$, can be modified at different frequencies by applying a duty cycle profile along the array. Similar to the two weighting methods discussed before, the duty cycle profile for the weighted reflective array can be calculated according to Equation 2.21 and desired $Mag_{corr}(f)$ as follows.

$$\left(\frac{w}{\lambda}\right)_{local} = \frac{1}{\pi} \cdot \arcsin\left(10^{\frac{-Mag_{corr}(f)}{40}}\right) \quad (4.11)$$

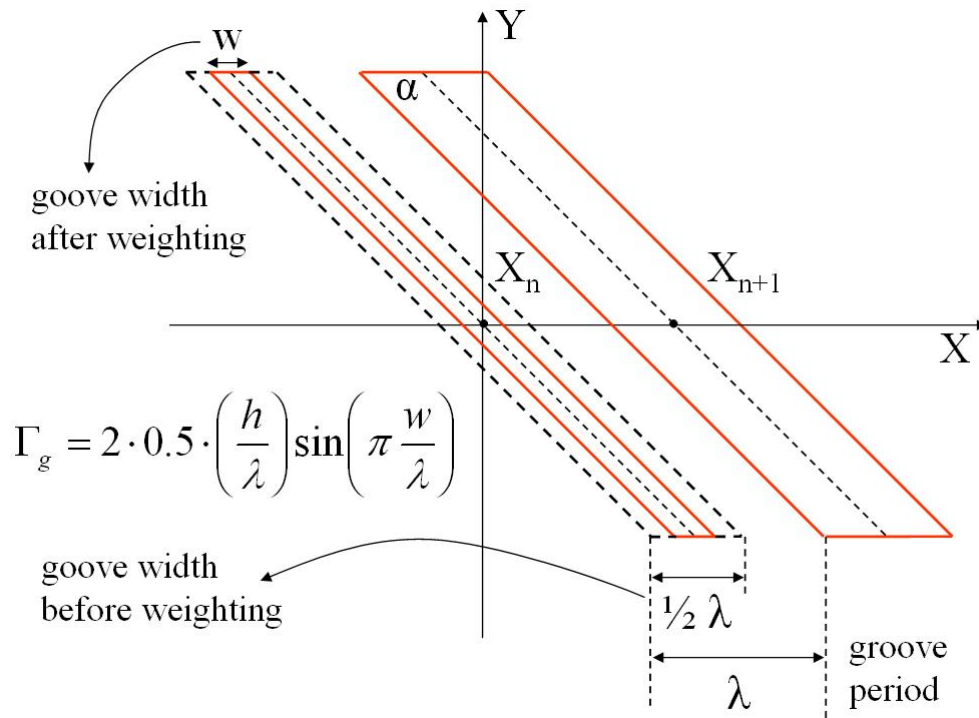


Figure 4.17: Principle of the groove array duty cycle weighting.

Figure 4.18 is a example of the duty cycle profile for a $B = 400$ MHz, $T = 10 \mu\text{s}$ and $f_c = 1$ GHz RAC for realizing a rectangular passband shape. For the exposure of this kind

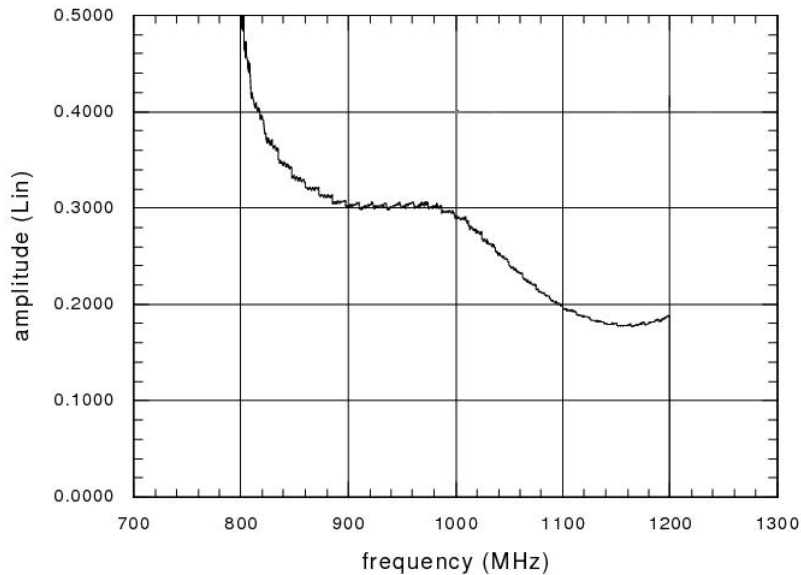
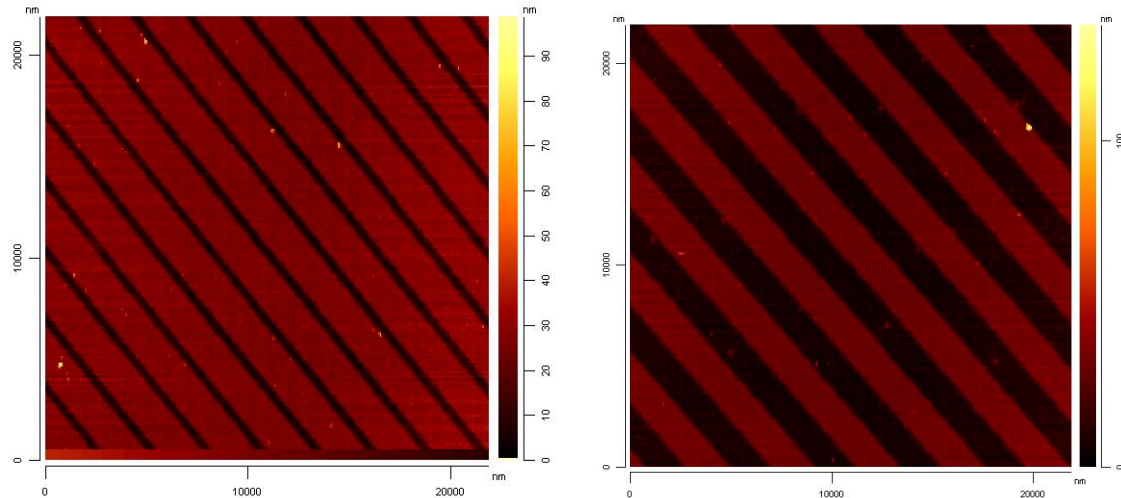


Figure 4.18: Duty cycle profile for $BT = 4000$, $f_c = 1$ GHz amplitude weighted RAC, the uniform groove depth h is 40 nm. The duty cycle weighting is to realize a desired rectangular shape passband of the down chirp filter.

of duty cycle weighted groove array, two methods were studied, and they are discussed in

detail in Chapter 6.

AFM images for the duty cycle weighted grooves are shown in Figure 4.19. The



(a) AFM image for 18% duty cycle high frequency grooves.

(b) AFM image for 50% duty cycle low frequency grooves.

Figure 4.19: The Atom Force Microscope (AFM) images for the 18% duty cycle high frequency grooves and 50% duty cycle low frequency grooves, they are all with 40 nm constant depth.

measurement result for the RAC fabricated using this weighting technology is shown in the following. Figure 4.20 is the measured magnitude, and Figure 4.22 is the measured phase deviation.

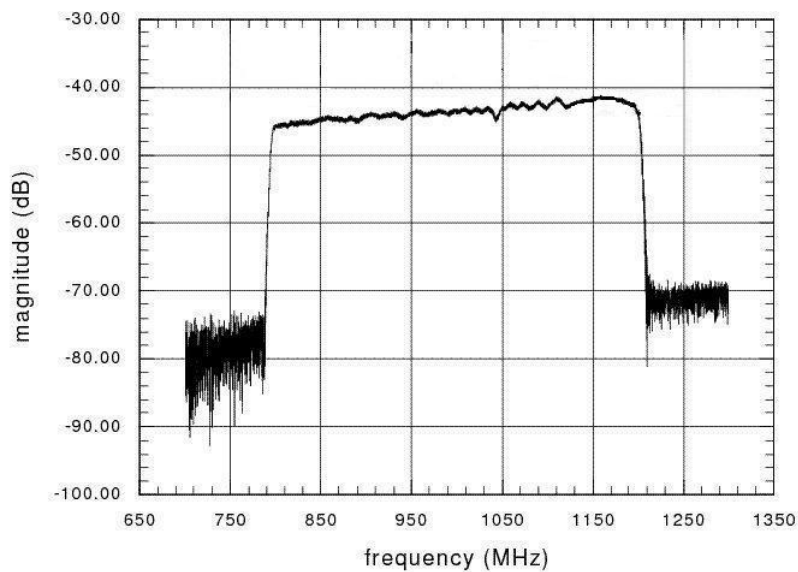


Figure 4.20: Measured filter magnitude using the duty cycle weighting for $BT = 4000$ and $f_c = 1$ GHz RAC filter, with uniform groove depth $h = 40$ nm.

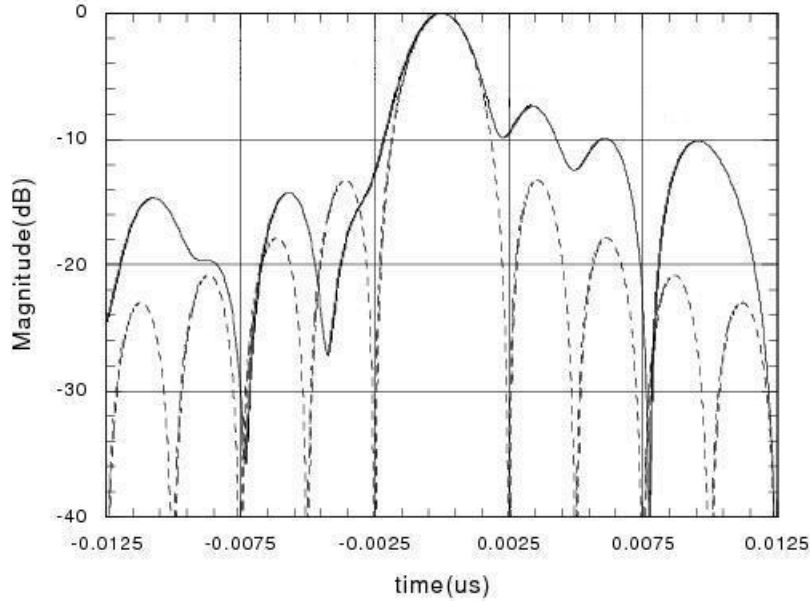


Figure 4.21: Compressed pulse from the $BT = 4000$, $f_c = 1$ GHz duty cycle weighted RAC filter. The compressed pulse main lobe -3 dB width is 2.319 ns, and the ideal $\frac{\sin(\pi Bt)}{(\pi Bt)}$ curve main lobe -3 dB width is 2.213 ns.

From the measurement, we can see that the weighting works well; the nonuniformity shown in Figure 4.1, about 14 dB, is reduced to only 4 dB in the whole bandwidth. This rectangular passband shape after weighting reduced the compressed pulse's main lobe -3 dB width. From the compressed pulse shown in Figure 4.21, we can see that the main lobe -3 dB width is reduced to $\tau_{-3 \text{ dB}} = 2.319$ ns, compared to the unweighted filter compressed pulse in Figure 4.2, where the main lobe -3 dB width is $\tau_{-3 \text{ dB}} = 2.632$ ns. As the theoretical ideal pulse width for the 400 MHz RAC filter is $\tau_{ideal} \approx 2.213$ ns, we can see that the compressed pulse width for the RAC after weighting is converging with the theoretical value. If we compare the CTSs using unweighted and weighted RAC filters, the frequency resolution is improved by 12% due to the reduction of the compressed pulse main lobe width by using the weighted RAC filter.

For this duty cycle weighted RAC, the etched groove depth is increased from 25 nm to 40 nm to improve the insertion loss level at the low frequencies in the bandwidth. The measured phase deviation for the RAC is shown in Figure 4.22, and the root mean square value $\Delta\varphi_{rms}$ in the passband is about 18° . It is approximately 1/3 less compared to the value from the measurement of RAC without weighting and of the same groove depth (i.e. 40 nm), the root mean square value $\Delta\varphi_{rms} = 28^\circ$ as shown in Figure 4.4. It demonstrates that the multiple reflections in the weighted groove array are suppressed to a low level, both magnitude ripple and phase deviations caused by the multiple reflections are suppressed.

However, if we compare the measurements of this duty cycle weighted RAC of 40 nm groove depth to the unweighted RAC of 25 nm groove depth, one see that the root mean square value of the phase deviation $\Delta\varphi_{rms} \approx 18^\circ$ in Figure 4.22 is about two times of the value $\Delta\varphi_{rms} \approx 9^\circ$ as shown in Figure 4.7. It demonstrates that although the multiple reflection is reduced by weighting discussed above, it is still stronger in the 40 nm duty

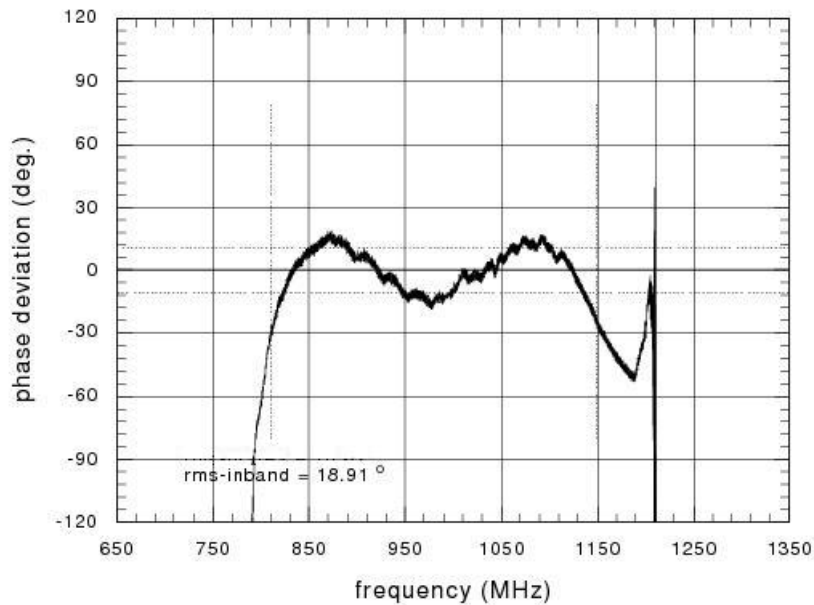


Figure 4.22: Phase deviation of the duty cycle weighted $BT = 4000$ and $f_c = 1$ GHz RAC filter, with uniform groove depth $h = 40$ nm.

cycle weighted groove array than in the 25 nm unweighted groove array. The larger phase deviation caused by the multiple reflection in the 40 nm duty cycle weighted groove array will lead to higher side lobes in the compressed pulse. One can see that the compressed pulse first side lobe as shown in Figure 4.21 is, therefore, higher than the one in Figure 4.2. Certain phase compensation technology is still needed for RACs with deep grooves. The technique of phase compensation will be discussed in detail in Chapter 5.

From the above discussions, we have proved that the duty cycle weighting method is an effective amplitude weighting method for RACs with constant groove depth. It is especially suitable for e-beam lithography. Because the grooves are far from each other (the groove period does not change with weighting coefficients), so the influence of the proximity effect of e-beam exposure is smaller compared to the other weighting method (e.g. the position weighting method that will be discussed in the next section), which is the main limitation for e-beam lithography. The basic principle of the e-beam lithography, the proximity effect and the reason for the exposure dose variation, are discussed in Appendix C.

Because e-beam lithography is undertaken with very high precision (2.5 nm resolution and 10 nm critical dimension) and the ability to vary the exposure dose, the duty cycle weighted very narrow grooves (the smallest 140 nm for $BT = 8000$ RAC) can be precisely exposed. The limitation of this kind of weighting method is that the grooves are approaching the critical dimension of the lithography, when the center frequency increases and also the weighting needs to be very heavy. To make such a kind of structure precisely, special tricks for varying the exposure dose are needed. The dose used for different filter structures need experimental evaluations. This is time consuming and also expensive.

4.3.4 Pair grooves position weighting

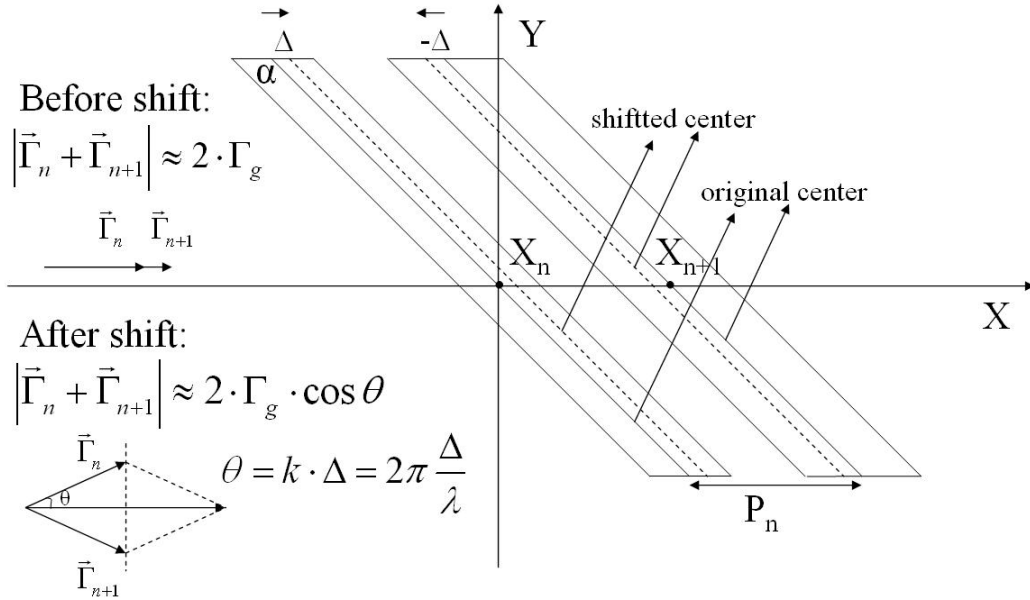


Figure 4.23: Principle of the couple groove position weighting.

This method was first proposed by S. Gopani in his paper [50] in 1990. The principle of the position weighting is shown in Figure 4.23. For this method, we can keep the groove depth and also the duty cycle (50%) uniform. Under these conditions, we can derive the single groove reflectivity as Equation 4.12 from Equation 3.11.

$$|\Gamma_g| = 2 \cdot 0.51 \left(\frac{h}{\lambda} \right) \quad (4.12)$$

If we shift every pair of grooves closer to each other from the original position as shown in Figure 4.23, then the reflection vectors for the two grooves at the synchronous frequency will not be in phase any more. However the pair of grooves as a group is still reflecting in phase with other pairs; only the total reflectivity of the two grooves was modulated by the shifting. Due to this lost phase, a $\cos \theta$ term is introduced into the single groove reflectivity as shown in Figure 4.23. Similar to the last few sections, one calculates the shifting distance Δ for this weighting method from the magnitude correction factor $Mag_{corr}(f)$.

$$\Delta(f) = \frac{1}{2\pi} \cdot \arccos \left(10^{\frac{-Mag_{corr}(f)}{40}} \right) \cdot \lambda \quad (4.13)$$

If one compares this method with the duty cycle weighting, one finds that for the same $Mag_{corr}(f)$, the distance between the weighted two grooves edges in position weighting is the same as the groove width in duty cycle weighting. The smallest structure for these two methods is the same. However, for position weighting it is the groove gap that approaches the critical dimension, and for duty cycle weighting it is the groove width. When using e-beam lithography, position weighting needs dose evaluations for different structures. For this method, we do not have experimental results, however.

To conclude the discussion of the above amplitude weighting techniques, we can see that for a good filter design, very heavy amplitude weighting should always be avoided, since it causes large difficulties in the lithography and other fabrication processes. For duty cycle weighting and pair grooves position weighting, the smallest structure approaches the critical dimension of the lithography when the weighting need to be heavy. One should optimize the magnitude carefully, and select the working bandwidth properly to avoid the weighting as much as possible. For the magnitude optimization process for the two developed RAC filters are shown in Chapter 6. For the other three types of RACs that can be developed, the optimizations are simulated in Appendices A.1, A.2 and A.3.

5 Phase deviation compensation for RAC devices

5.1 Determination of phase deviation from measurement

The RAC filter phase is obtained from the S_{21} parameter, measured using a vector network analyzer. The frequency dependent phase angle is given by Equation 5.1:

$$\varphi(f) = \arctan\left(\frac{\text{Im}(S_{21}(f))}{\text{Re}(S_{21}(f))}\right) \quad (5.1)$$

Here, $\text{Im}(S_{21}(f))$ is the imaginary part of the S_{21} parameter, and $\text{Re}(S_{21}(f))$ is the real part of the S_{21} parameter. In order to avoid the case of dividing 0 when $\text{Re}(S_{21}(f)) = 0$, the following special cases were dealt with.

$$\varphi(f) = \begin{cases} \frac{\pi}{2} & \text{Im}(S_{21}(f)) > 0, \text{Re}(S_{21}(f)) = 0 \\ -\frac{\pi}{2} & \text{Im}(S_{21}(f)) < 0, \text{Re}(S_{21}(f)) = 0 \end{cases} \quad (5.2)$$

Equation 5.1 is only correct when $\text{Re}(S_{21}(f)) > 0$ which is for $\varphi(f) \in [-\frac{\pi}{2}, \frac{\pi}{2}]$. When it is the case for $S_{21}(f).re < 0$, Equation 5.3 is used when $\varphi(f) \in [-\pi, -\frac{\pi}{2}] \cup [\frac{\pi}{2}, \pi]$.

$$\varphi(f) = \begin{cases} \arctan\left(\frac{\text{Im}(S_{21}(f))}{\text{Re}(S_{21}(f))}\right) + \pi & \text{Im}(S_{21}(f)) > 0, \text{Re}(S_{21}(f)) < 0 \\ \arctan\left(\frac{\text{Im}(S_{21}(f))}{\text{Re}(S_{21}(f))}\right) - \pi & \text{Im}(S_{21}(f)) < 0, \text{Re}(S_{21}(f)) < 0 \end{cases} \quad (5.3)$$

Using the above calculation, the phase is correctly calculated in $[-\pi, \pi]$. However, for the phase out of this range, the measurement will remove the part $N \cdot 2\pi$ in the phase; here N is an integer. Then in order to recover the continuous phase curve, the 2π phase jumps in the measurement are unwrapped for all the points in the array for $S_{21}(f)$ at different frequencies. The unwrapped phase curve for the RAC is shown in Figure 5.1. From the curve we can see that it is a typical quadratic shape and the total phase of RAC designed with $B = 400$ MHz, $T = 10 \mu\text{s}$ at $f_c = 1$ GHz is about $3500 \cdot 360 \approx 1.26$ million degrees.

We use the Chi-Square fitting to fit a typical quadratic polynomial with the following form in Equation 5.4 to the measured phase curve.

$$\varphi(f)_{fit} = C_0 + C_1 \cdot f + C_2 \cdot f^2 \quad (5.4)$$

Here, the phase $\varphi(f)$ is in degrees, and f is in MHz. To get rid of the influence of the unstable phase at the beginning and end of the passband, the fitting is only performed in 90% of the filter's working bandwidth (e.g. for the above $B = 400$ MHz RAC filter, the

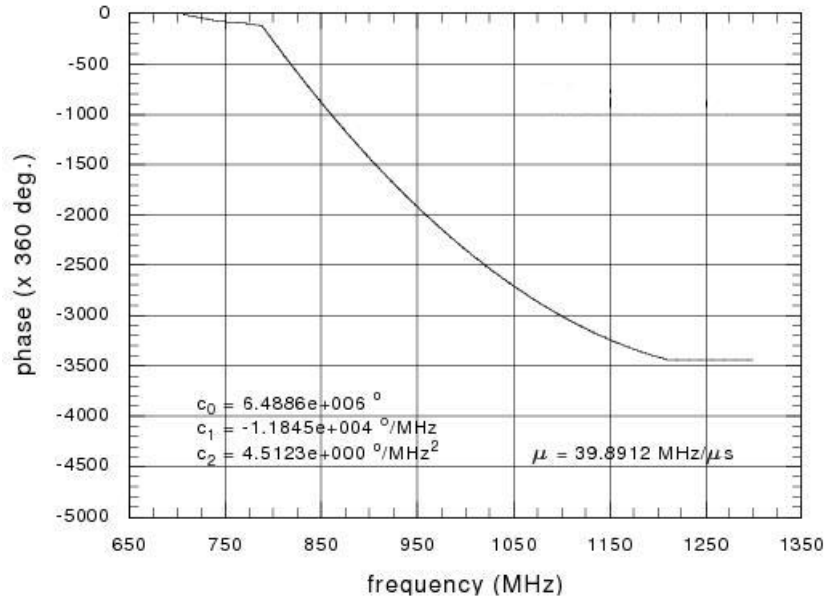


Figure 5.1: $B = 400$ MHz, $T = 10$ μ s and $f_c = 1$ GHz RAC filter's measured continuous phase curve.

fitting is performed using the measurement data from 820 MHz to 1180 MHz only). The coefficients C_0 , C_1 and C_2 can then be found, which is shown in Figure 5.1. The chirp slope μ of the RAC filter is then, by comparing Equation 5.4 and Equation 4.3:

$$\mu = \frac{360^\circ}{2 \cdot C_2} \quad (5.5)$$

The value of μ obtained is shown in Figure 5.1, agrees well with the designed value $\mu_{design} = \frac{B}{T} = 40$ MHz/ μ s. The measured RAC chirp slope can be used in the compressed pulse calculation for generating perfectly matched up chirp signals.

The phase deviation of the RAC is the difference between the measured phase and the fitted quadratic phase:

$$\Delta\varphi(f) = \varphi(f)_{meas} - \varphi(f)_{fit} \quad (5.6)$$

The phase deviation curve from filter RAC9C11 (see Section 1 in Chapter 6 for its design) is shown in Figure 5.2. The root mean square value of the phase deviation in Figure 5.2 is calculated using the following equation:

$$\Delta\varphi_{rms} = \sqrt{\frac{1}{N} \sum_{i=1}^N \Delta\varphi(f_i)^2} \quad (5.7)$$

Here, N is the total number of the frequency points in the chosen bandwidth for the RAC filter. As shown in Figure 5.2, in the 400 MHz bandwidth from 800 MHz to 1200 MHz, the $\Delta\varphi_{rms} = 18.91^\circ$. The phase deviation of the RAC will distort its compressed pulse shape, and make the side lobe of the compressed pulse higher than ideal -13.6 dB (as shown in Figure 4.2 and Figure 4.21). In order to have a better side lobe suppression in the RAC's compressed pulse, the phase deviation needs to be compensated.

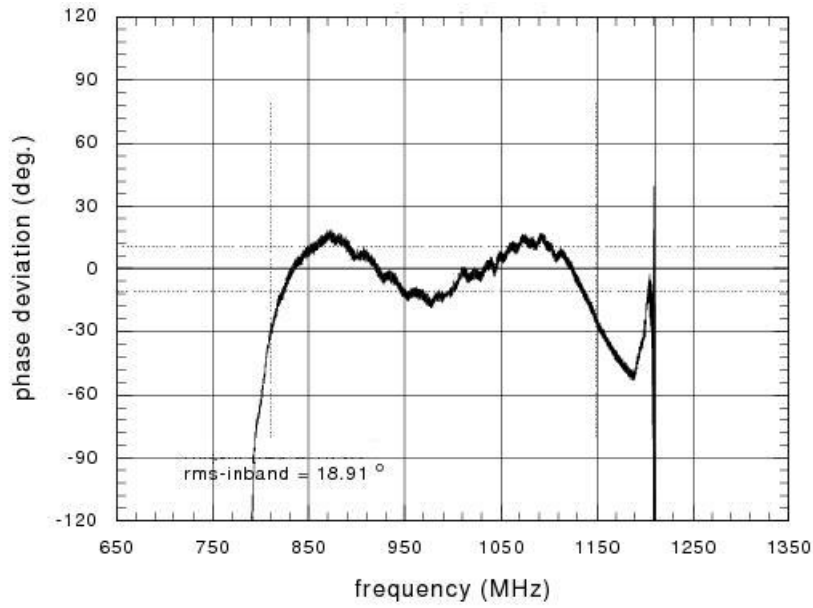


Figure 5.2: $B = 400$ MHz, $T = 10 \mu\text{s}$ and $f_c = 1$ GHz RAC filter's phase deviation from the ideal quadratic dependency.

5.2 Phase compensations by 50 nm Al stripe

It is well known that a thin metal film on the piezoelectric material surface can slow down the SAW propagation velocity due to the electrical loading and mass loading effects. The SAW velocity that depends on the Al film thickness on YX-LiNbO₃ is simulated using FEM/BEM in the following image. The simulation is supplied by Dr. Victor Plessky (GVR Trade, Neuchatel). Here, we choose the $h = 50$ nm Al film for the thickness of the phase compensation stripe. From this simulation, along the X-axis of LiNbO₃ the metalized phase velocity is $v_p^{50nm} = 3680.7$ m/s at 1 GHz frequency compared to the free surface phase velocity which is $v_p^{free} = 3717.8$ m/s. The simulation also shows that the SAW is dispersive when propagate under the 50 nm Al metallized surface, but the dispersion is only about 2 m/s in the frequency range from 800 MHz to 1200 MHz around the value $v_p^{50nm} = 3680.7$ m/s at 1 GHz frequency; it can, therefore, be ingored.

The phase deviation can be compensated using this type of metal stripe between the two reflective arrays by slowing down the SAW which propagate under it. The width calculation of the phase stripe in the X direction for a measured phase deviation $\Delta\varphi(f)$ can be derived with the two velocities mentioned above for free surface and metalized surface.

$$L(f) = \frac{\Delta\varphi(f)}{k_m - k_0} = \frac{\Delta\varphi(f)}{2\pi f} \cdot \frac{v_p^{free} \cdot v_p^{50nm}}{v_p^{free} - v_p^{50nm}} \quad (5.8)$$

Here, $k_m = \frac{2\pi f}{v_p^{50nm}}$ and $k_0 = \frac{2\pi f}{v_p^{free}}$ are the 50 nm Al metalized and the free surface wave number of the SAW along the X axis of LiNbO₃, respectively. The phase deviation as shown in Figure 5.2 can be compensated using a 50 nm Al stripe between the two reflective arrays with the width profile as shown in Figure 5.4. Here the integer number times of the wavelength is added into the phase stripe to get rid of the negative stripe width for

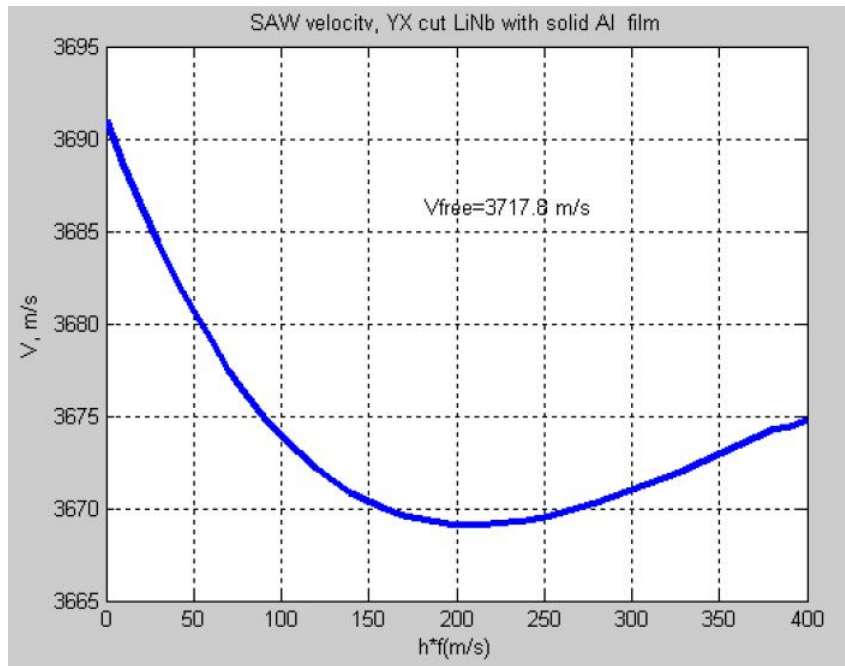


Figure 5.3: SAW phase velocity variation versus Al film thickness h times frequency f on YX-LiNbO₃ [59].

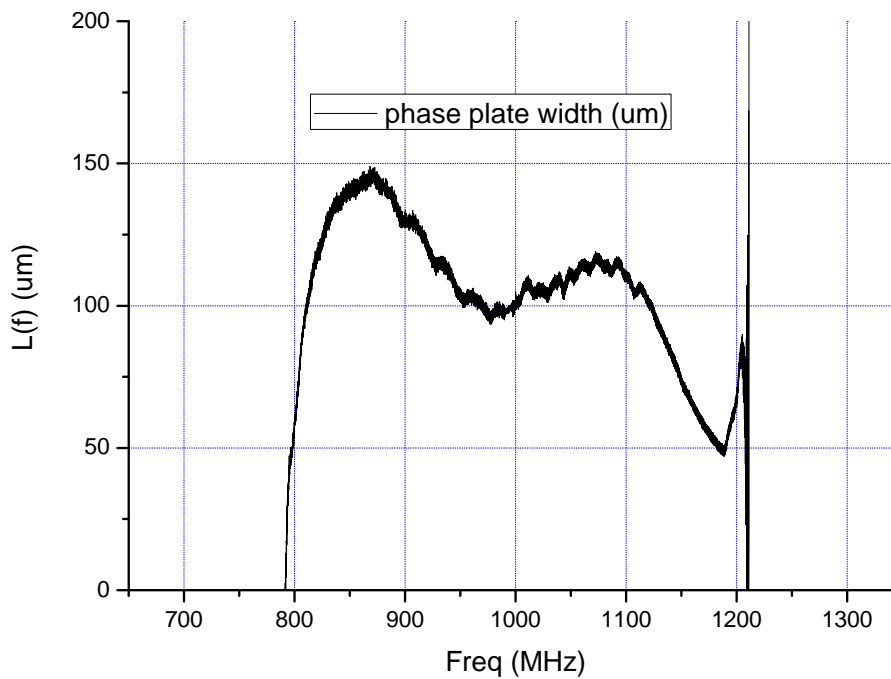


Figure 5.4: Calculated phase compensation stripe width from measured phase deviation shown in Figure 5.2.

negative phase deviations. The stripe width should be as small as possible otherwise it will attenuate the filter magnitude.

5.3 Experiments for phase compensation

However, in the experiments the compensation using the Al stripe discussed in last section was not so successful. The phase deviation after the compensation is even larger than before. The reason is still not clear. We think it could be that the FEM/BEM simulated SAW phase velocity on YX LiNbO₃ is not precise enough to use in the experiments. So we designed simple Al stripes between the groove array as shown in Figure 5.5 to extract the phase compensation constant $\frac{v_p^{free} - v_p^m}{v_p^{free} \cdot v_p^m}$ experimentally for 50 nm Al films. For the design

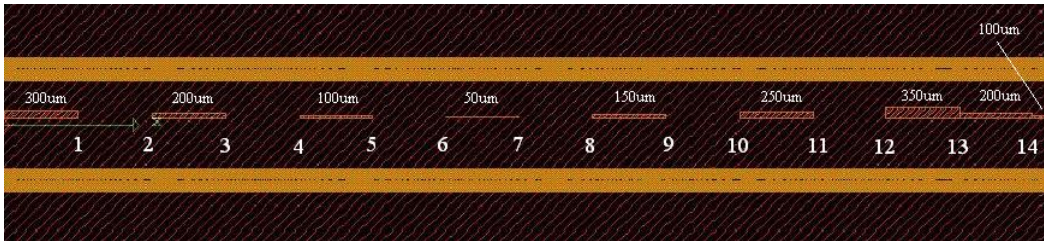


Figure 5.5: Phase plate layout for a $B = 400$ MHz and $T = 20 \mu\text{s}$ RAC, the Al stripes are $2500 \mu\text{m}$ long with varying widths (from $50 \mu\text{m}$ to $350 \mu\text{m}$) along the X-axis of LiNbO₃, spaces between the stripes are also $2500 \mu\text{m}$, the stripe width change positions are indexed from 1 to 14.

convenience, the width of the stripes on X-axis of LiNbO₃ are of integer values in microns (from $50 \mu\text{m}$ to $350 \mu\text{m}$). We want to know how much the relative phase will jump in the measurement due to the width change of the Al stripe (at the positions indexed from 1 to 14). The RAC filter performance was measured before and after the deposition of the Al stripe.

5.3.1 Extraction of compensation constant using measured magnitude

In Figure 5.6 we see the measured filter magnitude before the phase stripe was applied, and as we used the duty cycle weighting method, the filter has about -55 dB, quite flat magnitude in the wide 400 MHz bandwidth. After the phase plate was added, the magnitude showed big attenuation peaks at the positions where the stripe's width changes, as shown in Figure 5.7. These peaks are marked from 1 to 14 in Figure 5.7, and they are caused by the stripe width abrupt changes shown in Figure 5.5, which are also marked from 1 to 14 respectively. The reason for those attenuation peaks can be explained with the help of Figure 5.8 and Figure 5.9. For the total reflectivity of the groove array at a frequency f without the influence of stripes, the symmetrical groove pair reflection vector sum in an effective reflecting zone is as shown in Figure 5.9. When the stripes are added, the reflection vector summing will be different. At the frequencies where the attenuation peaks, the center of the in phase reflecting zone is at the position where the phase stripe

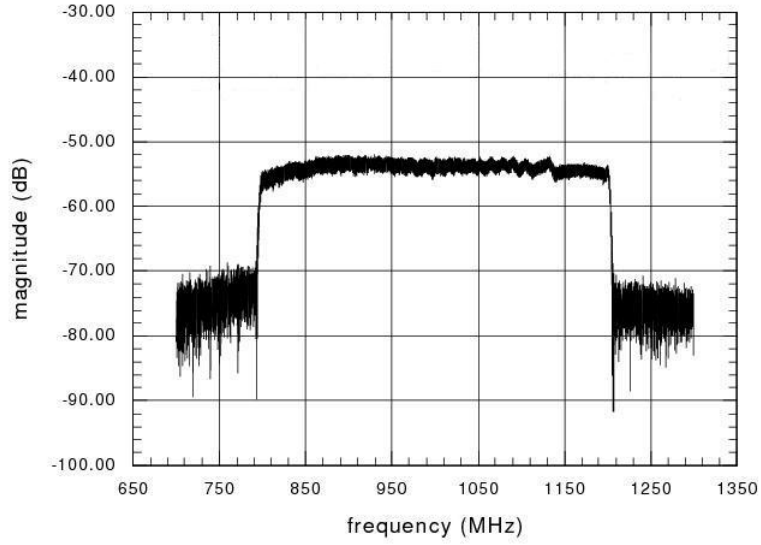


Figure 5.6: Measured magnitude of the $B = 400$ MHz and $T = 20 \mu\text{s}$ RAC before the Al stripes are added.

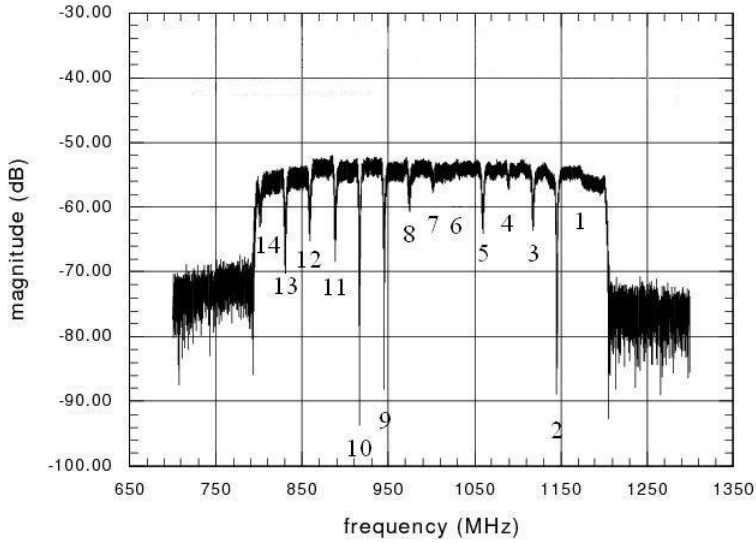


Figure 5.7: Measured magnitude of the $B = 400$ MHz, $T = 20 \mu\text{s}$ RAC after the Al stripes as shown in Figure 5.5 are added.

changes. As shown in Figure 5.8, the left half of the in phase reflected wave beam (\vec{S}_{left}) passes through the stripe and is slowed down by the stripe, while the right half (\vec{S}_{right}) of the in phase reflected wave beam remains uninfluenced. Then the left and the right half of the beam, when added up together at the IDT will then not be the same as before as shown in Figure 5.10. The magnitude at this frequency for the filter will be reduced ($\Delta\varphi \in (0, \pi)$) or even increased ($\Delta\varphi \in (-\pi, 0)$) due to the phase shift $\Delta\varphi$. In this analysis we assume that the 50 nm Al stripe only slows the SAW down but does not attenuate it. If we put S as the total array reflectivity for an effective reflection zone at frequency f without the

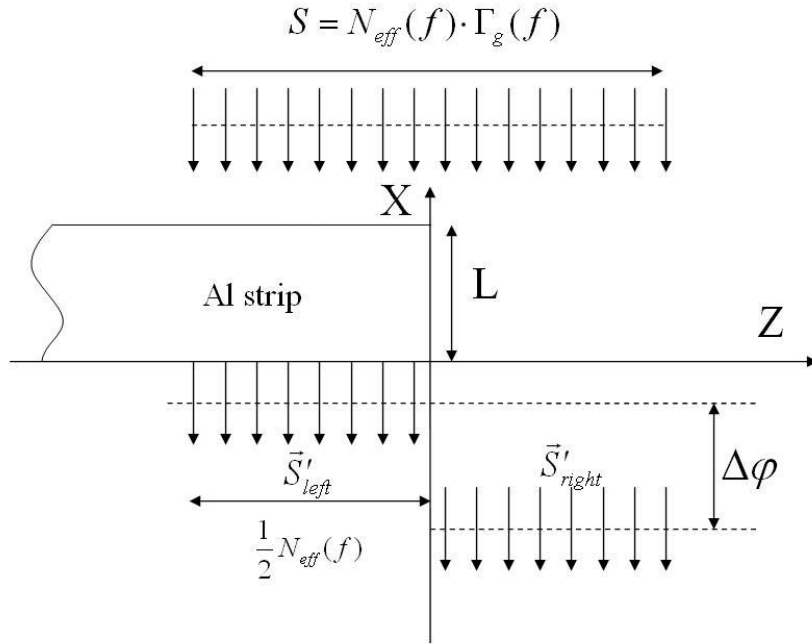


Figure 5.8: Influence of a Al stripe to the SAW beam in an effective reflecting zone; here we assume the $\Delta\varphi$ is the same in the effective reflecting zone (as the frequency change is small).

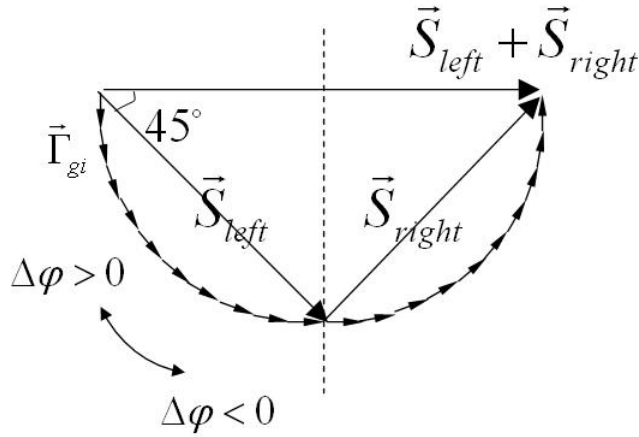


Figure 5.9: Illustration of the single groove pair reflection vector $\vec{\Gamma}_{gi}$ summing in an effective reflecting zone at frequency f according to the impulse response model; the $\Delta\varphi$ generated by the added stripe will rotate the SAW beam vector \vec{S}'_{left} as indicated.

influence of stripes, from Figure 5.10 we can deduce that:

$$|\vec{S}'_{left} + \vec{S}'_{right}| = \sqrt{2} \cdot |\vec{S}'_{left}| = \sqrt{2} \cdot |\vec{S}'_{right}| = S \quad (5.9)$$

When the stripe is added, the total reflectivity of an effective reflecting zone will become:

$$|\vec{S}'_{left} + \vec{S}'_{right}| = \sqrt{2} \cdot S \cdot \cos\left(\frac{\Delta\varphi}{2} + \frac{\pi}{4}\right) \quad (5.10)$$

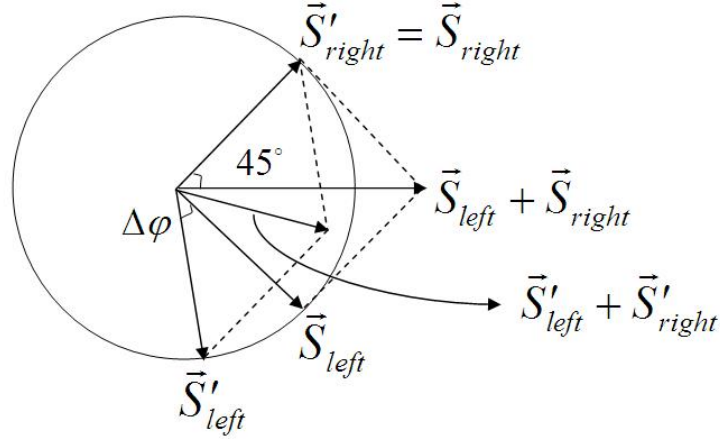


Figure 5.10: Comparison of the SAW beam vector summing ($\vec{S}'_{left} + \vec{S}'_{right}$) and ($\vec{S}_{left} + \vec{S}_{right}$) for with and without $\Delta\varphi$ in an effective reflecting zone at frequency f .

Then the relationship between the insertion loss change ΔIL_i at the stripe width change position i versus the related phase shift $\Delta\varphi_i$ can be deduced as follows:

$$\Delta IL_i = 10 \cdot \lg \left(\frac{|\vec{S}'_{left} + \vec{S}'_{right}|}{|\vec{S}_{left} + \vec{S}_{right}|} \right)_i^2 = 10 \cdot \lg \left(2 \cdot \cos^2 \left(\frac{\Delta\varphi_i}{2} + \frac{\pi}{4} \right) \right) \quad (5.11)$$

From Equation 5.11 we can determine the generated phase shift due to the stripe width change at position i from the measured magnitude attenuation ΔIL_i in Figure 5.7.

$$\Delta\varphi_i = 2 \cdot \arccos \sqrt{\left(\frac{1}{2} \cdot 10^{\frac{\Delta IL_i}{10}} \right)} - \frac{\pi}{2} \quad (5.12)$$

The extracted $\Delta\varphi_i$ according to the ΔIL_i is listed for $i = 1 \dots 14$ in Table 5.1, and this can be compared to the expected values calculated using the velocity simulated using FEM/BEM method in last section.

The relationship between the stripe width and the generated phase shift is given by Equation 5.8. In the measurement the frequencies f_i of the magnitude attenuation peaks can also be read from Figure 5.7 like ΔIL_i , the experimental phase compensation coefficients is then extracted as:

$$\left(\frac{v_p^{free} - v_p^{50nm}}{v_p^{free} \cdot v_p^{50nm}} \right)_i = \frac{\Delta\varphi_i}{2\pi f_i L_i} \quad (5.13)$$

The calculated phase compensation constant $\left(\frac{v_p^{free} - v_p^m}{v_p^{free} \cdot v_p^m} \right)_i$ at different index positions (2, 5, 7, 9, 10, 12, 13, 14) is plotted in Figure 5.11. The averaged value for all these eight points is about $2.2 \cdot 10^{-6} s/m$, which is quite close to the FEM/BEM simulated value of $2.7 \cdot 10^{-6} s/m$ in the last section. Here for the missing 6 points, 3 points (1, 4, 6) as the ΔIL_i is very small and can hardly be read out in Figure 5.7; and the remaining 3 points (3, 8, 11) because the ΔIL_i should be positive according to the FEM/BEM calculated phase shift; thus, they are not included in the parameter extraction.

Index i	Pos (μm)	Design f_i (MHz)	Exp f_i (MHz)	ΔL_i (μm)	ΔIL_i (dB)	$\Delta\varphi_i$ (FEM)	$\Delta\varphi_i$ (meas)
1	2550	1176.36	—	-300	—	344.45°	—
2	5050	1147.35	1145.29	+200	-33.90	-223.97°	-271.64°
3	7550	1117.91	1117.81	-200	-8.66	218.22°	—
4	10050	1089.93	—	+100	—	-106.38°	—
5	12550	1061.11	1059.52	-100	-9.03	103.56°	61.04°
6	15050	1032.59	—	+50	—	-50.39°	—
7	17550	1003.85	1002.28	-50	-2.47	48.99°	25.71°
8	20050	974.28	974.71	+150	-5.74	-142.64°	—
9	22550	946.40	944.92	-150	-33.14	138.56°	88.21°
10	25050	917.71	916.72	+250	-38.69	-223.93°	-270.94°
11	27550	888.49	888.49	-250	-13.39	216.80°	—
12	30050	860.24	858.82	+350	-10.25	-293.87°	-295.10°
13	32550	832.18	830.71	-150	-15.16	121.84°	75.82°
14	35050	802.99	800.92	-100	-8.15	78.37°	57.88°

Table 5.1: Aluminium plate width variation VS expected and experimental extracted phase jump from ΔIL_i .

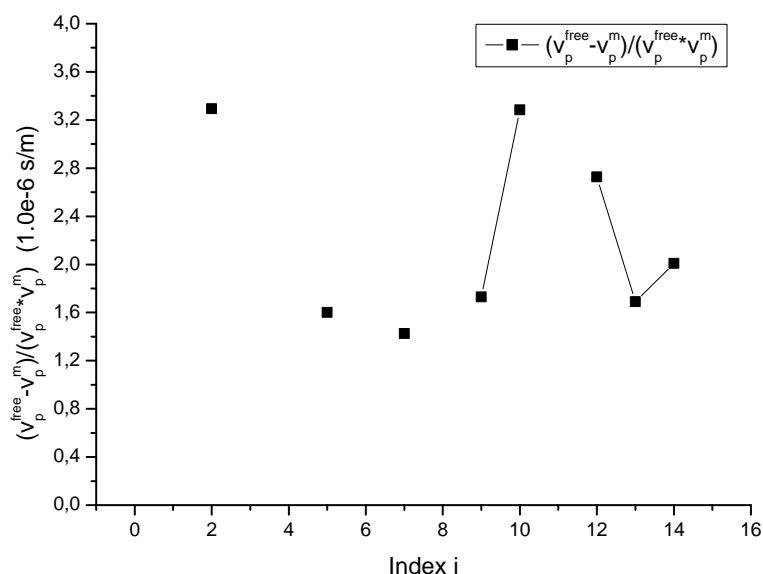


Figure 5.11: Extracted $\left(\frac{v_p^{\text{free}} - v_p^m}{v_p^{\text{free}} \cdot v_p^m}\right)_i$ from measured ΔIL_i values in Table 5.1.

5.3.2 Extraction of the compensation constant using measured phase

Using the direct phase comparison between the measurement before and after the phase compensation, a similar extraction for the constant phase compensation coefficient for

Index i	Design f_i (MHz)	ΔL_i (μm)	$\Delta\varphi_i$ (FEM)	$\Delta\varphi_i$ (meas)
1	1176.36	-300	344.45°	0.0°
2	1147.35	+200	-223.97°	-235.0°
3	1117.91	-200	218.22°	150.0°
4	1089.93	+100	-106.38°	-115.0°
5	1061.11	-100	103.56°	85.0°
6	1032.59	+50	-50.39°	-45.0°
7	1003.85	-50	48.99°	35.0°
8	974.28	+150	-142.64°	-140.0°
9	946.40	-150	138.56°	130.0°
10	917.71	+250	-223.93°	-220.0°
11	888.49	-250	216.80°	200.0°
12	860.24	+350	-293.87°	-280.0°
13	832.18	-150	121.84°	100.0°
14	802.99	-100	78.37°	65.0°

Table 5.2: Aluminium plate width variation versus FEM/BEM simulated and directly measured phase jumps.

50 nm Al films can also be done. Figure 5.12 shows the difference of the unwrapped phase from the measurement for the RAC ($\varphi_{after} - \varphi_{before}$). Here, φ_{after} is the measured phase after the plate is added, and φ_{before} is the measured phase before the plate is added. The phase jump shown in Figure 5.12, $\Delta\varphi_{10} = -940.0^\circ$, should be due to the incorrect

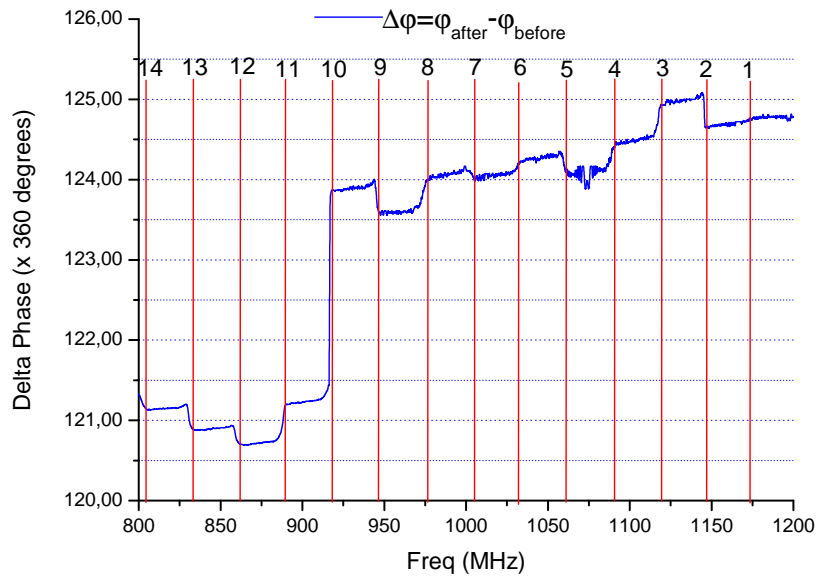


Figure 5.12: Measured phase jumps generated by the added Al stripes.

360° phase unwrapping, so we removed -720° from it, and left -220° for the calculation. For $\Delta\varphi_{11} = -160.0^\circ$ and $\Delta\varphi_{12} = 80.0^\circ$, their signs are both not correct according to their stripe width change. So we added the 360.0° phase correction for both of them; then they changed to $\Delta\varphi_{11} = 200.0^\circ$ and $\Delta\varphi_{12} = -290.0^\circ$. The value of $\left(\frac{v_p^{free} - v_p^m}{v_p^{free} \cdot v_p^m}\right)_i$ is calculated again according to the phase difference listed in Table 5.2, and is plotted in Figure 5.13. The averaged value for all these 12 points (the first point as the $\Delta\varphi = 0^\circ$) is

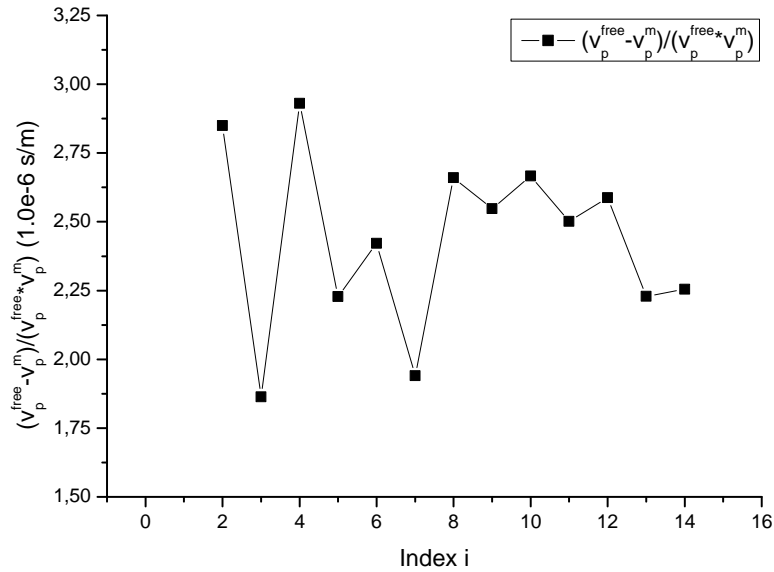


Figure 5.13: $\left(\frac{v_p^{free} - v_p^m}{v_p^{free} \cdot v_p^m}\right)_i$ extraction according to the measured phase jumps shown in Table 5.2.

about $2.44 \cdot 10^{-6} \text{ s/m}$, which also fits well to the FEM/BEM simulated value $2.71 \cdot 10^{-6} \text{ s/m}$ shown in the previous section.

From the above experiments, we conclude the following design rules for 50 nm Al phase compensation stripes.

1. The phase stripe should not have an abrupt width change, otherwise magnitude attenuation peaks will appear as shown in Figure 5.7.
2. For the phase compensation constant $\left(\frac{v_p^{free} - v_p^m}{v_p^{free} \cdot v_p^m}\right)$ of 50 nm Al stripes, we may use the value $2.44 \cdot 10^{-6} \text{ s/m}$ for the calculation of phase compensation stripe width according to Equation 5.8.

6 Developed RAC filters

In Chapter 1, the specifications of the two developed RAC filters during the PhD is listed in Table 1.2. In the following we shall discuss the development of these two types of RAC filters in detail including the design, fabrication and measurement.

6.1 Development of RAC filter I

The first RAC filter we have developed with good performance (filter I in Table 1.2) is centered at $f_c = 1$ GHz, with bandwidth $B = 400$ MHz and dispersive delay $T = 10$ μ s. It is a down chirp filter with time bandwidth product $BT = 4000$.

6.1.1 Design parameters of RAC filter I

The optimized IDT and also groove array aperture W is chosen to be 550 μ m according to:

$$W = 2 \cdot L_a = \frac{v_{px} \cdot T}{\sqrt{B \cdot T}} \approx 552 \mu\text{m}. \quad (6.1)$$

Here v_{px} is the SAW phase velocity along the Z-axis of LiNbO₃.

The IDT used in RAC filter I is eight electrodes with one pair reverted transducer centered at 1 GHz, its geometry is as shown in Figure 3.3. The performance of this kind of IDT is discussed in detail in Chapter 3. We used the duty cycle weighted rectangular groove array to obtain a desired rectangular filter passband shape, therefore, to achieve the minimum compressed pulse main lobe width. The uniform groove depth of the groove array is 40 nm.

6.1.2 Magnitude optimization for RAC filter I

In order to find the required groove array duty cycle profile $\frac{w}{\lambda}(f)$ for realizing a desired rectangular passband shape, a magnitude optimization routine is developed.

The routine first read in the the measured IDT S parameters, then time gating is perform as described in Chapter 3. The read in transduction loss curve of the IDT is shown in Figure 6.1a and its time gated smooth curve is shown in Figure 6.1b.

The reflection loss of the unweighted groove array of RAC filter I can be simulated using the stationary phase approximation as described in Chapter 2 using Equation 2.21. The result is shown in Figure 6.2.

The SAW propagation loss can be simulated according to Equation 2.26, and the result is shown in Figure 6.3.

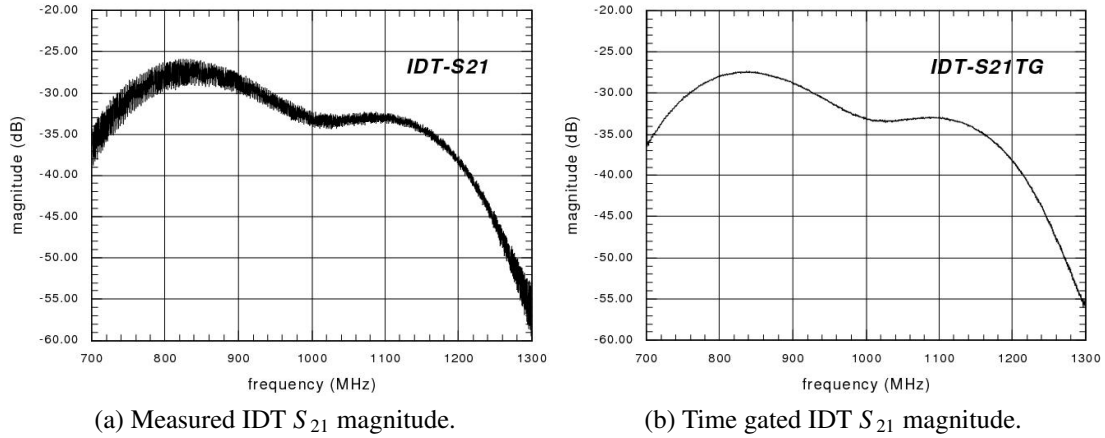


Figure 6.1: Upper one is the measured S_{21} magnitude for the aperture $W = 550 \mu\text{m}$ and eight electrodes transducer with one pair reverted IDT (the structure is shown in Figure 3.3). The lower one is its performance after the time gating shown in Chapter 3.

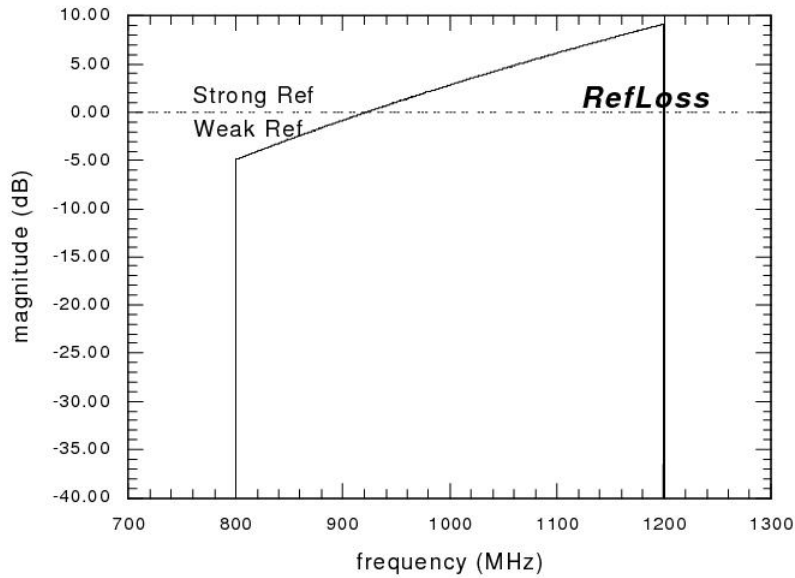


Figure 6.2: The simulated reflection loss for RAC filter I before weighting is applied.

With the measured IDT transduction loss and simulated reflection loss and SAW propagation loss for the unweighted groove array, the total RAC insertion loss (in dB) was synthesized according to Equation 6.2, and the synthesized result is shown in Figure 6.4.

$$IL(f) = R(f) + IDT(f) + PropLoss(f) \quad (6.2)$$

Equation 6.2 is similar to Equation 2.24, but the transmission loss of the SAW propagating through grooves on its path was not taken into account (filter I was developed at the beginning of this work). From Figure 6.4, one see that the magnitude nonuniformity is about 12 dB in the 400 MHz bandwidth. To obtain a desired rectangular filter response, duty cycle weighting method is used to correct the 12 dB nonuniformity as described in Chapter 4. The filter magnitude correction factor $Mag_{corr}(f)$ for duty cycle weighting is calculated

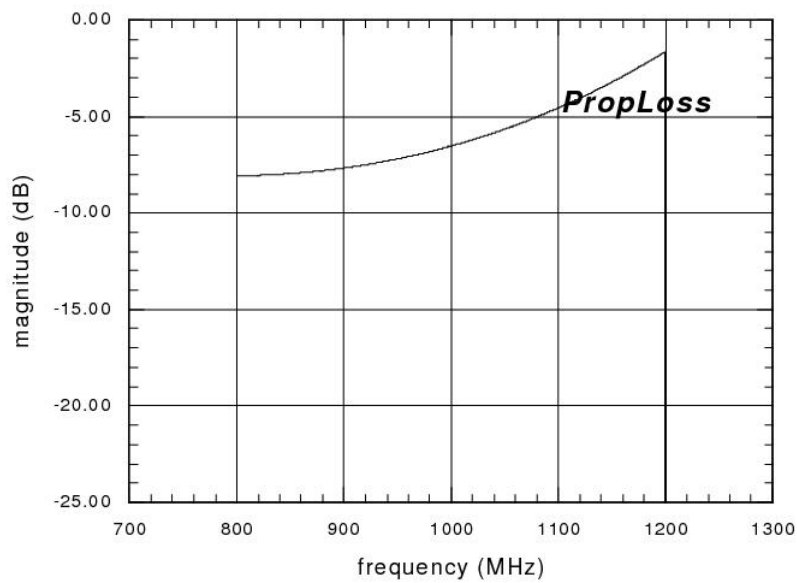


Figure 6.3: The simulated SAW propagation loss in RAC filter I.

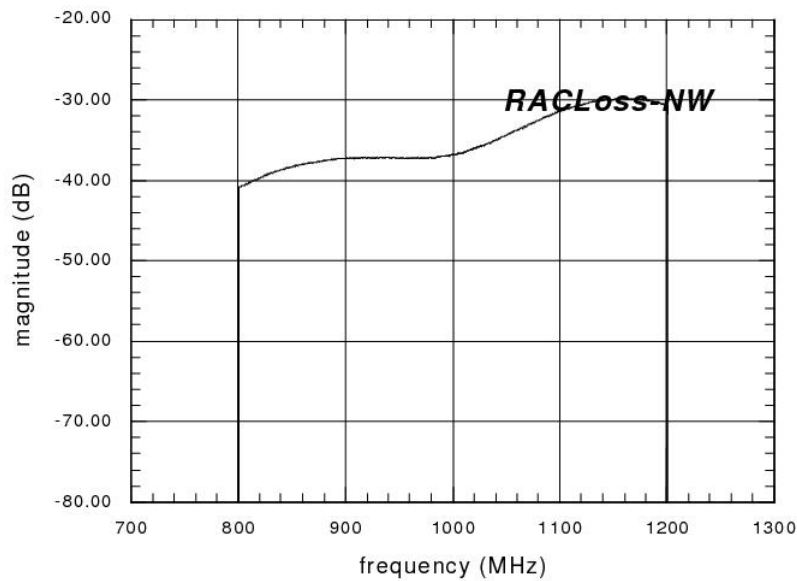


Figure 6.4: Insertion loss simulation for RAC filter I before weighting is applied.

using Equation 4.6. The desired filter response $Mag_{desired}(f) = -42$ dB is chosen, as this value is the lowest magnitude in the 400 MHz filter working bandwidth in Figure 6.4. By doing this, after the magnitude optimization the filter can achieve lowest insertion loss (maximum efficiency) and also the weighting can be minimum. According to Equation 4.11, the optimized duty cycle profile of the groove array can be calculated as shown in Figure 6.5. This duty cycle profile will then be used to add duty cycle modulation to the unweighted groove array structure.

The RAC's reflection loss become as shown in Figure 6.6 after the above duty cycle optimization. One can see that the reflection loss is below 0 dB in the 400 MHz filter bandwidth. It implies that the reflectivity of the groove array is small enough and the

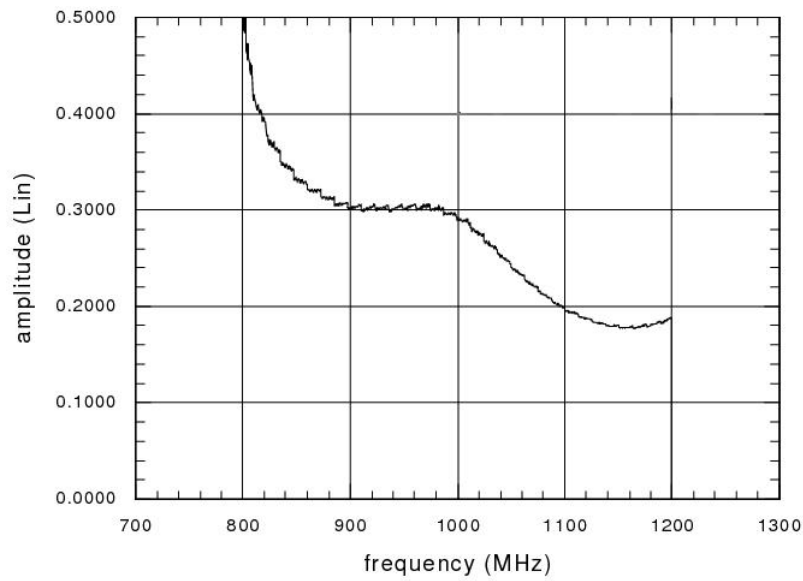


Figure 6.5: Optimized duty cycle profile for RAC filter I.

SAW multiple reflection in the array is, therefore, low.

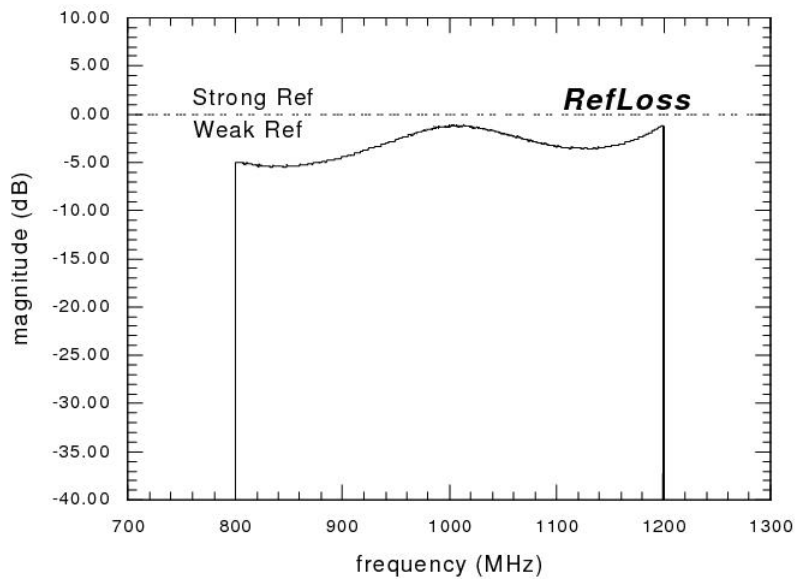


Figure 6.6: The simulated reflection loss of the groove array after duty cycle optimization.

The total insertion loss of RAC filter I after the duty cycle weighting can be simulated as discussed in Chapter 2 (the blue line as shown in Figure 6.17). Although the transmission loss is not included in the optimization routine of RAC filter I, it is included in this simulation for the purpose of comparison. If we compare the simulated insertion loss with the experimental result as shown in Figure 6.17, one can see that they fit each other well and the difference is less than 3 dB. It shows that the magnitude optimization routine discussed above have good precision.

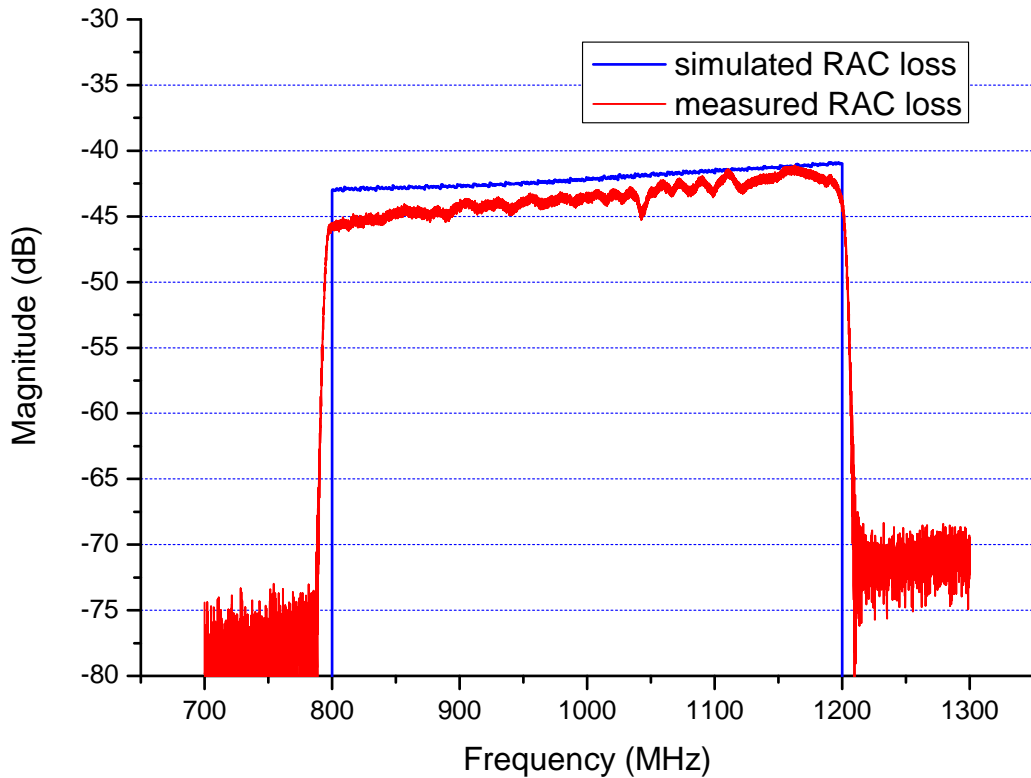


Figure 6.7: Comparison between the simulated (blue line) and measured (red line) insertion loss of RAC filter I with optimized duty cycle profile.

6.1.3 Dose variation for groove array exposure

For the exposure of the duty cycle weighted groove array in RAC filter I, we use linearly decreasing e-beam dose along the array. The whole groove array is divided into eight sections of equal length as shown in Figure 6.8. The exposure dose for the first and the last section was determined experimentally. The exposure dose for other sections is then linearly interpolated between the first and the last section.

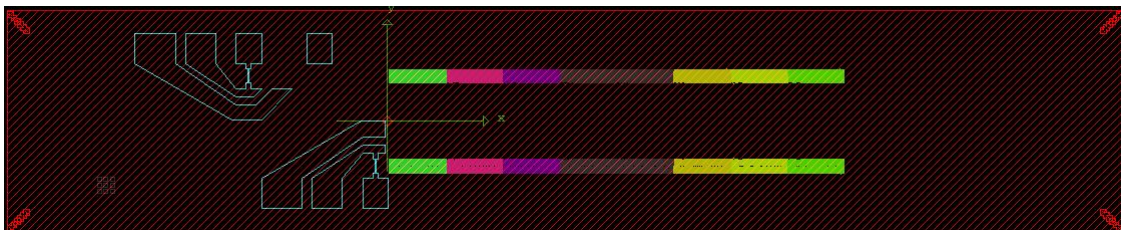


Figure 6.8: Layout of RAC filter I. Linear dose interpolation is used for duty cycle weighted groove array exposure. Each color in the groove array is exposed using a unique dose. The exposure dose for the first and last section was determined experimentally. The exposure dose for the other section are linearly interpolated in between.

6.1.4 Measurement result and discussion

The measured filter insertion loss is shown in Figure 6.17, the red line. We can see that it is quite flat in the whole 400 MHz working bandwidth, but still there is a 4 dB slope. According to the comparison between the blue line and the red line as shown in Figure 6.17, we can see that about 2 dB slope in the measurement is due to the groove array transmission loss. If we include the transmission loss in the duty cycle optimization routine, this 2 dB slope of the blue line will disappear. The origin for the rest 2 dB slope in the measurement is still not clear.

The other measured performances are plotted in Figure 6.9 and Figure 6.10. The compressed pulse in Figure 6.10b showed a quite narrow main lobe. This implies that the filter has a quite good rectangular passband shape after the duty cycle optimization. But the side lobe is quite high (the ideal sinc function side lobe suppression is 13.6 dB, here we only have about 7 dB). This implies that the phase deviation of the RAC is still too high ($\varphi_{rms} \approx 19^\circ$). Phase compensation is needed to suppress this high side lobe in the compressed pulse.

6.2 Development of RAC filter II

After the development of RAC filter I, we focused on the development of the $B = 400$ MHz, $T = 20 \mu\text{s}$ and $f_c = 1$ GHz RAC filter (filter II in Table 1.2). It is a down chirp filter with time bandwidth product $BT = 8000$.

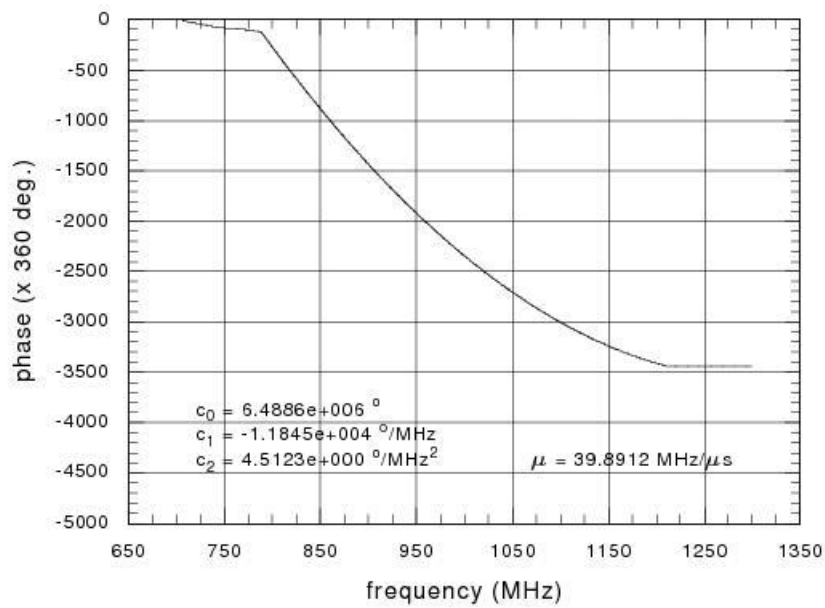
6.2.1 Design parameters for RAC filter II

The optimized aperture of the IDT and groove array of filter II can be calculated similarly as filter I according to Equation 6.1; and therefore we choose $780 \mu\text{m}$. The uniform depth of the groove array is chosen to be 20 nm; using this depth, the multiple reflection in the groove array is quite low. The IDT is of the same structure as the one in RAC filter I, except the aperture is longer.

6.2.2 Magnitude optimization

The magnitude optimization of RAC filter II is similar to the optimization process discussed in last section for RAC filter I. Here we only discuss the difference and give the related plots.

For the magnitude optimization process of RAC filter II, as the transmission loss was taken into account, the duty cycle optimization can not be done by once. Due to the energy conservation law, if the duty cycle profile of the groove array changes, the reflection loss and transmission loss both will change; but we only do the optimization by modifying the groove array's reflection loss, thus an iterative optimization procedure is needed. It is a simulation-optimization loop; at the end of every loop, we evaluate the difference between the optimized magnitude and the desired magnitude, the difference will be used for the next round duty cycle correction. By doing this, the filter magnitude approaches to our desired value rapidly; after three times of iterations, the difference between the optimized magnitude and our desired magnitude will converge to less than 0.5 dB. The total RAC



(a) Measured quadratic phase of RAC filter I.

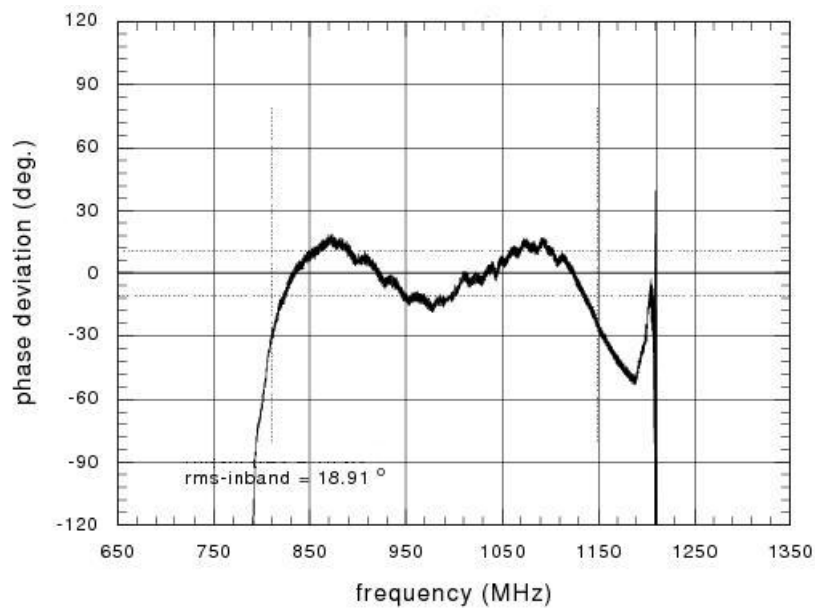
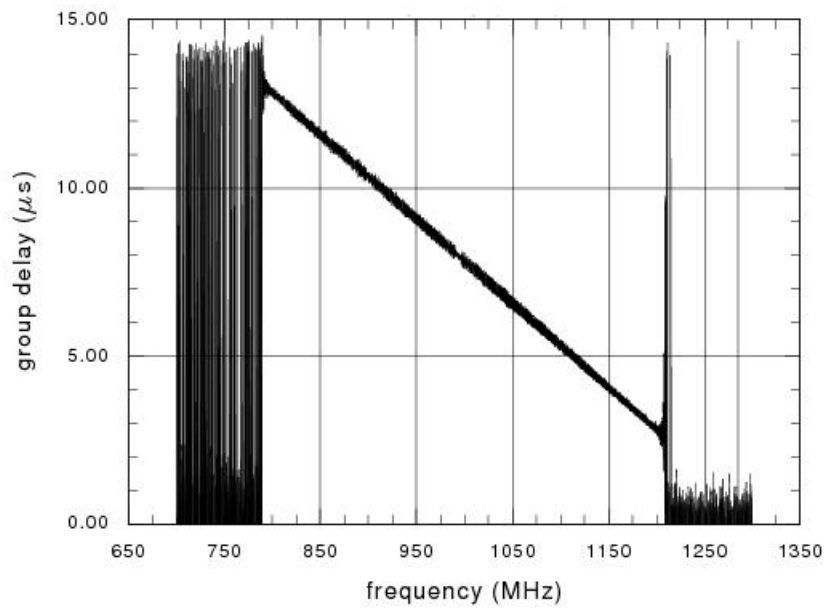
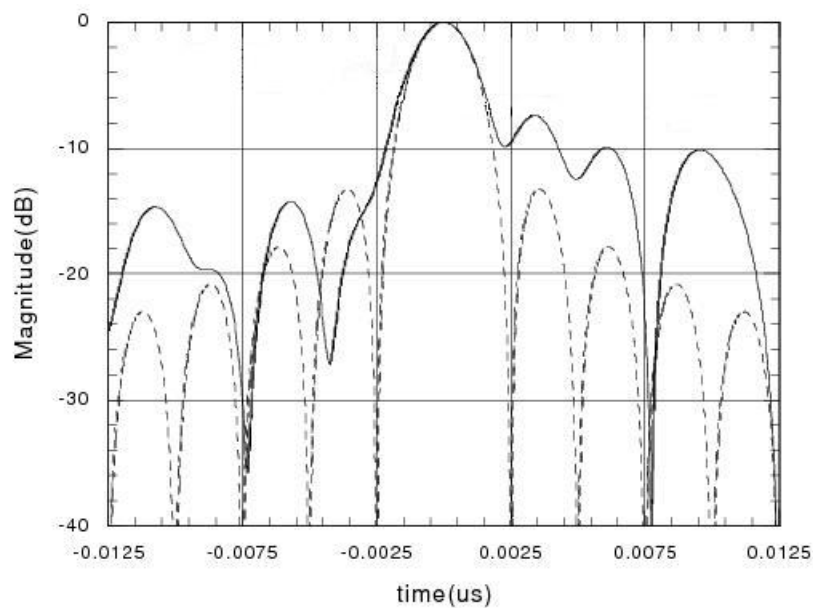
(b) Measured phase deviation from ideal quadratic dependency of RAC filter I. The root mean square value of the deviation in the 400MHz bandwidth is 18.91° .

Figure 6.9: Measured phase and the phase deviation of RAC filter I.

insertion loss is synthesized in Figure 6.14, we see that the magnitude nonuniformity in the 400 MHz bandwidth is about 18 dB. In Figure 6.17 we can see that there is a small peak in the measured magnitude at around 975 MHz. This attenuation is caused by a small scratch on the grooves, which is not expected. It shows that for SAW filters, any imperfections on the structures can cause serious problem to the filter performance, e.g. particles and scratches.



(a) Measured linear chirp delay of RAC filter I.



(b) Calculated compressed pulse (in dB) from the response of RAC filter I. The pulse main lobe -3dB width is 2.319 ns, the ideal sinc function main lobe -3 dB width is 2.213 ns.

Figure 6.10: Measured group delay and compressed pulse of RAC filter I.

6.2.3 Dose variation for groove array exposure

For the exposure of the duty cycle weighted groove array in RAC filter II, we used another dose variation strategy. In order to figure out the proper exposure dose for this structure, we used the Monte Carlo simulation for the e-beam exposure dose evaluation, the influence of the forward and backward scattered electron's proximity effect is included (the proximity effect is discussed in Appendix C). From the simulation result, we found that

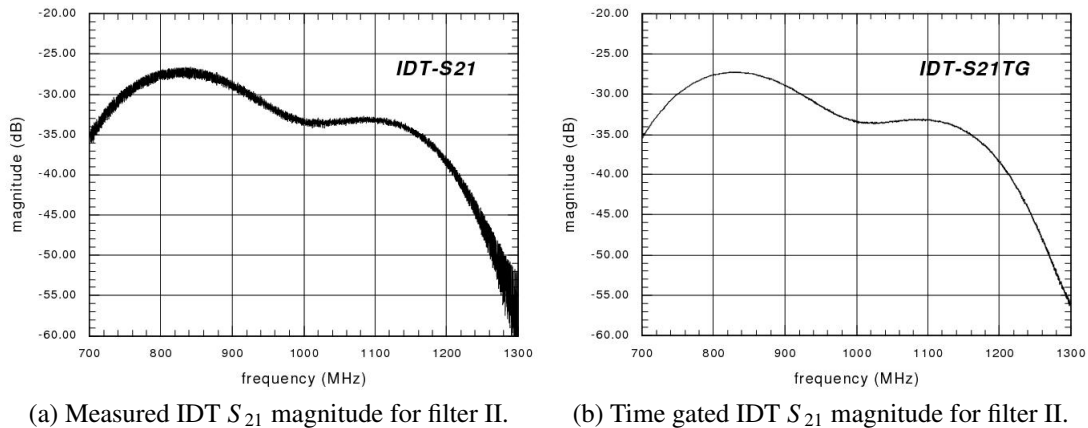


Figure 6.11: Upper one is the measured S_{21} magnitude for aperture $W = 780 \mu\text{m}$ and eight electrodes transducer with one pair reverted transducer as shown in Figure 3.3. The lower one is its performance after the time gating as shown in Chapter 3.

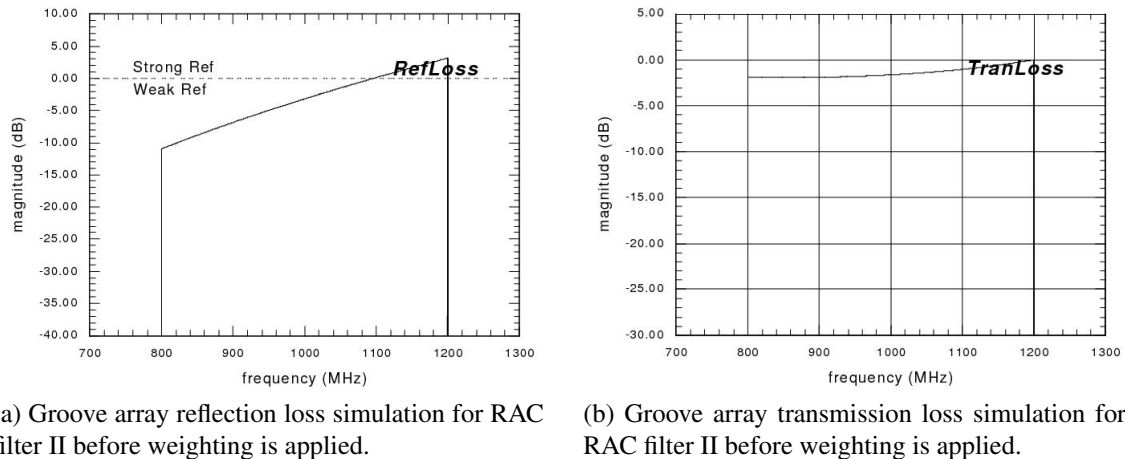


Figure 6.12: The simulated reflection loss and transmission loss of the groove array in RAC filter II before the weighting is applied.

the correct exposure dose should be linearly dependent on the groove's duty cycle. We then divided the whole layout into 20 segments according to the groove's duty cycle, each segment is with 2.5% duty cycle variation (20 segments cover 0 - 50% of groove's duty cycle). The exposure dose is specified to different segments inverse proportionally to the duty cycle value of the grooves in the segment. The layout becomes Figure 6.18, each color in a segment represent a layer for a unique exposure dose.

6.2.4 Measurement result and discussions

The measured insertion loss of RAC filter II is shown in Figure 6.17 in last subsection. The follows are plots for other measurement results.

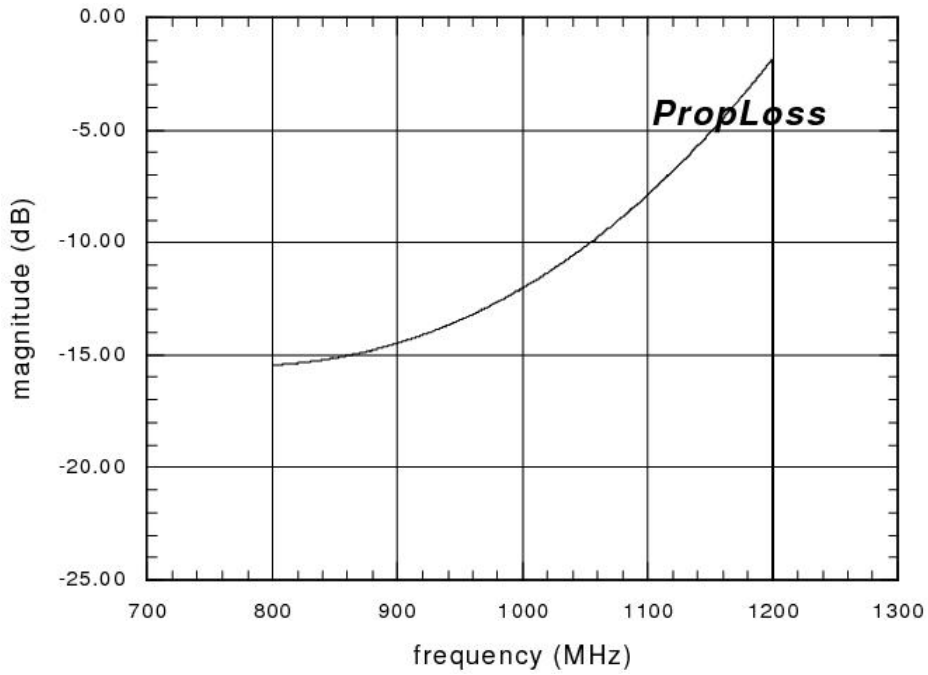


Figure 6.13: The simulated SAW propagation loss in RAC filter II.

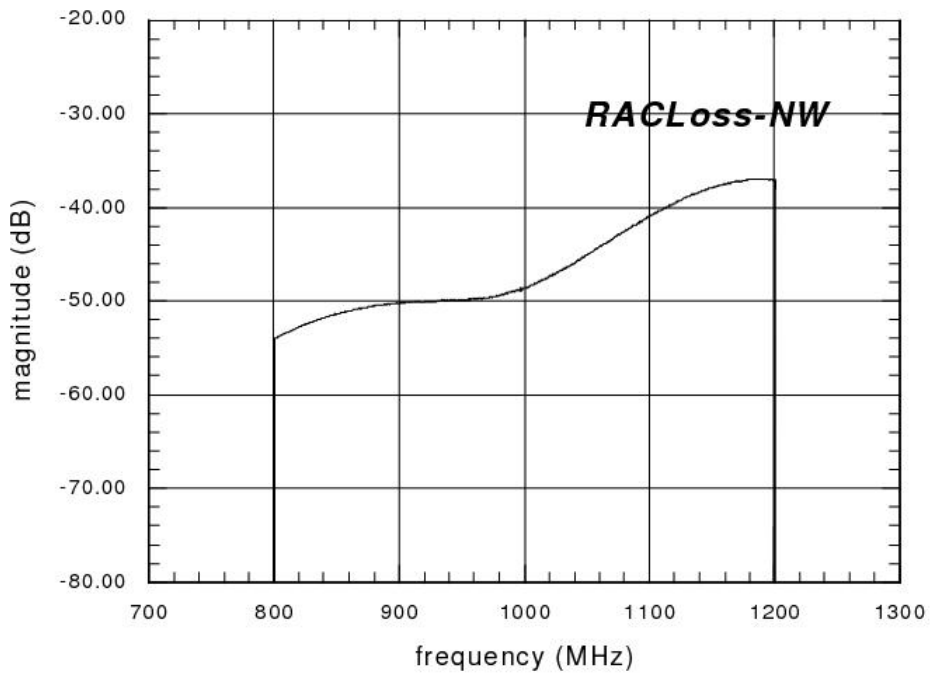


Figure 6.14: Synthesized insertion loss for RAC filter II before weighting is applied.

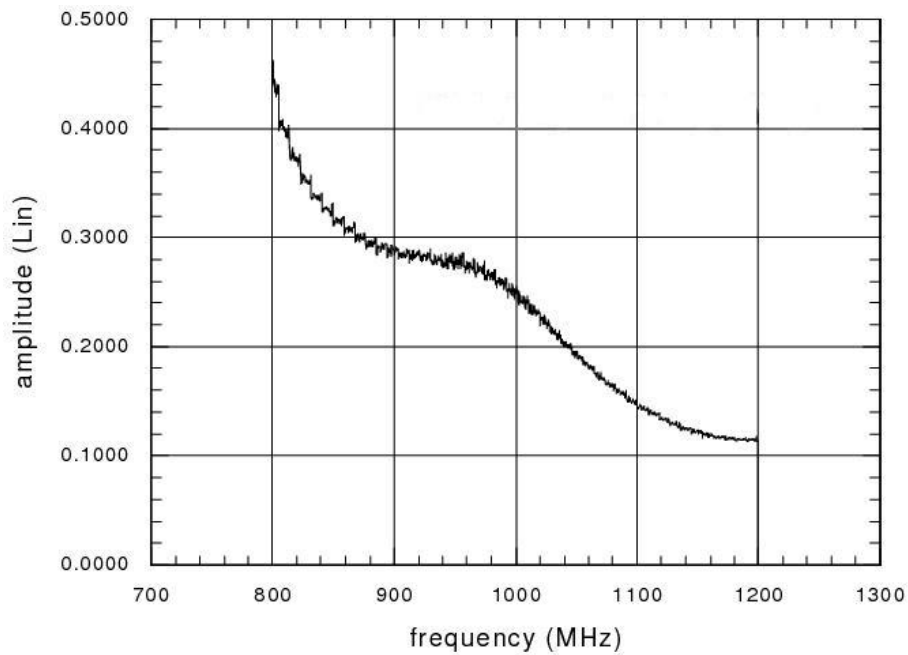
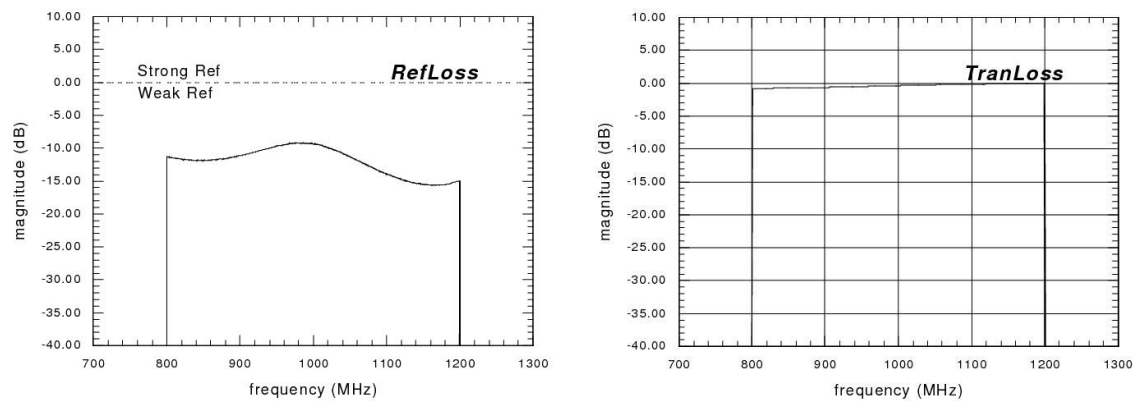


Figure 6.15: Optimized duty cycle profile of RAC filter II.



(a) Filter II groove array reflection loss simulation after the duty cycle weighting.

(b) Filter II groove array transmission loss simulation after the duty cycle weighting.

Figure 6.16: The simulated reflection loss and transmission loss of the groove array after the duty cycle profile of the groove array is optimized.

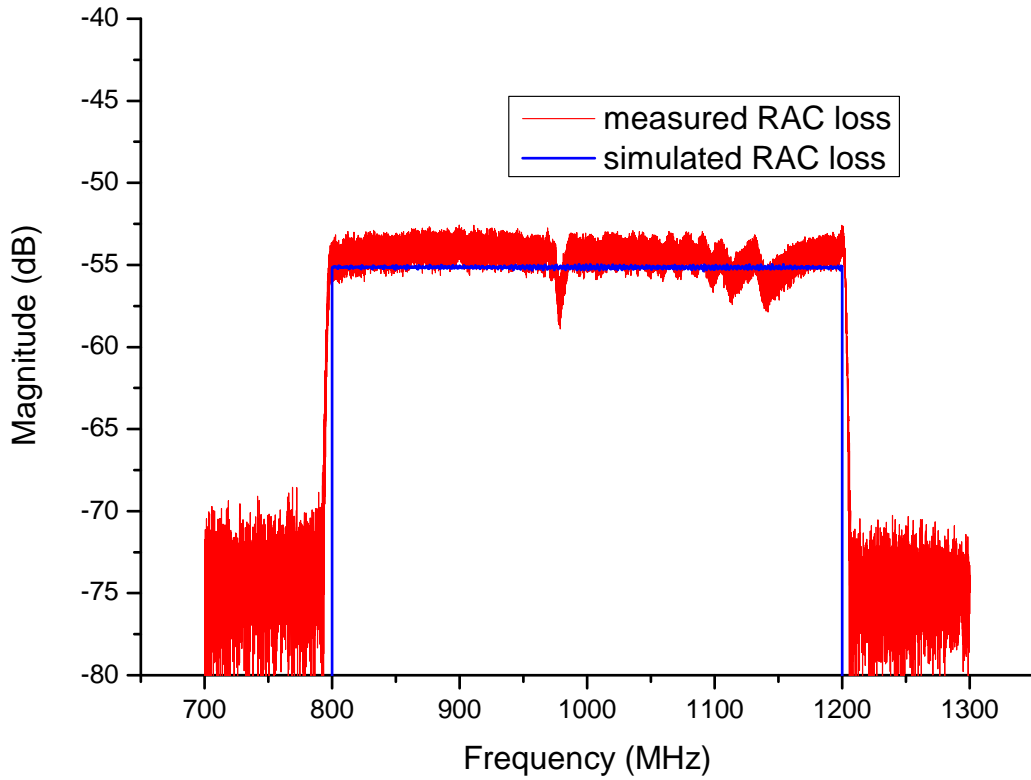


Figure 6.17: Comparison between the simulated (blue line) and measurement (red line) insertion loss of RAC filter II after the duty cycle profile of the groove array is optimized.

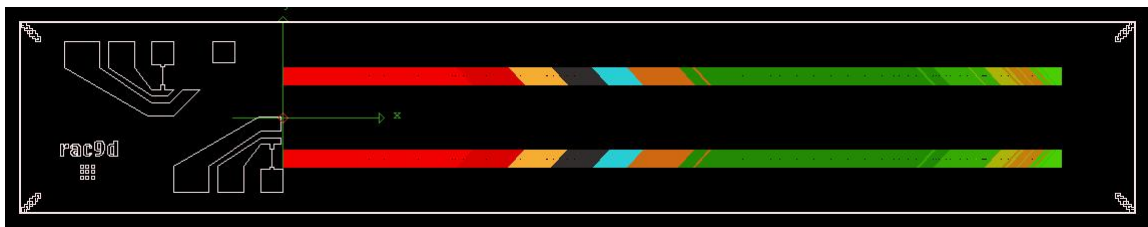
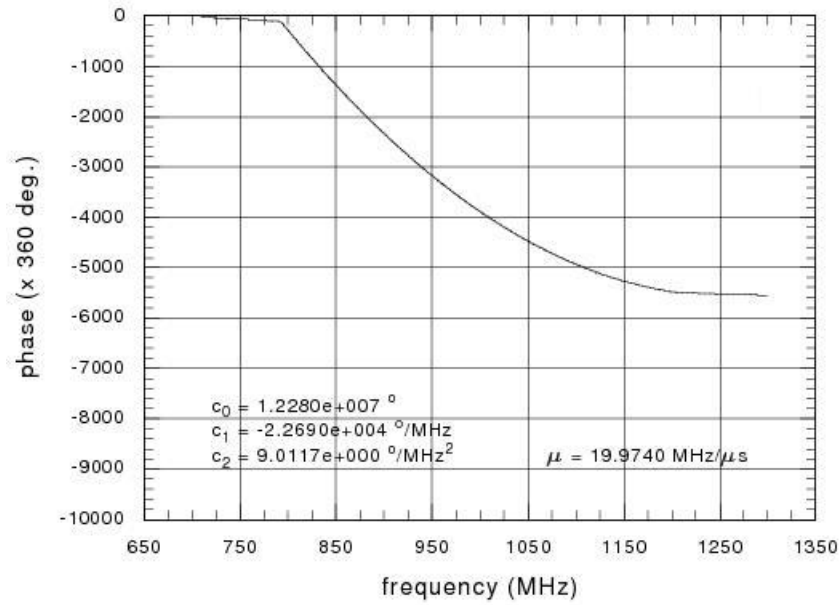
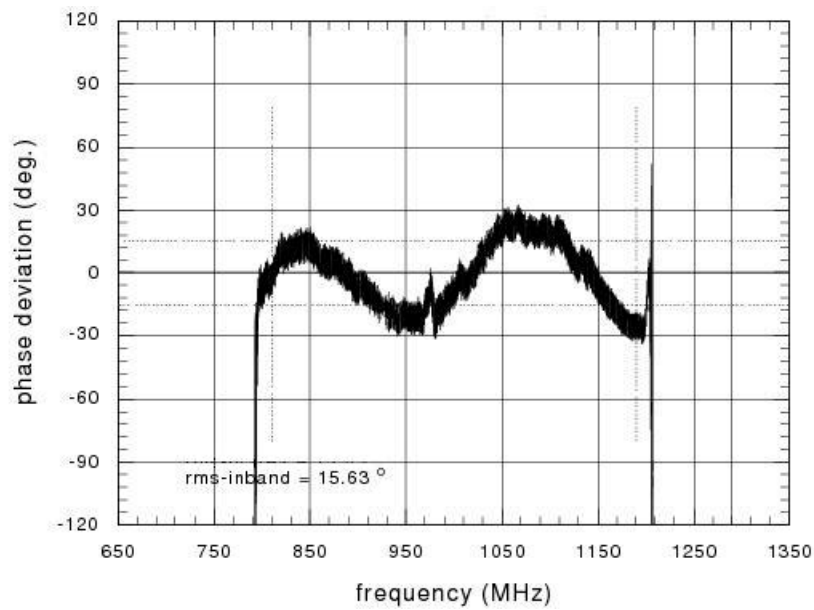


Figure 6.18: Layout of RAC filter II. Duty cycle dependent exposure dose is used in the lithography of weighted groove array. Each color in the layout represent a layer for a unique exposure dose.

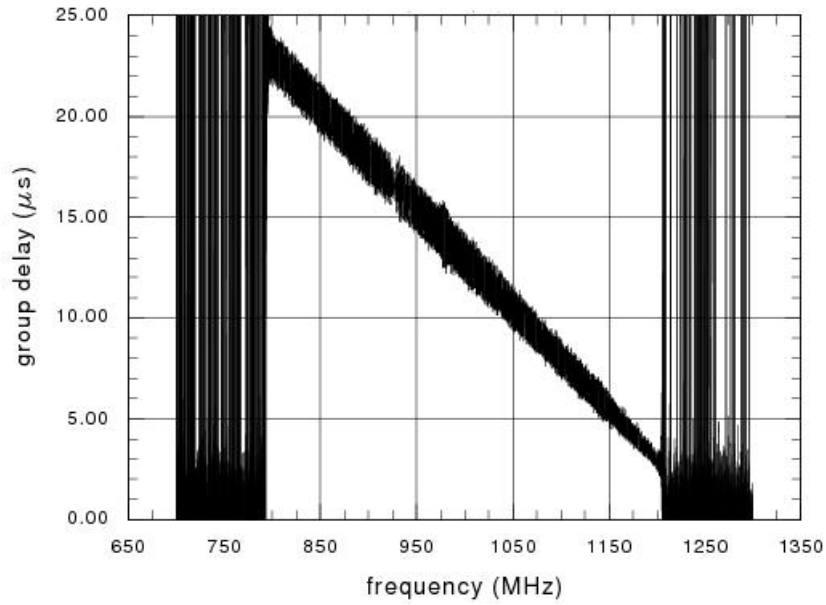


(a) Measured quadratic phase of RAC filter II.

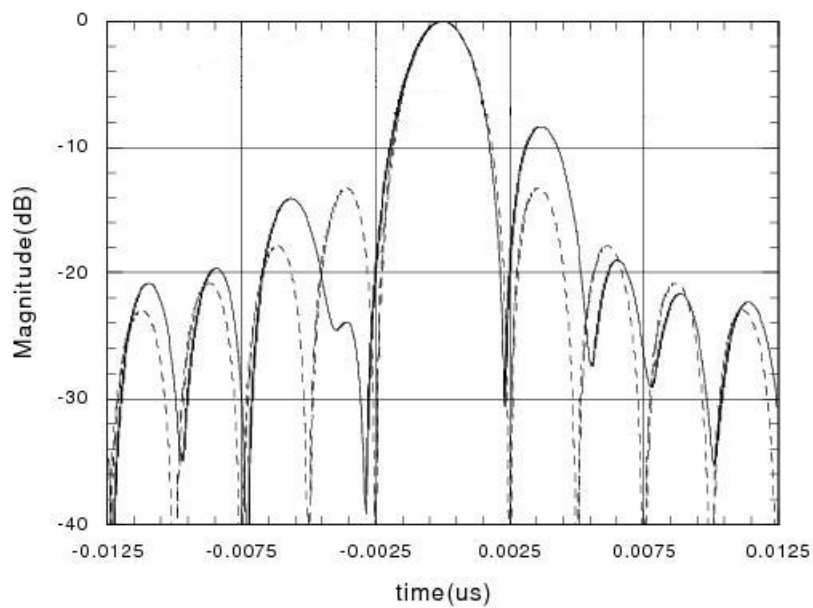


(b) Measured phase deviation from ideal quadratic dependency of RAC filter II. The root mean square value of the phase deviation in the 400MHz bandwidth is 15.63°.

Figure 6.19: Measured phase and phase deviation of RAC filter II.



(a) Measured linear chirp delay of RAC filter II.



(b) Calculated compressed pulse (in dB) from the response of RAC filter II. The pulse main lobe -3dB width is 2.216 ns, the ideal sinc function main lobe -3 dB width is 2.213 ns.

Figure 6.20: Measured group delay and compressed pulse of RAC filter II.

7 Summary and conclusion

7.1 Estimation of available RAC parameters on YZ-LiNbO₃

7.1.1 The maximum bandwidth on YZ-LiNbO₃

For down chirp filter fabricated on YZ-LiNbO₃, the maximum realizable bandwidth is determined by the piezoelectric material's electrical-mechanical coupling coefficient K_e^2 as shown in Equation 7.1 [13].

$$\left(\frac{B_{opt}}{f_c}\right)_{-3\text{ dB}} = \frac{1}{N_{opt}} = \sqrt{1.4355 \cdot K_e^2} \quad (7.1)$$

This equation is the approximation of the optimized bandwidth of the matched IDT on certain material. If we take the value for $K_e^2 = 4.5\%$ on YZ-LiNbO₃, the maximum fractional bandwidth can be calculated as follows $\frac{B_{opt}}{f_c} \approx 25\%$.

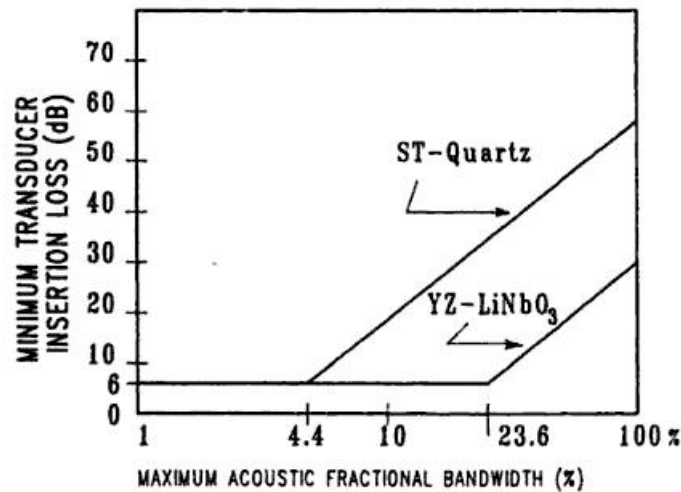


Figure 7.1: Theoretical maximum acoustic fractional bandwidth (%) versus insertion loss, for SAW filters with bidirectional IDTs on ST-quartz and YZ-LiNbO₃ [14].

For the matched bidirectional IDT with bandwidth less than this value, the insertion loss is rather small with only a 6 dB bidirection loss and other small loss items such as propagation loss etc. When the bandwidth of the IDT pair required is larger than this value, the insertion loss will increase (see Figure 7.1). So in order to find the trade-off between the bandwidth and the insertion loss, the number of finger pairs in the IDT needs

to be decided carefully. Therefore, for the estimation of the largest bandwidth of RAC type filter, if we use the center frequency $f_c = 1.5$ GHz, then for the 25% optimized fractional bandwidth, the bandwidth could be $B_{max} = f_c \cdot 25\% \approx 400$ MHz.

In Appendix A.3, $B = 700$ MHz, $f_c = 1.35$ GHz pair reverted IDT is used. It is already beyond the optimized maximum bandwidth, so sacrifice on the insertion loss is unavoidable (insertion loss is -47 dB for IDT at $f = 1.7$ GHz). After the duty cycle amplitude weighting, the magnitude for this $B = 700$ MHz, $T = 10 \mu s$ and $f_c = 1.35$ GHz RAC filter can be -56 dB, it is already very low. So for using the large bandwidth uniform IDT in the RAC, the dispersive delay can hardly be extended any more. Some special type of large bandwidth and very low loss transducer design (e.g. single phase unidirectional IDT) is needed, which will be discussed in the future work section.

7.1.2 The maximum dispersive delay on YZ-LiNbO₃

The maximum dispersive delay of the RAC type filter is determined by the maximum achievable chip size and also by the acceptable SAW propagation loss. If we use the 4 inches YZ-LiNbO₃ wafers, which is the largest size that is possible to be installed in our e-beam lithography machine EBPG5000+ in PTB. The diameter of the 4 inches wafer is about 100 mm, so the maximum usable length on the wafer can be about 80 mm; then, we can estimate the largest achievable dispersive delay for RAC type filters on 4 inch YZ-LiNbO₃ wafers as follows:

$$T_{max} = \frac{2 \cdot L_{max}}{v_p} = \frac{2 \cdot 80mm}{3488m/s} \approx 45\mu s$$

7.1.3 The maximum time bandwidth product (BT) on YZ-LiNbO₃

Several kinds of RAC setups are simulated in Chapter 6 and Appendix A, two types were developed (as shown in Chapter 6). It is possible to develop another three types with performances simulated as shown in Appendix A from A.1 to A.3.

In Appendix A.2 for the $B = 400$ MHz, $T = 40 \mu s$ and $f_c = 1$ GHz down chirp RAC filter, in order to have a rectangular passband, very heavy duty cycle amplitude weighting is needed. For using the duty cycle weighting profile obtained in A.2, the smallest groove width in the perpendicular groove direction will be only about 100 nm:

$$w_{min} = \frac{3.488 \mu m/ns}{1.2 GHz} \cdot 5\% \cdot \frac{1}{\sqrt{2}} \approx 100nm$$

For the high frequency end grooves after 5% duty cycle weighting, this is too small and already very close to the 10 nm critical dimension for e-beam lithography. The groove width would be very difficult to control in real fabrication at that scale. So we can see that for the time bandwidth product of the 1GHz center frequency RAC filter, $BT = 16\ 000$ is already on the boundary of the fabrication limitations for using e-beam lithography.

7.2 Future work

For the future of larger bandwidth, larger dispersive delay and less insertion loss dispersive delay lines, the following work in other directions can still be tried.

1. From Equation 7.1, the IDT optimized bandwidth is determined by the electro-mechanical coupling coefficient of the piezoelectric substrate material. Therefore, using large electro-mechanical coupling coefficient materials would be very interesting. From some of the publications [60; 61; 62], potassium niobate (KNbO₃) is favoured by many researchers, as its K_e^2 can reach up to about 53%, which is roughly more than 10 times the value of LiNbO₃. So theoretically the maximum fractional bandwidth of IDT on KNbO₃ could reach up to 87%. However, the 4 inch wafers for KNbO₃ are not available yet commercially. Also before building RAC devices on it, there will be many other problems to be studied relating the design of the reflective array.
2. To find ways of reducing propagation loss, one of the possibilities could be to make filters working in extremely low temperatures.

From the filter magnitude optimization simulations shown in Chapter 6 and Appendix A, we can see that as the dispersive delay of the filter increases, the propagation loss item increases drastically. It becomes a dominant item in the whole RAC insertion loss when the dispersive delay is long (i.e. $T \geq 20\mu\text{s}$).

This part of the insertion loss is caused by the interactions between the SAW phonons and thermal lattice wave of the crystal. If the filter is working at extremely low temperatures of about only several K (e.g. 4.2 K for liquid helium environment), then the thermal lattice wave of the crystal will be very weak, and the scattering of the SAW phonons by the thermal lattice wave will be small, and this will lead to a very small SAW propagation loss. With a small intrinsic SAW propagation loss item, the insertion loss of the dispersive delay line can be greatly reduced, especially for the very long dispersive delay RAC filters. Also, when the temperature is low enough (e.g. 4.2 K), due to the superconducting effect, the ohmic loss of the IDT fingers can disappear. Then the thickness of the IDT can be very thin and the aperture of the IDT could be as wide as we need without introducing more losses by the finger ohmic resistance.

Nowadays, the low temperature environment is more and more easily realizable. Also the mass and volume of the cooling machines are becoming smaller and smaller, mini portable cooling machines are already used in some high temperature superconducting antennas and transmission line filters [82]. Therefore, the low temperature RAC filters may become very practical in the future. For space applications it may be very interesting especially to take advantage of the low temperature environment available in outer space for the instruments.

3. In currently used IDTs, due to the very large bandwidth required, the number of finger pairs is very small. This leads to a large transduction loss of the IDT, usually about -30 dB (see Chapter 6 and Appendix A) and more. For the total RAC insertion loss, it is around the level of -50 dB, and we can see that the IDT loss item contributes about 60%. It should, therefore, definitely be reduced.

One of the options could be using SPUDT (Single Phase UniDirectional Transducer) [65] [66]. This kind of transducer could eliminate the -6 dB bidirectional loss of the bidirectional interdigital transducers. The basic principle is to insert a reflector in each period of the IDT, then the SAW generated on one direction is reflected

back by several percent in each period. For a certain number of periods, the total reflectivity of the IDT to one direction could be quite high even approaching 100%, then the -6 dB bidirection loss is greatly reduced. The disadvantage is that in order to reach such a high reflectivity to a certain direction, the number of periods must be large (assuming we have a fixed reflectivity in each period), otherwise it is hard to get certain unidirectivity, and this will lead to reduced bandwidth of the transducer (for SPUDT the fractional bandwidth is normally only about 5%). So dispersive SPUDT structures [63] are needed to obtain a quite wide bandwidth. Some structures can be studied, such as chirp SPUDT or fan SPUDT; these structures may satisfy our requirements for large bandwidths without sacrificing the insertion loss very much.

However, other problems may arise using the two structures mentioned above: for chirp SPUDT on YZ-LiNbO₃, the BAW scattering might be quite high for SAW propagating under the inactive electrodes (especially for the up chirp IDT), this needs to be verified experimentally and needs to be circumvented; and for fan SPUDT, the design of the reflective array will be quite difficult.

4. To reduce the SAW propagation loss for long dispersive delay chirp filter, another method that could be using very fast SAW velocity materials, such as sapphire, yttrium aluminium garnet (YAG) and diamond. For example, the SAW velocity can reach up to about 6000 m/s on sapphire and 9000 m/s on diamond. These materials have very low propagation losses of the SAW. For example for sapphire, the propagation loss of the SAW at 1 GHz is only about 1/5 of the loss on YZ-LiNbO₃.

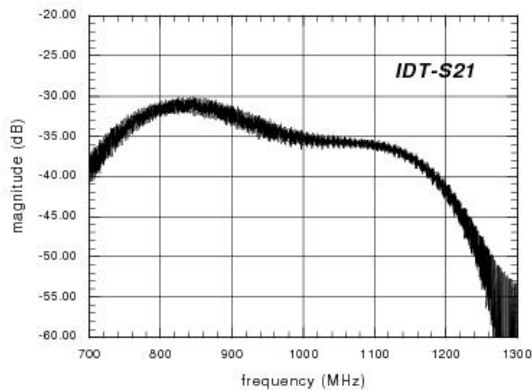
However, the materials mentioned above, have cubic symmetry, the electro-mechanical coupling coefficients being zero. Therefore, strong piezoelectric films are needed to excite the SAW on these substrates, such as LiNbO₃ and KNbO₃. Very special film deposition techniques are needed to deposit these piezoelectric films ideally with monocrystals. Tools like chemical vapor deposition (CVD) can be used for the fabrication of such LiNbO₃ and KNbO₃ films.

A Magnitude optimization of RACs (simulations)

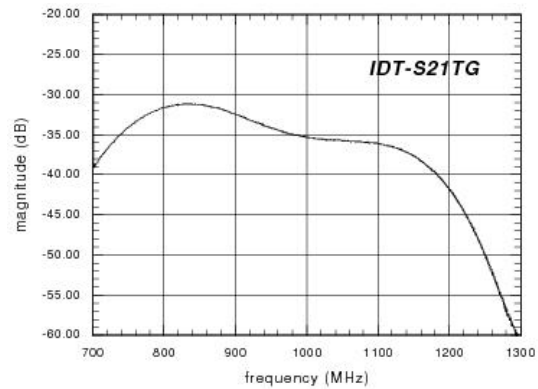
A.1 $B = 400$ MHz, $T = 30$ μ s, $f_c = 1$ GHz RAC

IDT design: $f_c = 1$ GHz, $B_f = 8$, $W = 960$ μ m, PRT, as in Figure 3.3. Groove array design: uniform depth: 30 nm, optimized groove duty cycle.

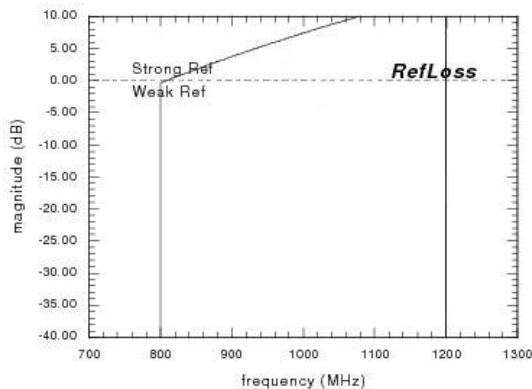
Filter specification: $B = 400$ MHz, $T = 30$ μ s, $f_c = 1$ GHz, down chirp; Insertion loss: IL = -57 dB as shown in Figure A.2d.



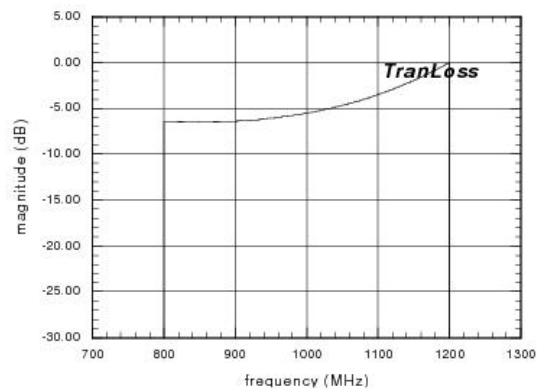
(a) Measured IDT S_{21} magnitude.



(b) Time gated IDT S_{21} magnitude.



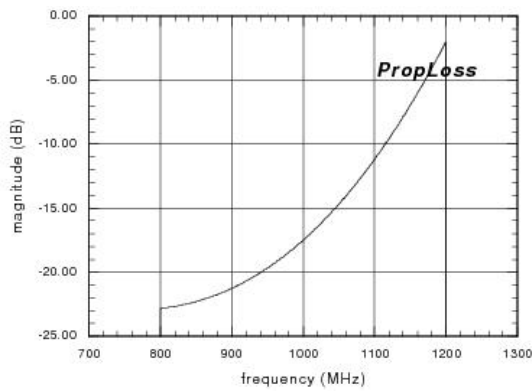
(c) Unweighted groove array reflection loss.



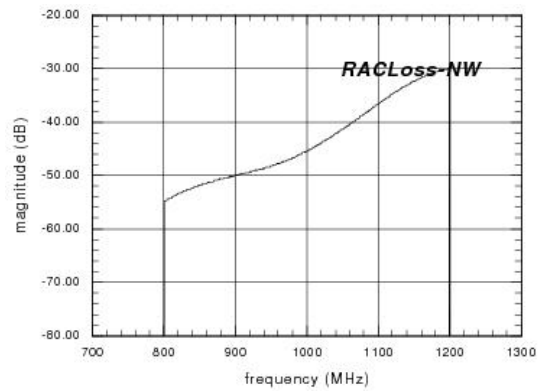
(d) Unweighted groove array transmission loss.

Figure A.1: Magnitude optimization for $B = 400$ MHz, $T = 30$ μ s, $f_c = 1$ GHz RAC filter (part 1).

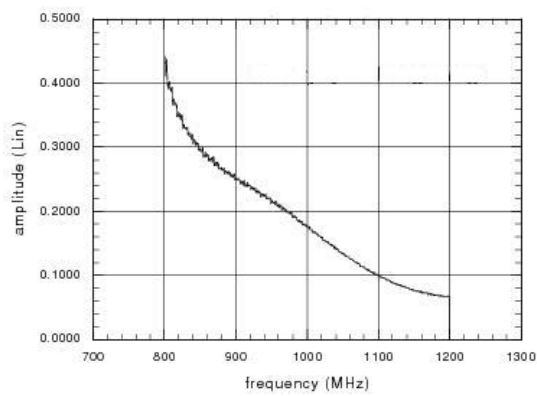
A Magnitude optimization of RACs (simulations)



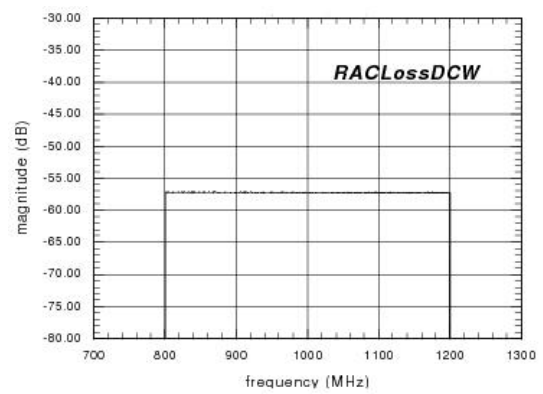
(a) SAW propagation loss.



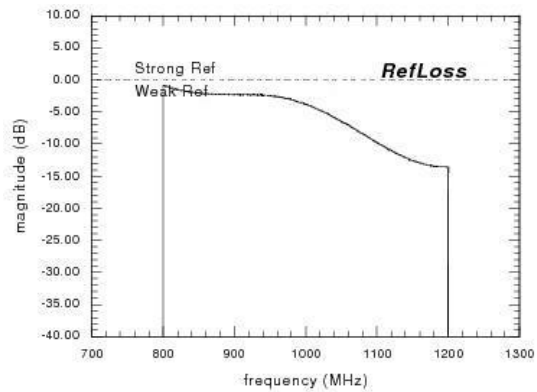
(b) Unweighted RAC insertion loss.



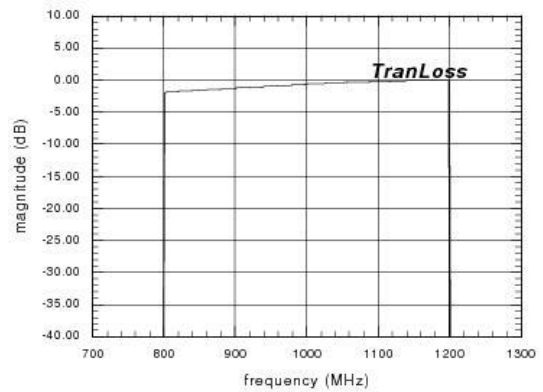
(c) Duty cycle profile.



(d) RAC insertion loss after duty cycle weighting.



(e) Reflection loss of weighted groove array.



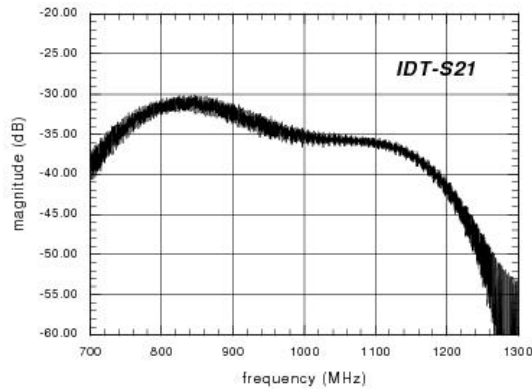
(f) Transmission loss of weighted groove array.

Figure A.2: Magnitude optimization for $B = 400$ MHz, $T = 30 \mu\text{s}$, $f_c = 1$ GHz RAC filter (part 2).

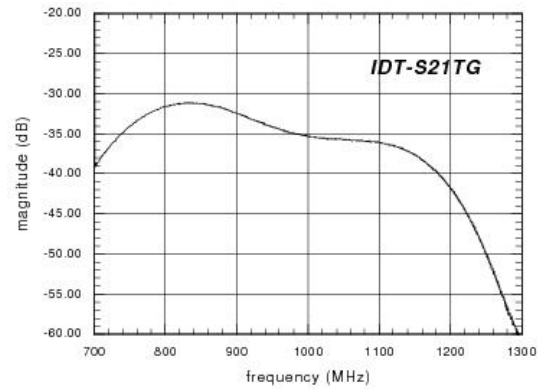
A.2 $B = 400 \text{ MHz}$, $T = 40 \mu\text{s}$, $f_c = 1 \text{ GHz}$ RAC

IDT design: $f_c = 1 \text{ GHz}$, $B_f = 8$, $W = 960 \mu\text{m}$, PRT, as in Figure 3.3. Groove array design: uniform depth: 30 nm, optimized groove duty cycle.

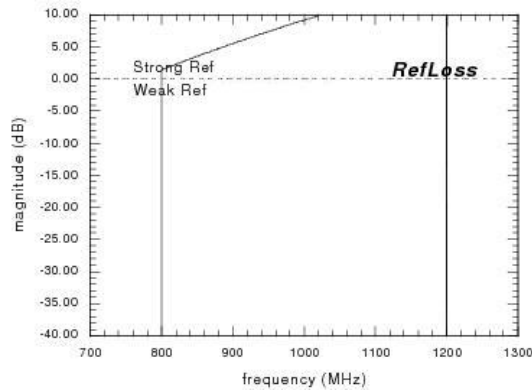
Filter specification: $B = 400 \text{ MHz}$, $T = 40 \mu\text{s}$, $f_c = 1 \text{ GHz}$, down chirp; Insertion loss: IL = -63 dB as shown in Figure A.4d.



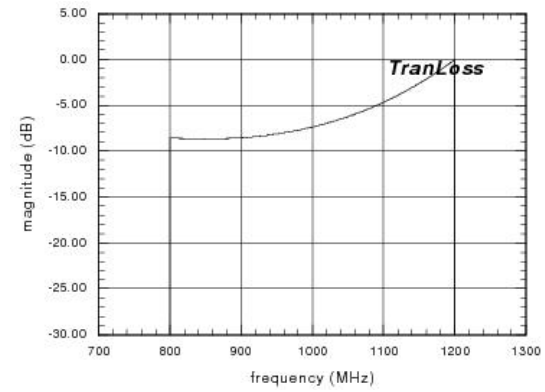
(a) Measured IDT S_{21} magnitude.



(b) Time gated IDT S_{21} magnitude.



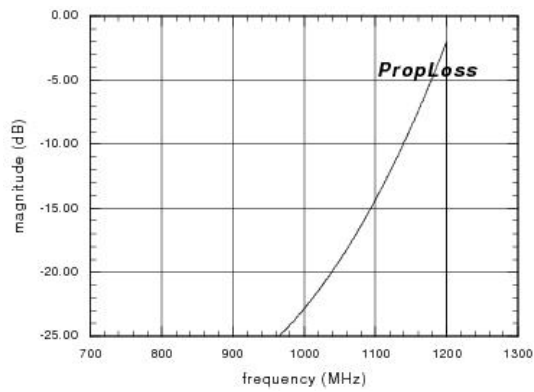
(c) Unweighted groove array reflection loss.



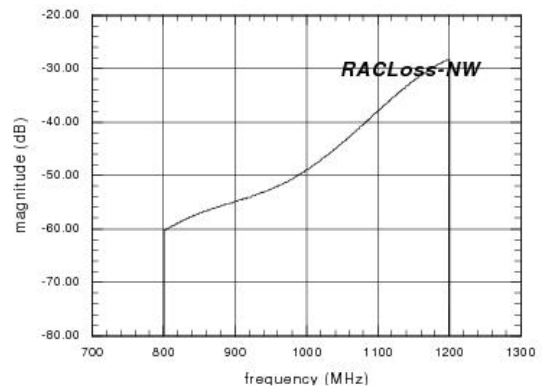
(d) Unweighted groove array transmission loss.

Figure A.3: Magnitude optimization for $B = 400 \text{ MHz}$, $T = 40 \mu\text{s}$, $f_c = 1 \text{ GHz}$ RAC filter (part 1).

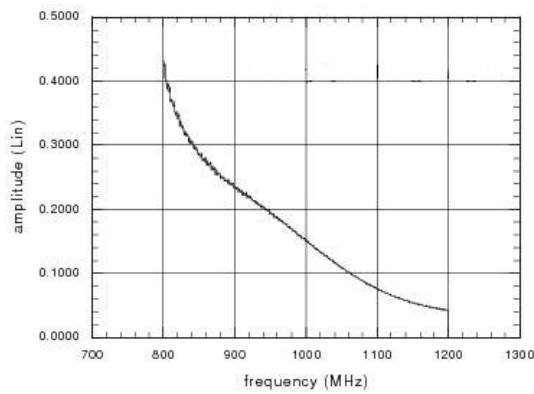
A Magnitude optimization of RACs (simulations)



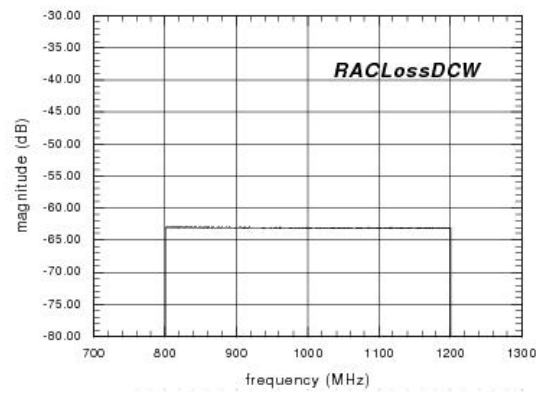
(a) SAW propagation loss.



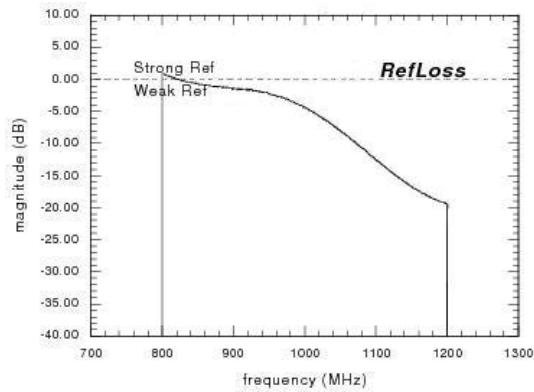
(b) Unweighted RAC insertion loss.



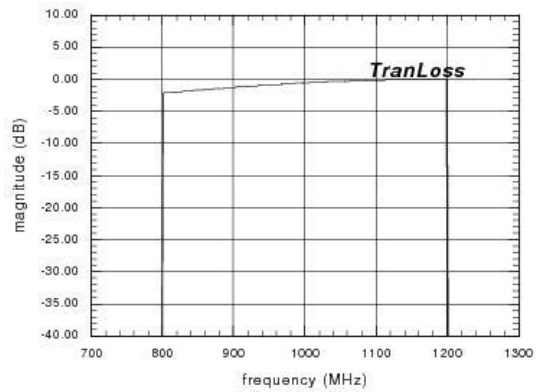
(c) Duty cycle profile.



(d) RAC insertion loss after duty cycle weighting.



(e) Reflection loss of weighted groove array.



(f) Transmission loss of weighted groove array.

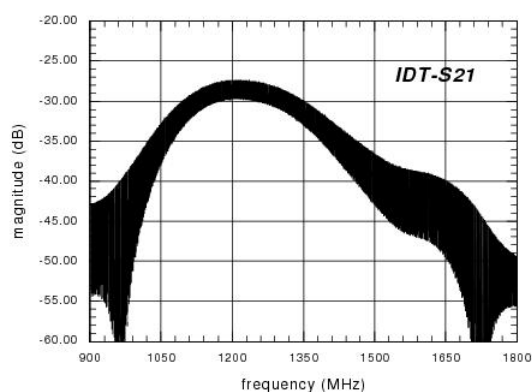
Figure A.4: Magnitude optimization for $B = 400$ MHz, $T = 40 \mu\text{s}$, $f_c = 1$ GHz RAC filter (part 2).

A.3 $B = 700$ MHz, $T = 10$ μ s, $f_c = 1.35$ GHz RAC

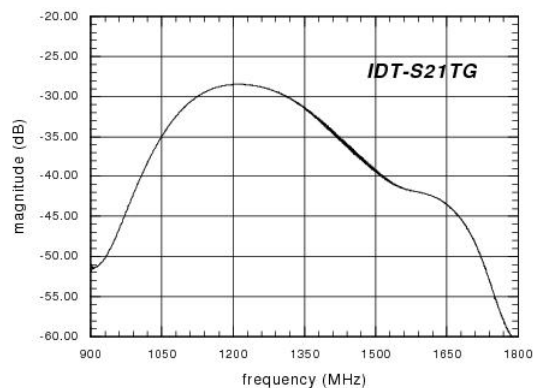
IDT design: $f_c = 1.35$ GHz, $N_f = 8$, $W = 960$ μ m, PRT, as in Figure 3.3. Groove array design: uniform depth: 40 nm, optimized groove duty cycle.

The PRT is simulated using FEM/BEM (supplied by Dr. Victor Plessky); Parasitic and matching: $C_{pak} = 1.0$ pF, $L_{series} = 10$ nH.

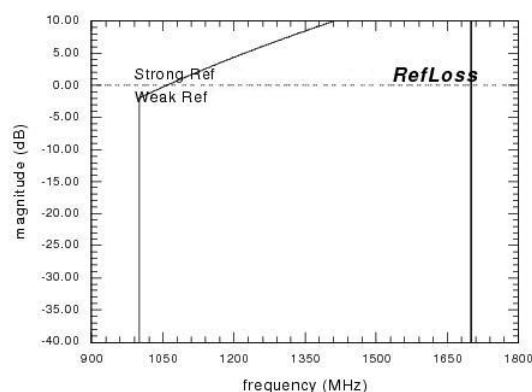
Filter specification: $B = 700$ MHz, $T = 10$ μ s, $f_c = 1.35$ GHz, down chirp; Insertion loss after duty cycle optimization: IL = -56 dB as shown in Figure A.6d.



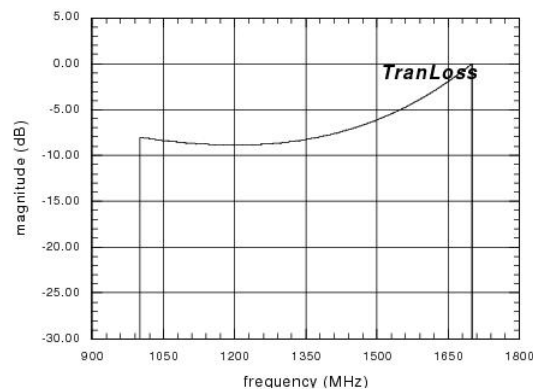
(a) Measured IDT S_{21} magnitude.



(b) Time gated IDT S_{21} magnitude.



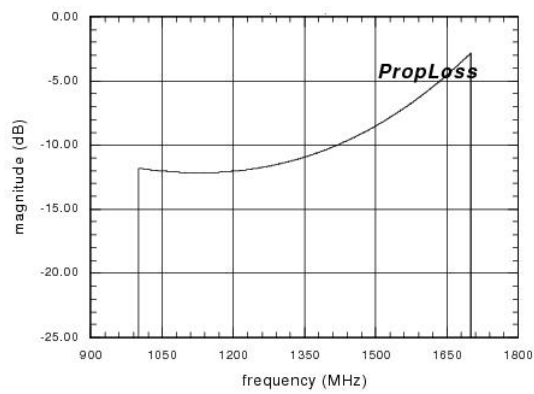
(c) Unweighted groove array reflection loss.



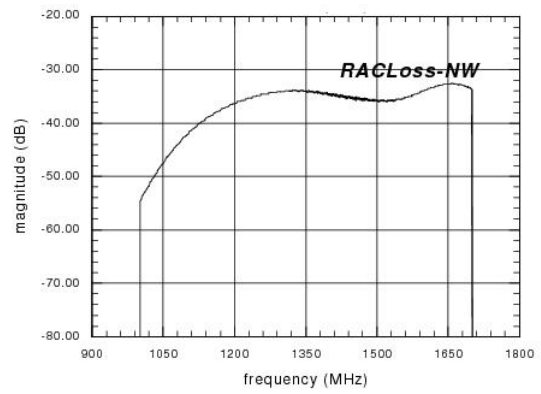
(d) Unweighted groove array transmission loss.

Figure A.5: Magnitude optimization for $B = 700$ MHz, $T = 10$ μ s, $f_c = 1.35$ GHz RAC filter (part 1).

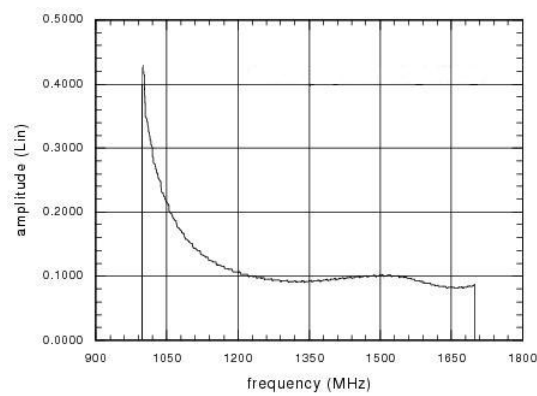
A Magnitude optimization of RACs (simulations)



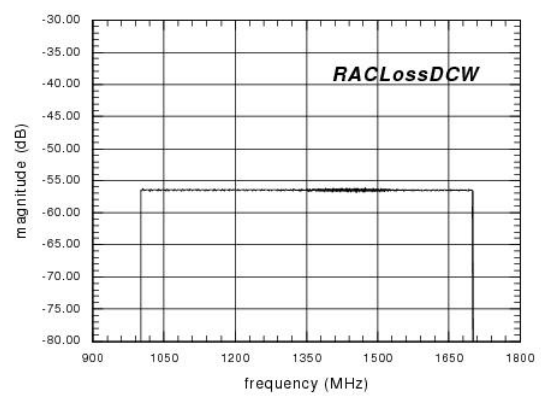
(a) SAW propagation loss.



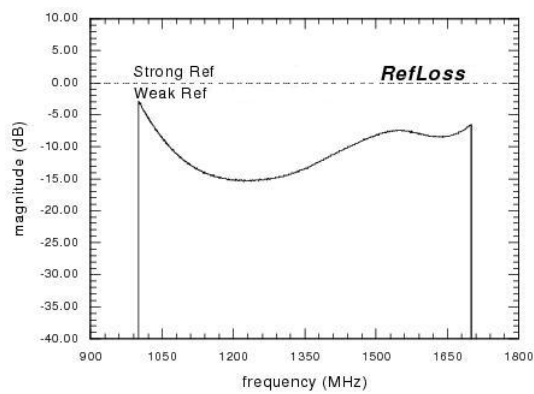
(b) Unweighted RAC insertion loss.



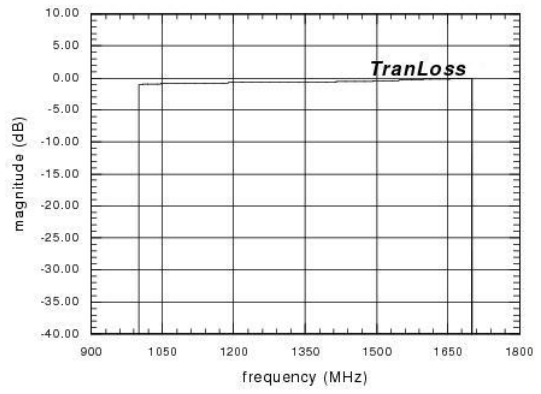
(c) Duty cycle profile.



(d) Unweighted RAC insertion loss.



(e) Weighted groove array reflection loss.



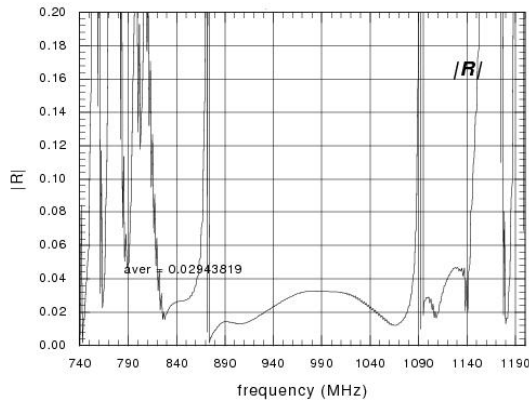
(f) Weighted groove array transmission loss.

Figure A.6: Magnitude optimization for $B = 700$ MHz, $T = 10 \mu\text{s}$, $f_c = 1.35$ GHz RAC filter (part 2).

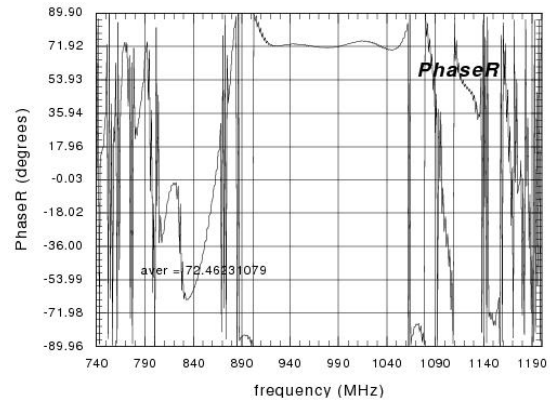
B Frequency dependent single electrode parameter extraction for TS1, TS2 and TS3 on 128° YX LiNbO₃

All the average values 'aver' are averaged in the frequency range from 950 MHz to 1050 MHz.

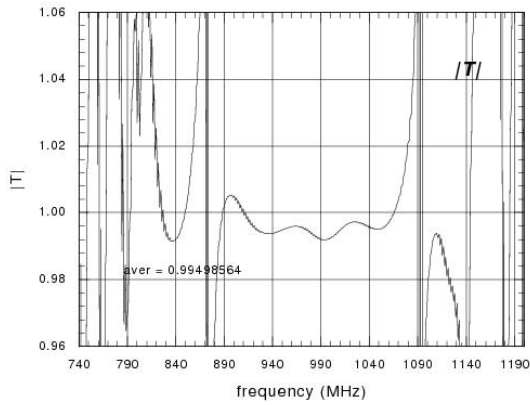
B.1 TS1, electrode: $a = 0.8 \mu\text{m}$, $a/p = 0.4$, $h = 100 \text{ nm}$



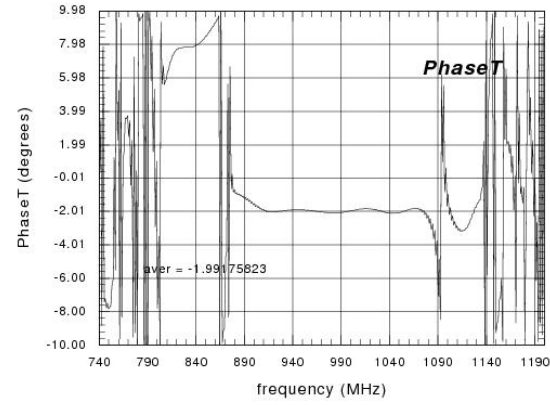
(a) Reflection coefficient magnitude r .



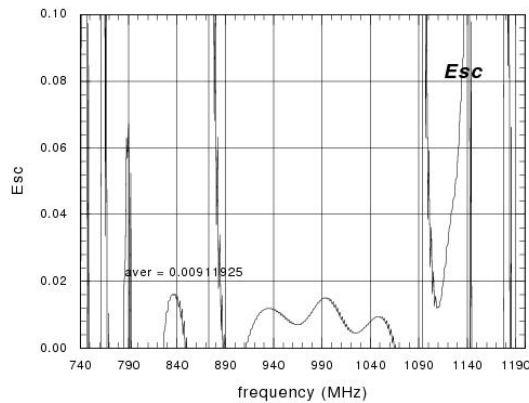
(b) Reflection coefficient phase Φ_R .



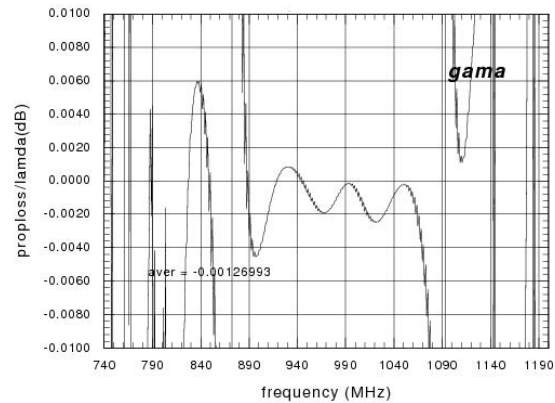
(c) Transmission coefficient magnitude t .



(d) Transmission coefficient phase Φ_T .



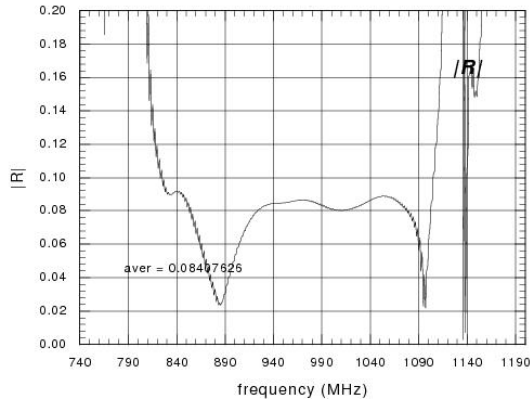
(e) Scattered energy $E_{sc} = 1 - r^2 - t^2$ to bulk wave.



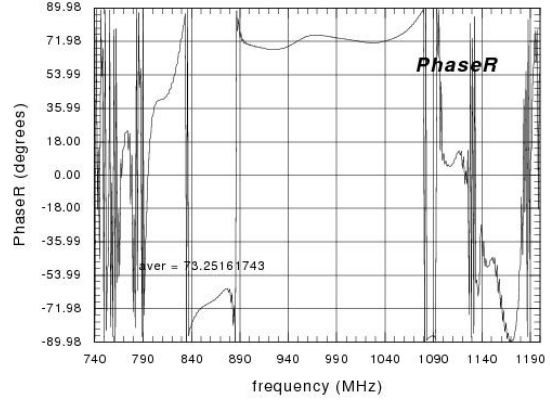
(f) Propagation loss coefficient in dB/λ .

Figure B.1: Parameter extractions from TS1 for floating electrode: $a = 0.8 \mu\text{m}$, $a/p = 0.4$, $h = 100 \text{ nm}$.

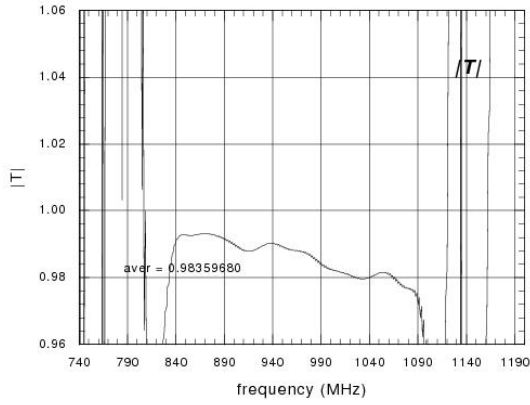
B.2 TS2, electrode: $a = 1.2 \mu\text{m}$, $a/p = 0.6$, $h = 200 \text{ nm}$



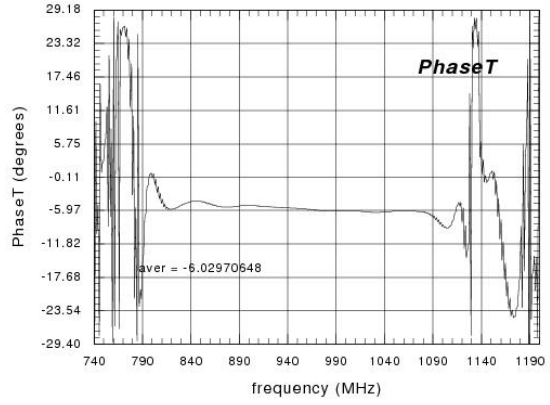
(a) Reflection coefficient magnitude r .



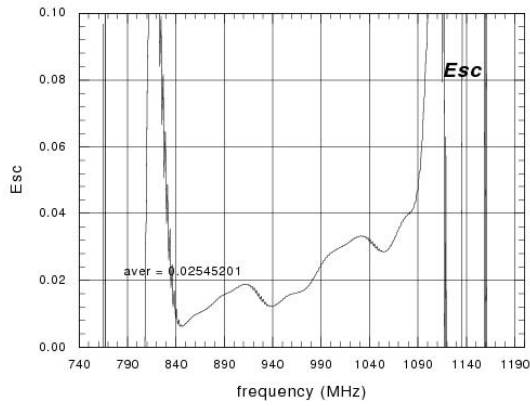
(b) Reflection coefficient phase Φ_R .



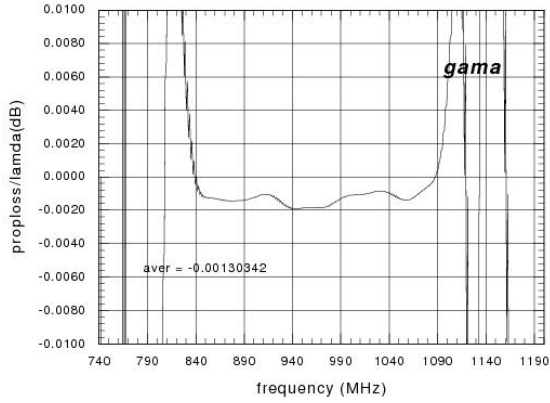
(c) Transmission coefficient magnitude t .



(d) Transmission coefficient phase Φ_T .



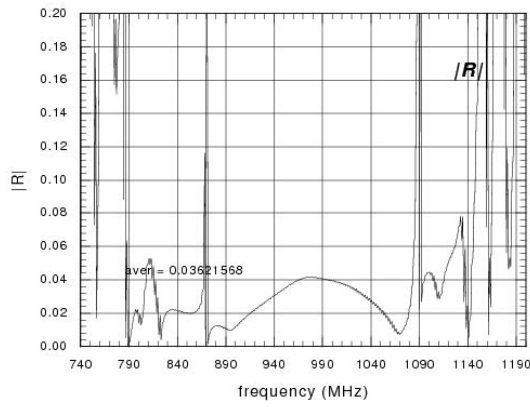
(e) Scattered energy $E_{sc} = 1 - r^2 - t^2$ to bulk wave.



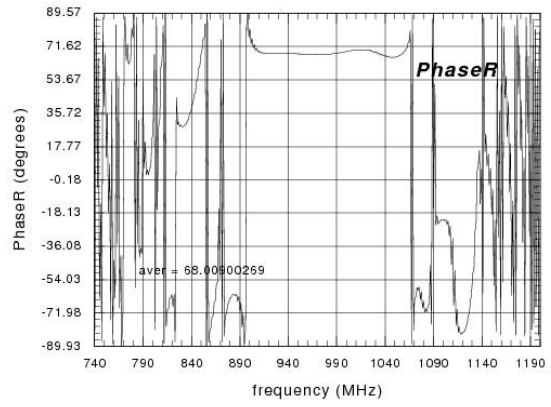
(f) Propagation loss coefficient in dB/λ .

Figure B.2: Parameter extractions from TS2 for floating electrode: $a = 1.2 \mu\text{m}$, $a/p = 0.6$, $h = 200 \text{ nm}$.

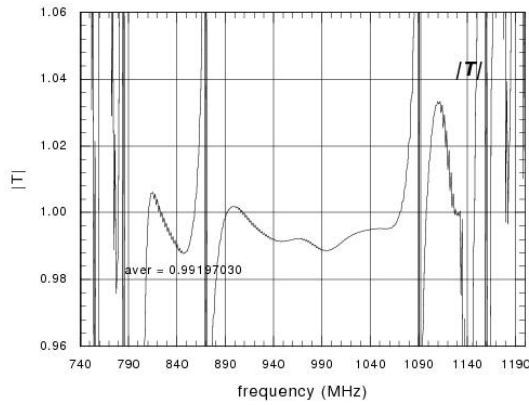
B.3 TS3, electrode: $a = 1.0 \mu\text{m}$, $a/p = 0.5$, $h = 100 \text{ nm}$



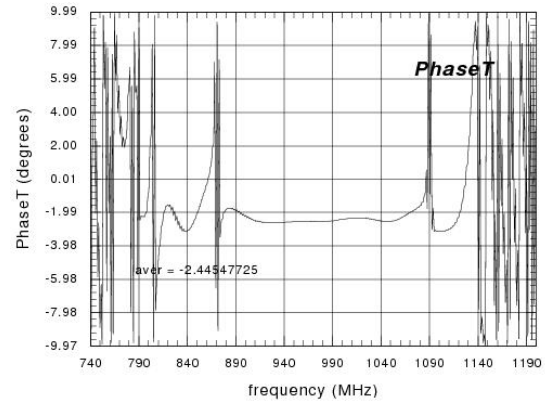
(a) Reflection coefficient magnitude r .



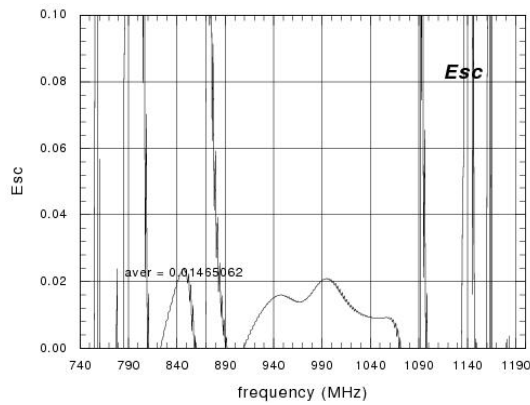
(b) Reflection coefficient phase Φ_R .



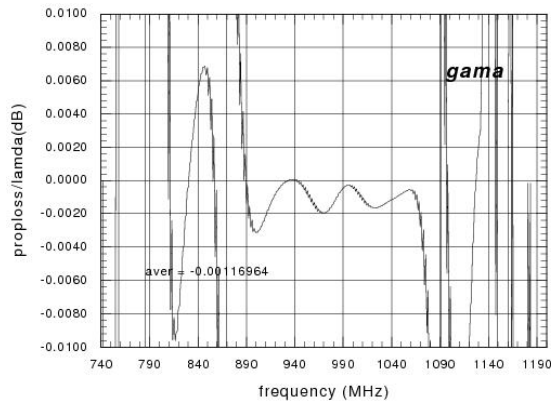
(c) Transmission coefficient magnitude t .



(d) Transmission coefficient phase Φ_T .



(e) Scattered energy $E_{sc} = 1 - r^2 - t^2$ to bulk wave.



(f) Propagation loss coefficient in dB/λ .

Figure B.3: Parameter extractions from TS3 for floating electrode: $a = 1.0 \mu\text{m}$, $a/p = 0.5$, $h = 100 \text{ nm}$.

C Electron beam lithography

C.1 Advantages and drawbacks of e-beam lithography

[80] Electron beam lithography (EBL) is the process of forming patterns by using a focused electron beam. Such a beam can be readily scanned and accurately positioned on the substrate to expose e-beam resist. The main advantages of EBL over optical lithography can be as follows:

1. EBL provides the ability to produce patterns with the critical dimension (CD) to about only 10 nm (single line) on a wafer, without the use of a mask and under control of a computer.
2. An e-beam can be used to accurately detect features on a substrate. This ability can be used to provide extremely accurate layer-to-layer registration.

The first advantage listed above is possible, because for the energies used in the EBL systems, the electrons' wavelengths are in the order of 0.02-0.05 nm. Hence, the diffraction effects which limit resolution in optical lithography (CD is about 60 nm) are avoided.

There are, however, still several drawbacks to the EBL including:

1. Its resolution is limited by the fact that the electrons are forward scattered in the resist and back scattered from the substrate. This results in exposure of the resist outside the desired areas. This kind of scattering will be discussed in detail in the last section.
2. EBL is very slow when compared to optical projection systems. As for the e-beam exposure, it is like drawing large patterns using an e-beam pencil with a spot size of around 25 nm, e.g. for a groove array pattern of the $T = 10 \mu\text{s}$ RAC filter, the typical exposure time is about 30 minutes using an EBPG5000+ lithography machine.

C.2 Building blocks of the EBPG5000+ electron beam lithography machine

The photograph of this lithography machine in the clean room center of PTB is shown in Figure C.1. The building blocks of the machine are shown in Figure C.2. From this block diagram we can see that there are seven main sub-systems for this device:

1. The electron source (electron gun). It is used to generate the electron beam with a certain current density for exposures.



Figure C.1: Photo of the EBPG5000+ e-beam lithography system in the clean room center of PTB.

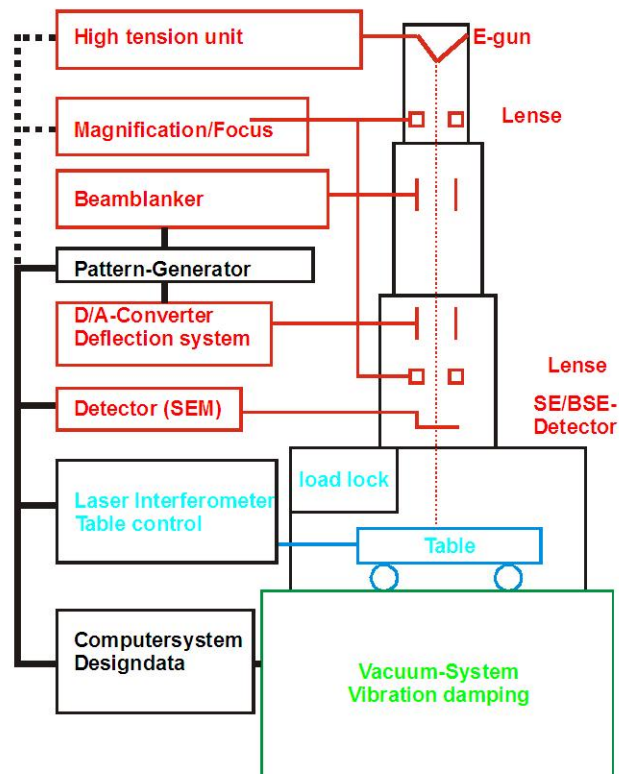


Figure C.2: Block diagram of the EBPG5000+ e-beam lithography system.

2. The magnification or focus lens. There are two levels of condenser lens to focus the e-beam into a small diameter spot to improve the resolution and to make the current

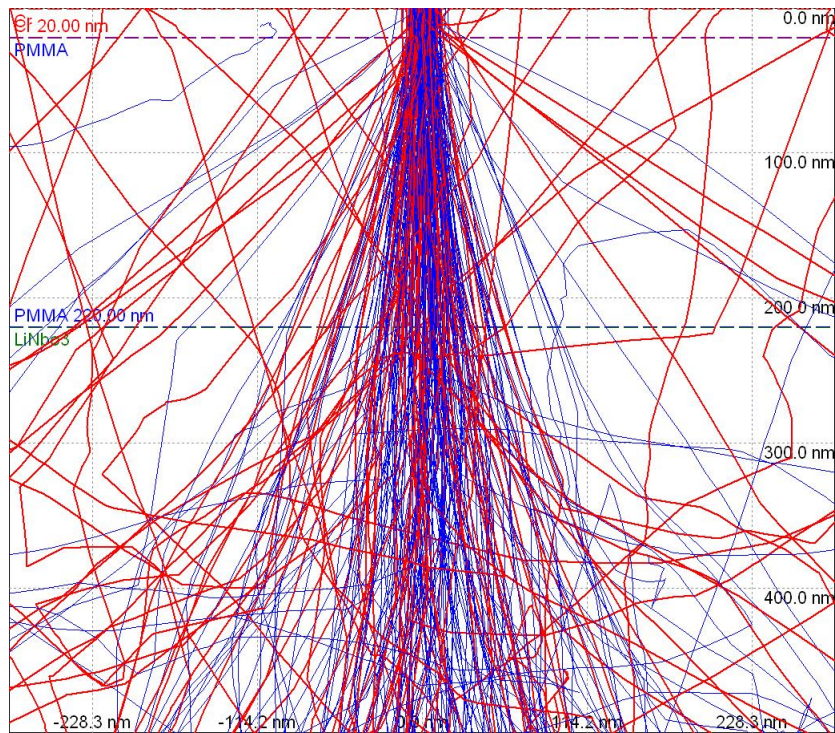
density in the small spot higher for reducing the resist exposing time.

3. Pattern generator controlled beam blanker and beam deflection system. The e-beam blanker is used to switch on or off the e-beam during exposures with requirements; and the beam deflection system will deflect the e-beam in a maximum $160\ \mu\text{m} \times 160\ \mu\text{m}$ area for exposure writing (the area is dependent on the exposure resolution and also the acceleration voltage; $160\ \mu\text{m} \times 160\ \mu\text{m}$ is when the resolution is 2.5 nm and the acceleration voltage is 50 kV). The deflection is controlled by a 16-bit digital to analog convertor (DAC) to have up to 2.5 nm addressing precision. The beam blanker and the deflection system are both under the control of the pattern generator according to the exposure patterns it has generated from layouts uploaded to the computer system.
4. The scanning electron microscope (SEM) detector is used to monitor the exposure process by the operator.
5. The wafer holder table holds the wafer, and when a maximum $160\ \mu\text{m} \times 160\ \mu\text{m}$ area for the deflection system is exposed, then the interferometer table control system will control the table to move the wafer to the next unexposed area in sub-nanometer precision.
6. The vacuum system for the working area supplies the exposure working vacuum condition, and the vibration damping system reduces the influence of the mechanical noises generated by the outside environment.
7. The computer system contains the required software interface for operating the whole system and handles the data analysis for the uploaded layout.

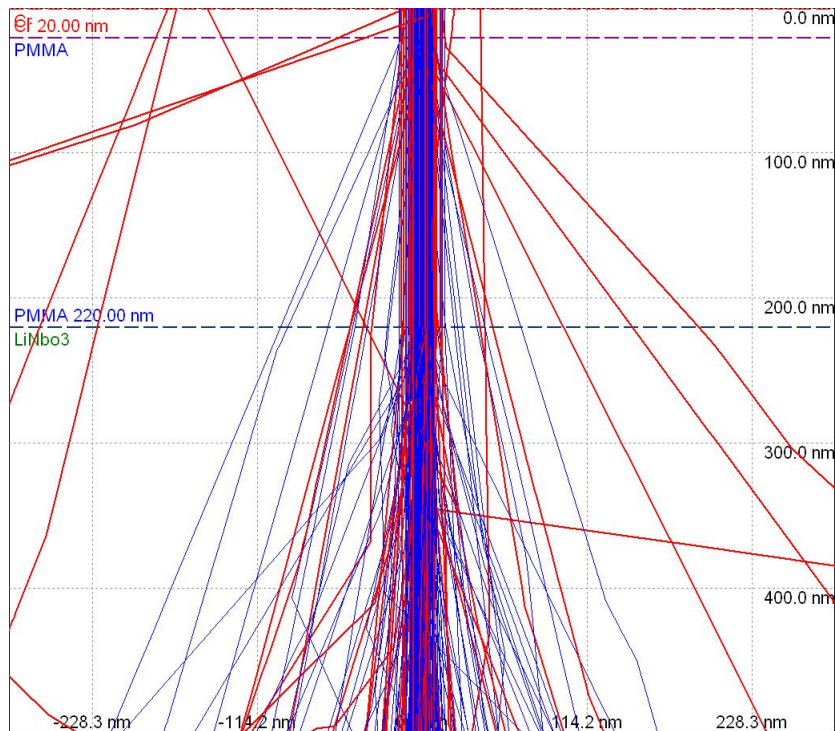
C.3 Electron scattering and proximity effect

During e-beam exposure the electrons entering the resist are scattered (forward and back) by interaction with the atoms of the resist and the substrate. Most of the electrons are forward scattered through small angles ($\leq 90^\circ$) from their original direction. This actually broadens the beam. Some of the electrons experience large-angle backscattering (e.g. $\geq 180^\circ$), causing them to return toward the surface. Figure C.3 and Figure C.4 shows the results of a Monte Carlo simulation (supplied by Dr. Thomas Weimann of PTB) of trajectories for 200 electrons projected on to the paper plane for 20 and 50 keV point sources with a 25 nm size.

Firstly we can see that the scattering broadens the incident electron beam in the resist (see Figure C.3). The broadening effect will put limitations on the density of the exposed structures. Therefore, in order to reduce this broadening effect, a higher acceleration voltage is used. For our exposure for the reflective groove array we usually use 50 kV rather than 20 kV. The difference of the broadening effect for the beam of 20 and 50 keV can be seen in Figure C.3. This results in a developed image wider than anticipated from the beam diameter alone. Such scattering is, thus, one of the mechanisms that limits the minimum linewidth.



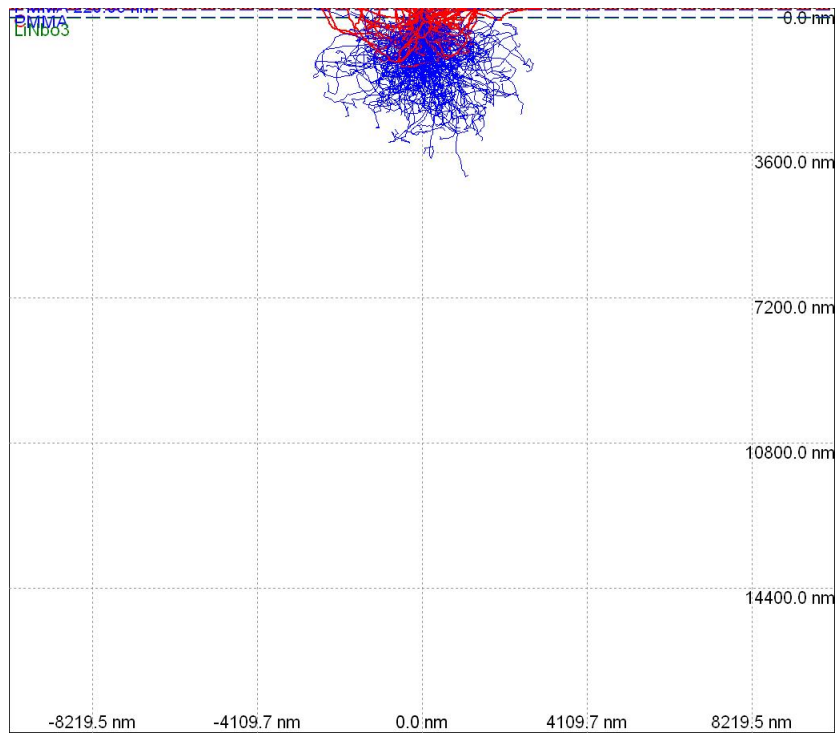
(a) Simulation for 20 keV electron beam.



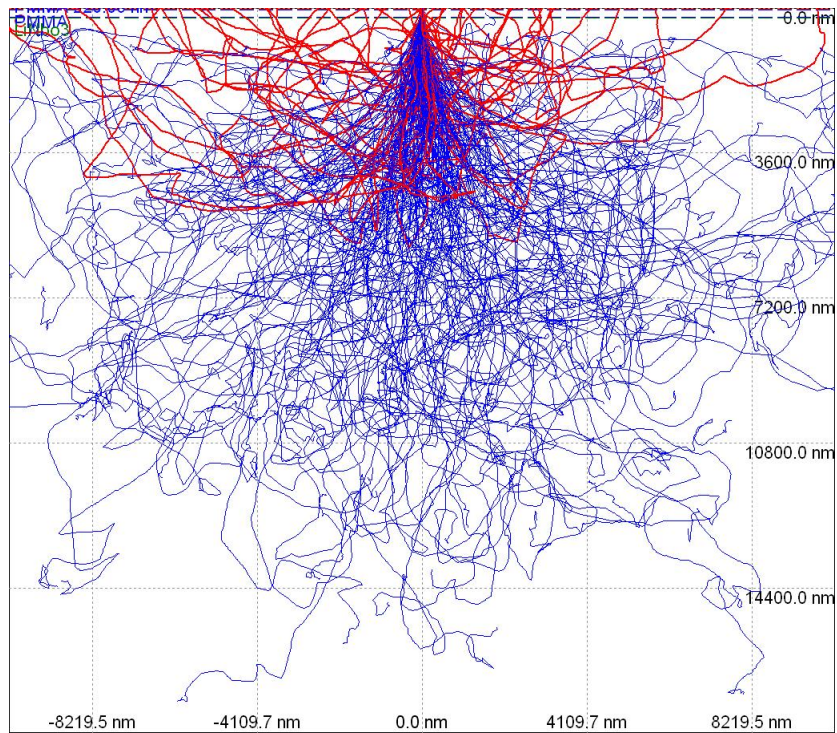
(b) Simulation for 50 keV electron beam.

Figure C.3: Monte Carlo simulation of trajectories for 200 electrons in Cr (20 nm)/PMMA (220 nm)/YZ-LiNbO₃ for 500 nm depth.

Secondly the electrons backscattered from the LiNbO₃ substrate return through the



(a) Simulation for 20 keV electron beam.



(b) Simulation for 50 keV electron beam.

Figure C.4: Monte Carlo simulation of trajectories for 200 electrons in Cr (20 nm)/PMMA (220 nm)/YZ-LiNbO₃ for 18 000 nm depth.

resist, contributing to additional resist exposures (see Figure C.4). Since the scattering

can extend over several microns, closely spaced patterns will receive electrons from the exposure of their neighbors; this is termed the proximity effect. Hence, for periodical patterns the minimum structure scale can only reach to about 40 nm. When using a 20 kV acceleration voltage (in Figure C.4 on the left), we can see that compared to a 50 kV acceleration voltage (in Figure C.4 on the right) the backscattering range is smaller but the electron density is higher. When using a 50 kV acceleration voltage, the proximity effect range is much wider, but the electron density of the backscattering is much lower, giving less exposures. This is also the reason for us to use the 50 kV acceleration voltage. The proximity effect forces us to vary the dose depending on the line width and also the density of the pattern. In other words, for the patterns with a very small line width and quite a high structure density, due to the proximity effect discussed above, it is not possible to get the required exposure using a uniform e-beam dose. That is the reason why we use a varying dose for exposures of the duty cycle weighted groove array described in the Section 4.3.3 of Chapter 4.

D Fabrication processes flow for RACs

	Process	Related Parameters
1	spin coating	PMMA: 200k 4%; spin: 2000 rpm, 90 s; bake: 160 °C, 600 s; $h = 220$ nm
2	spin coating	PMMA: 950k 2%; spin: 2000 rpm, 90 s; bake: 160 °C, 600 s; $h = 130$ nm
3	Cr evaporation*	chromium (Cr); rate: 0.2 nm/s; thickness: 30 nm
4	e-beam exposure	e-beam lithography using EBPG5000+; layout: markers
5	Cr etching	2 minutes in acid
6	develop	60 s in Glasgower** (developer) and 60 s in isopropanol (stopper)
7	markers evaporation	chromium (Cr), rate: 0.1 nm/s, thickness: 10 nm; gold palladium (AuPd), rate: 0.2 nm/s, thickness: 60 nm
8	lift off	one day in acetone
9	spin coating	PMMA: 200k 9%; spin: 2000 rpm, 90 s; bake: 160 °C, 1800 s; $h = 860$ nm
10	Cr evaporation	chromium (Cr); rate: 0.2 nm/s; thickness: 30 nm
11	e-beam exposure	e-beam lithography using EBPG5000+; layout: groove array
12	Cr etching	2 minutes in acid
13	develop	120 s in Glasgower (developer) and 120 s in isopropanol (stopper)
14	ion beam etching	Argon, pressure: 8 pa, ion beam current: 23 mA; etching rate: 0.12 nm/s; depth: determined by etching time according to design requirements. (physical bombardment etching)
15	lift off	one day in acetone
16	spin coating	PMMA: 200k 4%; spin: 2000 rpm, 90 s; bake: 160 °C, 600 s; $h = 220$ nm
17	spin coating	PMMA: 950k 2%; spin: 2000 rpm, 90 s; bake: 160 °C, 600 s; $h = 130$ nm
18	Cr evaporation	chromium (Cr); rate: 0.2 nm/s; thickness: 30 nm
19	e-beam exposure	e-beam lithography using EBPG5000+; layout: IDT
20	Cr etching	2 minutes in acid
21	develop	60 s in Glasgower (developer) and 60 s in isopropanol (stopper)
22	IDT evaporation	aluminium (Al); rate: 0.2 nm/s; thickness: 200 nm

continued on next page

D Fabrication processes flow for RACs

continued from previous page		
	Process	Related Parameters
23	lift off	one day in acetone
24	spin coating	PMMA: 200k 4%; spin: 2000 rpm, 90 s; bake: 160 °C, 600 s; $h = 220$ nm
25	dicing	automatic dicing saw; feeding: 1 mm/s; diamond blade rotating: 25000 rpm
26	lift off	one day in acetone
27	encapsulation	assemble the chip and case into a working filter
28	matching	adjust the matching network according to measurement
29	measure	measure the filter using VNA and analyze the phase deviation
30	spin coating	PMMA: 200k 4%; spin: 2000 rpm, 90 s; bake: 160 °C, 600 s; $h = 220$ nm
31	spin coating	PMMA: 950k 2%; spin: 2000 rpm, 90 s; bake: 160 °C, 600 s; $h = 130$ nm
32	Cr evaporation	chromium (Cr); rate: 0.2 nm/s; thickness: 30 nm
33	e-beam exposure	e-beam lithography using EBPG5000+; layout: phase plate
34	Cr etching	2 minutes in acid
35	develop	60 s in Glasgower (developer) and 60 s in isopropanol (stopper)
36	phase plate evaporation	aluminium (Al); rate: 0.2 nm/s; thickness: 50 nm
37	lift off	one day in acetone

Table D.1: Fabrication processes flow for RAC devices using lift-off technique and e-beam lithography

* In the above processes, the 30 nm Cr evaporations before every e-beam exposure are for two purposes: 1. To avoid charging on the substrate surface which will influence the height measurement for the e-beam system. 2. To make the substrate reflective and conductive for the electron beams.

** The composition of the ‘Glasgower’ developer is: 74.25% 2-propanol (IPA); 24.75% methyl-4-pentanone (MIBK); 1% ethyl-methyl-keton (MEK).

E Transformation between S, Y and Z parameters [81]

1. Transformation from the S parameter to the Z parameter.

$$Z_{11} = Z_0 \frac{(1 + S_{11})(1 - S_{22}) + S_{12}S_{21}}{\Psi_1}$$

$$Z_{22} = Z_0 \frac{(1 - S_{11})(1 + S_{22}) + S_{12}S_{21}}{\Psi_1}$$

$$Z_{12} = Z_0 \frac{2S_{12}}{\Psi_1}, \quad Z_{21} = Z_0 \frac{2S_{21}}{\Psi_1}$$

In the above equations: $Z_0 = 50\Omega$ is the characteristic impedance of the system and

$$\Psi_1 = (1 - S_{11})(1 - S_{22}) - S_{12}S_{21}$$

2. Transformation from the Z parameter to the Y parameter.

$$Y_{11} = \frac{Z_{22}}{\Delta Z}, \quad Y_{22} = \frac{Z_{11}}{\Delta Z}$$

$$Y_{12} = -\frac{Z_{12}}{\Delta Z}, \quad Y_{21} = -\frac{Z_{21}}{\Delta Z}$$

In the above equations:

$$\Delta Z = Z_{11}Z_{22} - Z_{12}Z_{21}$$

3. Transformation from the Y parameter to the S parameter.

$$S_{11} = \frac{(1 - Z_0 Y_{11})(1 + Z_0 Y_{22}) + Y_{12}Y_{21}Z_0^2}{\Psi_2}$$

$$S_{22} = \frac{(1 + Z_0 Y_{11})(1 - Z_0 Y_{22}) - Y_{12}Y_{21}}{\Psi_2}$$

$$S_{12} = \frac{-2Y_{12}Z_0}{\Psi_2}, \quad S_{21} = \frac{-2Y_{21}Z_0}{\Psi_2}$$

In the above equations, $Z_0 = 50\Omega$ is the characteristic impedance of the system and

$$\Psi_2 = (1 + Z_0 Y_{11})(1 + Z_0 Y_{22}) - Y_{12}Y_{21}Z_0^2$$

F Holder case design for $T = 10 \mu\text{s}$ RAC

The top view of the holder case for the $10 \mu\text{s}$ chirp filter is depicted in Figure F.1; the front view is in Figure F.2; and the bottom view is in Figure F.3.

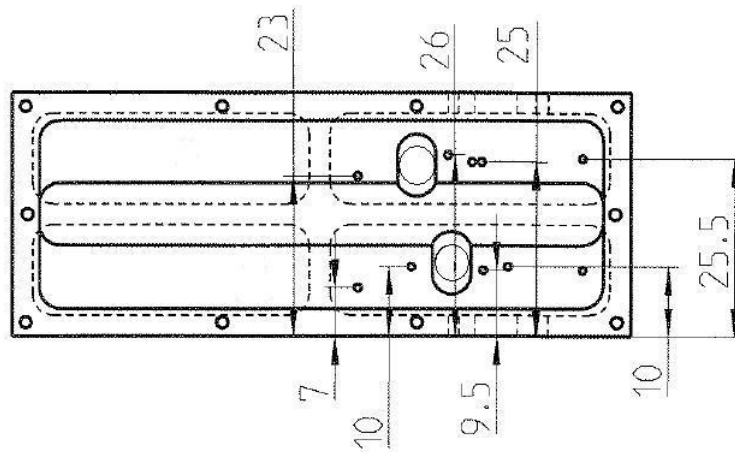


Figure F.1: Holder case top view for the $T = 10 \mu\text{s}$ chirp filters, unit: mm.

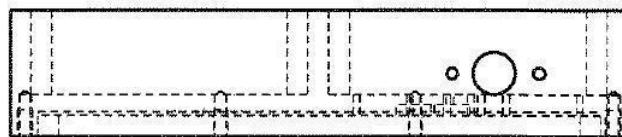


Figure F.2: Holder case front view for the $T = 10 \mu\text{s}$ chirp filters, unit: mm.

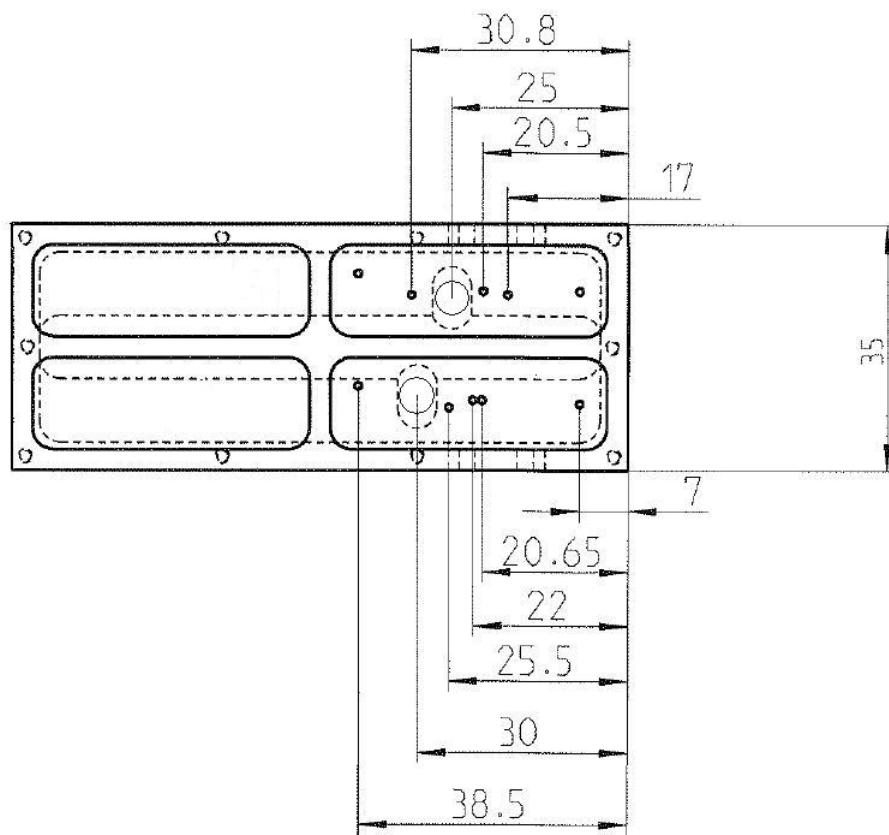


Figure F.3: Holder case bottom view for the $T = 10 \mu\text{s}$ chirp filters, unit: mm.

Bibliography

- [1] M. A. Janssen, *Atmospheric Remote Sensing by Microwave Radiometry*, John Wiley and Sons, 1993.
- [2] Miriam Rengel, Paul Hartogh, Christofer Jarchow, *HHSMT observations of the Venusian mesospheric temperature, winds, and CO abundance around the MESSENGER flyby*, Planetary and Space Science, Vol. 56, pp. 1688-1695, 2008.
- [3] S. Gulkis, M. Frerking, J. Crovisier, G. Beaudin, P. Hartogh, P. Encrenaz, T. Koth, C. Kahn, Y. Salinas, R. Nowicki, R. Irigoyen, M. Janssen, P. Stek, M. Hofstadter, M. Allen, C. Backus, L. Kamp, C. Jarchow, E. Steinmetz, A. Deschamps, J. Kreig, M. Gheudin, D. Bockelee-Morva, N. Biver, T. Encrenaz, D. Despois, W. Ip, E. Lellouch, I. Mann, D. Muhleman, H. Rauer, P. Schloerb and T. Spilker, *MIRO: Microwave Instrument for Rosetta Orbitor*, Space Science Reviews, Vol. 128, pp. 561-597, 2007.
- [4] Mervyn A. Jack, Peter M. Grant and Jeffrey H. Collins, *The theory, design, and applications of surface acoustic wave Fourier-Transform processors*, Proceedings of the IEEE, Vol. 68, No. 4, April 1980.
- [5] R. C. Williamson and H. Smith, *The use of surface-elastic-wave reflection gratings in large time-bandwidth pulse-compression filters*, IEEE Transactions on Sonics and Ultrasonics, Vol SU-20, pp. 113-123 1973.
- [6] R. C. Williamson, V. S. Dolat and Henry I. Smith, *L-Band Reflective-Array Compressor with a compression ratio of 5120*, IEEE Ultrasonics Symposium.
- [7] Junjie Gong, Yuxing Zhang, Xianwen Zhou and Paul Hartogh, *Wide Bandwidth SAW Chirp Filters with Improved Magnitude Response*, 2006 Ultrasonics Symposium Proceedings.
- [8] Henry I. Smith, R. C. Williamson and W. T. Brogan, *Ion Beam Etching of Reflective Array Filters*, IEEE Ultrasonics Symposium.
- [9] O. W. Otto and H. M. Gerard, *Nonsynchronous Scattering Loss in Surface Acoustic Wave Reflective Array Compression Filters*, J.Appl.Phys. Vol. 49, pp 3337-3340 1978.
- [10] O. W. Otto and H. M. Gerard, *On Rayleigh wave reflection from grooves at oblique incidence and an empirical model for bulk wave scattering in RAC devices*, 1977 Ultrasonics Symposium Proceedings, IEEE Cat. No. 77CH1264-1SU.

- [11] H. M. Gerard, O. W. Otto and R. D. Weglein, *Development of a Broadband Reflective Array 10000:1 Pulse Compression Filter*, 1974 Ultrasonics Symposium Proceedings, pp. 197-201.
- [12] S. M. Balashov, E. A. Garova and V. P. Plessky, *Theory of Rayleigh-wave Bragg reflection in quasiperiodic structures*, Physical Review B. Vol.42, 1990.
- [13] David P. Morgan, *Surface-Wave Devices for Signal Processing*, Amsterdam, the Netherlands: Elsevier, 1985.
- [14] Colin K. Campbell, *Surface acoustic wave devices for mobile and wireless communications*, California, the United States of America: Academic Press, 1998.
- [15] A. J. Slobidnik Jr., P. H. Carr and A. J. Buedreau, *Microwave Frequency Acoustic Surface Wave Loss Mechanisms on Lithium Niobate*, J. Appl. Phys., Vol. 41, pp. 4380-4387 (1970).
- [16] Evert N. Fowle, *The design of FM pulse compression signals*, IEEE Transactions on Information Theory, 1964.
- [17] T. A. Martin, *The IMCON Pulse Compression Filter and Its Applications*, IEEE Transactions on Microwave Theory and Techniques MTT21, April 1973, pp 111-119.
- [18] Yongan Shui, *Surface acoustic wave and surface acoustic wave devices*, Lecture book for Nan Jing University, 1998.
- [19] Weibiao Wang, *Rigorous simulation of finite length surface acoustic wave devices*, PhD thesis, PhD defense in Nan Jing University in 2004.
- [20] J. Melngailis and R. C. M. Li, *Measurement of impedance mismatch and stored energy for right-angle reflection of Rayleigh waves from grooves on Y cut LiNbO₃*, 1975 Ultrasonics Symposium Proceedings, IEEE Cat. Vol. 75 CHO 994-4SU.
- [21] R. C. M. Li and J. Melngailis, *The influence of stored energy at step discontinuities on the behavior of surface wave gratings*, IEEE transactions on Sonics and Ultrasonics, Vol. SU-22, pp. 189-198, May 1975.
- [22] Alexander Darinskii, Manfred Weihnacht, Hagen Schmidt, *SAW Reflection from Surface Inhomogeneities of Isotropic and Anisotropic Substrates*, IEEE transactions on Sonics and Ultrasonics, 2009.
- [23] Rudolf T. Schieder, Oliver Siebertz, Csaba Gal, Michael Olbrich, Frank Schloeder, R. Bieber, Frank Schmuelling, Volker Tolls and Jochen M. M. Horn, *Toward very large bandwidth with acousto-optical spectrometers*, SPIE Proceedings, Vol. 4855, pp. 290, June 2003.
- [24] Bernd Klein, Sabine D. Philipp, Rolf Guesten, Ingo Kraemer and Dorothea Samtleben, *A new generation of spectrometers for radio astronomy: Fast Fourier Transform Spectrometer*, Internet downloaded.

-
- [25] Sanna Harma, Victor Plessky, *Extraction of Frequency-Dependent Reflection, Transmission, and Scattering Parameters for Short Metal Reflectors from FEM-BEM Simulations*, IEEE Transactions on Ultrasonics, Ferroelectrics, and Frequency Control, Vol. 55, No. 4, April 2008.
- [26] Oberdan W. Otto, *Multiple Reflection in Acoustic Surface Wave Reflective Arrays*, IEEE Transactions on Sonics and Ultrasonics, Vol. SU-22, No. 4, July 1975.
- [27] P. D. Bloch, E. G. S. Paige and L. Solymar, *Reflection of surface acoustic waves from arrays of stripes*, IEEE Ultrasonics Symposium Proceedings, Cat. 78CH1344-1SU, 1978.
- [28] H. M. Gerard and G. W. Judd, *500MHz bandwidth RAC filter with constant groove depth*, 1978 Ultrasonics Symposium Proceedings, IEEE Cat. #78CH1344-1SU.
- [29] Paul Hartogh, *The Mars Volcanic Emission and Life Scout (MARVEL)*, Internal team seminar of Max Planck Institute for Solar System Research, 7th July, 2006.
- [30] Sanna Harma, *Surface Acoustic Wave RFID Tags: Ideas, Developments, and Experiments*, PhD thesis, Helsinki University of Technology, 2009.
- [31] Geronimo Luis Villanueva Sozzi, *The high resolution spectrometer for SOFIA-GREAT: Instrumentation, Atmospheric Modeling and Observations*, PhD thesis, Max Planck Institute for Solar System Research, 2004.
- [32] G. Villanueva and Paul Hartogh, *The high resolution chirp transform spectrometer for the SOFIA-GREAT instrument*, Experimental Astronomy, Vol. 18, pp. 77-91, 2004.
- [33] Lucas Paganini, *Power spectral density accuracy in Chirp Transform Spectrometers* PhD thesis, Max Planck Institute for Solar System Research, 2008.
- [34] S. Lehtonen, V. Plessky and M. Salomaa, *Short reflectors operating at the fundamental and second harmonics on 128°LiNbO_3* , IEEE Transactions on Ultrasonics, Ferroelectrics, and Frequency Control, Vol. 51, pp. 343-351, Mar. 2004.
- [35] S. Lehtonen, V. Plessky, N. Bereux and M. Salomaa, *Minimum-loss short reflectors on 128°LiNbO_3* IEEE Transactions on Ultrasonics, Ferroelectrics, and Frequency Control, Vol. 51, pp. 1203-1205, Oct. 2004.
- [36] S. Lehtonen, V. Plessky, N. Bereux and M. Salomaa, *Phases of the SAW reflection and transmission coefficients for short reflectors on 128°LiNbO_3* , IEEE Transactions on Ultrasonics, Ferroelectrics, and Frequency Control, Vol. 51, pp. 1671-1682, Dec. 2004.
- [37] W. Wang, T. Han, X. Zhang, H. Wu, and Y. Shui, *Rayleigh wave reflection and scattering calculation by source regeneration method*, IEEE Transactions on Ultrasonics, Ferroelectrics, and Frequency Control, Vol. 54, pp. 1445-1453, July 2007.
- [38] Peter V. Wright and Hermann A. Haus, *A closed-form analysis of reflective-array gratings*, IEEE Ultrasonics Symposium, 0090-5607/80/0000-0282, 1980.

- [39] Dr. Leland P. Solie, *A new low-loss, single-bounce, reflective array filter using hyperbolically tapered transducers*, IEEE Ultrasonics Symposium, 0090-5607/86/0000-0077, 1986.
- [40] V. S. Dolat and R. C. Williamson, *BGO reflective-array compressor (RAC) with 125 μ s of dispersion*, IEEE Ultrasonics Symposium Proceedings, IEEE Cat. 75 CHO 994-4SU, 1975.
- [41] B. R. Potter, C. S. Hartmann and W. R. Shreve, *Slanted Reflective Array Correlator*, IEEE Ultrasonics Symposium, CH1355-7/78/0000-0453, 1978.
- [42] C. Waterkeyn and H. Gautier, *Detailed analysis of slanted reflective array compressors*, IEEE Ultrasonics Symposium, 0090-5607/83/0000-0195, 1983.
- [43] H. Van de Vaart and L. P. Solie, *A SAW Pulse compression filter using the reflective dot array (RDA)*, Appl. Phys. Lett., Vol. 31, No. 1, pp1-3, July 1977.
- [44] R. E. Chapman, R. K. Chapman, D. P. Morgan and E. G. S. Paige, *Weighted in-line Reflective Array Devices*, IEEE Ultrasonics Symposium, CH1482-9/79/0000-0696, 1979.
- [45] T. Kitano, K. Nishikawa and K. Asakawa, *Amplitude weighted metal strip reflective array compressor*, IEEE Ultrasonics Symposium Proceedings, Cat. 77CH1264-1SU, 1977.
- [46] J. T. Godfrey, C. H. Grauling, R. A. Moore, C. E. Nothnick and R. J. Armantrout, *Improvements in metalized RAC design*, IEEE Ultrasonics Symposium Proceedings, Cat. 77CH1264-1SU, 1977.
- [47] Ziping Shen, Huaying Ren and Daihua Tang, *Long delay reflection grating dispersive delay line*, Piezoelectrics and Acoustooptics (China), Vol. 14, No. 5, October, 1992.
- [48] Chen Dongpei, Gong Junjie, Xianwen Zhou, Shu Jie and Yulan Wei, *Practical large bandwidth high resolution SAW linear frequency modulated transform power spectrometer*, Acta Acoustica (China), Vol. 16, No. 1, January, 1991.
- [49] Arne Ronnekleiv, *Amplitude and Phase compensation of RAC-type chirp lines on Quartz*, IEEE Ultrasonics Symposium, 0090-5607/88/0000-0169, 1988.
- [50] S. Gopani, R. B. Brown, J. H. Hines and B. H. Horine, *Reflective Array SAW Narrowband Filters*, IEEE Ultrasonics Symposium, 1051-0117/90/0000-0055, 1990.
- [51] Frederick Huang and Edward G. S. Paige, *The design of SAW RAC's using arrays of thin metal dots*, IEEE Transactions on Ultrasonics, Ferroelectrics, and Frequency Control, Vol. 41, No. 2, March, 1994.
- [52] Robert F. Milsom, N. H. C. Reilly and Martin Redwood, *Analysis of generation and detection of Surface and Bulk Acoustic Waves by interdigital transducers*, IEEE Transactions on Sonics and Ultrasonics, Vol. SU-24, No. 3, May 1977.

-
- [53] Pascal Ventura, Jean Michel Hode and Bruno Lopes, *Rigorous Analysis of Finite SAW Devices with Arbitrary Electrode Geometries*, IEEE Ultrasonics Symposium, 0-7803-2940-6/95, 1995.
- [54] Pascal Ventura, Jean Michel Hode and Marc Solal, *A new efficient combined FEM and Periodic Green's function formalism for analysis of Periodic SAW Structures*, IEEE Ultrasonics Symposium, 0-7803-2940-6/95, 1995.
- [55] Pascal Ventura, J. M. Hode, M. Solal, J. Desbois, J. Ribbe, *Numerical Methods for SAW Propagation Characterization*, IEEE Ultrasonics Symposium, 0-7803-4095-7/98, 1998.
- [56] G. Kovacs, M. Anhorn, H. E. Engan, G. Visintini and C. C. W. Ruppel, *Improved Material Constants for LiNbO₃ and LiTaO₃*, IEEE Ultrasonics Symposium, 1051-0117/90/0000-0435, 1990.
- [57] Jiming Lin, Ning Wang, Hui Chen and Yongan Shui, *Fast, precise and full extraction of the COM parameters for multielectrode-type gratings by periodic Green's function method*, IEEE Transactions on Ultrasonics, Ferroelectrics, and Frequency Control, Vol. 49, No. 12, December 2002.
- [58] David P. Morgan, *Quasi-Static Analysis of Generalized SAW Transducers Using the Green's Function Method*, IEEE Transactions on Sonics and Ultrasonics, Vol, SU-27, No. 3, May 1980.
- [59] Victor Plessky, *Simulation of SAW velocity dependency on deposited Al film thickness for YX LiNbO₃ using FEM/BEM*, Private communication.
- [60] Takashi Yamamoto, Hirotake Okino, Eiji Matsuzaki and Yuji Yamashita, *Piezoelectric properties of KNbO₃ in various crystal orientations by FEM analysis*, IEEE Ultrasonics Symposium, 7803-7414-2/02, 2002.
- [61] Julien Eschbach, Brice Vincent, Didier Rouxel, Mohamed El Hakiki and Omar Elmazria, *Temperature Study of Potassium Niobate (KNbO₃) Elastic Constants by Brillouin Spectroscopy*, IEEE Transactions on Ultrasonics, Ferroelectrics, and Frequency Control, Vol. 56, No. 3, March 2009.
- [62] Thomas B. Pollard, Thomas D. Kenny, John F. Vetelino and Mauricio Pereira da Cunha, *Pure SH-SAW Propagation, Transduction and Measurements on KNbO₃*, IEEE Transactions on Ultrasonics, Ferroelectrics, and Frequency Control, Vol. 53, No. 1, January 2006.
- [63] B.P. Abbott, C.S. Hartmann and D.C. Malocha, *A coupling of modes analysis of chirp transducers containing reflective electrode geometries*, IEEE Ultrasonics Symposium, 0090-5607/89/0000-0129, 1989.
- [64] B.P. Abbott and D.C. Malocha, *Closed Form Solutions for Multistrip Coupler Operation Including the Effects of Electrode Resistivity*, IEEE Ultrasonics Symposium, 1051-0117/90/0000-0025, 1990.

- [65] C.S. Harmann and B.P. Abbott, *Overview of design challenges for single phase unidirectional SAW filters*, IEEE Ultrasonics Symposium, 0090-5607/89/0000-0079, 1989.
- [66] Saku Lehtonen, Victor Plessky, *Unidirectional SAW Transducer for Gigahertz Frequencies*, IEEE Transactions on Ultrasonics, Ferroelectrics, and Frequency Control, Vol. 50, No. 11, November 2003.
- [67] Clemens C. W. Ruppel, Werner Ruile, Gerd Scholl, Karl Ch. Wagner and O. Maenner, *Review of Models for Low-Loss Filter Design and Applications*, IEEE Ultrasonics Symposium, 1051-0117/94/0000-0313, 1994.
- [68] Guenter Kovacs, *A generalised P-matrix model for SAW filters*, IEEE Ultrasonics Symposium, 0-7803-7922-5/03, 2003.
- [69] B. P. Abbott, *A Coupling-of-modes model for SAW transducers with arbitrary reflectivity weighting*, PhD thesis, Department of Electrical Engineering at the University of Central Florida, 1992.
- [70] K. Uehara, C. M. Yang, T. Shibata, S. K. Kim, S. Kameda, H. Nakase and K. Tsubouchi, *Fabrication of 5GHz Band SAW Filter with Atomically-Flat-Surface AlN on Sapphire*, IEEE Ultrasonics Symposium, 0-7803-8412-1/04, 2004.
- [71] K. Hohkawa, M. Yokota, K. Koh, K. Nishimura and N. Shigekawa, *Wideband Layer Mode Acoustic Devices on GaN/Sapphire Substrate*, IEEE Ultrasonics Symposium, 1051-0117/06, 2006.
- [72] Tsungtsong Wu and Weishan Wang, *An experimental study on the ZnO/sapphire layered surface acoustic wave device*, Journal of Applied Physics, Vol. 96, No. 9, November 2004.
- [73] T. Mitsuyu, O. Yamazaki and K. Wasa, *A 4.4GHz SAW filter using a single-crystal ZnO film on sapphire*, IEEE Ultrasonics Symposium, 0090-5607/81/0000-0074, 1981.
- [74] P. Hartogh and G.K. Hartmann, *A high-resolution chirp transform spectrometer for microwave measurements*, Meas. Sci. Technology, 0957-0233/90/070592+04, 1990.
- [75] A.O. Benz, P.C. Grigis, V. Hungerbuehler, H. Meyer, C. Monstein, B. Stuber and D. Zardet, *A broadband FFT spectrometer for radio and millimeter astronomy*, Astronomy and Astrophysics, Vol. 442, pp. 767-773, 2005.
- [76] A. Emrich, S. Andersson, Mikael Krus, *Spectrometers for (sub)mm radiometers*, IEEE, Millimeter Waves Systems, 1-4244-0400-2/06, 2006.
- [77] Gordon G. Brown, Brian C. Dian, Kevin O. Douglass, Scott M. Geyer, Steven T. Shipman and Brooks H. Pate, *A broadband Fourier transform microwave spectrometer based on chirped pulse excitation*, Review of Scientific Instruments, Vol. 79, 053103, 2008.

- [78] Michel Chomiki, *SAW-based solutions for UWB Communications*, European Radar Conference (EURAD), pp. 263-266, Oct 2005.
- [79] Victor Plessky, *SAW Modeling Techniques*, Short Course Lecture for IEEE International Ultrasonics Symposium 2008 in Beijing.
- [80] S. Wolf and R. N. Tauber, *Silicon Processing for the VLSI Era, Volume 1-Process Technology*, United States of America, Lattice Press, 1990, Chapter 14.
- [81] Reinhold Ludwig and Pavel Bretchko, *RF Circuit Design: Theory and Applications*, United States of America, Publishing House of Electronics Industry, 2002.
- [82] Superconductor Technologies Inc, www.supotech.com.

Publications

Journal Publications

[1] Feasibility of Ultra-Wideband SAW Tag Meeting FCC Rules.
IEEE Transactions on Ultrasonics, Ferroelectrics, and Frequency Control, 2008.
Authors: Sanna Harma, Xianyi Li, Victor Plessky and Paul Hartogh

[2] Duty Cycle Weighting using e-beam lithography in RACs with constant groove depth for Chirp Transform Spectrometers.
Advances in Geosciences, 2009.
Authors: Xianyi Li, Leonhard Reindl, Thomas Weimann, Victor Plessky and Paul Hartogh

Conference Publications

[3] Revisiting of RAC devices.
IEEE International Ultrasonic Symposium, 2009.
Authors: Xianyi Li, Victor Plessky, Thomas Weimann, Leonhard Reindl, Paul Hartogh and V.I.Grigorievsky

Acknowledgements

It is hard to express in this short statement my gratitude to all the people who contributed to the development of this thesis; their help has been invaluable. First I would like to thank Prof. Gao Jie of SiChuan University and Prof. Franz Josef Alhers at PTB. They supplied me with the opportunity for doing this PhD in Germany. I would especially like to thank my supervisor in MPS, Dr. Paul Hartogh, for constantly posing new challenges in this subject and sharing his knowledge of mm and submm wave remote sensing and chirp transform spectrometers. Also I feel honored and grateful to the Max-Planck-Society for providing financial support to an international student to undertake research on such an interesting topic.

I would like to thank my supervisor at Albert-Ludwigs-University Freiburg, Prof. Leonhardt Reindl, for his interest in my work and the constructive discussions in modeling of RAC devices.

I would like to thank Dr. Victor Plessky at GVR Trade Neuchatel for his guidance and for sharing his knowledge of SAW devices.

I thank my supervisor at PTB, Dr. Thomas Weimann for his training with all the clean room facilities, and for all the electron beam lithographies, also for his valuable help in establishing the research conditions for me in PTB.

Thanks also to my colleagues at MPS, Dr. Christopher Jachow for the fruitful discussions in the microwave remote sensing in atmospheric observations. Thanks go to Dr. Lucas Paganini, for his compressed pulse measurements for RAC filters in the CTS. And thank you to Mr. Anneman in the mechanical workshop at MPS for making all the RAC filter holders for me; without the holders, the RAC filter can hardly work.

I would also like to thank my colleagues at PTB. I am grateful to Mr. Peter Hinze for all the discussions with me about the nanostructure fabrications, and for all the atom force microscope measurements for my sample and also for the scanning electron microscope and transmission electron microscope photos he took for my RAC filters. Also I would like to thank Mr. Rudige Wendisch for all his helps with the Ar ion-beam etching processes of RACs.

For all the three years I lived in Braunschweig which is about 10 000 kilometers from my hometown in China, many close friends made me feel at home, thanks to Jinni Lee, Min Hu, Ang Li, Lili Zhang and Jan Kowalewski.

Finally, and most importantly, I would like to thank my parents, Changzhi Li and Qiao Fan, for their unconditional support in the completion of my dreams and my beloved, Fengjun Han, who was always there to accompany me with her love and patience. I am very grateful to you Fengjun!

Curriculum Vitae

Personal data

Name : Xianyi Li
Date of birth : 21st, July, 1981
Place of birth : Shihezi City, Xinjiang Province, China
Nationality : Chinese



Junior School

Aug. 1993 - Jun. 1999:
First junior school of Shihezi city, Xinjiang Province China.

Study

Bachelor: (Aug. 1999 - Aug. 2003)
University of electronic science and technology of China.
Major: Testing and control technology.

Master: (Sep. 2003 - Aug. 2006)
University of electronic science and technology of China.
Major: Metrology technology and instrument.

PhD: (Sep. 2006 - Apr. 2010)
Max Planck Institute for Solar System Research (MPS), Physikalisch-
Technische Bundesanstalt (PTB) and University of Freiburg, Ger-
many.
Major: SAW chirp filter and Chirp Transform Spectrometer de-
velopments for atmospheric remote sensing.